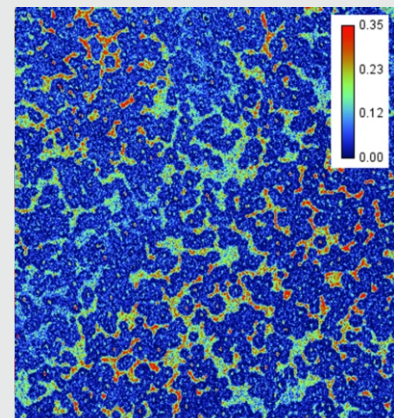
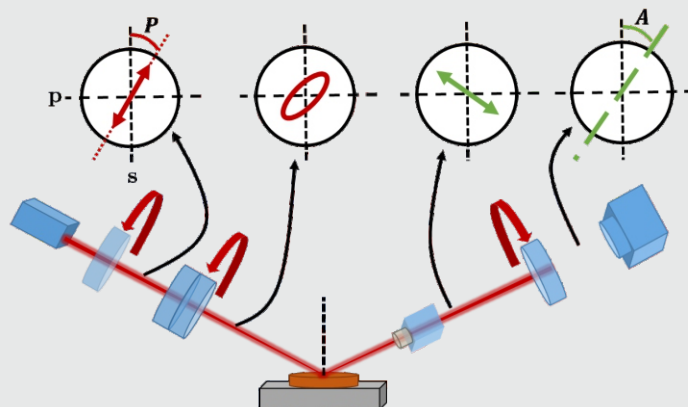
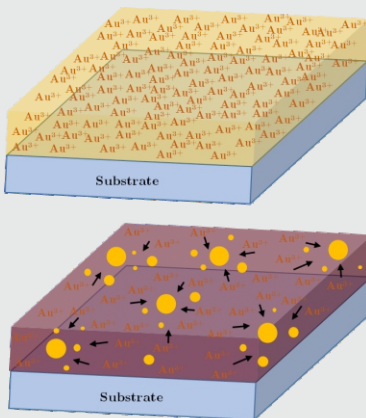


PhD Thesis
2020

Plasmonic nanocomposites embedding gold and silver nanoparticles: *in situ* synthesis and local optical properties by spectroscopic imaging ellipsometry

Corentin Guyot



Plasmonic nanocomposites embedding gold and silver nanoparticles: in situ synthesis and local optical properties by spectroscopic imaging ellipsometry

Guyot Corentin

Thesis presented in fulfilment of the requirements for the degree of
Doctor of Sciences

Thesis supervisor
Michel VOUE

University of Mons
Faculty of Sciences
Materials Physics and Optics Unit

Academic year
2019-2020

Supervisor

Prof. Michel Voué

University of Mons

Jury members

Prof. Yves Gossuin

University of Mons

Prof. Philippe Leclère

FRS-FNRS University of Mons

Prof. Bjorn Maes

University of Mons

Prof. Olivier Deparis

University of Namur

Dr. Yann Battie

University of Lorraine

University of Mons

Faculty of Sciences

Materials Physics and Optics Unit (LPMO)

Place du Parc 20

7000 Mons

Belgium

Tel.: +32-65/37.34.01

<http://www.umons.ac.be>

ISBN: 978-2-87325-127-7

Contents

Acknowledgements	i
Summary	iv
List of figures	vi
List of tables	ix
List of abbreviations	xii
Work Map	1
1 General introduction	1
1.1 Context	1
1.2 Outline	3
1.3 Publications	5
2 State of the art	7
2.1 Metallic nanoparticles	7
2.2 Plasmonic nanocomposites	10
2.2.1 Silver nanocomposites	14
2.2.2 Gold nanocomposites	19
2.3 Main outcomes of the literature survey	22
3 Theoretical concepts	25
3.1 Polarization states of light	25
3.1.1 Optical process	25

3.1.2	Optical coefficients	26
3.1.3	Complex refractive index	27
3.1.4	Polarization of light	28
3.1.5	Jones Matrix	29
3.2	Optical properties of noble metal nanoparticles	31
3.2.1	Lorentz model	31
3.2.2	Drude Model	34
3.2.3	Surface plasmon resonance	35
3.2.4	Localized surface plasmon resonance	36
3.2.5	Effective medium	40
3.2.6	The Kramers-Krönig relationships	43
3.3	Reflection and transmission of polarized light	43
3.3.1	Reflection and refraction between two isotropic media	44
3.3.2	Reflection and transmission by a thin film on a substrate	46
4	Materials and Methods	49
4.1	Experimental devices	49
4.1.1	Spectrophotometry	49
4.1.2	Spectroscopic reflectometry	51
4.1.3	Spectroscopic ellipsometry	53
4.1.4	Spectroscopic imaging ellipsometry	57
4.1.5	Atomic force microscopy	59
4.2	Preparation method of nanocomposites	61
4.2.1	Spin coating	62
4.2.2	Experimental process	63
4.2.3	Heating stage	66
5	Silver nanoparticles embedded in PVA matrix	67
5.1	Introduction	67
5.2	Optical properties of the polymer matrix	68
5.3	Spectrophotometry measurements of silver nanocomposites	71
5.3.1	Absorption spectrum of thick highly doped films	72
5.3.2	Real-time absorption spectra of AgNPs in PVA matrix	74
5.4	Variation of the film thickness at a constant metal/polymer mass ratio	76
5.5	Film thickness and silver doping effects	80
5.5.1	Modeling of the optical properties	81
5.5.2	Multivariate analysis on the resonance parameters	85
5.6	Topographic surface characterization	91
5.7	Conclusion	94
6	Gold nanoparticles embedded in PVA matrix	97
6.1	Introduction	97
6.2	Spectrophotometry measurements of gold nanocomposites	100
6.2.1	Absorption spectrum of highly doped films	100
6.2.2	Real-time absorption spectra of AuNPs in PVA matrix	102
6.3	Topographic surface characterization	104
6.4	Annealing and local optical properties	106

6.4.1	Time evolution of Ψ and Δ mappings	108
6.4.2	Statistical analysis of Ψ and Δ maps	112
6.4.3	Theoretical constant angle of incidence curves	117
6.5	Spectroscopic reflectometry measurements	123
6.6	Conclusion	125
7	Spectroscopic imaging ellipsometry of gold and silver nanocomposites	129
7.1	Introduction	129
7.2	Gold nanocomposites at low doping level	130
7.2.1	Modeling of the optical properties	131
7.2.2	Global optical properties of the Au–PVA thin films	132
7.2.3	Local optical properties of the Au–PVA thin films	134
7.3	Silver nanocomposites at high doping level	138
7.3.1	Modeling of the optical properties	139
7.3.2	Local optical properties of the Ag–PVA thin films	139
7.4	Conclusion	141
8	Conclusion and outlook	145
	Bibliography	151

Acknowledgements

Tout d'abord, des non-remerciements au SARS-CoV-2 qui ne m'aura pas permis de présenter la soutenance publique de thèse entouré de ma famille, mes amis et collègues. Néanmoins, je pense que beaucoup se souviendront de cette période de 2020 et moi le premier.

Mes remerciements commenceront donc ici. Attention, il est possible que ça soit long.

Mes premières pensées vont tout naturellement vers la personne qui m'a encadrée durant toutes ces années : Prof. Michel Voué. C'est peut-être votre passé en tant qu'assistant qui a joué, mais je voulais vous remercier pour ces presque huit années de collaboration sous le signe de l'humanité et du partage. Vous avez été d'une aide et d'une écoute incroyable, joignable à la moindre détresse tant en recherche qu'en enseignement. Toujours les mots justes et le petit coup de pouce quand il le fallait. Difficile de rêver mieux comme premier chef. En fin de Master 2, en 2012, je ne savais pas trop dans quoi je m'engageais : affronter les étudiants en devenant assistant et commencer un doctorat en ellipsométrie. Mais, grâce à vous, à vos encouragements constants et votre confiance en moi tout a été beaucoup plus simple. Merci aussi pour les moments de détente lors de nos voyages professionnels. Peut-être qu'un jour j'arriverai à te tutoyer. Encore merci !

Je remercie également les Profs. Yves Gossuin et Bjorn Maes qui m'ont encadré durant la thèse en faisant partie de mon comité d'accompagnement. Ils ont toujours su trouver les bons mots pour me motiver et m'encourager. Malgré la lourde tâche d'assistant, ils m'ont toujours soutenu en considérant que mon travail allait dans le bon sens. Pour les nombreuses discussions scientifiques ou sur d'autres sujets (bières, diables rouges, running, trail, ...), encore un grand merci !

Je remercie également les autres membres du jury qui ont lu, suggéré des corrections et m'ont aidé dans la rédaction finale de cette thèse. Merci aux Prof. Olivier Deparis, Prof. Philippe Leclère et Dr. Yann Battie pour les nombreuses discussions scientifiques lors de l'écriture d'articles scientifiques, lors de prises de mesure sur mes échantillons ou lors de conférences sur l'ellipsométrie.

De manière évidente, je remercie mes parents qui ont toujours été là pour moi. C'est grâce à eux qu'en 2012, je suis devenu physicien. Quelques années plus tard, c'est encore, en partie, grâce à eux que je vais être docteur en Sciences. Vous avez toujours su trouver les mots pour me faire relativiser. Merci pour les voyages en famille que vous avez organisés qui m'ont permis de prendre le temps de vivre des moments auprès de vous et des êtres qui me sont chers. Ces moments en famille sont incroyablement ressourçant et croyez-moi, cela m'a fait énormément de bien. Ce travail est aussi un peu pour vous. Vous dire merci et vous rendre fier. Vous êtes tellement incroyables ! Vous êtes mes héros.

Céline, merci à toi qui as dû endurer tout cela. Tu es une personne exceptionnelle et ces derniers mois me l'ont encore prouvé. Tu m'as constamment soutenu et tu m'as toujours motivé. Tu as été d'une patience incroyable avec moi et ce travail. Toujours à l'écoute et tellement avenante, tu m'as aidé plus que tu ne le crois. Tu as toujours les bons mots pour me faire avancer et en particulier dans les moments un peu moins faciles. Je sais que je n'applique pas tes méthodes pour être productif,

mais sache que parfois j'essaie... Merci pour nos magnifiques voyages, nos longues balades qui me permettent de relativiser et de prendre du temps pour nous. Je suis comblé grâce à toi. J'ai de la chance de t'avoir dans ma vie, merci encore, je t'aime.

Un énorme merci à ma sœur, mon frère, Julie, Yaya, Alice, Camille, Jules et Arthur ! Vous n'imaginez pas à quel point c'est un bonheur pour moi de passer du temps avec vous et vos enfants. J'en reviens toujours avec un grand sourire me faisant comprendre que j'ai beaucoup de chance ! C'est un sentiment tellement agréable. Merci pour votre soutien durant toute cette période importante pour moi.

Jules, j'espère qu'un jour tu liras ces quelques lignes (ou le livre en entier, on ne sait jamais) et que tu seras fier de ton parrain.

Je remercie aussi mes beaux-parents pour toutes les attentions qu'ils ont pour moi et Céline ! Vous êtes super gentils avec nous et toujours disponibles pour nous ! Merci à la famille de Céline pour les nombreux encouragements durant ces nombreuses années de doctorat. Merci à mon frère Alexandre, Sandy, Alice, Jérôme, Grégory et Perrine.

Il y a une personne que je dois remercier tout particulièrement c'est le Dr. Gilles Rosolen. Cet ami avec qui j'ai fait mes études et qui est devenu mon colocataire et aussi mon collègue. J'ai passé, grâce à toi, des années incroyables au bureau ! Je me demande ce que ça fera d'être dans un bureau sans toi. Je n'ose pas l'imaginer pour l'instant. Un remerciement spécial car tu as passé énormément de temps sur la relecture de ce manuscrit et pour ça je n'ai pas assez de mots pour te dire merci. Lorsqu'on m'a dit que ce manuscrit était bien écrit, j'ai directement eu une pensée pour toi ! Merci pour tout ce que tu as fait pour moi pour ce travail mais également durant toutes ces années où nous avons grandi ensemble ! Tu m'as apporté tellement de choses, plus que tu ne le penses ! Je n'oublierai jamais ces quelques années de collocation avec Céline et puis avec Lin ! Car bien évidemment, il n'y pas de Gilles sans Lin, alors merci à toi aussi pour les nombreux moments de détente passés entre nous ! Merci.

Je tiens aussi à remercier Céline et Jf qui ont toujours été présents pour moi. Dans les bons et mauvais moments. Vous êtes des amis extraordinaires ! Nous continuons à franchir les étapes ensemble et à se soutenir, c'est, je pense, ce qui fait la force de notre amitié ! Je suis tellement heureux que vous soyez dans ma vie et qu'on puisse vivre encore de belles choses tous ensemble. Merci pour votre soutien au quotidien !

Je remercie aussi mes amis brasseurs : Julien, Ludo et Lucas ainsi que le Dr. Julien de Grenoble. Merci pour ces moments de déconnexion entre nous à faire de la bière. Je reviens toujours d'un brassage avec le plein d'énergie et ce, grâce à vous. Merci aussi à Léa, Anne-k bien évidemment.

Merci à la Team BJ & BJB pour votre soutien et les nombreux moments de détente passés tous ensemble ! Merci au BC Mons Utd pour la bonne ambiance et l'esprit d'équipe qui permet de se surpasser au mini foot mais aussi au-delà du sport ! Merci à ces nombreuses 3ème mi-temps qui m'ont enlevé quelques heures de sommeil.

Je passe maintenant aux collègues du bureau si je peux encore les appeler comme ça vu qu'aux fils des années, ils sont devenus des amis. Merci à toi, Prof. Evelyne Daubie de m'avoir tout appris ! Tu m'as toujours bien encadré et toujours bien aidé

que ce soit pour les Tps, les cours ou même la recherche. Mais je n'oublie pas non plus ton aide pour qu'on se sente toujours bien au bureau et qu'on puisse prendre un peu de temps pour se détendre. Sans toi, je ne serai pas devenu l'assistant que je suis aujourd'hui. Merci à toi, Sabrina Devouge, pour tout ce que tu as fait pour moi ! Je me souviens de notre première rencontre, je ne le savais pas encore, mais quelle chance nous avons que tu aies accepté de travailler avec nous. Tu ne te rends même pas compte de l'aide que tu m'as apportée durant ces années. Tout a été plus simple grâce à toi. Et puis, nos discussions pour faire redescendre la pression ça fait du bien ! Merci pour les nombreuses manipulations faites ensemble. Toi et ta famille, vous êtes des personnes extraordinaires. Merci au Dr. Joseph Hanton qui est d'une gentillesse incroyable ! Merci pour ta bonne humeur constante et tes mots toujours justes. Merci pour tes encouragements et pour les quelques dégustations de bières que nous avons eues.

Je ne peux pas finir ces remerciements sans dire merci à Mathieu Stock, Dr. Fabio Vaianella, Dr. Galaad Altares, Dr. Nicolas Rivolta et, encore une fois, Dr. Gilles Rosolen pour les nombreuses parties de belote qui ont animé nos temps de midi ! Même durant ce confinement, nous avons trouvé un moyen de faire des parties de belote et je trouve ça vraiment beau ! Merci aussi pour votre aide et soutien constant durant tout mon doctorat ! C'est en partie grâce vous que l'assistantat et le doctorat a été compatible pour moi ! Toujours présents pour me faire rire, me faire parler, m'envoyer des vidéos ou des photos montages. Merci pour tout !

Finalement, je voudrais remercier les presque 1200 étudiants à qui j'ai donné cours de physique. Ils ont sans aucun doute apporté, chacun, un petit quelque chose qui fait que je suis devenu celui que je suis aujourd'hui. J'ai vraiment aimé donner ces cours et les étudiants me l'ont généralement bien rendu. Transmettre une partie de son savoir est une chance incroyable et j'y ai donné beaucoup de ma personne pour le faire correctement. Je remercie tout particulièrement Pauline D., Floriane H., Lea M., Romane D., Eduardo T., Guillaume H., Guillaume D., Emilien F. qui pour moi forment un groupe d'amis formidables et qui m'ont redonné goût à l'assistantat après une année difficile. Vous êtes incroyables et je vous souhaite le meilleur !

Merci à vous qui lisez cette thèse ou juste ces longs remerciements.

Je termine ces remerciements par une phrase que je répète souvent aux futurs étudiants lors d'expositions ou journées portes ouvertes : soyez curieux du monde qui vous entoure.

Summary

Plasmonic nanocomposites based on noble metals have numerous applications such as optical sensors, non-linear optical activity-based devices, spectrally selective coatings and sensors for bio-medical diagnostics. This class of new attractive materials, composed of a dielectric matrix and embedded metal nanoparticles (NPs), is a great topic of research due to a peculiar aspect of their optical properties: the Localized Surface Plasmon Resonance (LSPR). Well-known in its effect since e.g. the optical aspect of the Lycurgus cup (4th CE) or of the mosaics of Saint Sabina (5th CE), this LSPR appears when free electrons of the metal are excited by the electromagnetic field associated to the propagation of light. This collective oscillation depends on the geometry of NPs, on the properties of their environment and also their distribution inside the dielectric matrix.

The most popular way to synthesize these plasmonic nanocomposites is the "bottom up" approach, which has two separate steps: metal NPs are synthesized as colloidal solutions and dispersed in a dielectric matrix. In this thesis, we used a different approach based on a "one-pot synthesis" scheme to synthesize the plasmonic materials: an aqueous noble metal salt solution (AgNO_3 for silver or HAuCl_4 for gold) is directly mixed with a polymer solution, the poly-(vinyl) alcohol (PVA). The polymer directly plays the role of the reducing agent and acts as a stabilizer of the NPs, preventing them to aggregate. This synthesis approach has the advantages to be simpler, faster and lead to a concentration of NPs in the nanocomposite higher than other synthesis schemes. However, in the case of 'soft' matrices such as polymers, the reproducibility of the NPs distributions in size, shape ... remains difficult to achieve and slight variations in the experimental conditions leads to different results evidenced by modifications of the plasmon resonance band parameters. Moreover, the detailed mechanism linking the optical properties of the nanocomposite to their structural parameters is today not fully understood although still being the subject of an increasing number of publications.

In this context, we have prepared nanocomposites embedding silver or gold nanoparticles. We first studied the impact of the thickness of the film on the localized surface plasmon resonance parameters. We have shown that this experimental parameter has a large impact on the size of the nanoparticles in situ synthesized in the polymer matrix: the red shift of the plasmon band lead us to conclude that thin nanocomposite films induce a larger size of the produced nanoparticles than in the thicker ones. The variation in the spatial distribution in thin (2D) and thick films (3D) is a possible explanation for the different behavior on the optical properties.

In a second time, we presented an experimental study of the optical properties of gold-doped nanocomposites using single wavelength imaging ellipsometry. We have found that, for a thin polymer film (thickness less than 500 nm) and at low gold-doping level (volume fraction of gold lower than 0.2%), the growth of the gold NPs inhomogeneously occurred within the film. Superimposition of ellipsometric measurements recorded during the annealing and theoretical curves allowed us to decompose the global growth dynamics in two parts: the first one, at the early stage of annealing, corresponding to a decrease of film thickness while the second one is attributed to an increase of the refractive index.

Finally, at this low doping level, the optical constant determined by the conventional spectroscopic ellipsometry spectra is only relevant for the polymer matrix. We have shown the advantage of using imaging spectroscopic ellipsometry by choosing areas on the image with a different intensity contrast. The ellipsometric spectra of each region of interest were different, especially between 400 nm and 600 nm, the spectral region corresponding to the localized surface plasmon resonance of gold nanoparticles (AuNPs). Using a theoretical model based on Effective Medium Approximations (EMAs), we have shown that each zone presents a point-to-point variation of the volume fraction of gold in the polymer. From the ellipsometric maps near the resonance wavelength, we were able to calculate two maps decorrelated from each other: one of the local thickness of the film and a second one of the local volume fraction of AuNPs. Beyond unravelling the role played by the film thickness in the growth of the noble metal nanoparticles, this last result highlights the strength of the spectroscopic imaging ellipsometry as a local optical analysis technique.

List of figures

2.1	Lycurgus cup and stained glass “ <i>Les joueurs d’échecs</i> ”	8
2.2	Lamer diagram	12
2.3	Synthesis schemes of plasmonic nanocomposites	13
2.4	Free-standing films containing AgNPs	16
2.5	Extinction coefficient of the Ag-PVA films	18
2.6	TEM images of AuNPs in PVA films	19
2.7	Schematic representation of AuNPs grown in PVA by laser irradiation	20
3.1	Graphical representation of different optical processes	26
3.2	Schematic description of an electromagnetic wave	28
3.3	Schematic representation of different polarization states	29
3.4	Complex dielectric constant of a dipole oscillator	33
3.5	Complex dielectric function of gold	35
3.6	Representation of surface plasmon resonance	36
3.7	Representation of the localized surface plasmon resonance	37
3.8	Reflection and refraction between two isotropic media	44
3.9	Schematic illustration of an ambient-film-substrate system	46
4.1	Graphical representation of a spectrophotometer	50
4.2	Schematic description of the home-build spectroscopic reflectometer .	52
4.3	Schematic representation of a spectroscopic ellipsometer	55
4.4	Graphical depiction of the imaging ellipsometer	58
4.5	Schematic representation of an AFM	59
4.6	Representation of an artifact	60
4.7	Chemical formula of PVAc and PVA	61
4.8	Graphical illustration of the preparation method of the nanocomposites	64

5.1	Schematic description of the reduction scheme for AgNPs in PVA . . .	68
5.2	Schematic representation of the optical model for SE for PVA	69
5.3	Modeling of the ellipsometric data for PVA thin films	70
5.4	Calibration curve of the spin coater	71
5.5	Absorption spectrum of a glass coated with a thick film of AgNPs . . .	72
5.6	Calculated σ_{ext} for different radius of AgNPs	73
5.7	Real time spectrophotometry of a Ag-PVA film	75
5.8	Absorption spectra of AgNPs embedded in varying PVA concentration	78
5.9	Position of λ_{LSPR} as function of [PVA]	79
5.10	Schematic representation of the optical model of Ag-PVA	82
5.11	Ellipsometric spectra of Ag nanoparticles-doped PVA films	83
5.12	Optical properties of thin and thick silver NPs-doped PVA films . . .	84
5.13	Graphical illustration of the four classes of samples	85
5.14	Scatterplot of the thickness of the film versus A	87
5.15	Scatterplot matrix of the resonance parameters	88
5.16	Box-and-whiskers plots of the resonance peaks parameters	89
5.17	Classification of the weakly and highly Ag-doped film	91
5.18	Topography and phase AFM images of Ag-PVA film	92
5.19	AFM topographic and phase images of the PVA control films	93
5.20	Box-and-whiskers plots of the radius of the particles	93
5.21	Scheme of the NPs growth in thin (2D) and thick (3D) films	95
6.1	Theoretical complex dielectric functions	98
6.2	Calculations (MG-EMA) of the optical properties of AuNPs in PVA .	99
6.3	Absorption spectrum AuNPs embedded in PVA matrix	101
6.4	Real time spectrophotometry of a Au-PVA film	103
6.5	AFM images of AuNPs embedded in PVA matrix	105
6.6	Perimeter-Area relationship of the AuNPs	106
6.7	Ψ and Δ angles maps of Au-doped PVA films.	108
6.8	Intermediate Ψ maps of Au-doped PVA films	110
6.9	Intermediate Δ maps of Au-doped PVA films	111
6.10	Ψ and Δ angles maps of undoped PVA films.	112
6.11	Statistical distributions of the Ψ angles	113
6.12	Statistical distribution of the Ψ angles after annealing	113
6.13	Time evolution of the mean values of ellipsometric angles	115
6.14	Correlation plot between the standard deviation of the Ψ and Δ . . .	115
6.15	Time evolution of selected zones of the Δ map	116
6.16	Evolution of the mean value of the Δ angle in three different zones .	117
6.17	One-layer optical model	118
6.18	Constant angle of incidence Ψ - Δ curves for undoped PVA and Si . . .	119
6.19	Time evolution of the ellipsometric angles during annealing	120
6.20	Constant angle of incidence Ψ - Δ curves for AuNPs in PVA	122
6.21	Reflectivity measurement of undoped and doped PVA	124
7.1	Optical models used to interpret ellipsometric data of AuNPs in PVA	131
7.2	Global ellipsometric response obtained by SE	133
7.3	Ellipsometric enhanced contrast image of the Au-PVA film	134

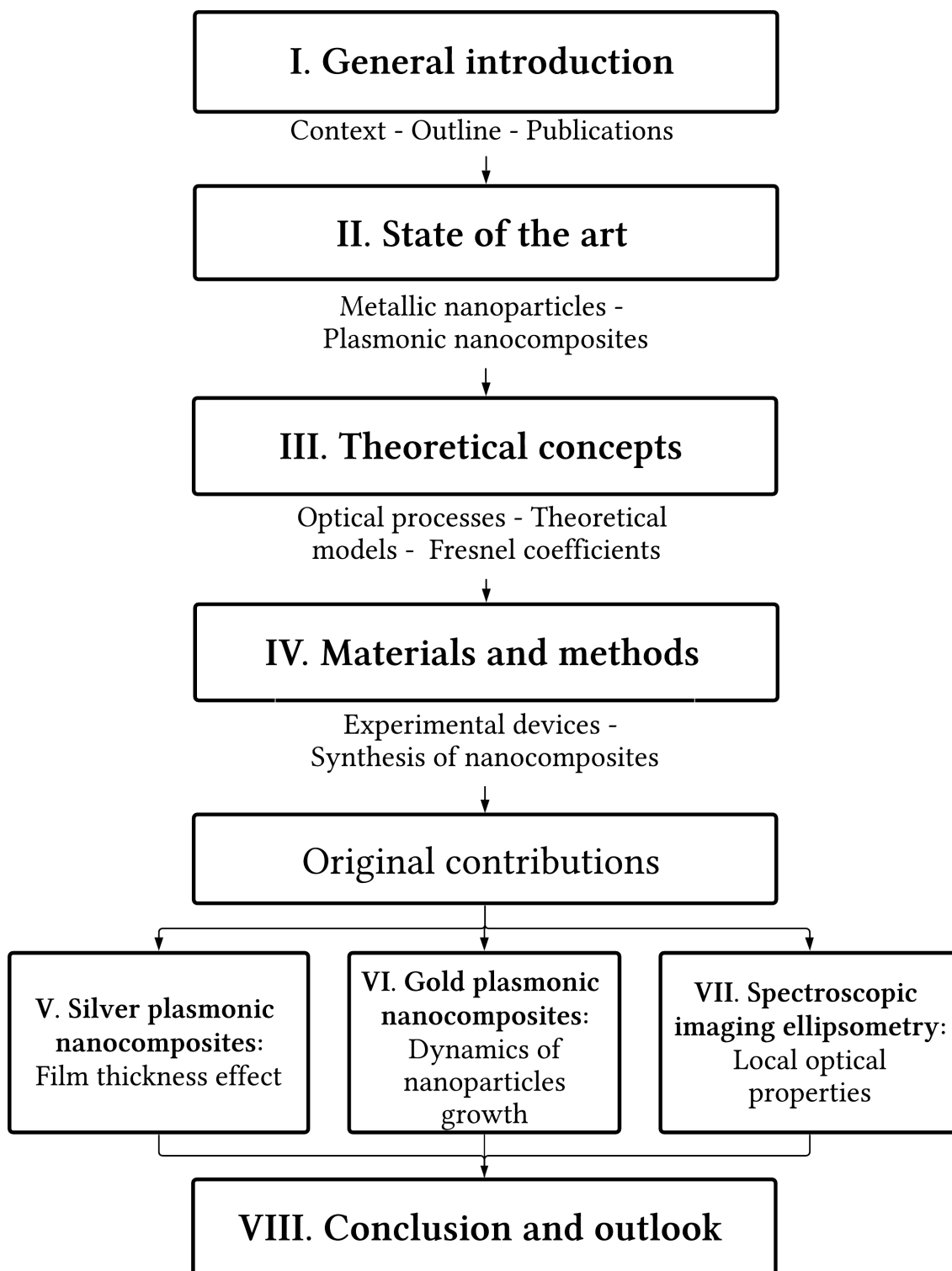
7.4	Ψ and Δ images of the Au–PVA film at different wavelengths	135
7.5	Local spectroscopic optical response of the Au–PVA film	136
7.6	Optical properties of a gold nanocomposite film	137
7.7	Results maps for the gold fraction, relative error and film thickness	138
7.8	Optical model used to interpret SIE data of AgNPs in PVA matrix	139
7.9	Ellipsometric enhanced contrast image of the Ag–PVA film	140
7.10	Optical properties of silver nanocomposite film	141
7.11	Mechanism of growth of AuNPs in PVA	142

List of Tables

2.1	Summary of articles on silver nanocomposites	23
2.2	Summary of articles on gold nanocomposites	24
4.1	Physical properties of gold, silver and PVA	63
5.1	Measured thicknesses of the silver nanocomposite by the EP3-SE	77
5.2	Coating conditions for the four types of samples	81
5.3	Typical parameters of the plasmon absorption peak	84
5.4	Means and standard deviations of the resonance parameters	86
5.5	Summary of the Kruskal-Wallis statistical test	90
5.6	Roughness parameters of doped and undoped PVA films	94
7.1	Best-fit results of the ellipsometric data using MG-EMA	136
7.2	Best-fit results obtained with the SIE on AgNPs embedded in PVA	140

List of abbreviations

AOI	Angle of incidence
AFM	Atomic force microscopy
AgNPs	Silver nanoparticles
AuNPs	Gold nanoparticles
CAI	Constant angle of incidence
DSC	Differential scanning calorimetry
EMA	Effective medium approximation
EMW	Electromagnetic wave
FTIR	Fourier transform infrared spectroscopy
FTIR-SE	Fourier transform infrared spectroscopic ellipsometry
FWHM	Full width at half maximum
IE	Imaging ellipsometry
LSPR	Localized surface plasmon resonance
MG-EMA	Maxwell-Garnett effective medium approximation
NA	Numerical aperture
NPs	Metallic nanoparticles
PCSA	Polarizer compensator sample analyzer (ellipsometer)
PEG	poly(ethylene glycol)
PMMA	polymethylmetacrylate
PS	Polystyrene
PVA	Poly-(vinyl) alcohol
PVP	Poly(vinyl pyrrolidone)
RMSE	Root-mean-squared error
ROI	Region of interest
rpm	Rotation per minute
SE	Spectroscopic ellipsometry
SEM	Scanning electron microscopy
SIE	Spectroscopic imaging ellipsometry
SPR	Surface plasmon resonance
SR	Spectroscopic reflectometry
STM	Scanning tunnelling microscopy
TEM	Transmission electron microscopy
T _g	Glass transition temperature



General introduction

1.1 Context

In the last 40 years, research on metallic nanoparticles (NPs) found an increasing interest due to the development of new techniques (atomic force microscope, scanning tunnelling microscope, ...) and the continuous progress of existing techniques (laser, electron microscopy, ...). These great experimental improvements provided a better understanding of the nanoworld. These days, numerous scientists develop new materials containing NPs that present unusual and fascinating properties. In order to create future applications using this new class of materials, it is important to develop both tools and characterization methods to produce and analyze them. A big challenge remains to understand all the physical phenomena that occur during the fabrication, but also the physical properties of the final product. Numerous new materials seem to be good candidates for applications and, among them, nanocomposite materials are full of promise. These latter ones, composed of nano-objects integrated in a dielectric matrix, present interesting new properties, which do not arise when considering bulk materials.

Among these nanocomposites, we focus our study on plasmonic nanocomposites, based on noble NPs (i.e. silver and gold NPs), which possess great optical and electrical properties. These properties come from their conduction electrons that can

be excited by incident electromagnetic waves. This excitation, that corresponds to resonating oscillations of the electron gas, leads to peculiar interactions with visible light called the Localized Surface Plasmon Resonance (LSPR). In fact, the excitation of the plasmonic NPs at their plasmon resonance wavelength results in an absorption of the electromagnetic energy, which is redistributed to their close environment. These plasmonic nanocomposites can be used for applications in optics, bio-detection, optoelectronics, optical sensors for example.

In order to take benefit of the interesting properties of the plasmonic nanocomposites, it is important to manufacture these new materials. In nanofabrication, two different approaches are possible:

- The top-down approach: starting from a bulk material, the final structure is obtained by breaking it into smaller pieces using mechanical, chemical or other forms of energy (electronic lithography or laser ablation for example).
- The bottom-up scheme: from atomic or molecular species, the principle of this method is to synthesize the material via chemical reactions, allowing the growth of particles from the precursors, usually a salt of the noble metal.

In the top-down approach, the finished structure is well controlled. However, it is difficult to prepare large surfaces at once for industrial process and beyond the upscaling problems, the fabrication costs can be an obstacle. On the contrary, in the second synthesis approach, the nano-objects are often prepared in solution, which is usually cheapest but their dispersion on the dielectric matrix can be difficult. Moreover, the nano-organisation of the NPs within the matrix is rather difficult to control. Nevertheless, the bottom-up approach has other advantages than the cost, such as the possibility to manufacture large surfaces at once with an industrial process.

In order to bypass the problem related to the dispersion of the NPs in the dielectric matrix, another fabrication method exists: the “*in situ* synthesis”. The idea of this approach is to directly form NPs inside a (soft) dielectric matrix, such as a polymer matrix. In fact, in a single step, both the metallic precursors and the polymer solutions are mixed together to prepare the nanocomposite. The reduction of the cations is provided by an external supply of energy (thermal energy, electromagnetic energy, ...).

Unfortunately, this synthesis method provides less control on the shape and the size of the NPs. In an isotropic film prepared from a homopolymer, we can expect the NPs to be spherical but their growth mechanisms are not yet completely understood and still subject to investigations. Nevertheless, this method, also known as “one-pot” synthesis, remains simpler, faster and leads to a higher concentration of NPs than in other synthesis schemes. Another advantage can be found in the role of the polymer matrix: reducing agent of the metallic precursors and stabilizer. However, in the case of “soft” matrices such as polymers, the reproducibility of the NPs distributions in size, shape ... remains difficult to achieve and slight variations in the experimental conditions leads to different results evidenced by modifications of the plasmon resonance band parameters. Moreover, the detailed mechanism linking the optical properties of the nanocomposite to their structural parameters is today

not fully understood although still being the subject of an increasing number of publications.

In this context, we try to provide more information about the growth of the NPs in a polymer matrix by using non destructive analytical optical methods such as spectroscopic ellipsometry and spectroscopic imaging ellipsometry. The main results that will be presented in this thesis are:

- Starting from the same silver-to-polymer mass ratio, nanocomposites with different refractive index can be obtained by simply tuning the film thickness.
- Despite a very low doping level, the growth of gold nanoparticles in polymer matrix can be recorded by imaging ellipsometry.
- By choosing areas on the image with a different contrast intensity, the optical properties at microscale can be obtained by spectroscopic imaging ellipsometry. Moreover, physical data maps, i.e. maps of the thickness or the volume fraction for example, can be calculated by using theoretical models.

1.2 Outline

This work is structured as follows. In chapter 2, we present a brief history of the metallic nanoparticles (NPs), followed by some of their applications. After an overview of the optical properties of the NPs, we will focus our state of the art on the use of bottom-up approaches to prepare plasmonic nanocomposites. This will mainly concern: (a) the synthesis of the NPs in colloidal solution followed by a dispersion in a dielectric matrix or (b) the *in situ* synthesis method of NPs in polymer matrix. Our investigation was focused on the latter method. Finally, we present recent developments of the scientific research on the plasmonic nanocomposites with a particular emphasis on thin polymer films embedding NPs.

We start this chapter with the context of our research and more precisely with a brief history of the metallic nanoparticles (NPs), followed by the some applications using NPs. Then, we present one existing approach used to prepare the plasmonic nanocomposites, as well as the resulting applications. Finally, we present recent developments of the scientific research on the plasmonic nanocomposites containing embedded noble metal NPs.

In chapter 3, we introduce various theoretical concepts used throughout the thesis. We start with the optical processes that occur when light propagates in an optical medium and we also define the optical coefficients. Afterwards, we introduce the optical properties of metallic nanoparticles and more particularly the LSPR. We also present the model used to interpret results obtained by optical measurements. Finally, at the end of this theoretical chapter, we introduce the coefficients of reflection and transmission of polarized light for an optical system defined by a one-layer model, i.e. a film over a substrate.

Chapter 4 presents all the experimental techniques we employ to optically analyze the nanocomposites. We also detail the selected method to prepare these nanocomposites. We start with the description of the optical devices: the spectrophotometer, the home-build reflectometer and the ellipsometers. Afterwards,

we introduce the atomic force microscopy (AFM) necessary for nanoscale measurements. At the end, we precisely explain the experimental procedure to generate the plasmonic nanocomposite thin films.

In chapter 5, we present our study on the optical properties of silver nanoparticles (AgNPs) embedded in a polymer matrix. We start by the analysis of the dielectric matrix that compose all our samples: the poly-(vinyl) alcohol (PVA) matrix. By using spectroscopic ellipsometry, we obtain the optical description of the undoped polymer, i.e. without NPs. In a second step, we analyze the optical properties of a thick silver nanocomposite with a high silver doping level during and after the annealing by spectrophotometry. Throughout this thesis, the term “doping” will be used to describe the addition of metal precursors or of metal nanoparticles to the dielectric matrix. It is therefore not relevant of the doping process usually considered in semiconductors. Then, by varying the thickness of the sample while keeping constant the mass ratio of silver-to-polymer matrix (i.e. concentration of silver in the polymer), we study the influence of the film thickness on the position of the resonance peak. Finally, we use the spectroscopic ellipsometry (SE) and the classical Lorentz model to demonstrate the influence of the film thickness and the silver doping of the nanocomposite films on the plasmon resonance parameters.

In chapter 6, we first focus our study on the optical properties of the gold nanoparticles (AuNPs) embedded in PVA using spectrophotometry. In a second time, we study the surface topography of a thick annealed nanocomposite film to acquire information of the AuNPs at the nanoscale. Afterwards, we present results obtained by single wavelength imaging ellipsometry (IE) on the kinetics of growth of the AuNPs embedded in the polymer matrix at low doping level. By recording the modification of the ellipsometric Ψ and Δ images taken by the IE, we follow the variations of the optical properties of the nanocomposite at the microscale. This non-conventional analysis allows us to detect some heterogeneities on the sample during the annealing and to decompose the dynamics of annealing in two separated parts (work published in [1]).

Finally, in chapter 7, we extend the work presented in the chapter 6. We provide additional information about the AuNPs growth in polymer films by reporting on the local spectroscopic characterization of these films, thanks to the spectroscopic imaging ellipsometer (SIE). Moreover, by measuring ellipsometric angles on small selected regions of interest, we can extract physical data, as the volume fraction of gold, at the microscale. We also compare the analysis carried out by conventional SE and by SIE, explaining the added value of a local analysis of the optical properties in this specific case. By taking Ψ and Δ ellipsometric maps near the LSPR wavelength and using the Maxwell-Garnett effective medium approximation model, we calculate physical maps of the sample such as local thickness of the film and the local volume fraction of AuNPs for example (work published in [2]). We also present Ψ and Δ ellipsometric maps of AgNPs embedded in polymer matrix, as well as local ellipsometric spectra of such plasmonic nanocomposites.

1.3 Publications

Publications in international journals

In this section we list all the contributions in international journals published or submitted during the PhD:

- C. Guyot, P. Vandestruck, I. Marenne, O. Deparis, M. Voué, “Growth dynamics and light scattering of gold nanoparticles in situ synthesized at high concentration in thin polymer films”, *Beilstein Journal of Nanotechnology*, 10, 1768-1777, 2019.
- C. Guyot, P. Leclère, M. Voué, “Gold nanoparticles growing in a polymer matrix: what can we learn from spectroscopic imaging ellipsometry?”, *Journal of Vacuum Science and Technology B*, 38, 013602, 2020.
- C. Guyot, M. Voué, “Intrinsic optical properties of Ag-doped poly-(vinyl) alcohol nanocomposites: an analysis of the film thickness effect on the resonance parameters”, submitted to *Thin Solid Films*, under revision, 2019.

Contributions to international conferences

In this section we list contributions to international conferences during the PhD, as participant as well as member of local organizing committees:

- C. Guyot, M. Voué, “Kinetics of growth of silver and gold nanoparticles in a polymer matrix: How do they modify its optical properties” in “Condensed Matter”, Poster, Paris, France, 2014.
- C. Guyot, M. Voué, “Anomalous optical behavior of metal-polymer nanocomposites” in “8th Workshop Ellipsometry”, Poster, Dresden, Germany, 2014.
- C. Guyot, M. Stock, D. Hoenig, P. Thiesen, M. Voué, “Speeding-up imaging ellipsometry data cubes processing: a multivariate approach” in “8th Workshop Ellipsometry”, Poster, Dresden, Germany, 2014.
- C. Guyot, M. Voué, “Thickness-dependent refractive index in plasmonic nanocomposites: a principal components and support vector machines analysis” in “18th Annual Symposium of the IEEE Photonics Benelux Chapter”, Oral presentation, Mons, Belgium, 2015.
- C. Guyot, C. O. Zogning, M. Stock, M. Voué, “Hybrid clustering methods in imaging ellipsometry of plasmonic nanocomposites” in “JMC15 - Journées de la Matière Condensée”, Poster, Bordeaux, France, 2016.
- C. Guyot, S. Desprez, Y. Paint, F. Maseri, M. Voué, “Thickness dependence of refractive index of Ag-PVA plasmonic nanocomposites” in “JMC15 - Journées de la Matière Condensée”, Oral presentation, Bordeaux, France, 2016.

- C. Guyot, P. Vandestruck, I. Marenne, O. Deparis, M. Voué, “Growth of gold nanoparticles in PVA films: imaging ellipsometry and diffraction pattern onset” in “7th International Conference on Spectroscopic Ellipsometry”, Poster, Berlin, Germany, 2016.
- C. Guyot, O. Deparis, M. Voué, “Light backscattering of gold nanoparticles at high concentration in a polymer matrix”, in “Metallic Nano-Objects”, Oral presentation, Lyon, France, 2018.
- C. Guyot, O. Deparis, M. Voué, “Gold nanoparticles growing in a polymer matrix : what can we learn from imaging ellipsometry?” in “The 8th International Conference on Spectroscopic Ellipsometry”, Poster, Barcelona, Spain, 2019.
- 12 contributions in the “Scientific meeting of the Belgian Physical Society”, Posters, Belgium, 2012-2018.
- Member of the organizing committee of the “Scientific meeting of the Physical Society”, BPS 2017, Mons, Belgium, 2017.
- Member of the organizing committee of the “Mardi des chercheurs 2019”, Mons, Belgium, 2019.
- Member of the organizing committee of the “Imaging Ellipsometry Workshop in Mons”, IEW2020, to be held in Mons, Belgium, May 18-20, 2020.

State of the art

In this thesis, we focus on the fabrication of plasmonic nanocomposites and their optical properties, i.e. their optical responses to incident electromagnetic waves. The electromagnetic waves are everywhere in our daily life and they are used in numerous applications. These waves are part of the electromagnetic spectrum, ranging from radio waves to gamma rays. Our work focuses on a region of this electromagnetic spectrum corresponding to wavelengths from 380 nm to 750 nm. As this wavelength range coincides with the spectral range of the human eye detection, the development of applications, like optical sensors, using visible light is very attractive.

We start this chapter with the context of our research and more precisely with a brief history of the metallic nanoparticles (NPs), followed by the some applications using NPs. Then, we present one existing approach used to prepare the plasmonic nanocomposites, as well as the resulting applications. Finally, we present recent developments of the scientific research on the plasmonic nanocomposites containing embedded noble metal NPs.

2.1 Metallic nanoparticles

One of the first scientific study on colloidal solutions of NPs was performed by Faraday in the nineteenth century [3]. However, colloidal system existed since the



Figure 2.1: (A) - (B) Pictures of the Lycurgus cup (from the British Museum Images, London). (A) Lit from the outside and (B) illuminated from the inside. (C) Stained glass “*Les joueurs d’échecs*” from the Cluny Museum, Paris.

Roman Empire period. Romans empirically developed processes to stain glass by incorporating small inclusions of gold, silver or copper. One of the best example of this period is the Lycurgus cup (4th century AD), stored at the British museum, which presents a peculiar coloration: green and opaque when lit from the outside and red when illuminated from the inside, as it is shown in the figure 2.1A and B, respectively. Despite the fact that the first description of the fabrication of ruby gold glass can be found in the 7th century BC, the industrial process of stained glass with colloidal particles was established in the seventeenth century by Kunckel [4]. These stained glasses were often prepared for European cathedrals during medieval period but also to decorate the homes of wealthy merchants. One example of these stained glass using silver salt for the yellow coloration is the “*Les joueurs d’échecs*” made during the fifteenth century, which is shown in the figure 2.1C.

As previously mentioned, Faraday was one of the first scientists to try to describe the physics of colloidal solutions of gold nanoparticles (AuNPs). He showed that different coloration of AuNPs colloidal solutions could be obtained from red to blue. He explained these coloration differences with the size of the AuNPs in the solution and, moreover, he showed that it was possible to obtain the blue solution from the red solution while the reverse was impossible. From this, he assumed that the size of the AuNPs in the red solution are smaller than in the blue solution. Later, other experimental researches were carried out by Kirchner and Zsigmondy on the inclusion of AuNPs in a gelatin matrix [5]. They also observed different colorations that they explained by varying the distance between NPs in the gelatin matrix.

The explanation of the origin of these changes in coloration came from Maxwell-Garnett in 1904 [6]. He theoretically explained that small inclusions, i.e. NPs, in a dielectric solution form a composite material presenting different optical properties than the addition of the two separately taken components. He described this combination of elements as an effective medium possessing its own effective optical properties depending on the optical properties of the dielectric solution, on the optical properties of the NPs and on the NPs volume fraction in the effective medium.

With his theory, he showed that the environment and the volume fraction of NPs play a role on the coloration of the solution.

In 1908, Gustave Mie suggested his solution for scattering and absorption of light by a single, isolated sphere [7]. By solving the Maxwell's equations, he explained the color of colloidal AuNPs of different sizes. He managed to calculate the spectra of small AuNPs with various sizes without any computer for calculations, nor electron microscopy for a direct determination of the size. Moreover, he explained that for NPs with a diameter smaller than 50 nm, at this size, the extinction of the light was dominated by the absorption process. For larger NPs, the scattering process is not negligible as it will be explained in the section 5.3. Nowadays, this theory is still widely used for the description of systems containing NPs.

The color of the stained glass or of the colloidal solutions containing noble NPs comes from the collective oscillations of their conduction electrons excited by incident light. This peculiar aspect of their optical properties is called the Localized Surface Plasmon Resonance (LSPR). A plasmon is a coherent oscillation of the free electron gas in a metallic material, as it will be shown in the section 3.2.3. In 1952, Pines and Bohm were the first ones to predict plasmons in metallic bulk [8]. Later, the possibility to excite the surface plasmon resonance (SPR) and detect its propagation at the interface between a metal and a dielectric has been demonstrated. For example, Otto and Kretschmann presented important experimental results based on the total reflection in a prism coated with a thin gold film in order to detect the SPR [9, 10]. As it will be presented in the section 3.2.4, the LSPR corresponds to the interaction between an incident electromagnetic wave and a metallic nanostructure in which the electrons are confined [11, 12]. For AuNPs and silver nanoparticles (AgNPs), the plasmon resonance occurs in the visible or near-infrared region. If we consider a group of homogeneous nanoparticles and a light beam going through it, the emerging beam presents a spectrum with a sharp absorption due to the LSPR. The coloration of the system comes from the transmitted light that presents a dip in the spectrum, which corresponds to the absorbed light.

It is clear now that in the Middle Ages, the fabrication of the stained glass or other objects containing noble NPs was made without the knowledge of the nanostructuration of the composite materials. The development of inorganic synthesis of AuNPs by Turkevitch in 1951 [13] and Frens in 1972 [14] corresponds to the increase of scientific interest of the nanoworld. Moreover, the development of new experimental devices to probe elements at the nanoscale allowed multiplying the research works on this topic. Nowadays, methods for manufacturing materials containing NPs have been developed and numerous synthesis paths can be found in the literature. As a proof of the important increase and continuous interest, the number of scientific documents that relate "plasmonic nanoparticles" has reached one thousand written communications in 2019 (Scopus).

The plasmonic effect is used for numerous applications in a wide range of research fields showing the importance of this research topic. For example, metallic nanostructures can be used in photonics in order to guide and control light beams at the nanoscale. The ultimate goal would be to replace electrons by photons in computer to process the information in order to improve the operating speed [15]. In medicine and biology, beside the bactericide effect provided by AgNPs, we can

use the plasmonic effect in very sensitive bio-sensors, while it can also help for the destruction of cancer cells by photothermal therapy [16–20]. In the field of green energy, the plasmonic NPs are used to improve the efficiency of solar cells [21].

As the topic of this thesis is the plasmonic nanocomposites, we now focus our state of the art on the progresses made by the scientific researches on this subject.

2.2 Plasmonic nanocomposites

As already explained, a nanocomposite material is a dielectric matrix containing nano-objects. In this thesis, we prepare the plasmonic nanocomposite by using a polymer host, more precisely the selected polymer is the poly-(vinyl) alcohol (PVA) as it will be explained in the section 4.2. Nevertheless, it is important to note that glass, silicon dioxide or titanium dioxide can play the role of the dielectric matrix [22–24].

If we take a look in the past, it seems that the oldest preparation using polymer and metallic inclusions is described in an abstract dating from 1835 [25]. In this process, a gold salt was reduced in gum arabic and a solid purple nanocomposite was obtained by coprecipitation with ethanol. Around 1900, uniaxial nanocomposites composed of polymer as a dielectric matrix and oriented inorganic particles as inclusions were made. In fact, the uniaxial orientation of the NPs was observed due to the dichroism of the sample, which changes its coloration as a function of the polarization state of the incident light [26]. In 1910, Kolbe showed for the first time that these kind of samples with AuNPs was composed by clusters of gold atoms and not by isolated ones nor cationic states [27]. In 1946, one of the first experimental design of NPs in PVA matrix was made in order to prepare numerous dichroic nanocomposites with different metals (Au, Ag, Hg, ...) in stretched PVA.

Nowadays, metal-polymer nanocomposites can be found in numerous applications such as optical sensors, non-linear optical activity-based devices [28–31], in spectrally selective coatings to block solar infrared radiation [32, 33], and in random lasers [34, 35]. More recently, nanocomposites containing AuNPs received even more attention due to their saturable absorption. Indeed, plasmonic nanocomposites can be used to design passively Q-switched or mode locked lasers [36–38]. In the organic solar system, i.e. solar cells based on polymers, the addition of noble NPs provides an improvement to the efficiency and the lifetime of the system [39, 40].

The optical properties of these nanocomposites are generally studied throughout the polarizability of the particles as it will be shown in the section 3.2.4. In fact, numerous studies of the optical properties of nanocomposites embedding NPs and also colloidal solutions are performed by UV-visible spectrophotometry, as it will be presented in the next sections. The measure of the transmitted intensity gives access to the extinction cross section σ_{ext} of the NPs, which consists in the sum of the absorption cross section σ_{abs} and the scattering cross section σ_{scatt} . In fact, an incident light beam going through a particle can either be absorbed or scattered. In the case of small NPs, the scattering process is negligible and only the absorption plays a role in the extinction cross section [41]. We can therefore determine the σ_{ext} by the measurement of the absorbance of the sample by spectrophotometry. Moreover, the computation of σ_{ext} has been made for numerous shape and size of

NPs [42]. These days, the improvement of the experimental devices provides the detection of more complex systems, thus several new theories have to evolve to take into account the shape, size and surrounding dielectric medium of the NPs [43, 44].

In this thesis, as it will be presented in the section 3.2.5, we use the effective medium approximations (EMAs) in order to theoretically interpret our experimental results. The well-known Maxwell-Garnett effective medium approximation (MG-EMA) [6] or the Bruggeman effective medium approximation [45] are the most used EMAs. These theories describe the nanocomposite as an effective medium by considering the optical properties, i.e. dielectric function, of each component and their volume fraction.

There are numerous experimental procedures to prepare plasmonic nanocomposites, i.e. noble NPs embedded in a dielectric matrix. As already explained, two different approaches exist in nanofabrication: the top down approach, which starts from a bulk material, and bottom-up synthesis, which starts from atomic or molecular species. In this thesis, we prepare the plasmonic nanocomposites following the second method. Nevertheless, there are numerous bottom-up synthesis methods for such nanocomposites, which globally belong to two categories: the synthesis of NPs in a liquid medium, which provides good control during their growth, or the “*in situ* synthesis” of NPs.

When NPs are synthesized in colloidal solutions, with the Frens-Turkevitch method for example [14], and stabilized with or without further specific coating to prevent their aggregation, several experimental factors can provide a considerable control of the formation of NPs. In this “wet chemistry” synthesis, the reduction of the cations can be provided by photochemistry reduction [46] or by a reducing agent like sodium borohydride (NaBH_4) or sodium citrate. By controlling the reducing agent, the reagent concentrations, the temperature and/or the reaction time, we can produce NPs with different size and shape. However, in order to produce plasmonic nanocomposites, the NPs in the colloidal solutions have to be dispersed and immobilized in a dielectric matrix such as glass or polymer [38, 43, 47, 48]. This approach has two separate steps: the synthesis of the NPs and their dispersion in the matrix. Additional reagents like hexadecyltrimethylammonium bromide (CTAB) can inhibit the isotropic growth of the NPs, resulting in nanorods or nanotriangles, for example.

In the literature, nanocomposites were generally prepared following these two-steps procedure in numerous scientific articles. The growth of NPs occurring in those processes of preparation of nanocomposites, i.e. colloidal solution, is often explained by the LaMer diagram [49]. This diagram is drawn in the figure 2.2 [50] and corresponds to a schematic explanation of the formation process of monodisperse particles. It represents the concentration of the precursor solute C as a function of the time during the growing process. The first part (region I in the graph) corresponds to an increase of the concentration of the precursor solute until the critical level C_{crit} . At this point, the system virtually enters in the nucleation stage (region II). Due to the balance between the supply rate of the precursors solute, the consumption rate for the nucleation and the growth of the generated nuclei, the concentration of the precursor solute rapidly reaches a maximum. Then, the curve goes down to C_{crit} because of the increasing consumption of the solute for the growth of the generated nuclei, corresponding to the end of the nucleation stage. Due to the

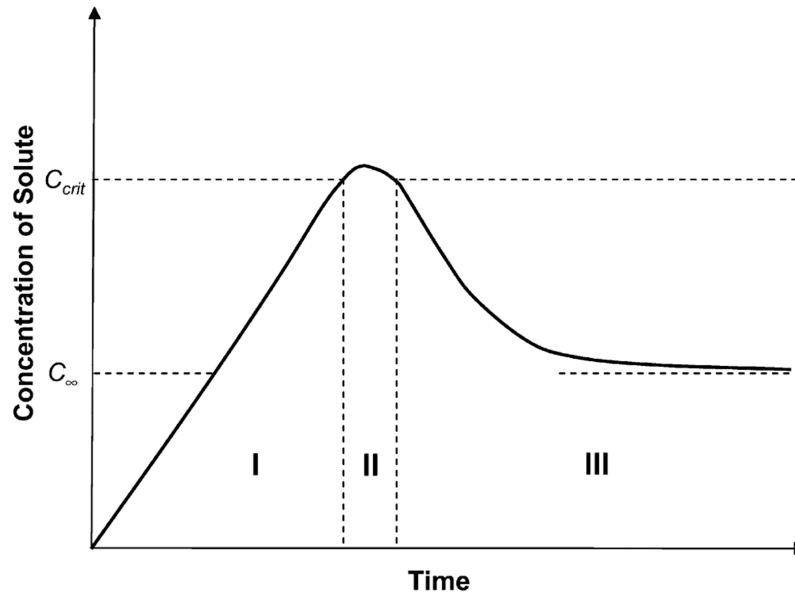


Figure 2.2: LaMer diagram as a schematic explanation for the formation process of monodisperse particles, where C_{∞} and C_{crit} are the equilibrium concentration of solute with the bulk solid and the critical concentration as the minimum concentration for nucleation, respectively. The regions I, II, and III represent the prenucleation, nucleation, and growth stages, respectively. Graph and caption from [50].

growth of the generated stable nuclei, the concentration of the precursors solute C decreases until it reaches the equilibrium concentration of solute with the bulk solid, i.e. C_{∞} (region III). In fact, the formation of noble metal NPs in solution is well documented [51]. However, the growth mechanisms of NPs occurring inside a polymer film are still under investigation because it occurs in a constrained environment subject to a (very) low mobility of the reactants.

In this thesis, we use another path to prepare the nanocomposites named “*in situ* synthesis” of NPs or “one-pot synthesis”. A noble metal salt (AgNO_3 or HAuCl_4) is directly mixed with a polymer solution followed by a thermal annealing of the solid phase. With this second approach, less control on the shape and the size of the NPs is available. Nevertheless, this method is simpler: in a single step, both the noble metal salt and the polymer are mixed together to prepare the nanocomposite. The simplicity of the method is regarded as a great advantage for the production of nanocomposites for various applications. The principle of *in situ* methods is the use of one of the matrix components as a reducing agent for the metal salt. We therefore need a matrix that plays the role of reducing agent but also contributes to the stabilization of the NPs: polymers like poly(vinyl pyrrolidone) (PVP) or PVA are good candidates for this purpose [52]. The self-stabilization process is another advantage of the *in situ* synthesis method since it avoids the use of additional stabilizers like citrate or borohydrate ions. The thermal annealing process allows the reduction of the metal cations and the *in situ* growth of metal NPs. Let us note that other treatments exist such as laser irradiation to induce the formation of the NPs, as it will be explained later. As we can see in the figure 2.3A with a thin film of AuNPs embedded in PVA matrix (e.g. $\simeq 350$ nm), this synthesis process

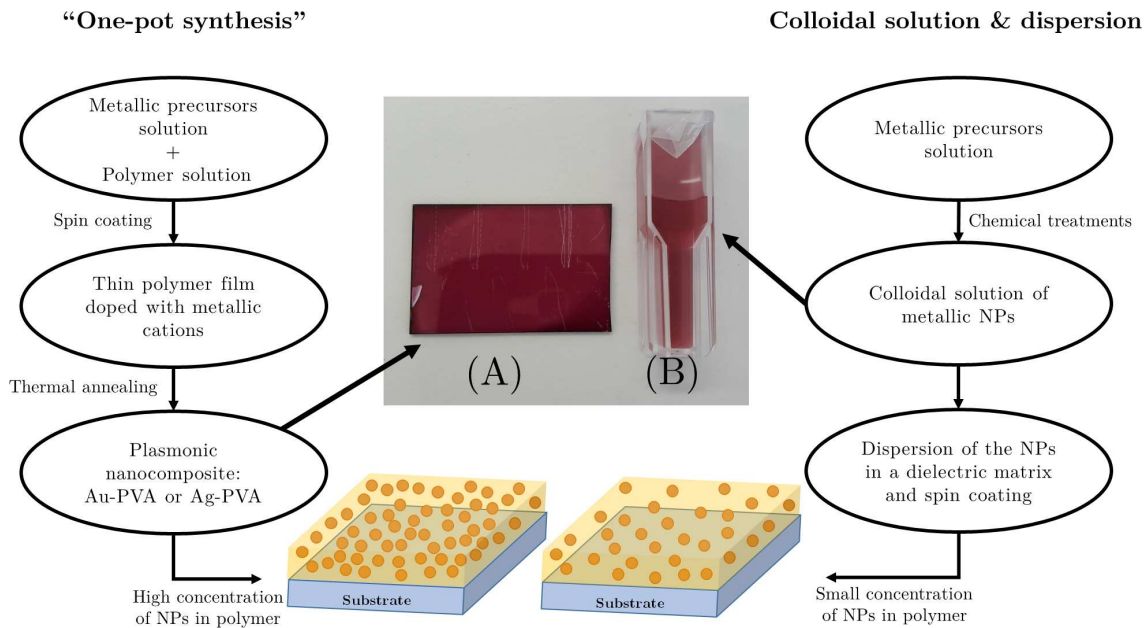


Figure 2.3: Graphical representation of the two bottom-up synthesis methods. (Left side) The “one-pot synthesis” and (Right side) the more classical way composed of a preparation of NPs in colloidal solution followed by a dispersion of the NPs in a dielectric matrix. Picture: (A) Thin polymer film with *in situ* grown AuNPs (optical path: $\simeq 350$ nm), (B) colloidal solution of AuNPs (optical path: 1 cm).

leads to higher concentration of NPs than other synthesis scheme such as colloidal solutions of NPs (Fig 2.3B), hence constituting another advantage of this synthesis scheme. More precisely, in this figure, we can see that the absorbance is equivalent to that measured with a “classical” AuNPs colloidal solution in a 1 cm optical path cuvette. This means that the same absorbance can be obtained with a material thickness $\simeq 2 \cdot 10^4$ times smaller.

As it will be presented later (Section 4.2), the polymer used throughout this thesis to prepare our plasmonic nanocomposites is PVA. In fact, PVA is found in numerous medical applications because of its biocompatibility and low toxicity [53]. This polymer has also interesting properties including the ability to form good films, a high tensile strength and flexibility and finally high oxygen barrier properties [54]. Moreover, in our case, the electrons originating from the -OH groups of the PVA molecules allows the reduction step of the silver or gold cations. The glass temperature transition of PVA is around 85°C for bulk PVA [55], which allows a growing process of the NPs at a moderate temperature. Another important advantage of using PVA as the dielectric matrix is its high transparency in the visible range, which is important for plasmonic applications in the visible range.

Let us note that it is possible to use other polymers to induce the *in situ* synthesis of the NPs. For example, poly(ethylene glycol) (PEG) or PVP can also play the role of reducing agents and stabilizers in the formation of NPs [56, 57]. Abargues and coworkers presented a comparison between numerous polymers containing AgNPs in 2009 [58] (except PVA). He showed that the position of the LSPR depends on the size of the AgNPs and the surrounding dielectric matrix. The studied polymers

were classified on their reduction capacities. He also showed that for the polymers of this study, the temperature needed for the growth of the AgNPs is higher than 180°C, which is much higher than for the PVA case.

Besides the fact that the *in situ* synthesis using “soft” matrices such as polymers is easy, the reproducibility of the size and shape distributions of NPs is difficult to achieve. In fact, slight variations in the experimental conditions lead to different results evidenced by modifications of the plasmon resonance band parameters. In an isotropic film prepared from a homopolymer, we can expect the NPs to be spherical but their growth mechanisms and also the detailed mechanism linking the optical properties of the nanocomposite to their structural parameters are today not fully understood. The investigation on these subjects leads to an increasing number of publications, as we will present in the two next sections.

Finally, in this section, we have presented a brief history of the use of plasmonic nanocomposites. We have also described experimental processes leading to the preparation of these nanocomposites. We showed the advantages to synthesize our NPs by the “one-pot synthesis” that is simpler, faster and provides a higher concentration of NPs than other synthesis schemes. As just mentioned above, the PVA presents numerous advantages for its use in future applications. For these reasons, we will focus now on recent scientific developments of silver and gold nanocomposites using usually PVA film as a dielectric matrix.

2.2.1 Silver nanocomposites

As already mentioned, a large number of publications has been devoted to the study of the optical properties of NPs in solutions, considering the effects of solvent, temperature synthesis, surfactants,... but much less authors have considered the growth of the NPs in a polymer film. As already reported before, interest for such Ag-PVA nanocomposites lays in their possible applications.

In 2005, Khanna *et al* presented the results obtained by doping the PVA matrix with AgNPs [59]. In aqueous solutions, they mixed AgNO₃, PVA and two different reducing agents: formaldehyde sulfoxylate and hydrazine hydrate to compare those. After the formation of the AgNPs in solution, in order to form nanocomposite films, they evaporated the solvent in air by using an oven at a temperature of 100°C until the film became solid. This corresponds to a casting method that creates a film with a thickness of the order of the micrometer. They showed spectrophotometry results that presented a resonance peak near 415 nm confirming the presence of the AgNPs in the film.

Another casting method of the formation of AgNPs embedded in PVA matrix was presented by Nimrodh *et al* [60]. The annealing conditions were 50°C during 24 hours. They measured the absorbance of their sample presenting a peak near 430 nm. By using differential scanning calorimetry (DSC), they also showed that the temperature of melting (melting point) and the glass temperature transition (T_g) changed due to the embedded NPs in comparison to the pure PVA. The temperature of melting increased from 191.65° to 193.40°C and the T_g decreased from 85.78°C to 80.64°C. As we can see, the *in situ* synthesis of NPs induces changes on the physical parameters of the polymer matrix.

In 2005, Karthikeyan presented spectroscopic analysis of Ag-PVA nanocomposites formed by casting at ambient temperature during 30 hours followed by a thermal annealing at 120°C [61]. He measured the absorbance of nanocomposites, presenting a peak near 420 nm, as a function of the annealing time, from 1 min to 30 min. From these measurements, he showed that the intensity of the absorbance of the sample increased as a function of the annealing time, although the full width at half maximum (FWHM) of the resonance peak decreased as a function of the annealing time. He also presented an analysis using a Fourier transform infrared spectroscopy (FTIR), which supports the presence of bonds between Ag and PVA.

From 2004, the research group of Porel developed an experimental process to prepare plasmonic nanocomposites. By mixing the metal salt (AgNO_3 , HAuCl_4) solution with the polymer solution (PVA or PVP), they spin coated the mixed solution on glass substrates [62–67]. These nanocomposite films were annealed in order to induce the growth of the NPs. As it will be explained in the section 4.2 of this thesis, we use the same experimental procedure to prepare our nanocomposites. Porel and coworkers generally measured the absorption spectra of their sample to detect the presence of the *in situ* synthesized NPs. In order to form free-standing films, their glass substrates were coated with a thin polystyrene (PS) film. With these free-standing films, they were able to detect the shape of their NPs by using transmission electron microscopy (TEM). The sizes of their NPs were measured by atomic force microscopy (AFM). For clarity, hereinafter, we present their results for AgNPs and AuNPs separately:

- For AgNPs, the annealing conditions were 110°C under various time duration ranging from 5 min to 60 min. They also modified the concentration of silver in the PVA matrix. They showed that the absorbance measured by spectrophotometry increased as a function of the annealing time. They also noticed a small blue-shift of the maximum of the absorbance position as a function of annealing time. The TEM analysis showed that the embedded AgNPs seem to be spherical. In [66], they studied the *in situ* synthesis of AgNPs in PVP with a varying time of annealing starting from 1 min to 30 hours. They measured the absorbance of each sample and they showed that the intensity of the absorbance increased with the annealing time. The figure 2.4 presents two free-standing nanocomposite films of AgNPs embedded in PVA matrix (picture and caption from [65]).
- Concerning AuNPs, they annealed the samples at different temperatures ranging from 100°C to 170°C under various time duration ranging from 5 to 60 min. They showed that the annealing conditions and the metal-to-polymer ratio induce large modification of the shape of the AuNPs. By TEM, they revealed different shapes of the AuNPs as triangles, hexagons, pentagons. They also measured the absorption of their nanocomposites as a function of the wavelength. They showed that the plasmon resonance position changed as a function of the shape of the AuNPs.

To sum-up their analysis, as demonstrated by the shape of the grown NPs, the formation of AgNPs and AuNPs in the PVA seems to be different. Despite the modification of the metal-to-polymer mass ratio, the AgNPs were spherical. AuNPs

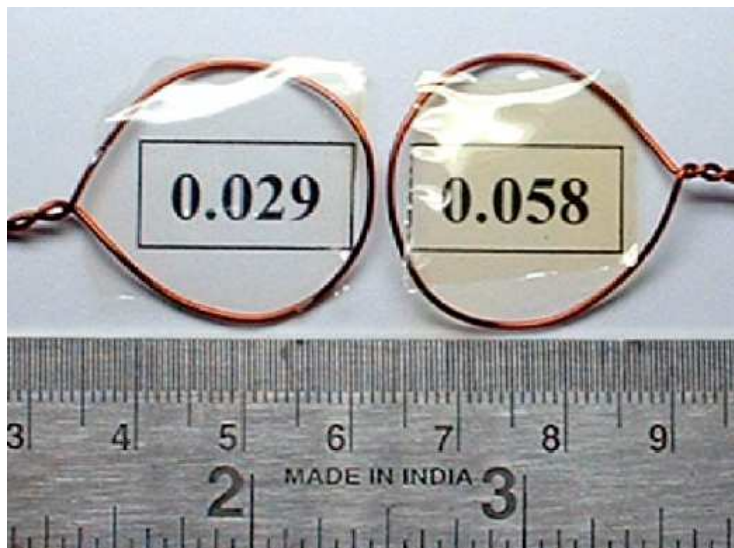


Figure 2.4: Photographs of free-standing films of AgNPs in PVA matrix; transparency of the films is demonstrated by placing them on wire frames above a paper on which the corresponding value of the Ag/PVA mass ratio is printed (picture and caption from [65]).

presented different shapes as a function of the temperature of annealing, the concentration of gold and also the annealing time. They followed the kinetics of growth of the AgNPs by using spectrophotometry measurements during the annealing and they showed that the value of the absorbance increased as a function of the annealing time. As we can see with these results from Porel *et al*, the annealing time with these spin coated samples is smaller than in the casting case. This represents an advantage in industrial processes for future applications.

After considering the annealing time as varying parameter, we look at the work of Clémenson *et al*, which focused on AgNPs embedded in the PVA matrix under different annealing temperatures [68, 69]. The experimental conditions were film thicknesses around 150 nm obtained by spin coating and a thermal annealing varying from 50°C to 160°C during 60 min. They also tested different concentrations of silver in the polymer. When the annealing temperature is higher than 90°C, i.e. higher than the T_g of the PVA (85°C [55]), they showed that the absorption spectrum presented a resonance peak near 415 nm. The modifications of the polymer induced by its glass transition seem to facilitate the diffusion process of atoms or ions to form AgNPs in the polymer matrix. Despite the modification of the concentration of silver in polymer, they measured similar values for the size of the AgNPs *in situ* synthesized at 110°C. At a temperature of annealing of 160°C, which corresponds to a temperature near the melting point of the polymer, they measured AgNPs with a larger size than the AgNPs formed at 110°C. In fact, at this annealing temperature, the crystalline phase of PVA started to melt, leading to an amorphous system composed of lamellae. The AgNPs started to grow between these lamellae, which induced more space for the diffusion and hence, therefore more space for the growing process. When the annealing temperature was around 110°C, the AgNPs were smaller due to a smaller polymer chain mobility. Finally, they showed that a long annealing at 160°C induces an insolubility of the PVA film due to cross-linking

phenomena.

As we have just seen, the optical properties of plasmonic nanocomposites are usually probed using reflection or transmission spectrophotometry in the UV-visible spectral range. In order to study the optical properties of Ag or Au-doped PVA films produced by thermal annealing, we can use spectroscopic ellipsometry (SE). This optical analysis has the advantages of being non-destructive and moreover of allowing the simultaneous determination of the film thickness and its complex refractive index values. To date, only a reduced number of studies have been carried out using SE as analysis technique. Let us note that Oates, Wormeester and Arwin published a review on spectroscopic ellipsometry studies of plasmon resonances at metal-dielectric interfaces of thin films and metallic nanostructures [70]. Nevertheless, the *in situ* synthesis of nanocomposite is not often mentioned. For the spectroscopic ellipsometry analysis of these kind of samples, we focus on articles published by Oates *et al* [71, 72] and Voué *et al* [73, 74].

In 2006, Oates published an interesting article, demonstrating the possibility to measure the size of the AgNPs during growth formation indirectly with theoretical models [71]. The nanocomposites were formed by mixing a silver hexafluoroacetate ($\text{Ag}(\text{hfac})$) solution in toluene with a PS/toluene solution. The thickness of the films were around 50 nm (spin coating) and different annealing temperatures were tested, from 120°C to 220°C. Despite the difference in experimental processes compared to the one used in this thesis, this article is interesting since it presents the optical properties of the nanocomposite during the annealing. They showed large changes on the optical properties when the samples were heated at 220°C, which were explained as a decomposition of the polymer matrix leaving the AgNPs on the silicon substrate. Moreover, the values of the melting point and glass transition temperature of the polymer were smaller when the polymer was doped by AgNPs.

They also published an experimental article using SE (375 – 1000 nm) on the growth of AgNPs in PVA matrix [72]. In this article, they tested two different concentrations of silver in the polymer, three different thicknesses (90, 60 and 40 nm) and two different annealing temperatures (120 and 150°C). At the end of each experiment they heated the sample at 350° to decompose the polymer. They showed by scanning electron microscopy (SEM) measurements that a higher concentration of silver led to a higher concentration of AgNPs embedded in the PVA. By using MG-EMA model, they tried to follow the kinetics of the growth of the AgNPs by a determination of the mean radii of AgNPs. They showed that the kinetics of growth seemed to be different at 120°C than 150°C. Finally, due to the evaporation of the polymer at 350°C, they showed that the AgNPs seemed to merge with each other and form larger AgNPs with different shapes.

By performing the ellipsometric measurements by a Fourier transform infrared spectroscopic ellipsometer (FTIR-SE), Voué *et al* measured the optical properties of AgNPs embedded in PVA matrix in the 600 – 6000 cm^{-1} spectral range [73]. The thickness of their nanocomposite films were 1 – 2 μm , the silver concentration in polymer was 8% (w:w) and the annealing temperature was set to 110°C. They first analyzed the topography of their films by AFM. They measured an increase of the root-mean-square roughness due to the presence of the AgNPs *in situ* synthesized. They determined the optical properties of the nanocomposite on the FTIR range

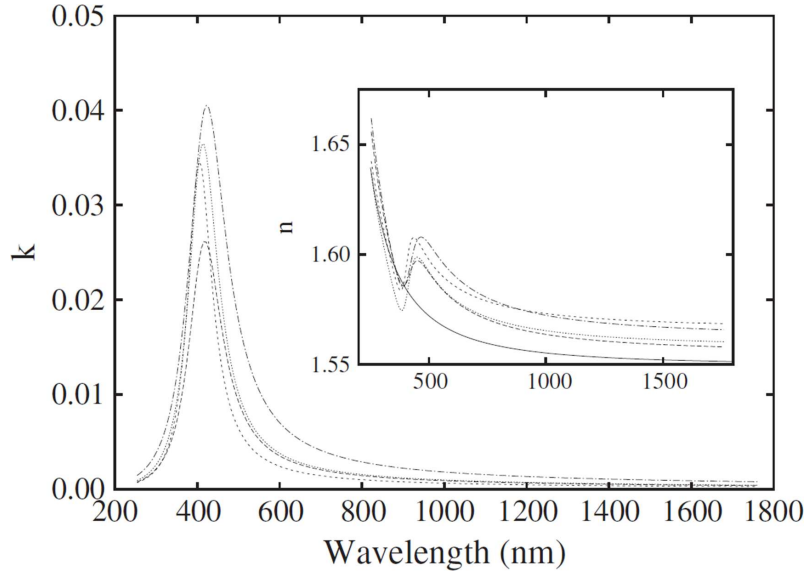


Figure 2.5: Extinction coefficient of the Ag-PVA films annealed at 90°C during 10, 30, 45 and 60 min (respectively from bottom curve to top curve) in UV, visible, near-infrared range. Inset: refractive index of the annealed films (same order as above; continuous line: refractive index of the pure PVA film). Graph and caption from [74].

by using Cauchy model and Lorentzian oscillators. When they compared the ellipsometric data between doped and undoped PVA, they noticed the presence of two new peaks on doped samples. Those, situated at 1036 and 1134 cm^{-1} , confirmed the bond between silver and the PVA matrix.

In 2011, they prepared nanocomposite films of the same kind and they measured their optical properties by SE in the UV-near infrared spectral domain [74]. The annealing temperature was set to 90°C , slightly above the T_g and SE measurements were taken every 10 min during 60 min. The thicknesses of the films were $1 - 2\ \mu\text{m}$ and $0.6 - 0.7\ \mu\text{m}$. In order to extract the optical properties of their ellipsometric measurements, they used a Cauchy model for the polymer and a Lorentzian oscillator for the AgNPs. They showed a sharp peak in the extinction coefficient spectrum near 420 nm , which confirmed the presence of the AgNPs in the PVA matrix, as it is shown in the figure 2.5. The amplitude of the peak increased as a function of the annealing time due to an increase concentration of AgNPs in the nanocomposite film.

From the point of view of the size of the AgNPs during the annealing, this last article is in contradiction with the article of Oates *et al* [72]. In fact, Oates *et al* assumed that the size of their AgNPs increased as a function of the annealing time. On the contrary, Voué *et al* showed that the size of their AgNPs *in situ* synthesized seemed to decrease as a function of the annealing time. Let us note that the thicknesses of the films of these two articles are different ($40 - 90\text{ nm}$ for Oates and $0.6 - 0.7\ \mu\text{m}$ for Voué). We can see here that the time evolution of the particle size seems to be a complex process and that the film thickness could play a role in the growth process.

To sum up this section, we have presented recent developments on plasmonic nanocomposites containing AgNPs. As we can see, the effect of annealing time and

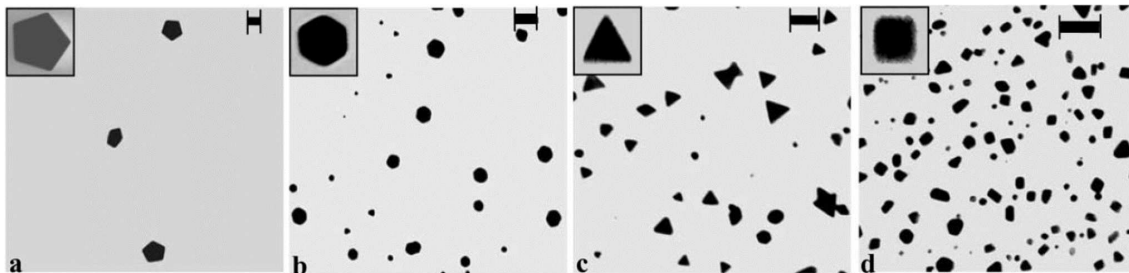


Figure 2.6: TEM images of Au-PVA films with polygonal nanoplates generated under different conditions. The Au/PVA mass ratio, temperature of heating ($^{\circ}\text{C}$) and time of heating (min) are indicated in that order in parenthesis: (a) pentagons (0.04, 170, 5); (b) hexagons (0.08, 130, 30); (c) triangles (0.12, 100, 60) and (d) squares/rectangles (0.18, 100, 60). Scale bar = 50 nm. Images and caption from [62]

temperature on these nanocomposite films have been intensively studied. Numerous studies determined the optical properties through the UV-visible spectrophotometry. Only few references presented the optical properties of these kind of nanocomposites by using SE and none by the spectroscopic imaging ellipsometry (SIE). The summary of the cited articles is presented in the table 2.1.

In the next section, we present recent scientific researches on plasmonic nanocomposites based on AuNPs grown in the polymer matrix.

2.2.2 Gold nanocomposites

Contrary to plasmonic nanocomposites containing *in situ* grown AgNPs, AuNPs synthesized *in situ* in a polymer matrix are not often discussed in the literature, despite the simplicity of the synthesis. Moreover, experimental procedures strongly differ from one publication to the other, making their results very difficult to compare. Nevertheless, as we have already explained in the previous section, Porel and coworkers showed the possibility to form AuNPs, more precisely polygonal nanoplates, in a polymer matrix [62]. These nanocomposites were prepared by spin coating the mixed solution containing PVA and HAuCl_4 and those were annealed to form the AuNPs. By changing the metal-to-polymer mass ratio, the temperature of annealing and the annealing time, the shape of AuNPs embedded in the PVA matrix changes, as we can see in the figure 2.6.

Sakamoto *et al* presented a study on AuNPs *in situ* synthesized in PVA matrix by irradiation instead of a thermal annealing [75]. In that purpose, they needed to add a reducing agent, benzophenone. To induce the growth of the AuNPs in the PVA matrix, the samples were exposed to laser pulses at 355 nm and 532 nm provided by a nanosecond–picosecond two-color two-laser flash photolysis system. They detected the presence of the AuNPs with the absorption spectra of the sample, which showed an absorption peak near 523 nm.

In 2009, Sun *et al* published an article reporting on studies using HAuCl_4 as the metal precursor and PVA as the polymer matrix [76]. In comparison with Porel, they formed their AuNPs by thermal annealing (80°C) of the mixed solution containing metal salt and polymer. After the reduction of gold cations in solution, the

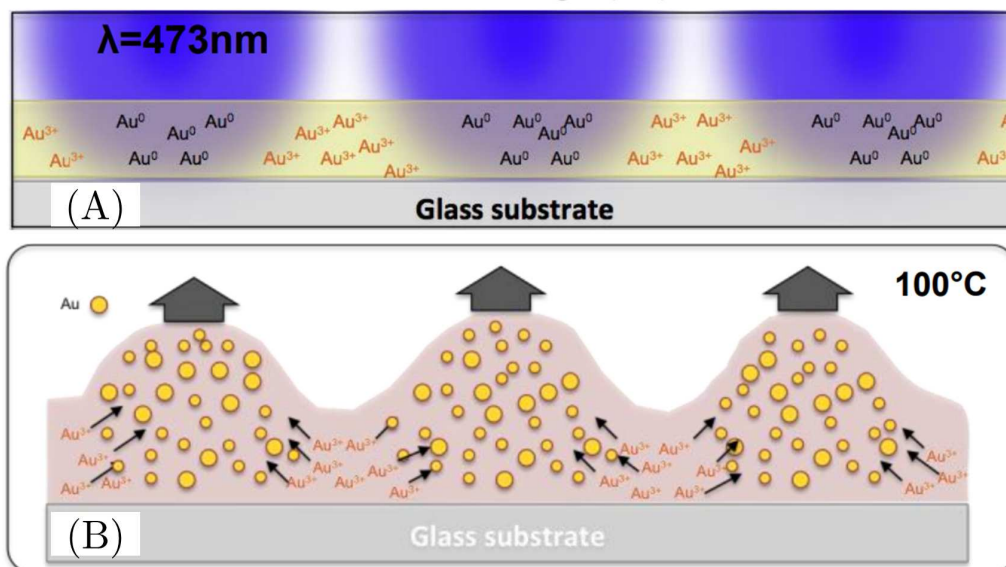


Figure 2.7: (A) Schematics of the local photoreduction in the polymer film induced by laser irradiation. (B) Representation of the effect of annealing: nanoparticles grow from reduced gold atoms as well as from the remaining gold ions that diffuse towards the nanoparticles, while simultaneously experiencing thermal reduction. Both images (A and B) and caption come from [78].

nanocomposite films were obtained by casting. They used numerous experimental devices to detect the presence of the AuNPs embedded in the PVA matrix. The UV-visible spectrophotometry showed an absorption peak near 530 nm, which corresponds to the LSPR of the AuNPs in PVA. By varying the annealing temperature, they also showed that a higher temperature of annealing accelerated the formation of the AuNPs in the solution. They confirmed the presence of bonds between PVA and gold atoms by Fourier spectra IR analysis. At the end of their analysis, they proposed a representation of interactions between PVA chains and AuNPs.

Vieaud presented an interesting work on AuNPs prepared by the well-known Frens-Turkevitch method [14] and dispersed in PVA matrix [77]. By using spin coating, the thicknesses of the nanocomposites were between 40 to 150 nm. He measured the ellipsometric spectra of these nanocomposites by SE and extracted the optical properties, i.e. $n(\lambda)$, $k(\lambda)$, by using the MG-EMA model. He also determined the volume fraction of gold in the polymer and the thickness of those films. He measured their topography by AFM.

In 2017, Nadal *et al* demonstrated the possibility to induce the spatially controlled formation of AuNPs in PVA matrix on glass substrates obtained with a laser irradiation followed by a short thermal annealing [78]. For that purpose, they used a Mach-Zender type interferometer to create interference patterns of light on irradiated samples. The growth of AuNPs occurred only on areas exposed to the incident irradiation, i.e. in bright fringes, which came from a 50 mW laser with an operating wavelength at 473 nm, as it is shown in the figure 2.7A. They showed that the optimal modulation in the refractive index between dark and bright fringes was obtained after 18 min of laser irradiation. This photoreduction led to the formation of gold

atoms, i.e. Au^{3+} to Au^0 , and a thermal annealing is used to trigger the formation of AuNPs (100°C during 1 min). They detected the presence of the AuNPs within the film by measuring the topography of the film and also by determining the extinction spectrum of nanocomposites, which showed an absorption peak near 550 nm. They also compared their results obtained with a Gaussian beam and with the interference pattern, which induced a displacement and a broadening of the plasmon band. Finally, they explained that the photoreduction was not complete and the thermal annealing of the sample allowed the reduction of the gold cations located in the dark fringes. Then, those can diffuse towards the region where the NPs grow. They assumed that AuNPs acted as seeds and tended to effectively drag the surrounding gold atoms and contribute to the growth of AuNPs as it is graphically represented in the figure 2.7.

In the recent study of Omar and coworkers [79], monodispersed gold nanocubes were synthesized by spin coating of a gold precursor-loaded polymethylmetacrylate (PMMA) dispersion on N-doped silicon. By using other metallic precursors as HAuCl_4 , KAuCl_4 and NaAuCl_4 , the shape of the AuNPs *in situ* synthesized were hexagonal, triangular or cubic, respectively. Due to different aspect ratios of the AuNPs, the plasmon band shifts towards larger wavelengths leading to the possibility of using this experimental process for medical applications for example. They used SE to determine the optical properties of these nanocomposites and more precisely to determine the position of the plasmon band.

Finally, very recently, Nadal and coworkers have published an original synthesis method of plasmonic nanocomposite under concentrated sunlight [80]. In order to prepare the nanocomposite films, they mixed a PMMA solution with a gold salt (HAuCl_4) solution (gold-to-polymer mass ratio: 5%) and spin coated it on glass substrates to obtain a film thickness around 500 nm. They showed that controlling the solar flux and the sample temperature induced variations of the size distribution and the shape of the AuNPs *in situ* grown (spherical to nanoprisms). Thanks to their experimental device, they presented the possibility to measure in real time the spectroscopic response of the film. Their results provided details about the growth of the AuNPs within the film thanks to the absorption spectra taken during the growth of AuNPs induced by the solar flux. As the solar simulator provided numerous wavelengths, in addition to the photoreduction, the excitation of the plasmonic resonance of the AuNPs could result in the production of hot electrons, which could induce an increase of the reduction rate of the gold precursor.

In the literature, numerous publications on AuNPs in a dielectric matrix describe a two steps procedure for the preparation of the nanocomposite, i.e. colloidal solution and dispersion in the dielectric matrix. Nevertheless, as we can see, few research groups develop the synthesis method preliminary presented by Porel and coworkers. We have focused our attention on studies using *in situ* synthesis of AuNPs in polymer matrix. As we can see, besides thermal annealing, the formation of AuNPs can be provided by laser irradiation or concentrated sunlight. Finally, the ellipsometric analysis of these AuNPs *in situ* synthesized are presented on few articles. The summary of the cited articles is presented in the table 2.2.

2.3 Main outcomes of the literature survey

As a summary of this chapter, we have presented a brief history of the development of the NPs and the development of the plasmonic nanocomposites. We have also described the “one-pot synthesis” method to prepare these plasmonic nanocomposites. Finally, we have reported numerous applications using NPs in polymer matrix. This state of the art has been focused on AgNPs or AuNPs *in situ* synthesized in polymer matrix by thermal annealing. We have tried to describe other techniques leading to the formation of NPs in polymer matrix, i.e. laser irradiation, concentrated sunlight, ... As we have seen, the fabrication method is simpler, faster but provides less control of the shape and size of the NPs. We also have presented articles in contradiction with one another, which proves that, despite being easy to produce, numerous questions on these kinds of nanocomposites remain open.

For AgNPs, the effects of annealing time and temperature have also been intensively studied. On the contrary, the influence of the thickness of the film has only been considered in very few references and most of the time a systematic study of its influence was not carried out. Moreover, the intrinsic optical properties of the nanocomposite is usually only considered as a function of the optical properties of the metal, the polymer and their volume fraction. In the chapter 5 of this thesis, we try to report in details on the influence the film thickness and on the silver doping of the nanocomposite films on the plasmon resonance parameters. More precisely, we compare the resonance parameters in thin (less than 50 nm) and thick films (more than 300 nm) at a given Ag-doping level. We will show how, starting from the same silver-to-polymer mass ratio, nanocomposites with different refractive index can be obtained by simply tuning the film thickness. To the best of our knowledge, the effect has not yet been reported in the literature.

We also try to provide more information on the growth of the AgNPs (chapter 5) and AuNPs (chapter 6) by measuring in real time the transmitted intensity every 30 seconds during the annealing of a thick highly doped silver or gold nanocomposite. This kind of analysis, on AuNPs, looks like the study of the concentrated sunlight of Nadal but the annealing process is different in our case.

In the case of AuNPs, we try to provide another information using an single wavelength imaging ellipsometer (IE) during the growth of the AuNPs at very low doping level in the polymer matrix by real time measurements of Ψ and Δ ellipsometric angles. We show that the imaging ellipsometer provides a local analysis of the optical properties and allows the optical detection of the AuNPs despite a doping level undetectable by conventional SE. Finally in chapter 7, by using spectroscopic imaging ellipsometer (SIE) and the MG-EMA model, we can measure the local optical properties of AuNPs embedded in PVA matrix at this low doping level. This real time analysis and detection of the optical properties at this doping level has not yet been described in the literature. Moreover, the optical properties of plasmonic nanocomposites have never been probed by spectroscopic imaging ellipsometry, which is a favorable reason to present the results of this thesis related to this topic.

Table 2.1: Summary of articles on AgNPs *in situ* synthesized in a polymer matrix. “d” is the thickness of the nanocomposite film, “T” is the annealing temperature and “t” is the annealing time.

Articles	Nanocomposite reagents	Experimental processes	Optical methods	Main achievements
Khanna [59]	AgNO ₃ , PVA and reducing agents	AgNPs formed in solution and casting, d: several micrometers	UV-visible spectrophotometry	Presence of AgNPs in thick PVA films
Nimrodh [60]	AgNO ₃ , PVA and NaBH ₄	Casting, d: several micrometers, T: 50°C, t: 24 h	UV-visible spectrophotometry, SEM and DSC	AgNPs induce changes on the physical parameters of the PVA matrix
Karthikeyan [61]	AgNO ₃ , PVA	Casting, d: several micrometers, T: 120°C, t: from 5 to 30 min	UV-visible spectrophotometry and FTIR	Increase of the absorbance as a function of the annealing time
Porel [63, 64, 66, 67]	AgNO ₃ , PVA or PVP	Spin coating, d: 3 - 6 μm or 500 - 600 nm, T: 110°C, t: from 5 to 60 min	UV-visible spectrophotometry, TEM and AFM	Blue-shift of λ _{LSPR} as a function of the annealing, spherical AgNPs
Clémenson [68, 69]	AgNO ₃ , PVA	Casting or spin coating, d: several micrometers or 150 nm, T: from 50 to 160°C, t: 60 min	UV-visible spectrophotometry, TEM	Variation of the annealing temperature, higher temperature larger AgNPs
Oates [71]	AgO ₂ , hfac, PS	Spin coating, d: 50 nm, T: from 120°C to 160°C, t: 30 min	SE, TEM and SEM	Determination of the size of the AgNPs using SE
Oates [72]	AgNO ₃ , PVA	Spin coating, d: 90, 60 or 40 nm, T: from 120°C to 150°C, t: 60 min	SE and SEM	Following the growth of AgNPs with SE in real time
Voué [73]	AgNO ₃ , PVA	Spin coating, d: 1 - 2 μm, T: 110°C, t: 60 min	FTIR-SE and AFM	Measurements in the IR region by FTIR-SE, bonds between Ag and PVA
Voué [74]	AgNO ₃ , PVA	Spin coating, d: 1 - 2 and 0.6 - 0.7 μm, T: 90°C, t: from 5 to 60 min	SE and AFM	Determination of the optical properties of AgNPs in PVA matrix by SE
This thesis	AgNO ₃ , PVA	Spin-coating, d: 350 and 30 nm, T: 110°C, t: 60 min	Real time UV-visible spectrophotometry, AFM, SE and SIE	

Table 2.2: Summary of articles on AuNPs *in situ* synthesized in a polymer matrix. “d” is the thickness of the nanocomposite film, “T” is the annealing temperature and “t” is the annealing time or irradiation time.

Articles	Nanocomposite reagents	Experimental processes	Optical methods	Main achievements
Porel [62]	HAuCl ₄ and PVA (from 4% to 12% mass ratios)	Spin coating, d: 1.4 μm, T: from 100 to 170°C, t: from 5 to 60 min	UV-visible spectrophotometry and TEM	Growth of AuNPs in PVA matrix, various shapes of AuNPs
Sakamoto [75]	HAuCl ₄ , PVA (5% w:w) and reducing agent	Casting, d: several micrometers, laser irradiation: λ = 355 and 532 nm	UV-visible spectrophotometry and TEM	Growth of AuNPs in PVA using laser irradiation
Sun [76]	HAuCl ₄ and PVA	Thermal annealing of the mixed solution (80°C), casting, d: several micrometers	UV-visible spectrophotometry, FTIR, DSC and TEM	Higher temperature leads to an acceleration of the formation of the AuNPs in solution, presence of bonds between Au and PVA
Vieaud [77]	HAuCl ₄ and PVA	Colloidal solution (Frens method) and dispersion, spin coating, d: from 15 nm to 150 nm	UV-visible spectrophotometry, AFM, SE and TEM	Ellipsometric spectra of AuNPs dispersed in PVA matrix and extraction of the optical properties
Nadal [78]	HAuCl ₄ and PVA (5% w:w)	Spin coating, d: 1 μm, laser irradiation (λ = 473 nm), t: 18, 40, 60 min + annealing T: 100°C, t: 1 min	UV-visible spectrophotometry and AFM	Growth of AuNPs in PVA matrix on glass spatially controlled with laser irradiation
Omar [79]	HAuCl ₄ , KAuCl ₄ , NaAuCl ₄ and PMMA	Spin coating, d: 130 nm, conducting substrates: N-doped silicon	UV-visible spectrophotometry, AFM, SE, SEM	By changing the metallic precursors the shapes of the AuNPs change
Nadal [80]	HAuCl ₄ and PMMA (20% w:w)	Spin coating, d: 500 nm, concentrated sunlight irradiation, t: 30 min	Real time UV-visible spectrophotometry and TEM	Growth of AuNPs using concentrated sunlight, measurements of the growth of AuNPs in real time
This thesis	HAuCl ₄ and PVA (2% w:w)	Spin coating, d: 350 nm, T: 135°C, t: 120 min	Real time UV-visible spectrophotometry, real time IE, SE and SIE	

Theoretical concepts

In this chapter, we will introduce the theoretical concepts to understand and interpret the results of this work. We will start with the optical processes that occur when light propagates in an optical medium and define the optical coefficients. We will continue with the optical properties of metallic nanoparticles. We will end this chapter presenting the coefficients of reflection and transmission of polarized light for an optical system defined by a one-layer system, i.e. a film over a substrate.

3.1 Polarization states of light

3.1.1 Optical process

As shown in the figure 3.1, an optical medium is defined by two interfaces that correspond to two medium changes. In the case of the light beam propagating towards the first interface, two optical processes can occur. A part of the incident wave is reflected corresponding to the reflection process, while the rest propagates through the medium that represents the transmission process. The same scheme is followed at the second interface, the back surface: another part of the wave is reflected and the rest of the wave is transmitted through the other side. In this simple example, we have access to three phenomena to describe the interaction of

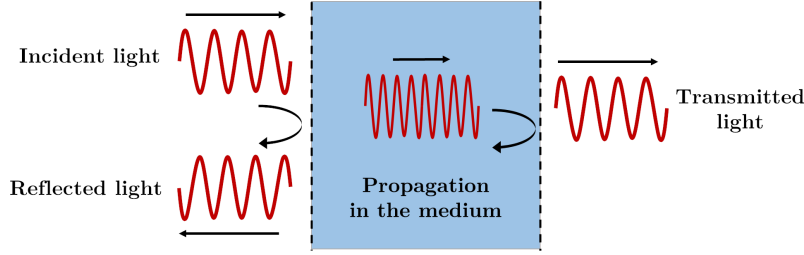


Figure 3.1: Optical processes, reflection, propagation and transmission, which can occur when a light beam propagating through an optical medium

light with an optical medium: reflection, propagation and transmission. During the propagation of the beam, some other phenomena can occur like refraction at the interface, absorption and scattering in the optical medium, for example [81]. Refraction, described by the Snell's law of refraction (Eq. 3.85), causes the bending of the light rays due to the increase or reduction of the wave velocity during the passing between two different media. The absorption process takes place when the frequency of the incident light is resonant with the transition frequencies of the atoms in the medium, or due to the oscillating electron cloud in the case of small nanoparticles for example [82]. Due to the absorption, the intensity of the beam will be attenuated and the transmittance of the medium depends on the absorption process as we will see later. A selective absorption in the visible range is responsible for the coloration of optical materials. Finally, Scattering occurs when the light presents direction changes after the interaction with the medium at the microscopic level. Despite a total number of photons unchanged, some photons are re-directed in directions other than the forward direction. In the case of this work, we will focus on the absorption process of light.

3.1.2 Optical coefficients

The reflection process at a surface is described by the reflectivity or the power reflection coefficient denoted by R . The definition of the reflectivity is the ratio of the reflected power to the incident power on the surface. The transmissivity or the power transmission coefficient T is determined by the ratio of the transmitted power to the incident power. In the absence of absorption or scattering processes, we have:

$$R + T = 1 \quad (3.1)$$

The refractive index, n , defined by $n = c/v$ where c is the velocity of the light in free space and v the velocity of the light in the medium, describes the propagation of the beam through a transparent medium. n depends on the frequency of the light source.

The absorption coefficient α describes the absorption of light by an optical medium. It can be defined as the fraction of the power absorbed per unit length. The decrease of the intensity at a position z of beam propagating in the z direction in an slice of thickness dz is given by:

$$dI = -\alpha dz \times I(z) \quad (3.2)$$

which leads to the Beer's law for absorption:

$$I(z) = I_0 e^{-\alpha z} \quad (3.3)$$

where I_0 corresponds to the optical intensity at $z = 0$. This coefficient of absorption is a function of frequency, which is used to describe, in some materials, the absorption of one color but not another. We will use this coefficient of absorption in the spectrophotometry experiments.

3.1.3 Complex refractive index

In the previous section, we mentioned the refraction and absorption processes. These phenomena can both be described by a single parameter called complex refractive index:

$$\tilde{n} = n + i\kappa \quad (3.4)$$

where \tilde{n} is a complex number. The real part of this equation is the usual refractive index n and the imaginary part is the extinction coefficient κ which is directly related to the absorption coefficient α by:

$$\alpha = \frac{4\pi\kappa}{\lambda} \quad (3.5)$$

Generally, we use the dielectric function to optically describe a material. The dielectric function is characteristic of each material: metals, transparent or opaque media, insulators or semiconductors for example. Its complex function is expressed by:

$$\tilde{\varepsilon}(\omega) = \varepsilon_1(\omega) + i\varepsilon_2(\omega) \quad (3.6)$$

This quantity encloses the entire optical information of the response of the material to an electromagnetic field wave for the whole frequency spectrum. By definition the dielectric function is linked to the optical complex refractive index by:

$$\tilde{\varepsilon}(\omega) = \tilde{n}^2(\omega) = [n + i\kappa]^2 = n^2 - \kappa^2 + 2i n \kappa \quad (3.7)$$

By identifying the terms of equations 3.6 and 3.7, we have:

$$\varepsilon_1 = n^2 - \kappa^2 \quad (3.8)$$

$$\varepsilon_2 = 2n\kappa \quad (3.9)$$

and also,

$$n = \frac{1}{\sqrt{2}} \sqrt{\varepsilon_1 + \sqrt{\varepsilon_1^2 + \varepsilon_2^2}} \quad (3.10)$$

$$\kappa = \frac{1}{\sqrt{2}} \sqrt{-\varepsilon_1 + \sqrt{\varepsilon_1^2 + \varepsilon_2^2}} \quad (3.11)$$

If ε_1 and ε_2 are known, n and κ can be calculated in a straightforward way. In the case of a medium with a weak absorption (e.g. insulators), we can consider κ very small and simplify these equations to:

$$n \simeq \sqrt{\varepsilon_1} \quad (3.12)$$

$$\kappa \simeq \frac{\varepsilon_2}{2n} \quad (3.13)$$

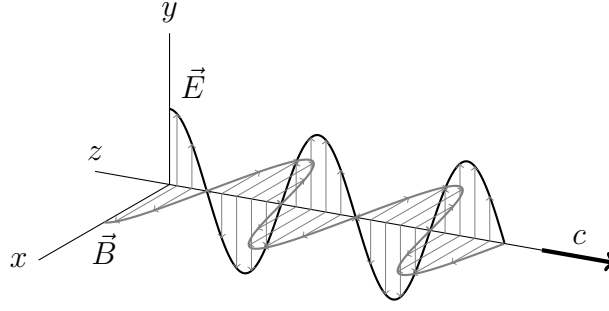


Figure 3.2: Schematic description of an electromagnetic wave propagating in vacuum in the z direction.

These last equations, valid in the weak absorption limit, show us that the refractive index is determined by the real part of the dielectric function, while the absorption is controlled by the imaginary part. For the rest of the manuscript, we will write n and ε without the tilde for the complex refractive index and for the complex dielectric function, respectively.

3.1.4 Polarization of light

As shown in the figure 3.2, an electromagnetic wave (EMW) is the superposition of an electric field coupled to a magnetic field which simultaneously propagate. The whole physical description of an EMW is described by the Maxwell's equations. The plane wave is the simplest solution of these equations and it is a convenient approximation of an EMW far from the source. In this work, the electric field \vec{E} and the magnetic field \vec{B} are described by a plane wave. In Cartesian coordinates, the full expression for the electric field vector of an optical plane wave travelling in the positive direction of the z -axis in an isotropic medium is given by:

$$\vec{E}(z, t) = \vec{E}_x(z, t) + \vec{E}_y(z, t) \quad (3.14)$$

$$\vec{E}(z, t) = E_{x0}e^{i(\omega t - k_0 z + \delta_x)}\vec{e}_x + E_{y0}e^{i(\omega t - k_0 z + \delta_y)}\vec{e}_y \quad (3.15)$$

In these expressions, E_{x0} and E_{y0} are the amplitude, ω the pulsation, $k_0 = \omega n/c$ the wave number with $c = 1/\sqrt{\varepsilon_0\mu_0}$ corresponding to the speed of the wave in void and δ_x and δ_y corresponding to the initial phase of the wave on x and y axes, respectively. With this, we can define the phase difference by: $\delta_y - \delta_x$ (or $\delta_x - \delta_y$). The direction of polarization is, by definition, the direction of the electric field. Indeed, when light interacts with matter, the force acting on the electrons due to the electric field dominates the force due the magnetic field of the wave. This is the reason why the polarization is usually defined from the direction of the electric field. Moreover, when the polarization of the electric field has been measured, the polarization of the other fields vectors can be found from the Maxwell's equations.

In order to describe the state of polarization of the light, the absolute values of the initial phases, i.e. δ_x and δ_y , are not required but only the relative phase difference has to be taken into account. The figure 3.3 presents the variation of the

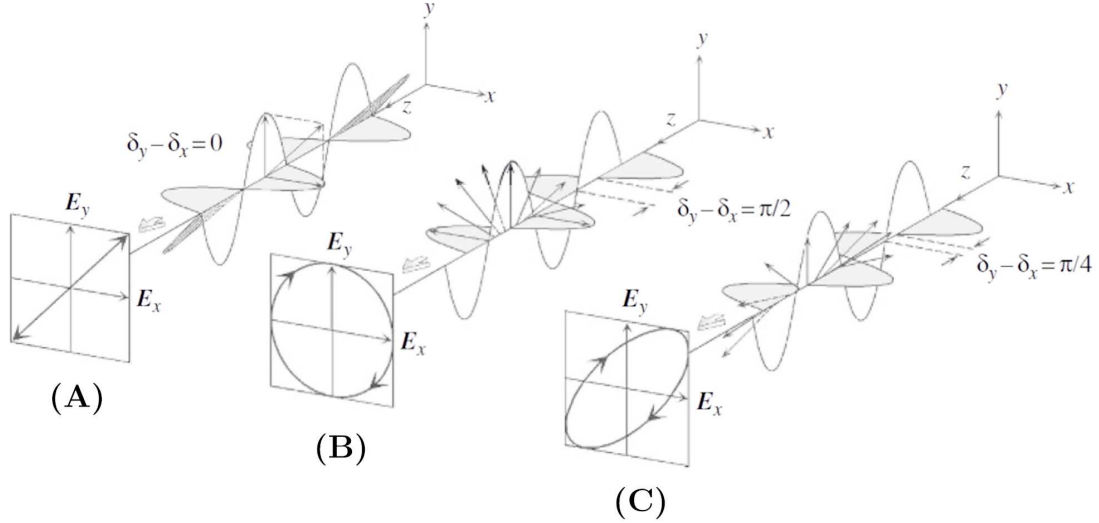


Figure 3.3: Schematic representation of (A) a linear polarization, (B) a right circular polarization and (C) a right elliptical polarization. The phase differences between \vec{E}_x and \vec{E}_y are (A) $\delta_y - \delta_x = 0$, (B) $\delta_y - \delta_x = \pi/2$ and (C) $\delta_y - \delta_x = \pi/4$. (Redrawn from [83]).

polarization state with the phase difference $\delta_y - \delta_x$ where $E_{x0} = E_{y0}$. This leads to three different cases:

- When $\delta_x = \delta_y$ or $\delta_x = \delta_y \pm \pi$, there is no difference phases between \vec{E}_x and \vec{E}_y . The orientation of the resultant vector is always 45° in the (x, y) plane and its amplitude is $\sqrt{2}$ times larger than that of E_{x0} or E_{y0} .
- When $|\delta_x - \delta_y| = \frac{\pi}{2}$ and $E_{x0} = E_{y0}$, the polarization is circular. The field describes a circle in the (x, y) plane. By choosing a point on the z axis, the synthesized vector on the point rotates towards the right, or clockwise, as the light propagates with time (the rotation is counterclockwise in the positive direction of the z axis).
- Other cases, the field follows an elliptic curve: the polarization is elliptic.

3.1.5 Jones Matrix

Introduced by R. Jones in 1941 [84], the Jones formalism allows the mathematical description of the polarization states of light in an optical setup. We can therefore represent each optical element by a matrix as we will see in the chapter 4 for polarizer and compensator, for example. By applying the Jones matrix, we can express variations in polarized light from matrix calculations, which is convenient. Moreover, this representation is interesting in our case because it allows the mathematical description of ellipsometry measurements since it considers totally polarized light. In this section, we want to present a brief description of the Jones matrices and of the Jones vectors.

As mentioned in the equation 3.15, the polarization state of light is represented by the superposition of two waves oscillating parallel to the x and y axes. The Jones

vector is defined by the electric field vectors in the x and y directions and is given by:

$$\vec{E}(z, t) = \begin{bmatrix} E_{x0}e^{i(\omega t - k_0 z + \delta_x)} \\ E_{y0}e^{i(\omega t - k_0 z + \delta_y)} \end{bmatrix} = e^{i(\omega t - k_0 z)} \begin{bmatrix} E_{x0}e^{i\delta_x} \\ E_{y0}e^{i\delta_y} \end{bmatrix} \quad (3.16)$$

This latter equation is generally written by omitting the time-dependent prefactor:

$$\vec{E}(z, t) = \begin{bmatrix} E_{x0}e^{i\delta_x} \\ E_{y0}e^{i\delta_y} \end{bmatrix} = \begin{bmatrix} E_x \\ E_y \end{bmatrix} \quad (3.17)$$

where

$$E_x = E_{x0}e^{i\delta_x} = |E_x|e^{i\delta_x} \quad (3.18)$$

$$E_y = E_{y0}e^{i\delta_y} = |E_y|e^{i\delta_y} \quad (3.19)$$

If we use the phase difference $(\delta_x - \delta_y)$, the last equation can be written:

$$E_x = E_{x0}e^{i(\delta_x - \delta_y)} = |E_x|e^{i(\delta_x - \delta_y)} \quad (3.20)$$

$$E_y = E_{y0} = |E_y| \quad (3.21)$$

As the light intensity of EMW is given by:

$$I = |E|^2 = EE^* \quad (3.22)$$

we can write:

$$I = I_x + I_y = E_{x0}^2 + E_{y0}^2 = |E_x|^2 + |E_y|^2 = E_x E_x^* + E_y E_y^* \quad (3.23)$$

During the ellipsometric measurements, we are interested by measuring the relative changes in amplitude and phase of the EMW after the reflection of the light on the sample. Therefore, in general, the Jones vector is expressed by the normalized light intensity, i.e. $I = 1$. In this case, we can write the linearly polarized waves parallel to the x and y directions by:

$$\vec{E}_{linear,x} = \begin{bmatrix} 1 \\ 0 \end{bmatrix} \quad \vec{E}_{linear,y} = \begin{bmatrix} 0 \\ 1 \end{bmatrix} \quad (3.24)$$

Linearly polarized light oriented at 45° with normalized light intensity (as drawn in the figure 3.3A) is written as:

$$\vec{E}_{+45^\circ} = \frac{1}{\sqrt{2}} \begin{bmatrix} 1 \\ 1 \end{bmatrix} \quad (3.25)$$

Finally, for example, the right-circular polarization (\vec{E}_R) (as drawn in the figure 3.3B) and the left-circular polarization (\vec{E}_L) are given by:

$$\vec{E}_R = \frac{1}{\sqrt{2}} \begin{bmatrix} 1 \\ i \end{bmatrix} \quad \vec{E}_L = \frac{1}{\sqrt{2}} \begin{bmatrix} 1 \\ -i \end{bmatrix} \quad (3.26)$$

Ellipsometry requires polarizers and/or compensators whose optical axis is oriented with a certain angle relative to the x or y axis. In this case, we have to take into account of the transformation of the coordinates. If we consider a rotation with an angle α in the clockwise direction and z axis, the rotational matrix is:

$$\mathbf{R}(\alpha) = \begin{bmatrix} \cos(\alpha) & -\sin(\alpha) \\ \sin(\alpha) & \cos(\alpha) \end{bmatrix} \quad (3.27)$$

Therefore, we determine the new state of polarization by left multiplying the initial state by the corresponding rotation matrix:

$$\vec{E}'(z, t) = \mathbf{R}(\alpha) \vec{E}(z, t) = \begin{bmatrix} \cos(\alpha) & -\sin(\alpha) \\ \sin(\alpha) & \cos(\alpha) \end{bmatrix} \begin{bmatrix} E_x \\ E_y \end{bmatrix} \quad (3.28)$$

Application of the Jones formalism to ellipsometric measurements will be considered in the section 4.1.3.

3.2 Optical properties of noble metal nanoparticles

In order to describe the optical properties of materials, we want to use a model to calculate the frequency dependence of the refractive index and absorption coefficient. A first simple model is the dipole oscillator which can be used to model several types of physical phenomena. For example, we have the atomic oscillators due to the oscillations of the bound electrons within the atoms, the vibrational oscillators caused by the vibrations of charged atoms and finally the free electron oscillators in the metal and doped semiconductors well described by the Drude model. Hereinafter, we will describe the dipole oscillator model using the classical Lorentz model.

3.2.1 Lorentz model

Let us consider an electromagnetic wave described by its electric field $\vec{E}_x = E_{x0} e^{i(\omega t - k_0 z + \delta_x)} \vec{e}_x$, which interacts with an atom with a single frequency $\omega_0 = \sqrt{K_s/\mu}$ where K_s is the spring constant and μ is the reduced mass ($\mu^{-1} = m_N^{-1} + m_0^{-1}$ where m_0 is the effective mass of the electron and m_N is the mass of the nucleus). Due to the bound electrons, the resulting interaction between light and atoms can be described as a damped harmonic oscillator. The oscillating dipoles can lose their energy by collisional processes represented by the inclusion of the damping in the oscillator model, while the electric field of the incident wave induces forced oscillations of the atomic dipole. In this model, we can ignore the motion of nucleus because its mass is higher than the mass of electron ($\mu \simeq m_0$). On each electron, there are three forces:

- the electric force due to the electric field:

$$\vec{F}_{\text{elec}} = q\vec{E}; \quad (3.29)$$

- the restoring force caused by the nucleus on the electron (Hooke's law):

$$\vec{F}_{\text{rest}} = -K_s x \vec{e}_x = -m_0 \omega_0^2 x \vec{e}_x; \quad (3.30)$$

- the damping force which is proportional to the electron mass and the damping constant:

$$\vec{F}_{\text{damp}} = -m_0 \Gamma \frac{dx}{dt} \vec{e}_x \quad (3.31)$$

Thus, the equation of motion is given by:

$$m \vec{a} = \vec{F}_{\text{elec}} + \vec{F}_{\text{rest}} + \vec{F}_{\text{damp}} \quad (3.32)$$

$$m_0 \frac{d^2 x}{dt^2} = -eE_0 - m_0 \omega_0^2 x - m_0 \Gamma \frac{dx}{dt} \quad (3.33)$$

$$m_0 \frac{d^2 x}{dt^2} + m_0 \Gamma \frac{dx}{dt} + m_0 \omega_0^2 x = -eE_0 \quad (3.34)$$

On the left-hand side, the first term corresponds to the acceleration of the electron while the second term is the frictional damping force. Looking for solutions of equation 3.34, of the form $x(t) = C e^{-i\omega t}$, it is possible to identify the constant C by:

$$C = -\frac{eE_0}{m_0 (\omega_0^2 - \omega^2 - i\Gamma\omega)} \quad (3.35)$$

The displacement of the electrons from their equilibrium position creates a time dependent dipole moment $\vec{p}(t) = -e\vec{x}(t)$. Thus the macroscopic polarization presents a resonant contribution:

$$\vec{P}_{\text{resonant}} = N\vec{p} = -Ne\vec{x} \quad (3.36)$$

$$= \frac{Ne^2}{m_0} \frac{1}{\omega_0^2 - \omega^2 - i\Gamma\omega} \vec{E} \quad (3.37)$$

where N corresponds to the number of electrons per unit volume. In order to obtain the total polarization of the material, we need to add the contribution of the non-resonant background terms which are presented by $\vec{P}_{\text{non-resonant}}$. Thus, the electric displacement \vec{D} of the material is given by [81]:

$$\vec{D} = \varepsilon_0 \vec{E} + \vec{P} \quad (3.38)$$

$$= \varepsilon_0 \vec{E} + \vec{P}_{\text{non-resonant}} + \vec{P}_{\text{resonant}} \quad (3.39)$$

$$= \varepsilon_0 \vec{E} + \varepsilon_0 \chi \vec{E} + \vec{P}_{\text{resonant}} \quad (3.40)$$

where χ represents the electric susceptibility associated to the non-resonant modes. We will assume that the material is isotropic and, in this case, the relative dielectric tensor is diagonal and reduces to a constant is defined by:

$$\vec{D} = \varepsilon_0 \varepsilon_r \vec{E} \quad (3.41)$$

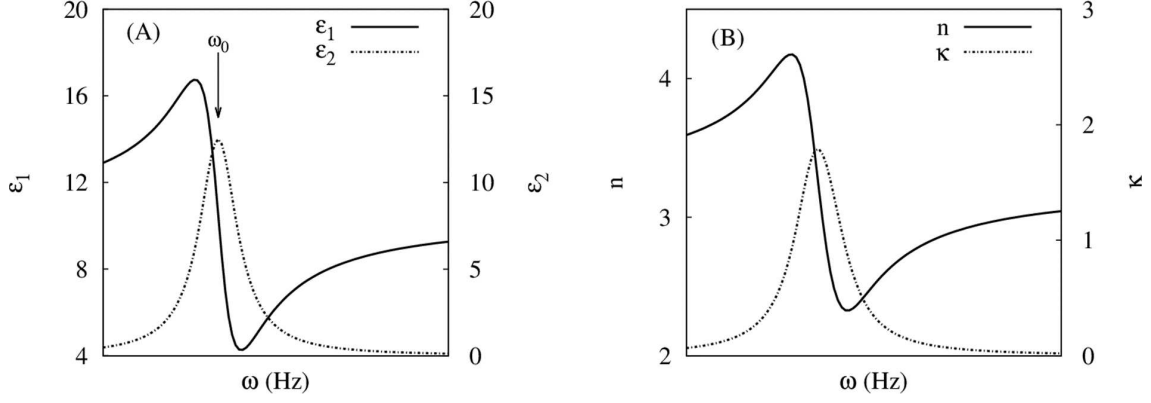


Figure 3.4: (A) Frequency dependence of the real and imaginary parts of the complex dielectric constant of a dipole oscillator at frequency close to the resonance. (B) Variation of the real and imaginary parts of the refractive index as a function of the frequency close to the resonance.

By combining the equations 3.37 and 3.41, we have:

$$\varepsilon_r = 1 + \chi + \frac{Ne^2}{\varepsilon_0 m_0} \frac{1}{\omega_0^2 - \omega^2 - i\Gamma\omega} \quad (3.42)$$

The low and high frequency limits of the relative permittivity is given when $\omega \rightarrow 0$ or $\omega \rightarrow \infty$, respectively:

$$\varepsilon_r(0) \equiv \varepsilon_{st} = 1 + \chi + \frac{Ne^2}{\varepsilon_0 m_0 \omega_0^2} \quad (3.43)$$

$$\varepsilon_r(\infty) \equiv \varepsilon_\infty = 1 + \chi \quad (3.44)$$

where ε_{st} represents the relative permittivity for the static case (i.e. caused by a static electric field). Moreover, we can show that:

$$\varepsilon_{st} - \varepsilon_\infty = 1 + \chi + \frac{Ne^2}{\varepsilon_0 m_0 \omega_0^2} - (1 + \chi) \quad (3.45)$$

$$= \frac{Ne^2}{\varepsilon_0 m_0 \omega_0^2} \quad (3.46)$$

As this quantity is always positive, we therefore have the $\varepsilon_{st} > \varepsilon_\infty$. By using the equations 3.42 and 3.46, we find that the relative permittivity in the Lorentz model is given by:

$$\varepsilon_r(\omega) = \varepsilon_\infty + \frac{\omega_0^2 (\varepsilon_{st} - \varepsilon_\infty)}{(\omega_0^2 - \omega^2 - i\Gamma\omega)} \quad (3.47)$$

From this equation, the real and the imaginary parts (ε_1 and ε_2 , respectively) of the complex dielectric function can be identified. In the figure 3.4A, the representation of ε_1 and ε_2 is given as a function of the frequency. We can see, in the graph of the ε_2 , a sharp peak with a maximum at the resonant frequency ω_0 and a full width at half maximum equal to Γ , the damping constant. The behavior ε_1 is more complex. At lower frequency, the real part of the complex dielectric function gradually

risks from the value of ε_{st} to a peak at $\omega_0 - \Gamma/2$ (not shown in the Fig. 3.4). Then, it rapidly falls to a minimum at $\omega_0 + \Gamma/2$ before rising again to the high frequency limit ε_∞ . From the figure 3.4B, we can follow the variation of the real part of the refractive index and the extinction coefficient as a function of the frequency. We see that n approximately follows the frequency dependence of the square of the real part of the complex dielectric function $n \sim \sqrt{\varepsilon_1}$ and κ keeps more or less the trend of ε_2 . This approximation is valid in the case of κ is much smaller than n , which corresponds to the case considered in this work. It is not valid in the case of bulk metal. We also notice that the refractive index is affected by the Lorentz oscillator over a larger frequency range than the absorption. This interesting fact will be used later during explanation of our results obtained by single wavelength ellipsometry.

3.2.2 Drude Model

The main properties of metals are their high conductivity and their high optical reflectivity in the visible spectral domain. These properties originate from the free electrons, which are not bound to a single atom but can freely move in the crystalline structure of the metal. Their behavior is described by the Drude model and, in this case, the equation of motion is slightly different from equation 3.34:

$$m_0 \frac{d^2 \vec{r}(t)}{dt^2} + m_0 \gamma \frac{d\vec{r}(t)}{dt} = -e \vec{E}(r, \omega) \quad (3.48)$$

where ω is the frequency of the light, m_0 is the (effective) electron mass. The first difference with the Lorentz model is γ , which corresponds here to the electron damping rate due to the electron-electron collisions. There is no restoring force in this case ($\omega_0 = 0$). This constitutes the second difference between the two models. By resolving the differential equation following the same calculations than the Lorentz model, using the definitions of polarization of an electron gas and of the electrical displacement, we can find the relative permittivity for the Drude model:

$$\varepsilon_r(\omega) = 1 - \frac{Ne^2}{\varepsilon_0 m_0 (\omega^2 + i\gamma\omega)} \quad (3.49)$$

$$= 1 - \frac{\omega_p^2}{(\omega^2 + i\gamma\omega)} \quad (3.50)$$

with ω_p the plasma frequency defined by:

$$\omega_p^2 = \frac{Ne^2}{\varepsilon_0 m_0} \quad (3.51)$$

In the case of a weakly damped oscillator the equation 3.50 simplifies as:

$$\varepsilon_r(\omega) \approx 1 - \frac{\omega_p^2}{\omega^2} \quad (3.52)$$

We can see that the oscillator model is a simple analytical way providing the Drude dielectric function of the metal $\varepsilon_r(\omega)$.

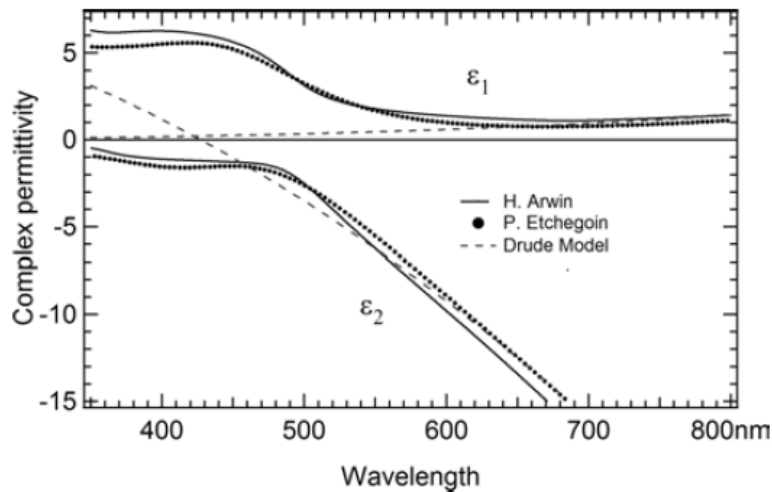


Figure 3.5: Complex dielectric function of gold obtained from ellipsometric experiments from H. Arwin [85] and from analytical model based on Johnson and Christy’s data [86].(Graphic from [20]).

The Drude model predictions can be compared with the experimental data of Johnson and Christy [86] for gold (Fig. 3.5 [20]). This graph shows us that the permittivity of the metal is well described by the model in the wavelength region above 600 nm corresponding to the intraband transitions dominated by the conduction electrons. But, under 550 nm, the model completely dismisses the contribution of the interband transitions. These interband transitions appears when the incident light has enough energy to excite bound electrons to the conduction band. Here, we can see the limitation of the Drude model and in order to describe the optical properties of gold on all spectral region, we need an explicit description of these interband transitions.

3.2.3 Surface plasmon resonance

At the plasma frequency ω_p usually situated in the UV range for metals, the dielectric constant of a weakly damped gas of free electrons is equal to zero (Eq. 3.52). A metal consists of a fixed lattice of positive ions together with a gas of free electrons, which leads to a global neutral charge (Fig. 3.6A). This plasma system can be perturbed and we can consider a displacement of the whole free electrons gas. Thus, the fixed lattice of positive ions will exert a restoring force to cancel this displacement of electrons. This may cause positive and negative surface charges and also create a restoring force in the opposite direction: the whole free electrons gas oscillates backward and forward as shown in the figure 3.6B and C. This oscillations are called plasma oscillations and quantized plasma oscillations are called plasmons.

Now, let us consider a large and flat infinite piece of metal with periodically arranged positive charges (nuclei) and bound cloud electrons which are weakly bound due to the coulombian attraction. When light at a suitable frequency interacts with the surface of the metal, an instantaneous displacement of electrons density is created by the coupling between of the electric field of the light and the electrons

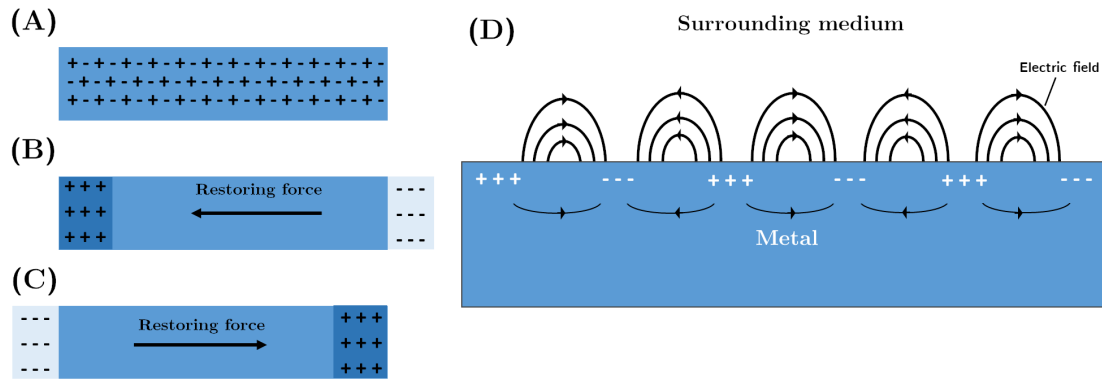


Figure 3.6: (A)-(C) Plasma oscillations in a metallic slab. Metal is considered neutral when there is a balance between the positive and negative charges inside (A). In (B) and (C) due to a perturbation, a displacement of the electron gas is created, which leads to positive and negative surface charges. The restoring forces, which maintain the oscillations at plasma frequency, are established and caused by this displacement of electrons (redrawn from [81]). (D) Schematic illustration of propagating surface plasmon in a bulk metal and the resultant electromagnetic field in both the surrounding medium and metal.

in the metal. Thus, the light is absorbed establishing a periodic oscillation of the positive and negative charges. As the restoring force originates from the interaction between negative charges and nuclei, its magnitude depends on the chemical nature of the metal. These rapid and coherent oscillating electrons produce a strong local electromagnetic field in the metal and the surrounding medium: the Surface Plasmon Resonance (SPR) or Surface Plasmon Polariton. A schematic illustration of this effect is represented in Fig. 3.6D. With this, we understand why the frequency used to excite the plasmon absorption is function of the metal and the dielectric medium around it. In this case of bulk metal, these surface plasmons can propagate along the surface. For certain types of metal used as waveguides or sensors, these surface plasmons appear in the infrared region of the electromagnetic spectrum.

3.2.4 Localized surface plasmon resonance

If we do not consider a flat metal surface or films anymore but nanoparticles, the charge oscillations will be different. In this case, as shown in the figure 3.7A, the size of nanoparticles being much smaller than the wavelength of the incident light, the electrons cloud of particle is fully surrounded by the electric field. A surface charge is created by all polarized electrons that accumulate successively at each side of the particle. This oscillating polarization of the particle creates an electric field opposed to the excitation field and results in a restoring force (red arrow in Fig. 3.7A). This oscillation is partially damped through the creation of heat and light scattering. This effect can be described by a dipolar oscillator with a resonance frequency of ω_0 . This resonance is called the Localized Surface Plasmon Resonance (LSPR). For gold and silver nanoparticles, the plasmon resonance occurs in the visible or near-infrared region. If we consider a group of homogeneous nanoparticles and a light beam going through it, the emerging beam presents a spectrum with a sharp absorption at ω_0 due

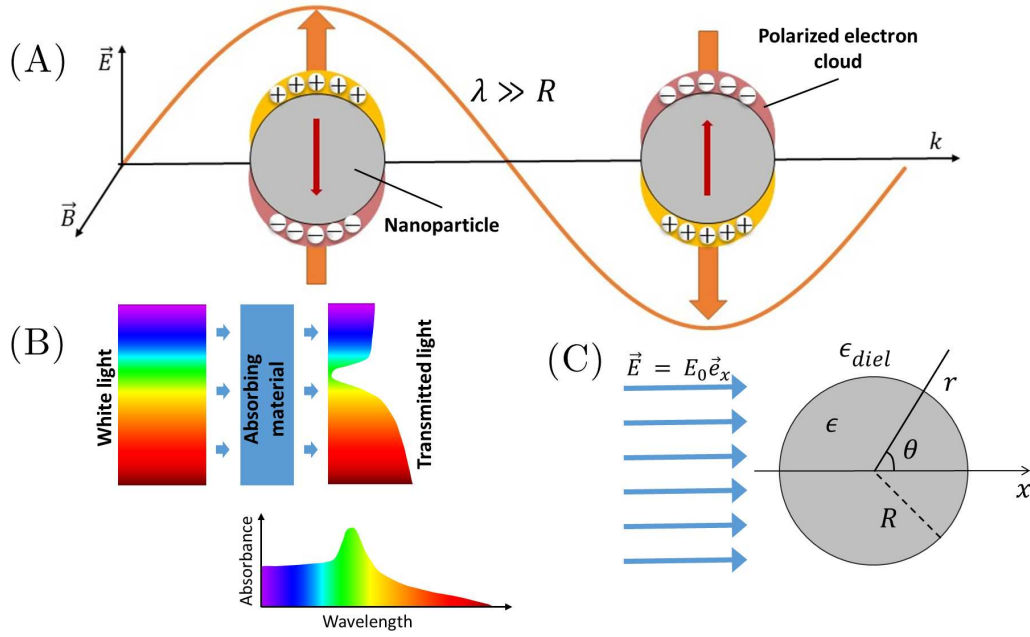


Figure 3.7: (A) Schematic representation of nanoparticles under the influence of an excitation wave with a wavelength longer than the radius of the sphere, the polarized electron cloud oscillate and the system can be represented by an oscillating dipole. (B) Graphical illustration of a white light travelling through an absorbing medium, which cause an absorption of the incident light. The transmitted light presents a dip in the spectrum. (C) Graphical representation of a sphere of radius R in a uniform static electric field.

to the LSPR. The figure 3.7B represents this absorption peak at a well determined wavelength. A polychromatic light (white light) is travelled through an absorbing medium and the transmitted light presents a dip in the spectrum, which corresponds to the absorbed light.

A theoretical approach for the resonance of a single particle was demonstrated by Gustav Mie in 1908 [7]. He proposed a general solution for scattering and absorption from single, isolated spheres based on the Maxwell's equations. He started this work in order to explain the color of colloidal gold nanoparticles solutions. With this theoretical method, he was able to calculate the spectra of gold nanoparticles of various sizes which is a great achievement even nowadays. In fact, Mie theory gives the exact solution of a plane wave interacting with a metallic sphere using multipole contributions. In the case of nanoparticles whose size is less than $R = 50$ nm, we can restrain this approach to a dipolar model called the quasistatic approximation.

We will see in the next section that the LSPR depends on the environment close to the nanoparticle surface. Experimentally, the LSPR is widely used for enhancing the sensitivity of biosensors [87–89].

Quasistatic approximation

In the quasistatic approximation, by considering a particle with a radius R (with $R \ll \lambda$, λ corresponding to a wavelength in the visible part of the electromagnetic spectrum) and a permittivity ϵ in a dielectric environment with ϵ_{diel} submitted to

an excitation electric field (Fig. 3.7C), along the x axis $\vec{E} = E_0\vec{e}_x$, the electronic polarization is totally in phase with the excitation field. As the displacement of the electrons can be treated as a whole, the charge distribution in the particle can be treated as if it was a static distribution. The inside \vec{E}_{int} and the outside \vec{E}_{ext} electric fields are linked to the electric potential $V_{\text{int}}(r, \theta)$ and $V_{\text{ext}}(r, \theta)$, where r is the distance from the center of the sphere and θ is the angle relative to the propagation axis in the polar coordinates, by:

$$\vec{E}_{\text{int}} = -\vec{\nabla}V_{\text{int}} \quad (3.53)$$

$$\vec{E}_{\text{ext}} = -\vec{\nabla}V_{\text{ext}} \quad (3.54)$$

where

$$\nabla^2V_{\text{int}} = 0 \quad (r < R) \quad (3.55)$$

$$\nabla^2V_{\text{ext}} = 0 \quad (r \geq R) \quad (3.56)$$

due to the boundaries conditions. Moreover, the electric potentials are independent of the azimuthal angle because of the symmetry of the problem. At the particle surface, the potential and its weighed derivative has to be continuous. It therefore obeys the continuity equations which lead to:

$$V_{\text{int}} = V_{\text{ext}} \quad (3.57)$$

$$\varepsilon(\omega)\frac{\partial V_{\text{int}}}{\partial r}\Big|_{r=R} = \varepsilon_{\text{diel}}(\omega)\frac{\partial V_{\text{ext}}}{\partial r}\Big|_{r=R} \quad (3.58)$$

These equations correspond to the continuity of the tangential components of the electric field \vec{E} and the continuity of the normal components of the electric displacement \vec{D} , respectively. Finally, the electric field far away from the particle should be the excitation field:

$$\lim_{r \rightarrow \infty} V_{\text{ext}} = -E_0x \quad (3.59)$$

where x is the direction of the electric field and \vec{e}_x is the unit vector in this direction. After some calculations, we can obtain V_{int} and V_{ext} :

$$V_{\text{int}} = -\frac{3\varepsilon_{\text{diel}}}{\varepsilon + 2\varepsilon_{\text{diel}}}E_0r \cos \theta \quad (3.60)$$

$$V_{\text{ext}} = -E_0r \cos \theta + R^3E_0\frac{\varepsilon - \varepsilon_{\text{diel}}}{\varepsilon + 2\varepsilon_{\text{diel}}}\frac{\cos \theta}{r^2} \quad (3.61)$$

If we look at the potential generated by the electrical dipole moment $\vec{p} = p\vec{e}_x$, we have:

$$V = \frac{\vec{p} \cdot \vec{r}}{4\pi\varepsilon_{\text{diel}}r^3} = \frac{p \cos \theta}{4\pi\varepsilon_{\text{diel}}r^2} \quad (3.62)$$

We can see that the equation 3.61 corresponds to the sum of the potential of the incident field and of the electric dipolar moment produced by the particle. This dipole is equivalent to the electric dipolar moment of the sphere:

$$p = 4\pi\varepsilon_{\text{diel}}R^3\frac{\varepsilon - \varepsilon_{\text{diel}}}{\varepsilon + 2\varepsilon_{\text{diel}}}E_0 \quad (3.63)$$

Therefore, the polarizability of the sphere is given by $p = \alpha E_0$ where α is:

$$\alpha = \frac{4}{3}\pi R^3 \varepsilon_{\text{diel}} \left(\frac{\varepsilon - \varepsilon_{\text{diel}}}{\varepsilon + 2\varepsilon_{\text{diel}}} \right) \quad (3.64)$$

The electromagnetic response of the particle is captured in the polarizability and it is clear that the external field will be maximum when the polarizability is maximized. As already shown, the permittivity depends on the frequency ($\varepsilon(\omega)$), which means that $|\alpha|$ can be maximized when:

$$|\varepsilon + 2\varepsilon_{\text{diel}}| \text{ is a minimum} \quad (3.65)$$

The permittivity of the surrounding medium $\varepsilon_{\text{diel}}$ can be approximated by a constant and real parameter and the equation 3.65 can be applied on the real part of the ε :

$$\varepsilon_1 + 2\varepsilon_{\text{diel}} = 0 \quad (3.66)$$

The last equation indicates the condition to observe an LSPR: an opposite sign between the permittivity of the surrounding medium and the permittivity of the sphere. It is the case for a metallic particle in a dielectric matrix and this equation is known as the Fröhlich equation or the Fröhlich resonance condition [90]. For example, in the case of gold particles in a poly-(vinyl) alcohol (PVA) matrix, $\varepsilon_{\text{diel}} = 2.18$, which leads to $\varepsilon_1 = -4.36$. It is easy to check from the plot of the dielectric function of gold (Fig. 3.5) that this value of ε_1 corresponds to an LSPR around 530 nm.

As we have just seen, the surrounding medium plays a role in the plasmon resonance through its refractive index n_{diel} related to the dielectric function ($\varepsilon_{\text{diel}} = n_{\text{diel}}^2$). The calculated frequency plasmon resonance in case of spherical gold nanoparticles in different media can be found in the book of Louis and Pluchery [20]. It shows that a higher optical refractive index shifts the plasmon resonance to large wavelengths. For example, the plasmon resonance in water ($n = 1.33$) occurs at 519 nm and in titanium oxide ($n = 2.79$) at 678 nm.

In the case of non-spherical particles, an analytical model to calculate the polarizability can be found in the case of ellipsoids and of infinite cylinders. For ellipsoids, three plasmon resonances are possible, corresponding to the oscillations of electrons along the three principal (semi-)axes. It is possible to tune the LSPR from the visible to the infrared region by changing the axes length, i.e. the shape factor of the nanoparticles. The excitation of one of these plasmon resonances depends on the direction of the incident electric field and thus on the direction of the light beam and on its polarization. The polarizability along the axis i ($i = x, y$ or z) of this kind of particles depends on the depolarization factor L_i , which is a purely geometric factor [20]:

$$\alpha_i = \frac{V_e}{4\pi} \frac{\varepsilon - \varepsilon_{\text{diel}}}{\varepsilon_{\text{diel}} + L_i(\varepsilon + \varepsilon_{\text{diel}})} \quad (3.67)$$

where V_e is the volume of the ellipsoids given by: $V_e = (4\pi abc)/3$ where a , b and c are the semi-axes of the ellipsoids. As we will show in the chapters 5 and 6, the nanoparticles that we produce seem spherical. In this case, we will not develop more this model and we consider the depolarization factor equals to $1/3$.

3.2.5 Effective medium

In the previous section, we have considered a homogeneous medium. In the case of an inhomogeneous medium with several components, the optical properties are not a simple combination of the optical properties of each component. Let us consider a composite material formed by nanoparticles and a homogeneous matrix, then the optical properties of this mixed material depend both on the nanoparticles and on the matrix optical and structural properties. This inhomogeneous nanocomposite can be substituted by an homogeneous material defined by a new complex dielectric function ε_{eff} , which is more suitable to determine its optical properties. The description of a composite material by an effective medium is called the effective medium approximation (EMA). A model, depending of the nanoparticle properties, their concentration and the surrounding matrix, has to be established in order to calculate the ε_{eff} . Nowadays, numerous equations for the effective dielectric function are available based on different approximative models [91].

As a starting point, we will come back on the Clausius-Mossotti relationship, which gives the permittivity of a medium composed of atomic or molecular dipoles. Second, we will introduce the simplest approach to an effective medium established by Maxwell-Garnett.

a) Clausius-Mossotti relation

The Clausius-Mossotti (CM) relation allows to determine the permittivity of a medium $\varepsilon_{\text{diel}}$ from the macroscopic polarizability α of atoms or molecules [92, 93]. The local electric field for a given dipole is the sum of four contributions:

$$\vec{E}_l = \vec{E}_0 + \vec{E}_1 + \vec{E}_2 + \vec{E}_3 \quad (3.68)$$

In this equation, \vec{E}_0 is the external field and \vec{E}_1 is the depolarization field created by its superficial charges. \vec{E}_2 is the field due to the surface charge density and we can find:

$$\vec{E}_2 = \frac{\vec{P}}{3\varepsilon_{\text{diel}}} \quad (3.69)$$

where \vec{P} is the polarization of the dielectric. The electric field \vec{E}_3 created by the other dipole can be assumed to be zero due the symmetry of the system. The local electric field on the dipole becomes:

$$\vec{E}_l = \vec{E}_0 + \vec{E}_1 + \frac{\vec{P}}{3\varepsilon_{\text{diel}}} \quad (3.70)$$

More over, $\vec{E} = \vec{E}_0 + \vec{E}_1$ where \vec{E} is the total macroscopic electric field in the sample due to the external and depolarization fields. We can write the local electric field on the dipole:

$$\vec{E}_l = \vec{E} + \frac{\vec{P}}{3\varepsilon_{\text{diel}}} \quad (3.71)$$

The definition of the macroscopic polarization is $\vec{P} = n\vec{p} = n\alpha\vec{E}_l$ where n is the volume number of dipoles and α the polarizability. By combining this equation and

the equation 3.71, we have:

$$\vec{P} = \frac{n\alpha\vec{E}}{1 - \frac{n\alpha}{3\varepsilon_{\text{diel}}}} \quad (3.72)$$

As the relative permittivity is given by:

$$\vec{D} = \varepsilon_{\text{eff}}\vec{E} \quad (3.73)$$

$$= \varepsilon_{\text{diel}}\vec{E} + \vec{P} \quad (3.74)$$

therefore, we can write the CM relation:

$$\varepsilon_{\text{eff}} = \varepsilon_{\text{diel}} + \frac{n\alpha}{1 - \frac{n\alpha}{3\varepsilon_{\text{diel}}}} \quad (3.75)$$

or its well known version:

$$\frac{\varepsilon_{\text{eff}} - \varepsilon_{\text{diel}}}{\varepsilon_{\text{eff}} + 2\varepsilon_{\text{diel}}} = \frac{1}{3\varepsilon_{\text{diel}}}n\alpha \quad (3.76)$$

b) Effective medium approximation models

As already explained, in the case of an inhomogeneous layer, which is the combination of two or more different materials, we can substitute this layer by a homogeneous material defined by a new complex dielectric function ε_{eff} . Minor inclusions in a matrix or a rough surface are good examples and in this kind of situation, it is convenient to use EMA. The most famous EMAs are the Maxwell-Garnett (MG), the Lorentz-Lorenz (LL) and Bruggeman's one. For all of these, the dielectric properties of the mixture are described by a global equation:

$$\frac{\varepsilon_{\text{eff}} - \varepsilon_{\text{h}}}{\varepsilon_{\text{eff}} + 2\varepsilon_{\text{h}}} = \sum_{j=1}^m f_j \frac{\varepsilon_j - \varepsilon_{\text{h}}}{\varepsilon_j + 2\varepsilon_{\text{h}}} \quad (3.77)$$

where m the number of components, ε_j , ε_{h} and ε_{eff} are the complex dielectric functions of inclusions of type j , of the host and of the nanocomposite film, respectively. f_j corresponds to the volume fraction of inclusions of type j in the host material with a permittivity of ε_{h} . The sum of the volume fractions equals unity:

$$\sum_{j=1}^m f_j = 1 \quad (3.78)$$

In the case of two different materials, 1 and 2, the equation 3.77 becomes:

$$\frac{\varepsilon_{\text{eff}} - \varepsilon_{\text{h}}}{\varepsilon_{\text{eff}} + 2\varepsilon_{\text{h}}} = f_1 \frac{\varepsilon_1 - \varepsilon_{\text{h}}}{\varepsilon_1 + 2\varepsilon_{\text{h}}} + f_2 \frac{\varepsilon_2 - \varepsilon_{\text{h}}}{\varepsilon_2 + 2\varepsilon_{\text{h}}} \quad (3.79)$$

where ε_1 , ε_2 , ε_{h} and ε_{eff} are the complex dielectric functions of inclusions of type 1, of inclusions of type 2, of the dielectric host and of the nanocomposite film, respectively. In this equation, f_1 and $f_2 = 1 - f_1$ correspond to the volume fractions of metallic inclusions with a permittivity ε_1 and ε_2 , respectively, in a dielectric matrix with a permittivity ε_{h} . The choice of the host medium defines different EMAs, yielding either MG, LL or Bruggeman models.

In the case of the MG approximation, the host is the majoritary component (i.e. the matrix). Using $\varepsilon_h = \varepsilon_2$, the second term of the equation 3.79 vanishes. Therefore, the complex dielectric function of a dielectric medium containing spherical inclusions is given by:

$$\frac{\varepsilon_{\text{eff}} - \varepsilon_2}{\varepsilon_{\text{eff}} + 2\varepsilon_2} = f_1 \frac{\varepsilon_1 - \varepsilon_2}{\varepsilon_1 + 2\varepsilon_2} \quad (3.80)$$

The MG model is one of the most commonly used EMA. This model was proposed in 1904 to explain the coloration of glasses containing metallic inclusions [6]. This MG-EMA model will be used in the chapter 7 to determine the local optical properties of gold nanoparticles (small inclusions) in polymer matrix (host) at low doping level.

The equation 3.80 was developed for spherical particles without interaction with neighbouring particles. They are completely encapsulated in an insulating matrix and their size has to be small in comparison with the wavelength of the incident light. Moreover in the equation 3.80, the volume fraction of the metal f cannot be higher than 0.3 (i.e. $f < 0.3$) in order to neglect the particle-particle interactions [94].

In the LL approximation, the $\varepsilon_h = 1$ which corresponds to point polarizable entities embedded in vacuum. The equation 3.79 becomes:

$$\frac{\varepsilon_{\text{eff}} - 1}{\varepsilon_{\text{eff}} + 2} = f_1 \frac{\varepsilon_1 - 1}{\varepsilon_1 + 2} + f_2 \frac{\varepsilon_2 - 1}{\varepsilon_2 + 2} \quad (3.81)$$

with always the same meanings for ε_1 , ε_2 , ε_h , ε_{eff} , f_1 and f_2 .

Finally, the Bruggeman's EMA is also a well-known effective medium approximation which treats both materials on an equal basis and defines the host as the effective medium itself [45]. The left part of the equation 3.79 equals to zero, leading to the complex dielectric function of the effective medium of the Bruggeman theory:

$$f_1 \frac{\varepsilon_1 - \varepsilon_{\text{eff}}}{\varepsilon_1 + 2\varepsilon_{\text{eff}}} + f_2 \frac{\varepsilon_2 - \varepsilon_{\text{eff}}}{\varepsilon_2 + 2\varepsilon_{\text{eff}}} = 0 \quad (3.82)$$

As we can see, in this equation ε_1 and ε_2 play the same role and can be exchanged. This Bruggeman EMA is an interesting model to optically describe interfacial roughness and materials prepared from totally miscible components with aggregate structure.

Extensions of these formula for a mixture with more than two components exist [95].

As it will be shown later, in order to analyse our ellipsometric measurements of gold nanoparticles embedded in a polymer matrix, we use the Maxwell-Garnett effective medium approximation (MG-EMA) because the volume fraction f of nanoparticles embedded in our plasmonic nanocomposite is small.

In order to be precise, the calculation of the optical properties of materials can be separated in two paths. In A. Heilmann's book [96], Mie theory is presented as the results of the rigorous route calculations of the optical properties of the plasmonic nanocomposites films. The calculations of the optical extinction of single particles by solving Maxwell's equations and their use in e.g. the fitting of the UV-visible extinction spectra is achieved by multiplying the single particle result by a concentration factor. On the other hand, MG-EMAs, have to be seen as the result

of a statistical route yielding an effective dielectric function. The concentration delimiting the use between the former and the latter approach is not clearly defined and, from a practical point of view, the choice remains difficult and confusing: Mie theory is commonly used to determine the average size of the nanoparticles in solution, so far away from the “single particle hypothesis”. Moreover, the size of the particles appears in the Mie theory only in the prefactor describing the concentration effect, as the result of the quasi-static approximation. The MG-EMA under its classical versions only takes into account the metal volume fraction and the shape parameters, but not the direct size of the particles. Some extensions of the theory have been proposed to include the particle size [97]. From the ellipsometric point of view, MG-EMA is easier to introduce in the data analysis. In conclusion, we have chosen the MG-EMA model to analyze our ellipsometric result as it will be described in the chapter 6.

3.2.6 The Kramers-Krönig relationships

The discussion of the dipole oscillator and more precisely the Lorentz model shows that ε_1 and ε_2 , which correspond to the real part and imaginary part of the complex dielectric function, respectively, are related to each other. In the figure 3.4, we clearly see that a variation of ε_2 induces a variation of ε_1 . Furthermore, the real and imaginary parts of the refractive index, n and κ respectively are associated to ε_1 and ε_2 , which means that a variation of κ induce a variation of n and inversely. In fact, it is possible to give general relationships between the real and imaginary parts of the refractive index. These are the Kramers-Krönig (KK) relation and are given by [83, 98]:

$$n(\omega) = 1 + \frac{2}{\pi} P \int_0^{\infty} \frac{\omega' \kappa(\omega')}{\omega'^2 - \omega^2} d\omega' \quad (3.83)$$

$$\kappa(\omega) = -\frac{2}{\pi} P \int_0^{\infty} \frac{n(\omega') - 1}{\omega'^2 - \omega^2} d\omega' \quad (3.84)$$

where P is the principal part of the integral. These equations are very useful because they allow us to measure the absorption as a function of the frequency and then calculate the refractive index without any measurements of n , provided $\kappa(\omega)$ is known over a (very) large spectral domain.

3.3 Reflection and transmission of polarized light

We will see in other chapters that we use ellipsometry to analyse our samples. In order to interpret ellipsometric data when polarized light is reflected by the sample, the electromagnetic theory of light should be used to have access to the complex amplitude reflection and transmission coefficients. In this section, we will start with a simple case of a planar interface between two homogeneous media. After, we will focus on a system with a film on a substrate.

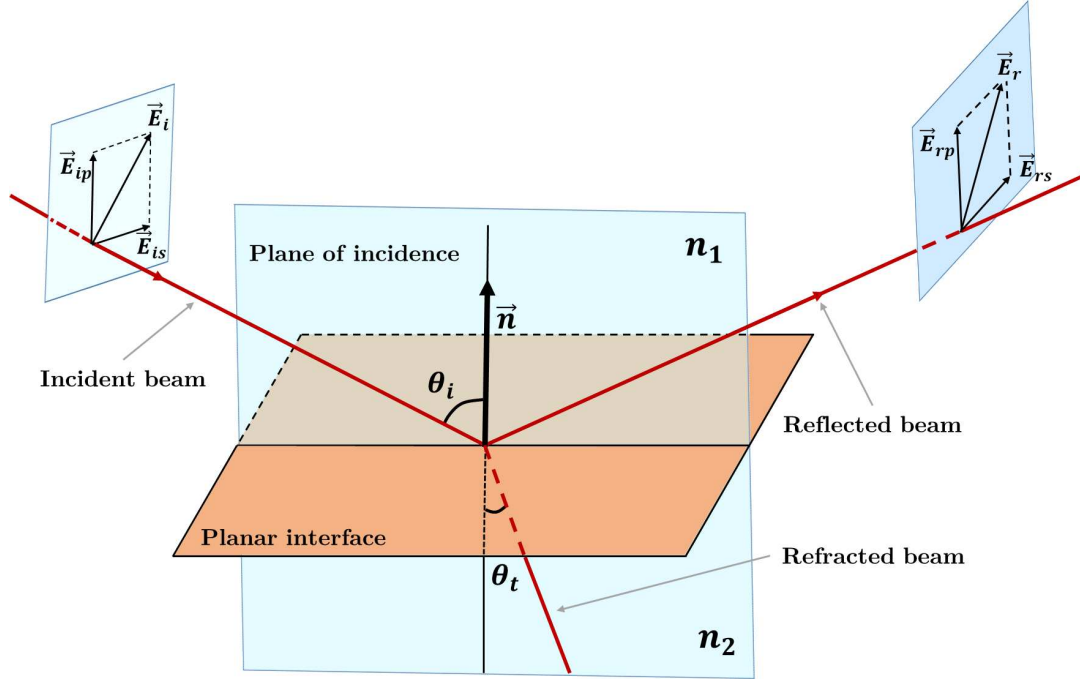


Figure 3.8: Schematic illustration of an incident beam reflected and refracted at the planar interface between two media n_1 and n_2 . The electric field is decomposed in s and p components corresponding to the perpendicular and parallel orientation to the plan of incidence, respectively. Due to the reflection, the direction of the reflected electric field is modified.

3.3.1 Reflection and refraction between two isotropic media

Consider an incident optical wave at the planar interface between two semi-infinite homogeneous, optically isotropic media described by their complex index of refraction n_1 and n_2 . As we showed in the section 3.1.1, at an interface, two optical processes can occur: reflection and refraction. The incident wave from the first medium gives rise to a reflected wave in the same medium and a refracted (or transmitted) wave in the second medium. As we can see in the figure 3.8, the angle of incidence θ_i and the angle of refraction θ_t are determined from the normal to the interface (dashed line). The direction of propagation of the incident, reflected, refracted waves must be in the same plane called the plane of incidence. Due to the law of reflection, the angle of reflection is equal to the angle of incidence. Finally, the angles of incidence and refraction are related by the Snell's law given by:

$$n_1 \sin(\theta_i) = n_2 \sin(\theta_t) \quad (3.85)$$

In optics, depending on the electric field's oscillation, a general polarization can be described in terms of superposition of p and s polarizations. When the electric field is parallel to the plane of incidence, the light is said to be p polarized. In the other case, when the electric field is perpendicular to the plane of incidence, the light is s polarized (Fig. 3.8). At the interface, for a given amplitude and polarization of the incident wave, the amplitude and polarization of the reflected and transmitted waves can be calculated from the continuity of the tangential components of the

electric \vec{E} and magnetic field \vec{H} vectors and from the continuity of the normal components of the electrical displacement \vec{D} and the magnetic flux density $\vec{B} = \mu\vec{H}$ (μ corresponds to the permeability). In this thesis, as we only consider non magnetic materials, $\mu = \mu_0$. It is suitable to determine the amplitudes of reflected and transmitted waves in terms of those of the incident wave for the p and s polarizations. The advantage is the p and s components can be resolved separately and combined at the end. In the p polarization, we have [83, 99]:

$$E_{ip} \cos \theta_i + E_{rp} \cos \theta_r = E_{tp} \cos \theta_t \quad (3.86)$$

$$B_{ip} + B_{rp} = B_{tp} \quad (3.87)$$

where the indices i , r and t corresponds to incident, reflected and transmitted field, respectively. In the s polarization:

$$E_{is} + E_{sp} = E_{ts} \quad (3.88)$$

$$-B_{is} \cos \theta_i + B_{rs} \cos \theta_r = -B_{tp} \cos \theta_t \quad (3.89)$$

Using the relation $nE = cB$, we can rewrite the equation 3.87 as:

$$n_i (E_{ip} + E_{rp}) = n_t E_{tp} \quad (3.90)$$

The reflection coefficient is defined by $r_p \equiv E_{rp}/E_{ip}$. By combining the previous equations, it is possible to eliminate E_{tp} and using the relation $\theta_i = -\theta_r$ (reflection law), the reflection coefficient becomes:

$$r_p \equiv \frac{E_{rp}}{E_{ip}} = \frac{n_t \cos \theta_i - n_i \cos \theta_t}{n_t \cos \theta_i + n_i \cos \theta_t} \quad (3.91)$$

Following the same method, we have access to the transmission coefficient:

$$t_p \equiv \frac{E_{tp}}{E_{ip}} = \frac{2n_i \cos \theta_i}{n_t \cos \theta_i + n_i \cos \theta_t} \quad (3.92)$$

These equations correspond to the p polarization. For the s polarization:

$$r_s \equiv \frac{E_{rs}}{E_{ip}} = \frac{n_i \cos \theta_i - n_t \cos \theta_t}{n_i \cos \theta_i + n_t \cos \theta_t} \quad (3.93)$$

$$t_s \equiv \frac{E_{ts}}{E_{ip}} = \frac{2n_i \cos \theta_i}{n_i \cos \theta_i + n_t \cos \theta_t} \quad (3.94)$$

These coefficients are the Fresnel complex amplitude reflection (r) and transmission (t) coefficients for the p and s polarizations. These terms can be written in another form to easily examine the effect of reflection and refraction on the amplitude and phase:

$$r_p = |r_p| e^{i\delta_{r_p}} \quad r_s = |r_s| e^{i\delta_{r_s}} \quad (3.95)$$

$$t_p = |t_p| e^{i\delta_{t_p}} \quad t_s = |t_s| e^{i\delta_{t_s}} \quad (3.96)$$

$|r_p|$ and $|t_p|$ ($|r_s|$ and $|t_s|$) correspond to the ratios of the amplitudes of the vibrations of the electric vectors of the reflected and transmitted waves to the incident waves when the polarization is parallel (perpendicular) to the plane of incidence. δ_{r_p} and δ_{t_p} give the phase shifts upon reflection and transmission, respectively, for the p polarization, with similar meanings for δ_{r_s} and δ_{t_s} .

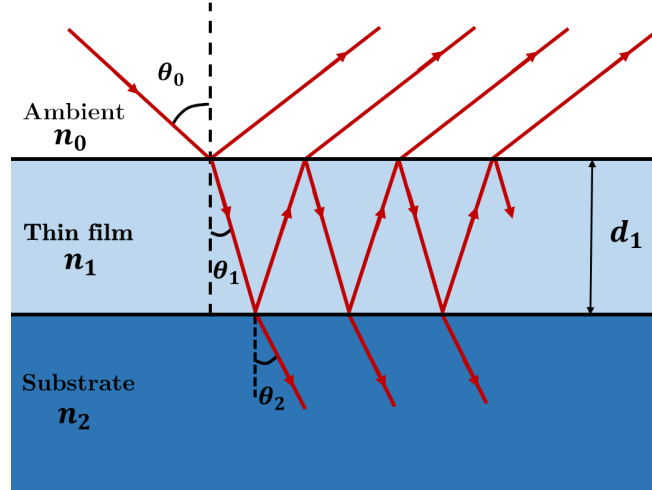


Figure 3.9: Schematic illustration of an ambient-film-substrate system. Multiple reflections and transmissions of partial waves coming from an incident wave on a thin film with a thickness d_1 . n_0 , n_1 and n_2 correspond to the complex refractive index of the ambient, the film and the substrate, respectively.

3.3.2 Reflection and transmission by a thin film on a substrate

Numerous ellipsometric studies perform the analysis of the optical properties of substrate covered by a single film. As shown in the figure 3.9, the simple case corresponds to a film with parallel-plane boundaries of separation (film thickness d_1) and sandwiched between two semi-infinite ambient (generally air) and substrate media. The ambient (0), the film (1) and the substrate (2) are homogeneous and optically isotropic with indices of refraction n_0 , n_1 and n_2 , respectively.

A plane wave incident in the ambient with an angle of θ_0 will give rise to a resultant reflected wave in the ambient and to a resultant transmitted waves in the substrate. The goal of this part is to relate the complex amplitudes of the resultant reflected and transmitted waves to the amplitude of the incident wave when this incident wave is linearly polarized for polarizations p and s . We assume that when the incident wave first meets the ambient-film interface, a part of it is reflected in the ambient and a part is refracted in the film, in agreement with the interface Fresnel reflection and transmission coefficients. The refracted wave inside the film suffers multiple internal reflections at the film-substrate and film-ambient interfaces. These interfaces are the delimitation of the film and they are not perfectly reflecting. Then, each time the multiply-reflected wave in the film strikes the film-substrate (1-2) or film-ambient(1-0) interface, a partial wave is transmitted into the semi-infinite substrate or ambient medium. The Fresnel reflection and transmission coefficients at the 0-1 and 1-2 interfaces are designated by r_{01} , t_{01} and r_{12} , t_{12} respectively, thus the complex amplitudes of the successive partial plane waves that form the resultant reflected wave in the ambient are given by r_{01} , $t_{01}t_{10}r_{12}e^{-2i\beta}$, $t_{01}t_{10}r_{01}r_{12}^2e^{-4i\beta}$, $t_{01}t_{10}r_{01}^2r_{12}^3e^{-6i\beta}$, The complex amplitudes of the successive partial plane waves that form the resultant transmitted wave in the substrate are given by $t_{01}t_{12}e^{-i\beta}$, $t_{01}t_{12}r_{01}r_{12}e^{-3i\beta}$, $t_{01}t_{12}r_{01}^2r_{12}^2e^{-5i\beta}$. β is the

propagation phase of the beam inside the film, and is given by:

$$\beta = 2\pi \left(\frac{d_1}{\lambda} \right) n_1 \cos \theta_1 = 2\pi \left(\frac{d_1}{\lambda} \right) \sqrt{n_1^2 - n_0^2 \sin^2 \theta_0} \quad (3.97)$$

where λ is the free space wavelength, d_1 the film thickness, n_1 the complex refractive index of the film, θ_1 the angle of refraction in the film, n_0 the refractive index of the ambient and θ_0 correspond to the angle of incidence.

The total reflected amplitude r_{012} is given by the addition of the partial waves which leads to an infinite geometric series:

$$r_{012} = r_{01} + t_{01}t_{10}r_{12}e^{-2i\beta} + t_{01}t_{10}r_{10}r_{12}^2e^{-4i\beta} + t_{01}t_{10}r_{10}^2r_{12}^3e^{-6i\beta} + \dots \quad (3.98)$$

Leading to:

$$r_{012} = r_{01} + \frac{t_{01}t_{10}r_{12}e^{-2i\beta}}{1 - r_{10}r_{12}e^{-2i\beta}} \quad (3.99)$$

And using the relations $r_{10} = -r_{01}$ and $t_{10} = (1 - r_{01}^2)/t_{01}$ [99], the total reflected amplitude is:

$$r_{012} = \frac{r_{01} + r_{12}e^{-2i\beta}}{1 + r_{01}r_{12}e^{-2i\beta}} \quad (3.100)$$

In the same way, the total transmitted amplitude t_{012} is given by an infinite geometric series for which summation gives:

$$t_{012} = \frac{t_{01}t_{12}e^{-i\beta}}{1 + r_{01}r_{12}e^{-2i\beta}} \quad (3.101)$$

These equations (Eqs. 3.100 and 3.101) give the overall complex-amplitude reflection and transmission coefficients for the substrate covered by a single film in terms of:

- the interface Fresnel reflection and transmission coefficients at the ambient-film (0-1) and film-substrate (1-2) interfaces;
- the film thickness that is included in the phase change defined by β (Eq. 3.97), which is also called the phase film thickness.

These equations are valid when the incident wave is linearly polarized either parallel p or perpendicular s to the plane of incidence. We can write with j for s or p :

$$r_j = \frac{r_{01_j} + r_{12_j}e^{-2i\beta}}{1 + r_{01_j}r_{12_j}e^{-2i\beta}} \quad \text{and} \quad t_j = \frac{t_{01_j}t_{12_j}e^{-i\beta}}{1 + r_{01_j}r_{12_j}e^{-2i\beta}} \quad (3.102)$$

where β is the same for both p and s polarizations. The Fresnel reflection and transmission coefficients at the 0-1 and 1-2 interfaces can easily be found from equations 3.91, 3.92, 3.93 and 3.94. The overall complex-amplitude reflection (r_p, r_s) and

transmission (t_p, t_s) coefficients can be written in terms of their absolute values and angles to determine the change of amplitude and phase separately:

$$r_p = |r_p|e^{i\delta_{r_p}} \quad r_s = |r_s|e^{i\delta_{r_s}} \quad (3.103)$$

$$t_p = |t_p|e^{i\delta_{t_p}} \quad t_s = |t_s|e^{i\delta_{t_s}} \quad (3.104)$$

where $|r_p|$ and δ_{r_p} represent the amplitude attenuation and the phase shift respectively when a p -polarized light is reflected by the substrate covered by a single film. $|t_p|$ and δ_{t_p} correspond to the transmitted case. The similar explanation holds true for $|r_s|$, $|t_s|$, δ_{r_s} and δ_{t_s} in the case of a s polarization.

As previously explained, the figure 3.9 represents a thin film sandwiched between two semi-infinite ambient (generally air) and substrate media. Let us consider a very thin film, which means that the phase film thickness β is small. In the case where the complex refractive indexes of the substrate and the film are similar, i.e. $n_1 \simeq n_2$ (typically a very thin polymer film or an organic self-assembled monolayer on glass), the complex reflection coefficient (Eq. 3.93) at the interface between thin film and substrate can be written:

$$r_{12} = \frac{n_1 \cos \theta_1 - n_2 \cos \theta_2}{n_1 \cos \theta_1 + n_2 \cos \theta_2} \quad (3.105)$$

$$\approx \frac{n_1(\cos \theta_1 - \cos \theta_2)}{n_1(\cos \theta_1 + \cos \theta_2)} \quad (3.106)$$

$$\approx 0 \quad (3.107)$$

thanks to the Snell's law because when $n_1 \simeq n_2$ then $\cos \theta_1 \simeq \cos \theta_2$. This analysis leads to another expression of the total reflected amplitude:

$$r_{012_j} = \frac{r_{01_j} + r_{12_j}e^{-2i\beta}}{1 + r_{01_j}r_{12_j}e^{-2i\beta}} \quad (3.108)$$

$$\approx \frac{r_{01_j} + 0 \cdot 1}{1 + r_{01_j} 0 \cdot 1} \quad (3.109)$$

$$\approx r_{01_j} \quad (3.110)$$

with β and r_{12} small. In conclusion of this analysis, with a weak optical contrast, i.e. $n_1 \simeq n_2$, and a small phase film thickness, the optical properties of the thin film cannot be distinguished from the substrate properties using optical reflection or transmission measurements. In other words, the optical system composed by a thin film surrounded by two semi-infinite media becomes two semi-infinite media with only one interface. In order to have appropriate ellipsometric measurements of a system with a low optical contrast, the thickness of the film has to be considerable to detect the film deposited on the substrate.

Materials and Methods

In this chapter, we explain the methods we use to synthesize our plasmonic nanocomposites and all the techniques we employ to analyze these samples. We start with an explanation of the optical devices used in this work: the spectrophotometer, the home-build reflectometer and the ellipsometers. Afterwards, we will introduce the atomic force microscopy necessary for topography measurements at the nanoscale. Finally, we will explain the experimental procedure to create the plasmonic nanocomposite thin films.

4.1 Experimental devices

4.1.1 Spectrophotometry

The spectrophotometry is the study of the transmission and reflection properties of a material as a function of the wavelength of the incident radiation. The spectrophotometry works in the visible range and is more specific than the electromagnetic spectroscopy, which works in a larger spectral range. In order to measure the reflectance or the transmittance of the sample, we need a multi-wavelength light source with an incident intensity I_0 . A detector is placed after the sample to measure the

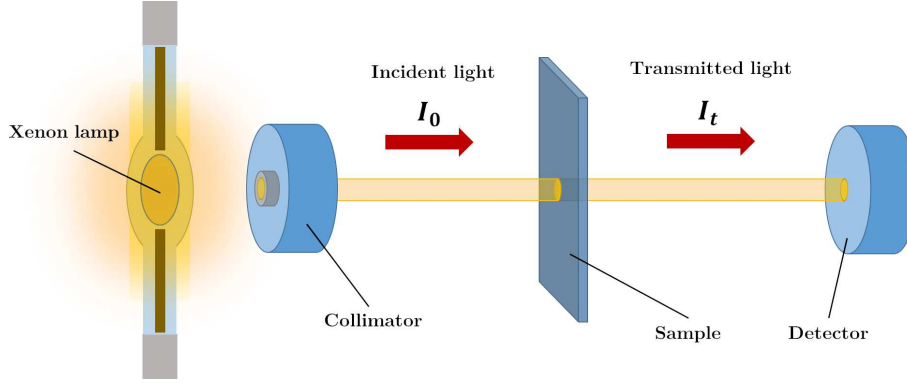


Figure 4.1: Principle of the spectrophotometer used in the laboratory. A xenon flash lamp illuminates the sample at normal incidence. Then, the transmitted light goes to the detector, allowing to measure the absorption spectrum of the sample.

transmitted or reflected intensity $I_t(\lambda)$ and $I_r(\lambda)$, respectively.

$$T(\lambda) = \frac{I_t}{I_0} \quad \text{and} \quad R(\lambda) = \frac{I_r}{I_0} \quad (4.1)$$

For this thesis, we use a Genesys 10S UV-visible spectrophotometer (Thermo Fisher Scientific). A light source (xenon flash lamp) illuminates the sample and the measurement of the transmittance is given by the detector (silicon photodiode), as depicted in the figure 4.1. Thanks to the light source and the monochromator, the spectral range of this device is 190 nm to 1100 nm. We have used this setup to measure the transmittance at normal incidence of films deposited on glass.

By previously measuring the transmittance of the non-doped polymer, we have access to the absorbance of the sample by:

$$A = -\log_{10} \left(\frac{T_{\text{sample}}}{T_{\text{polymer}}} \right) \quad (4.2)$$

where T_{sample} and T_{polymer} are the measured transmittances of the sample and the polymer without doping, respectively. We can use this expression if we assume that the reflexion of the sample and the polymer are the same. We assumed this approximation in the rest of the manuscript. The absorption is useful, since the Beer-Lambert's law (Eq. 3.3) [100] gives access to the extinction cross-section of the particle σ_{ext} via:

$$A \ln 10 = \sigma_{\text{ext}} N_{\text{particle}} d \quad (4.3)$$

where N_{particle} is the number of particles per unit volume and d is the distance crossed by the beam, corresponding to the thickness of the films in our case. In order to fulfill the Beer's law, the diffusion of the light by particles is supposed to be negligible and the extinction is dominated by the absorption: $\sigma_{\text{ext}} \approx \sigma_{\text{abs}}$. By measuring the absorbance A , it is possible to calculate σ_{ext} and have access to the optical properties of the particles. As a part of this work, we used the spectrophotometer to measure the absorption spectrum of our samples. Due to the Localized Surface Plasmon Resonance (LSPR) (Section 3.2.4), the absorption spectra of our nanocomposites

present a sharp absorption peak in the visible range that can be described by three parameters:

- the position of the peak λ_{LSPR} can be related to the size of the nanoparticles inside the polymer matrix;
- the height of the peak A_{LSPR} can be connected to the concentration of nanoparticles;
- the full-width at half maximum (FWHM) of the peak, which can be related to the polydispersity of the nanoparticles embedded in the polymer.

4.1.2 Spectroscopic reflectometry

Another technique to optically study the samples is the spectroscopic reflectometry (SR). Instead of the spectrophotometry where, in our case, the light travels through the sample and the transmission spectrum is recorded, the reflectivity of the sample is recorded with SR (as shown in Fig. 4.2A). This technique is often used to measure the thickness of transparent or semi-transparent thin films usually on reflective substrates (silicon, metals, ...). SR is adequate for samples with thicknesses ranging from few hundred nanometers to several micrometers. This method can be called spectroscopic interferometry because a part of the light is reflected at the surface of the film while another part travels into the film before being reflected on the substrate. All the reflected rays recombine, leading to constructive and destructive interferences, depending on the difference of the optical paths. As we can see in the figure 4.2B, there is a phase shift between the light reflected at the top of the film and the light that has travelled into the film and reflected on the substrate. During a spectroscopic measurement, the intensity of the reflected light is recorded and, as it is also shown in the figure 4.2C, the number of interferometric peaks depends on the thickness of the film. A thick film presents more interferometric peaks than a thinner one in the measurement spectral range. This partially explains the operating range of thickness of this technique. The variation in the phase β is explained in the section 3.3.2 and more precisely in the equation 3.97. In our case, we have worked with a home-build spectroscopic reflectometer. The light source is a SLS201L stabilized Tungsten-halogen lamp with a working range from 360 nm to 2600 nm and the spectrometer is a CSS200 CCD spectrometer (Thorlabs). With this instrument, we are able to analyze the intensity of the reflected light from a sample as a function of the wavelength. The measurements are made at normal incidence, as it is presented in the figure 4.2A.

The intensity recorded by the SR is given by:

$$I(\lambda) = R(\lambda) I_0(\lambda) \quad (4.4)$$

where $R(\lambda)$ is the reflectivity of the sample and $I_0(\lambda)$ correspond to the intensity of the light source. This type of measurement requires a preliminary measurement of a highly reflecting (ideally, 100%) calibrated sample, Spectralon[®] surfaces for example. The goal of this measurement is to determine the reflectivity of a film

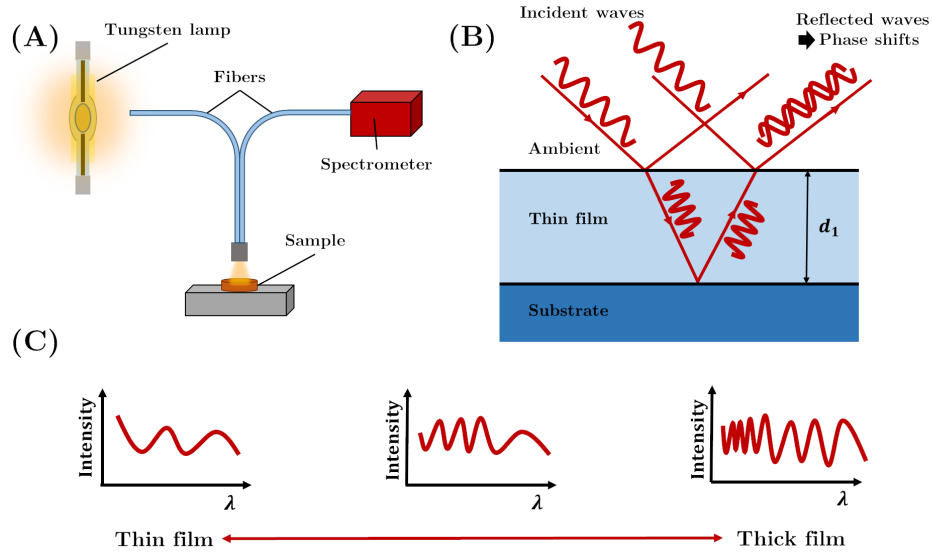


Figure 4.2: A: Schematic description of the home-built spectroscopic reflectometer which is composed by a tungsten lamp as a polychromatic light source, a bifurcated fiber, which guides the incident light to the sample and the reflected light towards the spectrometer. B: Representation of an incident beam reflected on a thin film during a reflectometry analysis. The difference in optical path induces phase shifts which leads to interferometric patterns on the measured intensity. C: The measured intensity changes as a function of the thickness of the film deposited on the substrate: higher thickness means more interferometric peaks.

deposited on a substrate. In our study, we always proceed to two measurements in the same condition, one for the substrate (our reference) and one for the sample:

$$I_{\text{ref}}(\lambda) = R_{\text{ref}}(\lambda) I_0(\lambda) \quad (4.5)$$

$$I_{\text{sample}}(\lambda) = R_{\text{sample}}(\lambda) I_0(\lambda) \quad (4.6)$$

where $R_{\text{ref}}(\lambda)$ and $R_{\text{sample}}(\lambda)$ are the reflectivity of the reference (the bare substrate in our case) and the sample, respectively. By dividing the equation 4.5 by the equation 4.6, it is possible to calculate the reflectivity of the sample knowing the reflectivity of the substrate. In this thesis, we use silicon wafers fragments as substrate, for which the reflectivity is well known [101]. This method takes advantage of the fact that the reflectivity of the silicon substrate is not modified by the presence of the 2 nm-thick native oxide layer over the 400 - 1000 nm spectral range. Thus the reflectivity of the sample is given by:

$$R_{\text{sample}}(\lambda) = \frac{R_{\text{ref}}(\lambda) I_{\text{sample}}(\lambda)}{I_{\text{ref}}(\lambda)} \quad (4.7)$$

During the measurements, two other parameters are important: the fiber-sample distance and the exposure time. The distance between the fiber and the sample determines the illuminated area of the sample due to the conical shape of the light beam coming out from the fiber (as illustrated in Fig. 4.2A). More precisely, in our case the numerical aperture (NA) of the fiber is 0.39. This NA can be related to the

maximal half-angle of the cone of light θ that can exit the fiber by: $\text{NA} = n \sin \theta$ where n is the refractive index of the medium in which the fiber is operating.

The exposure time corresponds to the recorded time by the spectrometer of the global reflected intensity. The latter parameter is automatically chosen by using an automatic setup of the spectrometer gain and its value is always approximatively 10 ms. The fiber-sample distance is of the order of centimeter and is maintained during all experiments. By using homemade routines, we are able to measure the reflectivity of the sample as a function of time, during the growing process of the nanoparticles for example. It is important to keep in mind that this technique leads to a global measurement of the reflectivity, since it measures the mean value of the reflected intensity received by the sensor.

4.1.3 Spectroscopic ellipsometry

Spectroscopic ellipsometry (SE) is a non destructive method that analyzes at once the optical properties of materials and the thickness of the different layers of the sample. This technique is based on the change of polarization of light after reflection of an incident light beam on a substrate or on a stratified sample [99, 102]. More specifically, one measures at a given wavelength the ellipticity ρ , defined by:

$$\rho = \frac{r_p}{r_s} \quad (4.8)$$

where r_p and r_s are the complex reflectance coefficients of the p - and s -component of the incident light, respectively. These Fresnel's coefficients are demonstrated in the chapter 3 (Eqs. 3.91 and 3.93):

$$r_p = \frac{n_t \cos \theta_i - n_i \cos \theta_t}{n_t \cos \theta_i + n_i \cos \theta_t} \quad (4.9)$$

$$r_s = \frac{n_i \cos \theta_i - n_t \cos \theta_t}{n_i \cos \theta_i + n_t \cos \theta_t} \quad (4.10)$$

Using the complex notation of equation 3.96, we have:

$$\rho = \left| \frac{r_p}{r_s} \right| e^{i(\delta_{r_p} - \delta_{r_s})} = \tan \Psi e^{i\Delta} \quad (4.11)$$

where δ_{r_p} and δ_{r_s} are the phase-shifts undergone by the p - and the s -components of the incident wave during the reflection. Ψ and Δ are the ellipsometric angles defined by:

$$\tan \Psi = \left| \frac{r_p}{r_s} \right| \quad (4.12)$$

$$\Delta = \delta_{r_p} - \delta_{r_s} \quad (4.13)$$

Ψ corresponds to the angle whose tangent is the ratio of the magnitudes of the complex reflectance coefficients and Δ measure the relative phase-shift between the perpendicular and parallel components of the propagating light wave. Polarizers and retarders are the main optical components used in all types of ellipsometers.

- A polarizer (P) is an optical component that gives to light a special state of polarization at the output. The most common polarizer is the linear polarizer that suppresses one component of the incident light, while allowing the other component to go through. If the linear polarizer can be rotated, one may create a linearly polarized light beam with the direction of polarization corresponding to the angle of rotation of the axis of the polarizer.
- The analyzer (A) is a second polarizer placed after the sample. It allows to measure the ratio of the p and s components.
- Retarders, often called compensator (C), are used to shift the phase of one component of the incident light. A well-known retarder is the “quarter-wave plate”, which has a “fast” and a “slow” axis leading to a phase-shift equals to 90° in the components of the electric field. Retarder can transform the ellipse of polarization depending on the orientation of the quarter-wave plate. For example, it can transform linearly polarized light to a circular polarization when set to 45° with respect to the linear polarization axis. We will use in this manuscript the term compensator to describe a retarder.

The transformation of polarization state by optical elements can be described from the Jones matrix (Section 3.1.5). For example, in the case of a polarizer (P) and an analyzer (A), whose the transmission axis is parallel to the x axis, the Jones matrix is given by:

$$P = A = \begin{bmatrix} 1 & 0 \\ 0 & 0 \end{bmatrix} \quad (4.14)$$

On the other hand, the Jones matrix of the compensator (C), whose the fast axis is parallel to the x axis is expressed by:

$$C = \begin{bmatrix} 1 & 0 \\ 0 & e^{-i\delta} \end{bmatrix} \quad (4.15)$$

In this thesis, we have worked with two different ellipsometers. The first one is a SOPRA GESP5 rotating polariser spectroscopic ellipsometer (Fig. 4.3) and the second one is an EP3 imaging ellipsometer (Fig. 4.4). The latter one, which will be described in the next section, was a single wavelength ellipsometer (IE) that was upgraded to a spectroscopic imaging ellipsometer (SIE) in summer 2019.

For the spectroscopic ellipsometer (SE), a white light source and a monochromator are used to collect ellipsometric measurements in the visible spectral range. The monochromator can be placed after the analyzer or before the polarizer. The configuration of a SE is shown in the figure 4.3. As we can see in this figure, the non-polarized white light travels through the rotating polarizer. Then, the linear polarized wave becomes an elliptic polarized wave due to the reflection on the sample. Finally, the light gets through the fixed analyzer and entering the detector. The signal received by the detector presents a sinusoidal component due to the rotation of the polarizer at the rotation speed ω during the measurement: $P_{\text{rotating}} = \omega t$.

The state of polarization of the beam can be described by the Jones matrix formulation [103]. The amplitude of the electric field can be decomposed following

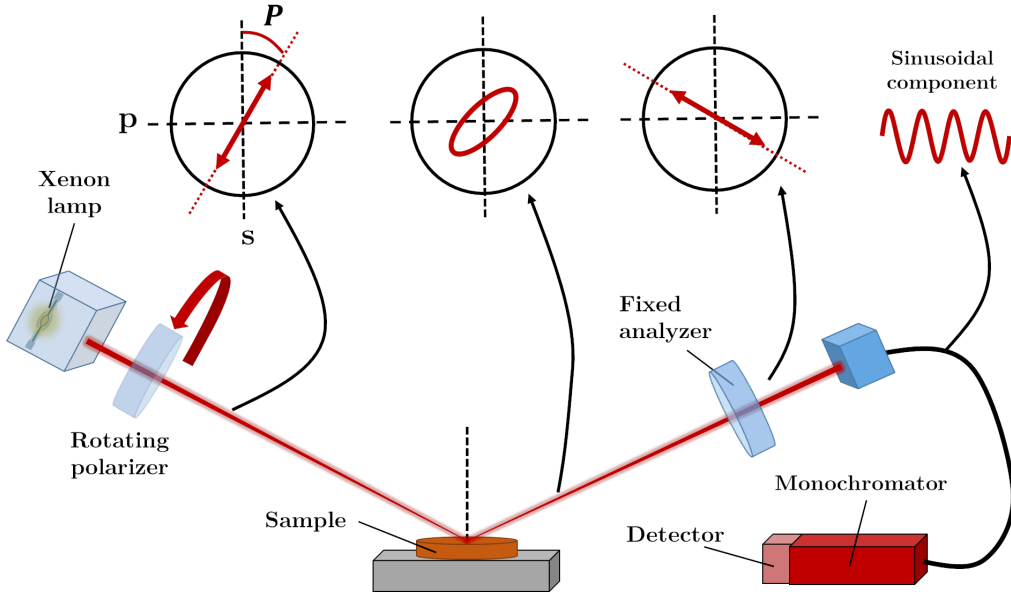


Figure 4.3: Schematic representation of a spectroscopic ellipsometer, corresponding to a SOPRA GESp5. A xenon lamp as a light source, a rotating polarizer and a fixed analyzer compose it. After the polarizer, the polarization of the incident beam is linear and the reflection on the sample leads to an elliptical polarization. After the analyzer, the monochromator disperses the light and, so the detector intercepts a sinusoidal component

the s and p axes and each operation due to an optical element can be represented by a 2×2 matrix:

- Polarizer and analyzer:

$$\mathbf{P} = \mathbf{A} = \begin{bmatrix} 1 & 0 \\ 0 & 0 \end{bmatrix} \quad (4.16)$$

if the transmission axis is parallel to the x axis.

- Sample:

$$\mathbf{S} = \begin{bmatrix} r_p & 0 \\ 0 & r_s \end{bmatrix} \quad (4.17)$$

- Rotation matrix:

$$\mathbf{R}(\alpha) = \begin{bmatrix} \cos \alpha & -\sin \alpha \\ \sin \alpha & \cos \alpha \end{bmatrix} \quad (4.18)$$

where α is the rotation angle of the analyzer or the polarizer.

- Isotropic light source:

$$\vec{E} = \begin{bmatrix} E_0 \\ E_0 \end{bmatrix} \quad (4.19)$$

Therefore, the detected amplitude received by the detector is [83]:

$$\vec{E}_{out} = \mathbf{AR}(\mathbf{A})\mathbf{SR}(-\mathbf{P})\mathbf{P}\vec{E}_{in} \quad (4.20)$$

where \vec{E}_{in} and \vec{E}_{out} are Jones vectors corresponding to the polarization states of light entering and exiting the ellipsometer, respectively. The full notation in Jones matrices is given by:

$$\begin{bmatrix} E_p \\ E_s \end{bmatrix} = \begin{bmatrix} \cos A & -\sin A \\ \sin A & \cos A \end{bmatrix} \begin{bmatrix} r_p & 0 \\ 0 & r_s \end{bmatrix} \begin{bmatrix} \cos \omega t & \sin \omega t \\ -\sin \omega t & \cos \omega t \end{bmatrix} \begin{bmatrix} E_0 \\ E_0 \end{bmatrix} \quad (4.21)$$

After calculation, the intensity received by the detector [104]:

$$I = |\vec{E}_d|^2 = [|r_p|^2 \cos^2 A \cos^2 P + |r_s|^2 \sin^2 A \sin^2 P + (r_p r_s^* + r_p^* r_s) \cos A \sin A \cos P \sin P] |\vec{E}_0|^2 \quad (4.22)$$

where A is the fixed angle of the analyzer, r_p^* and r_s^* are the complex conjugate of r_p and r_s , respectively. Using the equations 4.12 and 4.13 and the linearization of sinus and cosines, the intensity can be written:

$$I = I_0 [\alpha \cos(2P) + \beta \sin(2P) + 1] \quad (4.23)$$

where,

$$\alpha = \frac{\tan^2 \Psi - \tan^2 A}{\tan^2 \Psi + \tan^2 A} \quad (4.24)$$

$$\beta = 2 \cos \Delta \frac{\tan \Psi \tan A}{\tan^2 \Psi + \tan^2 A} \quad (4.25)$$

$$I_0 = \frac{|r_s|^2 |E_0|^2}{2} \cos^2 A (\tan^2 \Psi + \tan^2 A) \quad (4.26)$$

With these equations, we have access to the definition of α and β (Note that α and β are different than those presented in equation 3.5 and 3.97). These coefficients will reveal useful in the chapter 5 for the analysis of the ellipsometric spectra of the silver nanocomposites when the angle of the analyzer is set to 45° :

$$\alpha = \cos 2\Psi \quad (4.27)$$

$$\beta = \cos \Delta \sin 2\Psi \quad (4.28)$$

The SOPRA GESP5 used in the laboratory is a rotating polarizer ellipsometer. It can measure the ellipticity of the samples in the range 1.37 to 4.96 eV (250 nm to 904 nm) due to the spectral range of the xenon flash lamp and a 1024 channels CCD spectrograph. The arms of the ellipsometer are installed on a high precision motorised goniometer which allows to measure the ellipsometric parameters as a function of the wavelength, but also as a function of the angle of incidence (AOI). The light is polarized by a rotating Rochon polarizer composed by two quartz prisms adapted to the visible range of the light. The analyzer is adjustable and is fixed during measurements. During our experiments, the AOI of the SOPRA GESP5 is set to 70° . SE results are processed using the SOPRA Winelli II software.

4.1.4 Spectroscopic imaging ellipsometry

Spectroscopic imaging ellipsometry measurements of the ellipsometric angles Ψ and Δ are performed with an EP3-SE spectroscopic nulling ellipsometer (Accurion GmbH). Before introducing the instrument, we focus first on the measurement method used by this device: the nulling ellipsometry [99]. The optical configuration for a nulling ellipsometer corresponds to a polarizer-compensator-sample-analyzer, usually called “PCSA” ellipsometer. The combination of a polarizer and a compensator in the incident arm allows to polarise elliptically the incident beam, such that the reflected beam is perfectly linearly polarized. By using, in the detector arm, an analyzer set to 90° position with respect to the axis of the reflected linear polarization, it is possible to extinguish the beam. This method is called the “nulling” method. Finding the “null” during a measurement, corresponds to identify the right combination of P, C and A that gives a minimum in the signal of the photo-detector situated in the detection arm of the ellipsometer. As we can see in the figure 4.4, the incident light gets through a first combination of P-C. After the P, the beam is linearly polarized and the polarization becomes elliptic after the C. Due to the reflection of the beam on the sample, the polarization of the beam changes. By using the appropriate combination of PC, it is possible to get a linearly polarized reflected beam. By rotating A, the beam can be extinguished in order to determine the minimum of the signal received by the photo-detector. In the case of the null ellipsometry, the Jones matrix of this optical system is given by [99]:

$$\vec{E}_{out} = \mathbf{AR}(A)\mathbf{SR}(-C)\mathbf{CR}(P-C)\mathbf{PR}(P)\vec{E}_{in} \quad (4.29)$$

The ellipsometric parameters Ψ and Δ can be determined by:

$$\tan \Psi e^{i\Delta} = -\tan A \frac{\tan C - \tan(P-C)}{1 + i \tan C \tan(P-C)} \quad (4.30)$$

where P , C and A are the angle of the polarizer, the compensator and the analyzer, respectively, with respect to the plane of incidence. The most used method, which is the method that we used in this work, is the so-called “fixed compensator nulling scheme”. This mode fixes the compensator at a given angle and P and A are rotated to find the nulling condition. In practice, for the PCSA ellipsometer, the compensator C is usually set at an angle of 45° or -45° and the nulling is found by moving the P and the A, assuming that measurements are made on an isotropic surface [99]. Two steps are enough to reach the nulling condition: first, rotating the polarizer to minimum intensity, and second moving the analyzer to the nulling, while leaving the polarizer at its angle position. Nevertheless, the nulling procedure can be more complicated to improve the precision of the measurement [105]. As it can depend on the ellipsometer routines, these procedures can be different from one type of ellipsometer to the other, and therefore, we do not enter in too much details. By choosing values of the $C = \pm 45^\circ$ in the equation 4.30, the ellipsometric angles measured by the ellipsometer are directly related to P_{\min} and A_{\min} given by:

$$\Delta = 90^\circ - 2 P_{\min} \quad \text{and} \quad \Psi = -A_{\min} \quad (4.31)$$

where P_{\min} and A_{\min} are the angle value of the polarizer and the analyzer, respectively, when the nulling procedure is completed.

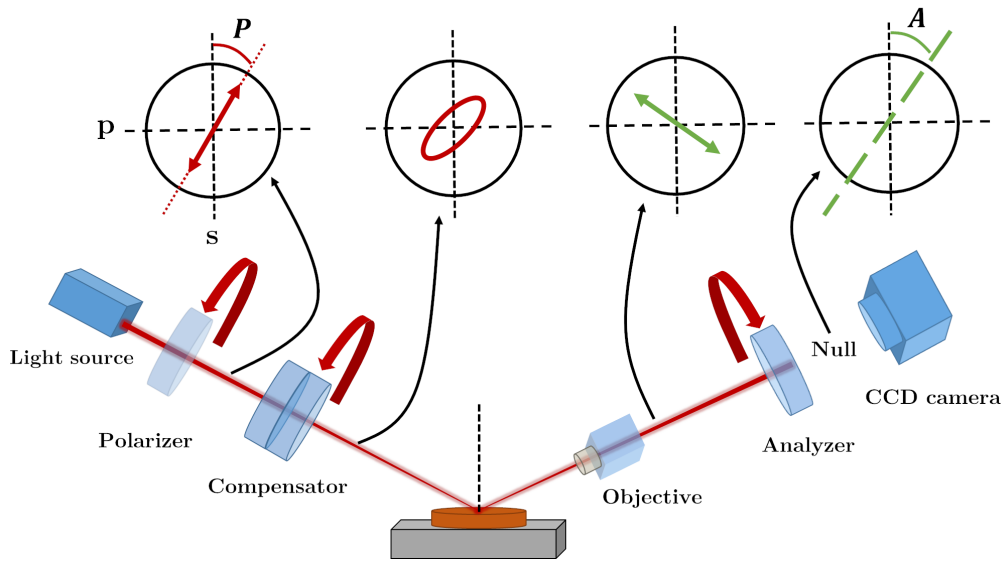


Figure 4.4: Graphical depiction of the imaging ellipsometer used in this work. The light source is either a laser diode (single wavelength) or a xenon flash lamp with a filter wheel composed of 44 filters (spectroscopic). The polarizer, compensator and analyzer can be rotated in order to extinguish the beam before the detector (a CCD camera). The polarization states of the beam are drawn for each step of the measurement.

One of the advantages of using IE or SIE instead of conventional SE is the possibility to acquire an image of the optical properties of the sample. In order to have a mapping of the optical properties of the sample, a microscope objective is placed before the analyzer. Furthermore, the detector located after the analyzer is a spatially resolved detector (a CCD camera in our case). Thus, different zones of the sample with different optical properties cause a different signal in the camera images. It means that different areas can fulfil different nulling conditions, i.e. different areas can have different settings of P, C and A to extinguish the beam. As we will see in the chapters 5 and 6, the main advantage of using a IE or a SIE is that the received signal is not averaged over the entire laser spot as it is for the global SE. The optical response is spatially resolved, which allows to reveal the details at the microscale of the sample. Moreover, with IE and SIE, it is possible to reduce the ellipsometric measurements to a particular region of interest (ROI), which is in the field-of-view of the instrument. As it will be presented later, the definition of multiple ROIs allows to measure different areas at the same time, which is interesting with samples presenting different local optical behaviors. By applying different routines (called “mapping routines”), it is possible to record two ellipsometric maps, Ψ and Δ maps, of the sample probed by the IE or SIE. From these maps, using optical modelling, it is possible to have access to a thickness map or another quantities, such as the volume fraction of metal in the nanocomposite for example.

As mentioned before, we used, in this work, an EP3-SE spectroscopic nulling ellipsometer. The objective of the EP3 is a Nikon CF Plan SLWD 10X objective (NA = 0.21). The wavelength range is 360 – 1000 nm for the spectroscopic version and 658 nm for the single wavelength version (laser diode) and the measurements are carried out at different AOI, typically 42°, 45°, 55°. More precisely, for the

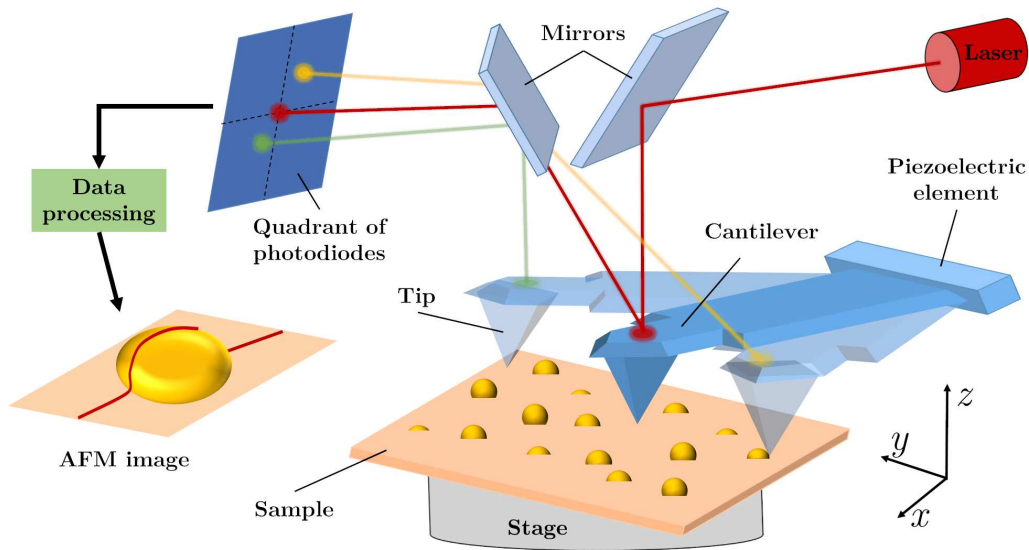


Figure 4.5: Representation of the operation of an AFM on a coated substrate fixed on a xyz stage. The tip placed at the edge of the cantilever allows measuring the topography of the sample at the nanoscale. The deviation of the cantilever can be tracked thanks to a quadrant of photodiodes receiving a laser beam, which is reflected at the top of the cantilever. The AFM image is obtained after data processing.

spectroscopic version of the instrument, the light source of the ellipsometer is a xenon flash lamp and a filter wheel (44 filters) is used to select the operating wavelength between 360 nm and 1 μm . Unless otherwise specified, the bandpass of the filters is 10 nm. The IE and SIE results are processed using the EP4 software (Accurion GmbH).

It is important to keep in mind that the IE and SIE measurements give information about local optical properties of the probed sample. In order to measure the topography of the sample at the nanoscale, we introduce, hereinafter, the atomic force microscopy.

4.1.5 Atomic force microscopy

Invented by Calvin F. Quate and Christophe Gerber in 1986 [106], the atomic force microscopy (AFM) is a nearfield microscopy. This technique is derived from the scanning tunnelling microscopy (STM) developed by Gerd Binnig and Heinrich Rohrer, for which they received the Nobel prize in 1986. The AFM uses the Van der Waals and adhesion forces to probe the surface at the nanoscale of the sample.

A typical configuration of an AFM is shown in the figure 4.5. As we can see, the sample is placed on a stage that can move in the xyz direction thanks to a xyz drive, which is a piezoelectric element. The surface of the sample is probed by the tip, which is fixed at the edge of the cantilever. This latter one is driven at its eigen frequency with another piezoelectric element attached at the end of the cantilever. A laser beam that is first reflected on the top of the cantilever follows the deflection and motion of the cantilever and a detector composed by a quadrant of photodiodes intercepts the reflected beam. During a measurement, the tip can meet an obstacle

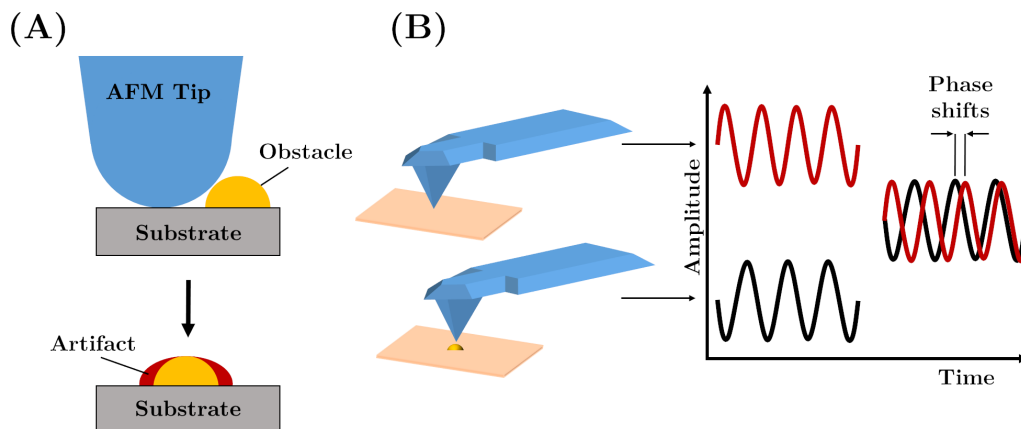


Figure 4.6: A Representation of an artifact due to a large radius of curvature of the AFM tip. B Variation of the film stiffness leading to a phase shifts in the oscillations of the cantilever

which leads to a deflection of the cantilever. These deflections and the motion of the cantilever can be recorded thanks to the displacement of the beam on the quadrant. As shown in the figure 4.5, the deflection of the cantilever leads to displacement of the beam illustrated by different laser spots on the quadrant of photodiodes (note that the changes in coloration of the laser beam do not correspond to changes of the beam wavelength). Then, the recorded displacement is converted in a topographic image. In general, this configuration leads to two types of measurement: static and dynamic modes.

In the static mode or “contact mode”, a permanent contact between the tip and the surface is maintained. It is possible to measure the topography of the surface but the artifacts are important due to additional forces like adhesion forces and, moreover, the tip can cause damages on the surface. An unsuitable probe, a poor operating environment or a rough sample can lead to image artifacts. As shown in figure 4.6A, the fidelity between the measurement and the surface is not respected.

To avoid the deterioration of the surface caused by the contact mode, we used in this work a second mode: the dynamic or “tapping” mode. In this setup, the probe oscillates at a high frequency thanks to a piezoelectric element located at the end of the cantilever (Fig. 4.5). In this mode, two sorts of image can be acquired: topographic and phase images. Topographic images give measurements of the height variation of the sample surface, from which roughness parameters can be calculated. Phase images bring information about the stiffness of the surface. As shown in the figure 4.6B, the recorded phase changes due to the variation of the surface. In our case, both images have an important meaning. As we will explain at the end of this chapter, the nanocomposites are prepared by growing metallic nanoparticles embedded in a polymer matrix. Due to their composition, the stiffness of polymer and nanoparticles are different. In this case, the phase image is appropriate to enhance the contrast between nanoparticles and polymer, which is less visible in the topographic image. The latter image can give information of the roughness of the film, and more specifically, an idea of the position at the surface of the nanoparticles.

In this work, the surface of the films is studied with a Park XE70 AFM (Park

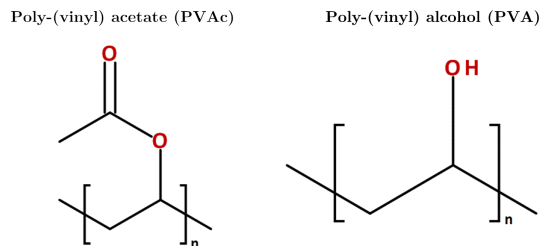


Figure 4.7: Chemical formula of poly-(vinyl) acetate (PVAc) and poly-(vinyl) alcohol (PVA)

Systems Corp., Korea), operated in air in intermittent contact mode with commercial ACTA tips (resonance frequency: 309 kHz). Areas of $5\ \mu\text{m} \times 5\ \mu\text{m}$, $2\ \mu\text{m} \times 2\ \mu\text{m}$ and $1\ \mu\text{m} \times 1\ \mu\text{m}$ are imaged for numerous samples. The resolution of the images is 256 pixels x 256 pixels. The data are processed with the Gwyddion software¹ [107].

4.2 Preparation method of nanocomposites

In this section, we explain the method we used to synthesize our plasmonic nanocomposites. First, we start with a reminder on the definition of a plasmonic nanocomposite. In order to generate this type of new materials, we need to include nano-objects in a dielectric matrix. These nano-objects, and more particularly in our case, metallic nanoparticles (NPs) present plasmonic optical properties: LSPR. We present hereinafter these two elements to form a nanocomposite plasmonic: NPs and the dielectric matrix.

As shown before in the chapter 2, the gold and silver nanoparticles have many applications due to their LSPR well situated in the visible range. The NPs have to be spherical and small compared to the incident wavelength to have one resonating mode (Section 3.2.4). In this case, the interaction with the incident electromagnetic wave is large and it makes it possible to maximize the optical effect.

The second element to manufacture the nanocomposite plasmonic is the dielectric matrix. It is well known that polymers are excellent host materials for metal or semiconductor NPs [52]. Thus, a polymer matrix is selected: the poly-(vinyl) alcohol (PVA), which is a linear chain polymer and has the advantage to be soluble in water and transparent in the visible range. The PVA was first prepared by W. O. Herrmann and W. Haehnel in 1924 by saponifying poly(vinyl esters) with stoichiometric amounts of caustic soda solution [108]. Nowadays, the PVA is obtained by a hydrolysis of poly-(vinyl) acetate (PVAc), which is synthesized from the vinyl acetate monomer [54, 109]. This hydrolysis reaction is never a complete reaction and is controlled with the purpose of yielding some groups of vinyl acetate on the polymer chain. If the reaction of hydrolysis is total, the PVA is insoluble in water due to the hydrogen bonds binding the hydrolyzed segments. In order to guarantee the solubility of the PVA in water, the hydrolyzed PVA is a copolymer $[\text{PVA}]_m[\text{PVAc}]_{n-m}$. The chemical formula of PVAc and PVA is presented in the figure 4.7. PVA is used in numerous medical applications because of its biocompatibility and low toxicity [53].

¹<http://gwyddion.net>

This polymer has interesting properties including the ability to form good films, a high tensile strength and flexibility and finally high oxygen barrier properties [54]. Nevertheless, these properties can be strongly influenced by the relative humidity surrounding the polymer. In the case of this work, the PVA is purchased from Sigma-Aldrich and its characteristics are: 87–89% hydrolyzed and $M_w = 13\text{k} - 23\text{k}$. The physical properties of gold, silver and PVA are summarized in the table 4.1.

There are numerous synthesis methods for such nanocomposites, which globally belong to two categories:

- The most popular way to synthesize these plasmonic nanocomposites is the “bottom up” approach: metal NPs are synthesized in colloidal solutions, by the Frens-Turkevitch method [14] for example, and stabilized with or without further specific coating to prevent their aggregation. In this synthesis, several experimental factors can provide a considerable control of the formation of NPs. However, producing plasmonic nanocomposites requires that the NPs in the colloidal solution are dispersed and immobilized in a dielectric matrix such as glass or polymer (see e.g. [43, 47, 48, 77, 110] and the references therein). Therefore, this approach has two separate steps: the synthesis of the NPs and their dispersion in the matrix.
- The second method, also known as “one-pot synthesis”, is a simpler method: in a single step, both the metallic salt and the polymer are mixed together to prepare the nanocomposite. The simplicity of this second approach, derived from the polyol method, is regarded as a great advantage for the production of nanocomposites for various applications in nanoptic techniques for example. The principle of *in situ* methods is the use of one of the matrix components as a reducing agent for the metal salt. The self-stabilization process is another advantage of the *in situ* synthesis method, since it avoids the use of additional stabilizers like citrate ions, sodium borohydride, or polyvinyl pyrrolidone (PVP). The thermal annealing process allows the reduction of the metal cations. Once in their neutral state, the metal atoms have to diffuse in the polymer matrix and to aggregate, then yielding nanoparticles. These steps are improved by annealing the films at a temperature higher than the glass transition temperature (T_g) of the polymer. For bulk PVA, T_g equals 85°C [55]. However, the drawback of this method is a reduced control on the shape and the size of the NPs.

4.2.1 Spin coating

In order to get a thin film on a glass or on a silicon substrate, we used the spin coating technique, which consists to obtain a thin solid film by sprawling and drying. In practice, a drop of solution is placed on the substrate at the center of the spin coater. Then, the system enters in rotation in order to sprawl the solution. When the liquid film is created, the solvent in excess evaporates. Then, at the end of the process, a thin solid film is obtained. The sprawling depends on the speed and the initial acceleration of the rotation, on the chemical compounds of the solution and the

Table 4.1: Physical properties of gold, silver and PVA [20]

Property	Gold	Silver	PVA
Atomic number	79	47	-
Atomic mass (amu)	196.9665	107.868	-
Electronic configuration	[Xe]4f ¹⁴ 5d ¹⁰ 6s ¹	[Kr]4d ¹⁰ 5s ¹	-
Structure	fcc	fcc	-
Metallic radius (nm)	0.14420	0.14420	-
Specific mass (g/cm ³)	19.32	10.5	1.25
Electrical resistivity ^a (μΩ cm)	2.35	1.59	10 ¹⁸
Fermi velocity v_f (×10 ⁶ m/s)	1.40	1.39	-
Melting temperature (°C)	1063.85	960.85	≈ 200
Glass transition temperature (°C)	-	-	85
Molar weight (kDa)	-	-	13 - 23
Hydrolysis (%)	-	-	87 - 89

^aat 20°C

substrate and, also, on the viscosity of the solution. A description of the formation of a Newtonian liquid film is given by [111]:

$$\frac{dh}{dt} = -\frac{2\rho\omega^2 h^3}{3\eta_0} \quad (4.32)$$

where h is the thickness of the film, ω the speed of rotation, ρ the specific mass of the solution and η is the viscosity of the solution. Recently, Danglad-Flores *et al* [112] demonstrated that the final thickness of a polymer obtained by a spin coating is given by:

$$h_f = c x_0 \left(\frac{\eta_0}{\rho_0}\right)^{1/3} \omega^{-1/2} \quad (4.33)$$

where $c = (3e/2)^{1/3}$ is a constant reflecting the evaporative conditions and e the evaporative rate, x_0 the concentration of polymer in the solution, ρ_0 the specific mass, η_0 the viscosity of the polymer and finally ω the speed rotation. With this approach, it is possible to predict the final thickness h_f as a function of the four main parameters: concentration x_0 , the rotation speed ω and the ratio between the viscosity and the specific mass η_0/ρ_0 . In this work, we used a Laurell WS-650-23B spin-coater and the parameters are adjusted in order to prepare nanocomposites with a range of thicknesses from 30 nm to 500 nm as explained hereinafter.

4.2.2 Experimental process

As previously explained, the “one-pot” synthesis has numerous advantages and this method is chosen to create the nanocomposites. This *in situ* synthesis method is used previously in the laboratory [73, 74], and is based on the initial experimental protocol for Ag–PVA nanocomposites of Porel and coworkers [67]. Hereinafter, we

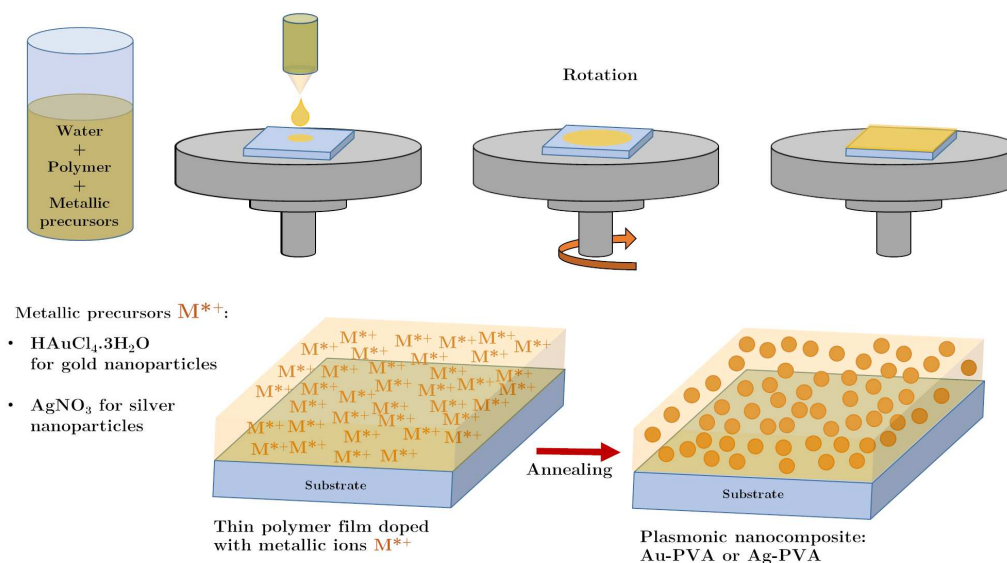


Figure 4.8: Graphical illustration of the preparation method of the nanocomposites. First, an aqueous solution including polymer and metallic precursors is prepared. Then, a small volume of the doped polymer solution is dropped on a clean substrate (glass or silicon wafers). The thin dry film containing the metallic precursors is realized by a high-speed rotation of the sample. Then, the samples are annealed to allow the reduction of the metallic cations in their neutral state.

explain the experimental procedure for both AgNPs and AuNPs, as described in figure 4.8:

- A 10% (w:w) PVA stock solution is prepared by heating the required amount of PVA at 85°C under reflux until complete dissolution of the polymer, followed by the cooling of the solution to room temperature.
- After cooling the solution to room temperature, an aqueous solution of HAuCl_4 or AgNO_3 is added to the polymer solution to obtain the desired percentage of polymer solution containing the wanted percentage of metallic nanoparticles. The latter percentage refers to the $[\text{Au}]/[\text{PVA}]$ or $[\text{Ag}]/[\text{PVA}]$ mass ratio.
- After mixing and filtrating the solution on a $0.45 \mu\text{m}$ Millipore filter, the solution containing polymer and metallic cations is spin-coated on $\langle 100 \rangle$ silicon wafers fragments or glass substrate. We choose silicon substrates due to their high optical contrast with polymer films and their low intrinsic roughness. The speed of the spin coater is adapted to obtain the desired thickness of the nanocomposite.
- In order to allow the reduction of the metal cations, the nanocomposites are annealed in air using a laboratory oven or a high precision heating stage.

All the synthesis are done using $18 \text{ M}\Omega$ MilliQ water. Moreover, in order to measure the absorbance of the nanocomposites, these solutions are spin-coated with the same method for glass and silicon wafers.

As mentioned here above, we use percentage to refer to the mass ratio between metal (“m”) and polymer (“p”). From this mass ratio, it is possible to determine the volume fraction of metal inside the polymer. Assuming that f_m is the volume fraction of metal inside the polymer matrix and Φ is the mass fraction defined by:

$$\Phi = \frac{m_m}{m_m + m_p} = \frac{\frac{m_m}{m_p}}{\frac{m_m}{m_p} + \frac{m_p}{m_p}} \quad (4.34)$$

$$= \frac{r}{r + 1} \quad (4.35)$$

where $r = m_m/m_p$ corresponding to the mass ratio. As seen in the Maxwell-Garnett effective medium approximation (MG-EMA) model (Section 3.2.5), the dielectric functions are combined as a function of the volume fractions. They can be related to the mass ratio and specific masses by:

$$f_m = \frac{V_m}{V_m + V_p} \quad (4.36)$$

$$= \frac{\rho_m V_m}{\rho_m V_m + \rho_p V_p} \quad (4.37)$$

$$= \frac{m_m}{m_m + \rho_p V_p} \quad (4.38)$$

$$= \frac{\frac{m_m}{m_p}}{\frac{m_m}{m_p} + \frac{\rho_p}{\rho_m} \frac{m_m}{m_p}} \quad (4.39)$$

$$f_m = \frac{r}{r + \frac{\rho_p}{\rho_m}} \quad (4.40)$$

The specific mass of PVA is $\rho_{\text{PVA}} = 1.25 \text{ g/cm}^3$, gold $\rho_{\text{Au}} = 19.32 \text{ g/cm}^3$ and silver $\rho_{\text{Ag}} = 10.5 \text{ g/cm}^3$.

Substrates cleaning

The cleaning procedure of our substrates are the following: microscope glass and silicon wafer fragments were first soaked in RBS35 alkaline soap solution in water (3%) during 30 min in an ultrasonic bath. Oils and organic residues are cleaned using a two-solvent method: a) the substrates are dipped (10 min) in a warm acetone bath (not exceeding 55°C) before being removed and placed in methanol for 2-5 min. Before coating, they are dried by blowing a nitrogen stream. This solvent cleaning procedure is sufficient to obtain uniform polymer coatings that adhere to the substrates. As no activation of the surface is required, it is not mandatory to use either piranha nor RCA1/RCA2 cleaning solutions.

Au-PVA nanocomposites

In the case of gold nanocomposites, a 0.1 M $\text{HAuCl}_4 \cdot 3 \text{H}_2\text{O}$ (from Sigma-Aldrich) solution is prepared. These stock solutions, HAuCl_4 and PVA (13-23k), are mixed together in adequate proportions to finally lead to a 8% w:w polymer solution with a 2% $[\text{Au}]/[\text{PVA}]$ mass ratio. After the cleaning process, $\langle 100 \rangle$ Si wafer fragments

or glass substrates are coated with that solution by spin coating at 2000 rpm during 90 s. The mass ratio of 2% of gold in polymer corresponds to a volume fraction $f_{\text{Au}} = 0.13\%$ in the dry film.

Ag-PVA nanocomposites

In the case of silver nanocomposites, a AgNO_3 (99.99%, Sigma-Aldrich) is added to the polymer solution to obtain a silver concentration of 2.5% or 25%. This percentage corresponds to the w:w silver-to-polymer ratio. Afterwards the required amount of water is added to the polymer stock solution to obtain 2% and 8% polymer solutions. Then, a small volume of the doped polymer solution is spin-coated on silicon wafers fragments or glass substrates cleaned as previously explained. Depending on the coating conditions, the final thickness of the dried film ranged from 25 nm (2% PVA, 60 sec at 6000 rpm) to 300 nm and above (8% PVA, 60 sec at 1600 rpm). The variation of the polymer concentration leads to a variation of the viscosity of the polymer solution. The solution with a higher viscosity leads to films with a higher thicknesses (Eq. 4.33). The mass ratio of 2.5% and 25% of silver in polymer corresponds to a volume fraction $f_{\text{Ag}} = 0.3\%$ and $f_{\text{Ag}} = 2.9\%$ in the dry film, respectively.

4.2.3 Heating stage

In order to allow the reduction of the metal cations, the thermal annealing process is an important part of the experiment. During the thesis work, we used a traditional laboratory oven and a high precision heating stage. For the oven, concerning AgNPs, the settings of the annealing are 110°C during 60 or 120 min, while for AuNPs, it is 135°C during 60, 90 or 120 min. Numerous samples are annealed with the THMS600 Linkam heating/cooling stage in order to follow the kinetics of growth of the AuNPs or AgNPs during the annealing. In a typical annealing experiment, a temperature ramp of $10^\circ\text{C}/\text{min}$ starting at room temperature is applied. When the temperature reached 110°C in the case of AgNPs, or 135°C for AuNPs, it is stabilized during 60, 90 or 120 minutes. Thermal fluctuations are less than 0.1°C .

The ramp temperature and the temperature of annealing are two important parameters. Changes in these parameters could lead to another results for the nanocomposites like the size of NPs embedded in the polymer matrix, the number of NPs, the distribution of the NPs in the polymer, ... ([66, 67, 69, 113]). In this work, these parameters are never changed.

Silver nanoparticles embedded in PVA matrix

5.1 Introduction

As previously explained, the plasmonic nanocomposites formed by a polymer matrix and silver nanoparticles (AgNPs) have numerous applications. The simplest method to prepare this kind of materials is the one called “one pot synthesis”: in the case of AgNPs, a noble metal salt (AgNO_3) is directly mixed with a polymer solution (e.g. PVA), see section 4.2 for its synthesis. This approach leads to a concentration of metallic nanoparticles (NPs) in the final nanocomposite higher than in a colloidal solution. Another advantage of this synthesis scheme is its simplicity because NPs are synthesized *in situ* thanks to the thermal annealing of the solid phase. This thermal annealing provides the energy to promote the reduction of the metal cations. The reduction step of the silver cations is carried out by the electrons originating from the -OH groups of the PVA molecules (Fig. 5.1A). Depending on the temperature, cross-linking of the polymer matrix can also be induced, as shown in the figure 5.1B, reducing the solubility of the composite [114]. Due to the temperature of annealing that is higher than the glass transition temperature of the PVA ($T_g = 85^\circ\text{C}$ for bulk PVA [55]), the silver cations or, after their reduction in their neutral state,

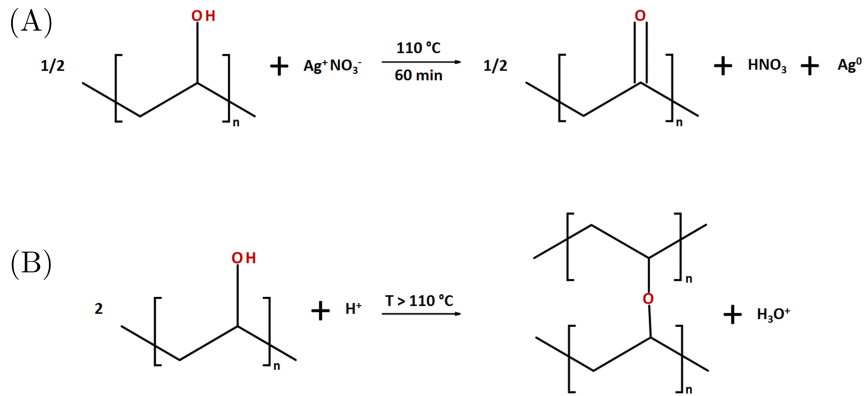


Figure 5.1: (A) Reduction scheme for the silver cations. (B) Cross-linking of the PVA chains at high temperature (redrawn from [114]).

the silver atoms can diffuse in the polymer. This displacement corresponds to a diffusion process. After that, a nucleation process occurs, which leads to the onset of the nanoparticles. Despite the simplicity to synthesize the silver nanocomposites, the detailed mechanism linking the final optical properties of such nanocomposites to their structural parameters is not fully understood nowadays.

In this chapter, we will first focus our study on the optical properties of the PVA matrix in order to obtain an optical description of the undoped polymer matrix (i.e. without NPs). This description provides the variation of the refractive index as a function of the wavelength (Section 5.2). In a second time, we will analyze the optical properties of a thick silver nanocomposite with a high silver doping level during and after the annealing by spectrophotometry (Section 5.3.2). Then, by varying the thickness of the sample while keeping constant the ratio of silver-to-polymer matrix, we will demonstrate the influence of the film thickness on the position of the resonance peak (Section 5.4). Finally, we will use the spectroscopic ellipsometry (SE) and the classical Lorentz model to demonstrate the influence of the silver doping and the film thickness of the nanocomposite films on the plasmon resonance parameters (Section 5.5).

5.2 Optical properties of the polymer matrix

In this section, we present the optical properties of the PVA obtained by SE. In this purpose, we prepare films with different thicknesses in order to determine and confirm the values of the optimized parameters obtained from the Cauchy model.

As previously explained, the PVA has been selected as the polymer matrix for embedding the NPs (Chapter 4, section 4.2). This polymer is a linear chain polymer and has the advantage of being soluble in water and transparent in the visible range. As PVA is used in numerous applications, its optical properties are well-known and can easily be described by a Cauchy model (see supporting info of [115]). The use of the Cauchy model for the polymer matrix is justified by the monotonous increase of the refractive index of the polymer when going from the infrared to the UV, as expected for dielectric materials far from the fundamental absorption edge. The schematic representation of the optical model used for PVA is shown in the

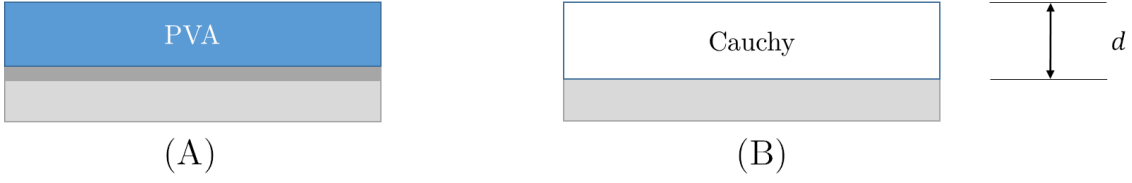


Figure 5.2: Schematic representation of the optical model used to interpret SE data of the polymer matrix: (A) PVA layer on silicon, (B) Cauchy model used to describe the optical properties of the PVA layer. Shaded area between the polymer layer and the substrate: SiO_2 layer. (Not to scale)

figure 5.2.

Typically, in order to determine and confirm the optical properties of the PVA films by spectroscopic ellipsometry, two different samples are prepared:

- Film A to determine the optical properties, with spinning parameters: 2000 rpm during 90 s.
- Film B to confirm the optical properties, with spinning parameters: 6000 rpm during 90 s.

Films of PVA have been prepared by spin-coating of a 8% (w:w) polymer solution in water. Spinning conditions were adjusted to obtain a film thickness in the 200-500 nm range.

Due to the rotation speed of the spin-coater, Film A is thicker than Film B (Eq. 4.33). The ellipsometric angles Ψ and Δ were measured using an EP3-SE spectroscopic ellipsometer. As a reminder, the spectroscopic ellipsometer measures the ellipticity ρ at a given wavelength, which is the ratio of the complex reflection coefficients of p and s polarizations. Ψ and Δ are the ellipsometric angles and they are explicitly defined by:

$$\rho = \frac{r_p}{r_s} = \tan \Psi e^{i\Delta} \quad (5.1)$$

$$\tan \Psi = \frac{|r_p|}{|r_s|} \quad \text{and} \quad \Delta = \delta_p - \delta_s \quad (5.2)$$

where δ_p and δ_s are the phase-shifts undergone by the p - and the s -components of the incident wave during the reflection. The angle Δ therefore measures the relative phase-shift between the perpendicular components of the propagating light wave, see section 4.1.3.

The refractive index and the thickness of the PVA film are determined for Film A using a Cauchy dispersion law [95]:

$$n_{\text{PVA}}(\lambda) = A_{\text{PVA}} + \frac{B_{\text{PVA}}}{\lambda^2} \quad \text{and} \quad k_{\text{PVA}}(\lambda) = 0 \quad (5.3)$$

where A_{PVA} and B_{PVA} are the Cauchy coefficients. Higher order terms in the Cauchy law do not significantly improve the optimisation results. After the processing of the measurements, the optimized parameters obtained by the ellipsometric measurements are $A_n = 1.509 \pm 0.002$ and $B_n = 3172 \pm 296 \text{ nm}^2$ (RMSE = 0.966). The

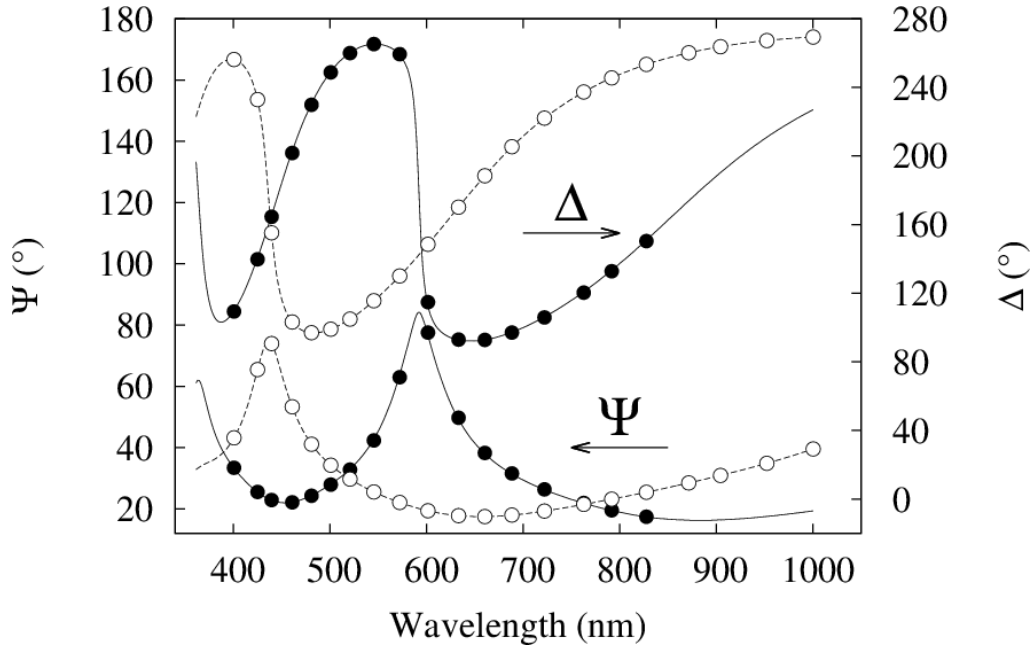


Figure 5.3: Modeling of the ellipsometric data for PVA thin films. Ellipsometric spectra: the two curves at the top of the graph correspond to Δ and the two curves at the bottom are Ψ . Closed symbols: 365 nm-thick film (modeling of the refractive index and the thickness). Open symbols: 266 nm-thick film (modeling of the thickness only, using the refractive index of the 365 nm-thick sample). Plain and dashed lines: best-fit results.

thickness of Film A is 365.2 ± 0.6 nm. Optical response of Film B is optimized with respect of the film thickness only to validate the optical properties of the material. The experimental spectra, as well as the optimization results are presented in the figure 5.3. The adjusted thickness is 266.1 ± 0.1 nm with a RMSE equal to 1.858. For both films, the simulated spectra are in very good agreement with the experimental data.

In order to validate the optical model used for the PVA thin films, we measure thickness d of a series of film obtained by changing the rotation speed of the spin coater using the same solution of undoped PVA in water (8% w:w). This corresponds to calibrate our spin coater for the PVA solution. The results are presented in the figure 5.4 by black point (errors bars in points). The red curve is the fit of the data by using a power law $d \approx \omega^\xi$. The final thickness of the film is expected to vary as the inverse of the square-root of the rotation speed (Eq. 4.33 [112]). The adjusted value of ξ is -0.468 ± 0.017 , in good agreement with the theoretical value. In the graph, we can also see that the “Film A” and “Film B” thickness used in the figure 5.3 lay on the calibration curve, which allows us to confirm the measured thickness and also the model used for the PVA matrix.

As demonstrated here, the Cauchy model is appropriate to describe the optical properties of the PVA matrix in the visible range. From now on, we will use the Cauchy model to describe the optical properties of the PVA matrix for both AgNPs and gold nanoparticles (AuNPs) cases.

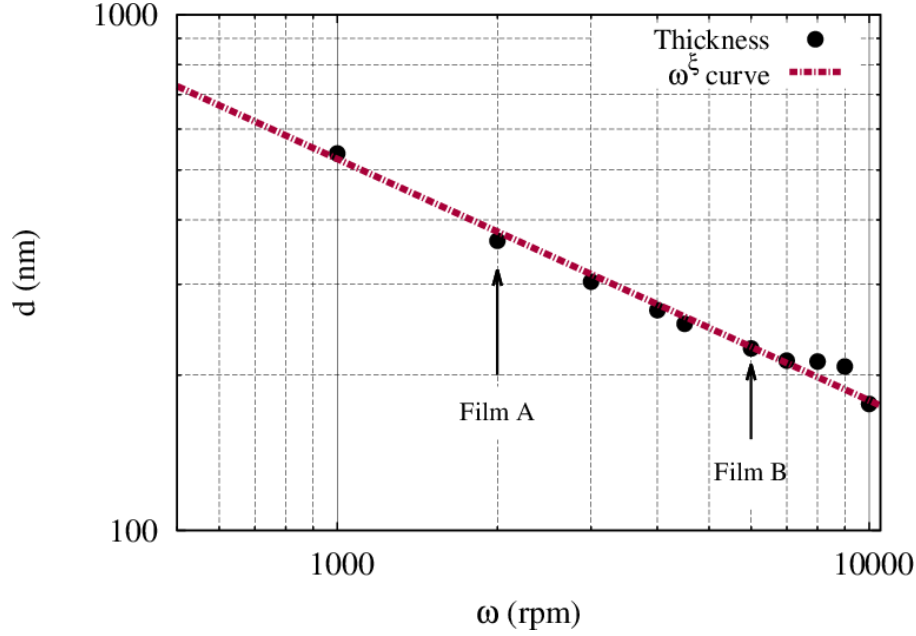


Figure 5.4: Calibration curve of the spin coater from undoped PVA solution in water (8% w:w). Black points: measured thickness as a function of the rotation speed of the spin coater. Red curve: power law ω^ξ with $\xi = -0.468 \pm 0.017$.

5.3 Spectrophotometry measurements of silver nanocomposites

In this section, we first analyze the variation of the absorbance of the silver nanocomposite as a function of the wavelength. As previously described in the chapter 4 in section 4.1.1, the measure of the absorbance A is related to the total extinction cross section σ_{ext} by:

$$A = \frac{\sigma_{\text{ext}} N_{\text{particle}} d}{\ln 10} \quad (5.4)$$

where N_{particle} is the number of particles per unit volume and d the distance crossed by the beam, corresponding to the thickness of the film in this case. The extinction cross section σ_{ext} characterizes the extinction suffered by a beam going through a particle, this beam being either absorbed or scattered. The absorption cross section σ_{abs} and the scattering cross section σ_{scatt} describe the absorbed and scattered light, respectively, upon interaction with the particle. These three cross sections are related by:

$$\sigma_{\text{ext}} = \sigma_{\text{abs}} + \sigma_{\text{scatt}} \quad (5.5)$$

However, in order to fulfill the equation 5.4, the diffusion of the light by particles must be supposed negligible and the extinction is then dominated by the absorption: $\sigma_{\text{ext}} \approx \sigma_{\text{abs}}$. Actually, for small particles, only the absorption plays a role in the extinction, since the scattering is negligible (Fig 5.6). It was shown by El-Sayed and co-workers that, for diameter of NPs equals to 20 nm, no scattering occurs and the particle only absorbs radiation [41]. Starting from a diameter of 80 nm, both

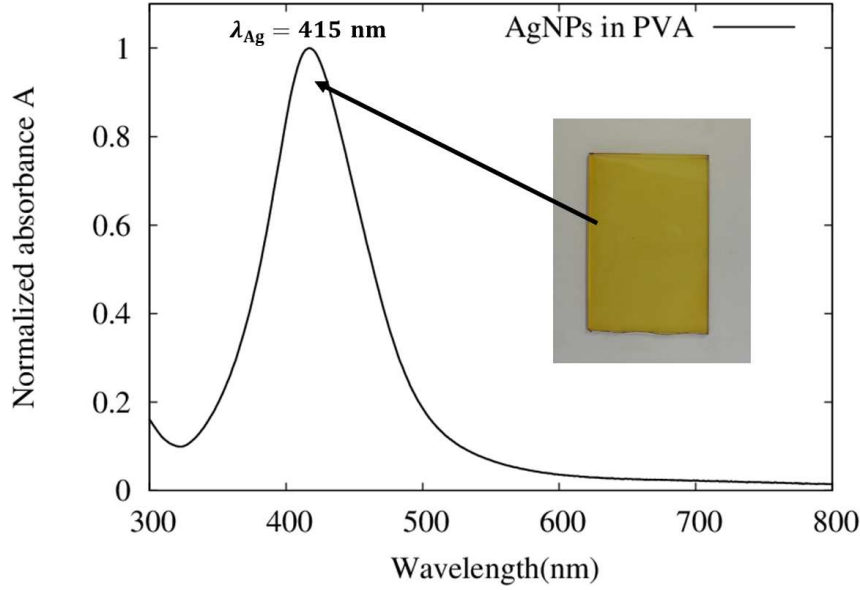


Figure 5.5: Absorption spectrum of a glass coated with a thick film of AgNPs embedded in a PVA matrix at high doping level ($[Ag]/[PVA] = 25\%$ w:w). The inset picture is the analyzed sample.

cross sections, i.e. σ_{abs} and σ_{scatt} , are equivalent and for larger particles, scattering dominates. In our case, the size of the *in situ* synthesized AgNPs is smaller than 40 nm, as we will see from the AFM measurements at the nanoscale in the section 5.6.

Following this analysis, we assume in the rest of this thesis that the extinction is dominated by the absorption. Therefore, the absorbance spectrum presents adequately the extinction that enduring a beam going through the nanocomposite embedding NPs.

Now, we are able to investigate the variation of the absorbance of the silver nanocomposites as a function of the wavelength of the incident light. This absorption spectrum will be presented in the next section. Thanks to this absorption spectrum, we confirm that the preparation method of samples provides the good conditions for the growth of AgNPs inside the polymer matrix (section 5.3.1). Then we will show the real time variation of the absorbance will provide information on the kinetics of growth of the AgNPs (section 5.3.2).

5.3.1 Absorption spectrum of thick highly doped films

In order to detect the Localized Surface Plasmon Resonance (LSPR), defined in the section 3.2.4, we perform a spectrophotometric measurement through a thick sample with a high doping level (TH), i.e. 25% of silver in a 8% w:w PVA matrix. Let us clarify that a thick sample, for us, is not a sample with a thickness of the order of a few micrometers (corresponding to a casting technique) but a sample with a thickness near 400 nm, as it will be shown in the section 5.4.

The absorption spectrum is shown in the figure 5.5 and reveals a sharp peak centered at $\lambda_{LSPR} = 415 \text{ nm}$. The Fröhlich resonance condition (Eq. 3.65) for silver nanoparticles in PVA ($\epsilon_{PVA} = 2.18$) leads to $\epsilon_{Ag} = -4.36$. The plot of the

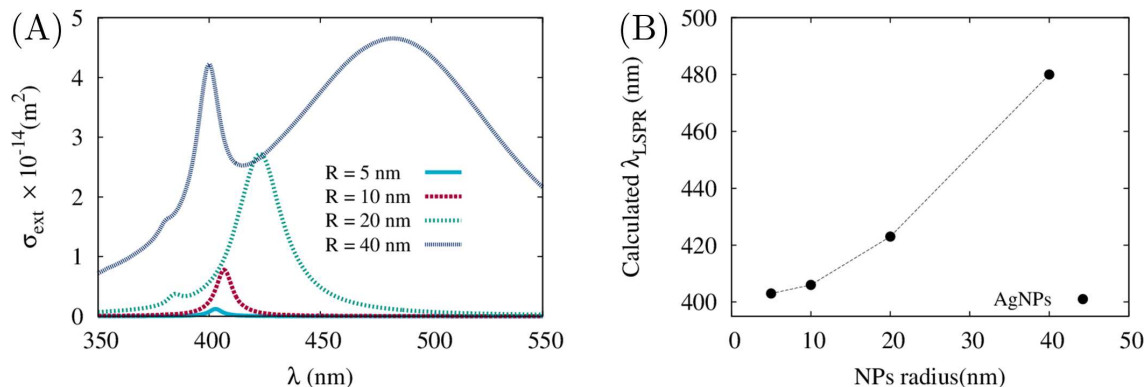


Figure 5.6: (A) Calculated σ_{ext} for different radii of AgNPs. (B) Calculated λ_{LSPR} as a function of the radius of the AgNPs.

dielectric function of silver is given by Johnson and Christy [86] and it is possible to check that this value of ε_{Ag} corresponds to an LSPR around 2.95 eV (415 nm). The inset corresponds to the picture of the analyzed sample that was used for the spectrophotometric measurement. As explained in the section 3.2.4, when polychromatic light (white light) is travelled through an absorbing medium, the transmitted light presents a dip in the spectrum, which corresponds to the absorbed light. In this case, the absorption takes place at 415 nm, i.e. in the blue part of the visible range, resulting in a yellow coloration of the coated glass.

From the position, height and width of the absorption peak, we can characterize the synthesized NPs. First, the position of the resonance is related to the size of the NPs [11]. A red shift corresponds to an increase of the size of the NPs and blue shifts to a decrease of their size. Second, the width of the resonance can be associated to the polydispersity of the size of the NPs in a first approximation. In our case, the width of the resonance peak probably corresponds to a narrow distribution of the nanoparticles size. Third, the height of the peak is connected to the concentration of the nanoparticles. Let us note that, in figure 5.5, the absorbance is normalized to be equal to 1 at the LSPR wavelength in order to have a improved view of the LSPR.

In the purpose of analyzing our absorption spectrum, these three parameters, position, width and height of the resonance peak, are good indicators of the AgNPs embedded in the polymer matrix. It is possible to compute the value of these parameters with the Mie theory [11] (Fig. 5.6A). This graph is obtained from MiePlot computer program which is freely available¹. This program was originally developed to provide a user-friendly interface to Bohren and Huffman's code known as BHMIE [42]. The graph represents the extinction cross section σ_{ext} of AgNPs in PVA with different radii as a function of the wavelength. The extinction cross section σ_{ext} increases with the radius of the AgNPs. For AgNPs with $R = 40$ nm, we can clearly see a second peak at larger wavelength [41]. The interesting point of these calculated spectra is the displacement of the λ_{LSPR} as a function of the AgNPs radius as shown in the figure 5.6B. This allows us to relate the size of the NPs and the position of the resonance.

¹<http://www.philiplaven.com/MiePlot.htm>.

In this work, we use these parameters to have a global analysis of the nanoparticles embedded in the PVA matrix. Following these parameters in real time during the annealing can bring information on the growing process of the AgNPs, as it will be presented in the next section.

5.3.2 Real-time absorption spectra of AgNPs in PVA matrix

Thanks to a small aperture in the central part of the heating block of the high precision heating stage, we are able to measure the transmitted intensity during the annealing of our samples. Starting at room temperature, the temperature is raised up to 110°C at a rate of 10°C/min and stabilized for 60 min. The experimental setup is similar to the one used for the spectrophotometer (Fig. 4.1) with the following differences:

- the light source is a Tungsten-halogen light source with a operational range from 360 nm to 2600 nm;
- the detector is a CSS200 CCD spectrometer (Thorlabs);
- the sample is placed on the heating stage and the beam passes through it thanks to the small aperture in the heating block.

By using Python home-made routines, we measure in real time the transmitted intensity every 30 seconds during the annealing of a thick highly doped silver nanocomposite (total duration: 60 min). Each spectrum is the result of an averaging process of 20 spectra taken every 10 ms. Thanks to the OSA software (Thorlabs), the recorded intensities are automatically transformed in (120) absorption spectra. The analysis of these spectra are made by the SpectraGryph software. As shown in the figure 5.7A, an absorption peak near 415 nm appears during the annealing, which can be assimilated to the growth of the AgNPs in the PVA film.

In the figure 5.7B, the variation of the absorbance at λ_{LSPR} as a function of the annealing time is plotted. At the beginning ($t < 10$ min), the absorbance is zero, since we start heating the sample. Near ten minutes ($T \simeq 110^\circ\text{C}$), a large increase of the absorbance shows that the AgNPs start to growth in the polymer matrix. At this time, we can clearly see that the temperature of the nanocomposite has reached the glass transition temperature of the polymer ($T_g = 85^\circ\text{C}$) [55] (blue lines in the graph). The black dashed line corresponds to the temperature setup at the level of the heating stage². The last spectra plotted on the graph only show a weak increase of the absorbance. After a linear regression of the absorbance data as a function of the time t for t between 20 and 60 min, it can be shown that the growth rate of the absorbance, which can be related to the increasing number of AgNPs in the polymer matrix, is given by the following equation: $A(t) = (0.00585 \pm 0.00005) t + (0.2481 \pm 0.0023)$ (with t corresponding to the time in minute).

²The addition of a thermocouple attached at the surface of the nanocomposite was tested without satisfactory results due to mechanical constraints exerted on the sample and their influence of the optical measurements.

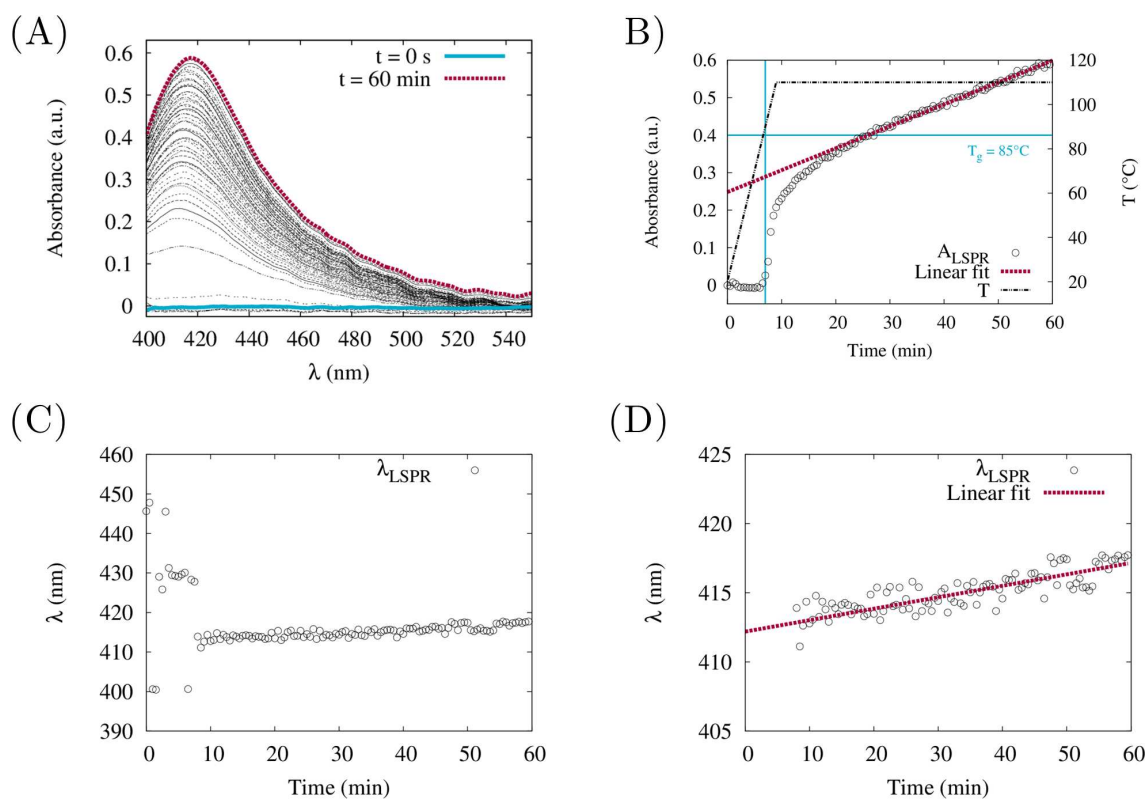


Figure 5.7: (A) Absorption spectra recorded during the annealing of a (~ 370 nm-thick) Ag-PVA nanocomposite ($[Ag]/[PVA] = 25\%$ w:w). (B) Variation of the absorbance during the annealing time: open circles are the experimental data and the dashed line is the linear fit of the linear part of the curve: $A(t) = (0.00585 \pm 0.00005) t + (0.2481 \pm 0.0023)$. The horizontal blue line is the glass transition temperature T_g and the vertical blue line shows the time when the temperature of the sample reaches T_g . (C) Variation of the position of the resonance peak as a function of time. (D) Variation of the position of the resonance peak in a limited range in order to see the increase of the λ_{LSPR} as a function of the annealing time: open circles are experimental points and the dashed line is the linear fit: $\lambda(t) = (0.083 \pm 0.008) t + (412.19 \pm 0.32)$.

This increase of the absorbance and of the number of AgNPs in the PVA matrix as a function of the annealing time have been shown by Porel and co-workers [66]. However, in our case, the measurement can be directly made during the heating of the sample, which leads to a higher precision in timing, temperature and position. As the measurements are carried out without moving/repositioning of the sample, the transmission changes over time relate to the same position, making our results independent of the sample thickness variation. Moreover, in our experiment, we can have access to more data due to the speed of acquisition.

Another analysis can be made on the position of the resonance peak, which seems to shift during the annealing, as shown in the figure 5.7C. Points corresponding to the absorbance measured at $t < 10$ min are not relevant because there is no absorption peak in the early stage of the experiment. After the ten first minutes, we can see a weak increase of the position of the λ_{LSPR} . This observation is highlighted in the figure 5.7D where the y -scale is limited to improve the analysis. In this graph, we can see a slight increase of the position of the resonance peak, given by a linear equation: $\lambda(t) = (0.083 \pm 0.008) t + (412.19 \pm 0.32)$, where t is the time in minute. As shown by the positive slope, the position of the resonance peak increases during the annealing time, which can be related to a small increase of the size of the AgNPs in the polymer matrix [11, 91].

To sum up, the analysis of the absorption spectra during the annealing of the sample can provide information about the growth of AgNPs. After a first period of heating, the resonance peak appears, i.e. the value of absorbance increases. That is attributed to the growth of the AgNPs inside the polymer. The absorbance increase during the annealing, which corresponds to an increase of the number of the *in situ* synthesized AgNPs. A last conclusion is the weak variation of the position of the resonance peak during the annealing that can be attributed to a slight increase of the size of the AgNPs.

After these first analyzes of a thick and highly doped silver nanocomposite, which confirm the growth of the AgNPs in the polymer matrix, we want to investigate the influence of experimental parameters on the resonance parameters. As the annealing time and the temperature of annealing have been already studied [66, 67, 69, 113], we consider the variation of another parameter: the thickness of the film, which is not often studied. For this purpose, we prepare samples with different thicknesses while keeping a constant metal-to-polymer mass ratio. As it will be shown in the next section, despite the same silver/polymer ratio, the variation of the thickness induces changes on the resonance parameters, a result, which to the best of our knowledge has not been reported in the literature.

5.4 Variation of the film thickness at a constant metal/polymer mass ratio

As previously described, the influence of the thickness of the film on the resonance parameter has not often been studied. On this basis, we want to measure the absorption spectra of our silver nanocomposites by changing the film thickness, while maintaining a constant metal-to-polymer mass ratio. In other words, starting with

Table 5.1: Measured thicknesses of the silver nanocomposite by the EP3-SE using Cauchy model. The model is applied on the ellipsometric data far from the resonance, i.e. for incident wavelength larger than 545 nm.

Samples ID	Polymer conc. (%)	Thickness (nm)	RMSE
[PVA] = 8%	8	374.9 ± 1.4	1.683
[PVA] = 4%	4	121.1 ± 0.1	0.709
[PVA] = 2%	2	54.5 ± 0.3	0.271
[PVA] = 1%	1	28.9 ± 0.1	0.205
[PVA] = 0.5%	0.5	15.8 ± 0.1	0.093

a solution where the [Ag]/[PVA] mass ratio is 25% in a 8% polymer solution, we add the required amount of water to dilute the solution by 2, 4, 8 and 16 factors. This leads to less viscous solutions yielding therefore thinner films after spin coating (Eq. 4.33). Due to the dilution by 2, 4, 8 and 16, the polymer solution concentrations become 4%, 2%, 1% and 0.5%, respectively. Experimental spinning conditions on the glass substrates are 1600 rpm during 90 sec. These samples are annealed during 1 hour at 110°C in oven. After the annealing, the absorption spectra of the glass-coated samples is recorded by the Genesys 10S UV-visible spectrophotometer. The ellipsometric response of silver nanocomposites prepared under the same experimental conditions on silicon substrate are measured by spectroscopic ellipsometry in order to measure the thickness of the films.

The values are presented in table 5.1. They are determined by using the Cauchy model on ellipsometric data far from the resonance ($545 \leq \lambda_i \leq 1000$ nm). As expected, the dilution of the polymer concentration leads to a large variation of the thickness of the nanocomposite films. Let us note that the thicknesses obtained on silicon substrates are also valid for the films prepared under the same conditions on the glass substrates.

The samples prepared on glass substrates are analyzed by spectrophotometry and their absorption spectra are shown in the figure 5.8A. As we can see, the height of the peak rapidly decreases as a function of the polymer concentration. The highest peak corresponds to the 8% polymer solution and the smallest to the 0.5% polymer solution. The inset in the figure 5.8A shows that the two thinner films nevertheless present a weak but distinct absorption peak. This decrease of the absorbance can be explained by the reduction of the thickness of the film, while keeping the same silver-to-polymer mass ratio. This leads to a smaller number of silver nanoparticles embedded in the PVA matrix located on the path of the spectrophotometer beam although we expect the AgNPs density to remain constant. This analysis is well presented in the figure 5.8B where the analyzed samples are shown. The sample “[PVA] = 8%” presents a strong yellow coloration, although the sample “[PVA] = 0.5%” is almost transparent. More striking than the decrease in the saturation of the intensity is the apparent change of the color, which seems to evolve from yellow to orange as the thickness of the film decreases.

Another interesting fact is the weak increase of the width of the resonance. This

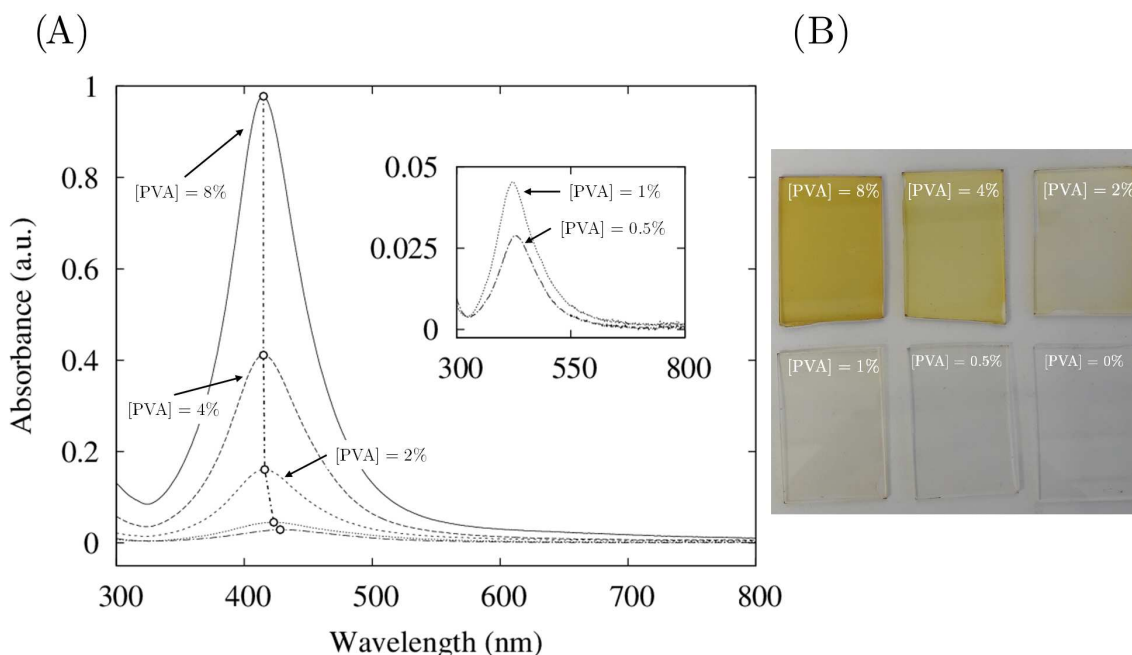


Figure 5.8: (A) Absorption spectra of AgNPs embedded in PVA matrix. The variation of the film thickness is obtained by dilution of the AgNO_3 -Polymer solution by adding the required amount of water. Polymer solution concentrations, varying from $[\text{PVA}] = 8\%$ to $[\text{PVA}] = 0.5\%$. The highest resonance peak corresponds to the thicker film and the smallest peak is the thinner film (Table 5.1). The inset graph exhibits the weak resonance peak of the thinner films. A line is drawn in order to guide the eye along the maximum value of the absorption. (B) Picture of the analyzed samples.

means that a decrease of the thickness of the film leads to a slight increase of the polydispersity of the size of the AgNPs in the PVA matrix.

Finally, the most interesting information obtained with this analysis is the displacement of the position of the resonance peak as a function of the thickness. As it is shown in the figure 5.8A by a dashed line connecting the highest values of the absorbance of each resonance peak. This highest value of the absorbance remains approximately constant for $[\text{PVA}] = 8\%$, 4% and 2% , however it shifts for $[\text{PVA}] = 1\%$ and 0.5% . As already explained, this displacement can be related to the size of the AgNPs in the PVA matrix. Confirming the visual perception of the film color, this evolution corresponds to a red-shift that can be interpreted by a larger size of the AgNPs in the thin films than in the thick films.

In order to confirm this trend observed on a batch of samples, the same experiment has been repeated several times and, for each experiment, the position of each resonance peak, i.e. λ_{LSPR} , is recorded. The results of these experiments is shown in the figure 5.9. This graph presents the variation of the position of the LSPR as a function of the polymer concentration. As previously shown (Table 5.1), the variation of the polymer concentration, i.e. “[PVA]”, while keeping a constant metal-to-polymer mass ratio leads to a variation of the thickness of the nanocomposite films: the more diluted solution, the thinner film. As showed by the figure 5.9,

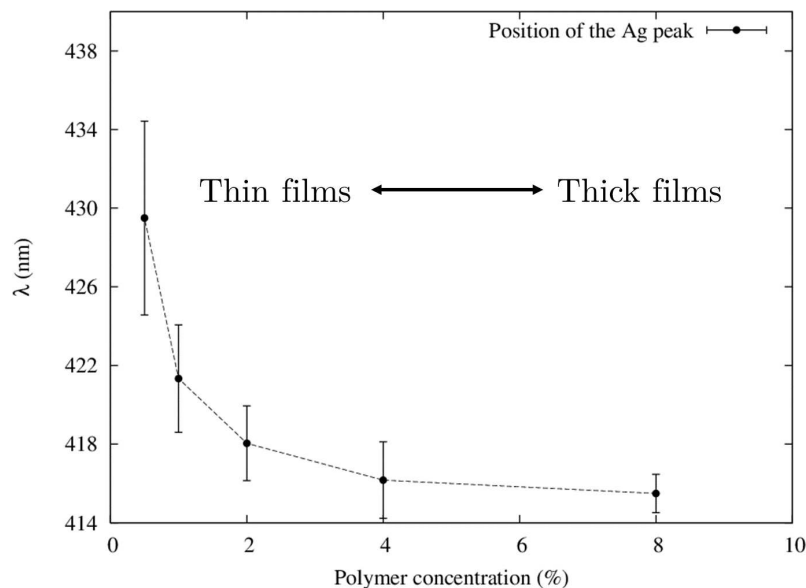


Figure 5.9: Graphical representation of the position of the resonance peak as a function of the polymer concentration. As the polymer concentration can be related to the thickness of the film, the λ_{LSPR} shows a displacement for thin films. The errors bars represent the standard deviations of the measured λ_{LSPR} .

the value of the LSPR stays at 415 nm for “[PVA]” = 8% and “[PVA]” = 4% polymer concentration. There is a small peak displacement for the “[PVA]” = 2% (418 nm) and a larger shift for “[PVA]” = 1% (420 nm) and “[PVA]” = 0.5% (429 nm). These shifts are statistically significant. This plot demonstrates the red shift of the position of the resonance peak when going from high polymer concentration solution to small polymer concentration solution, i.e. from [PVA] = 8% to [PVA] = 0.5%. Using the results shown in the table 5.1, we can assume that this plot shows the red-shift of the position of the resonance peak when going from thick to thin films. This displacement of the position of the resonance peak can probably be interpreted as a control of the AgNPs size by the film thickness: decreasing the thickness below 30 nm increases the size of the *in situ* synthesized AgNPs in PVA matrix.

In fact, the position of the λ_{LSPR} can be related to the size of the nanoparticles using the Mie theory. As explained by Quinten [91], the position of the resonance peak shifts as a function of the size of the particles for nanoparticles formed in an aqueous suspension and dispersed in a gelatin matrix. For particles with mean radii between 5 and 35 nm, the displacement of the peak position of the localized surface plasmon as a function of the size of the particle is linear for AgNPs (and also for AuNPs). Remembering that the position of the peak depends also on the refractive index of the surrounding medium via the Fröhlich equation (Eq. 3.65), for AgNPs with a mean radius of 10 nm the peak position is near 405 nm. For larger silver particles with a mean radius of 35 nm, the position of the resonance peak is located near 437 nm.

Moreover, as demonstrated by Berg and co-workers [116], the size of particles can be attributed only by the measured λ_{LSPR} in the case of small particles with radii between 5 and 25 nm. They considered small silver particles obtained by sodium-

silver ion exchange in glass. They have shown a nice representation of their data in a δ vs λ_{\max} graph called Berger diagram (Fig. 2 in [116]). This plot shows the variation of the width of the resonance δ , i.e. the full width at half maximum (FWHM), as a function of the position of the resonance λ_{\max} . Their data are computed from results obtained by Kreibig [117] and based on the Mie theory for monodisperse size of particles. From their analysis, two conclusions can be drawn: first, even if there exists a size distribution of the particles, with an experimental determination of the (λ_{\max}, δ) pair values, it is possible to attribute a mean diameter from its position on the δ vs λ_{\max} curve computed for monodisperse system. Secondly, for particles with a mean radius between 5 and 25 nm, only the peak position is sufficient to attribute a size at the AgNPs.

According to these analyzes, we can assume that the size of the AgNPs can be attributed from the position of the resonance peak. In our case, we measure a red shift of the position of the resonance peak as a function of the thickness of nanocomposite films. This displacement can be explained by a size difference of the *in situ* synthesized AgNPs in the PVA matrix between thin and thick films: although the silver-to-polymer mass ratio remains constant, larger AgNPs are obtained in thin films than in thicker ones.

From this, let us conclude that the variation of one experimental parameter, thickness, can lead to a variation of one resonance parameter, the position of the resonance. In order to investigate deeper the role of the thickness on the resonance parameters, we present in the next section a more detailed analysis of this thickness effect by using spectroscopic ellipsometry (SE). One of main advantages of SE over conventional spectrophotometric methods is that by keeping tracks of the relative phase changes (in the Δ ellipsometric angle) it allows in most cases a simultaneous determination of the optical properties and of the thickness of the layers and not only the measurement of absorption or of transmission spectra. Finally, at the end of the chapter, we will try to give an explanation on the growing process leading to these changes between thick and thin films.

5.5 Film thickness and silver doping effects

In this section, we use SE in order to get detailed information about the influence of the thickness of the film on the resonance parameters. With this non-destructive technique described in the chapter 4, we are able to measure the thickness and the optical properties of the silver nanocomposites and, thus, determine the resonance parameters with theoretical models.

The purpose of this analysis is two-fold:

- to compare the optical properties of thick and thin films embedding AgNPs grown *in situ* from the same polymer solution;
- to investigate the effect of the doping of the film at those thicknesses.

This comparison can lead to a variation of the resonance parameters in both films, which relates to a modification of the growing process of the AgNPs.

Table 5.2: Coating conditions for the four types of samples

Samples ID	Polymer conc. (%)	[Ag]/[PVA] mass ratio (%)	Coating speed (rpm)	Coating time (s)	Approx. thickness (nm)
TH	8	25	1600	60	300
TI	8	2.5	1600	60	300
tH	2	25	6000	60	30
tl	2	2.5	6000	60	30

On that purpose, four types of samples are prepared by varying the film thickness ('T': thick ; 't': thin) and the doping level in silver ('H': high (25%); 'l': low (2.5%)). In the following, these categorical variables will be referred to as the class of the sample ('TH', 'TI', 'tH' or 'tl') (Table 5.2). The total number of samples is 90 and they are equivalently distributed in each class.

In order to study the optical properties of these samples, the complex refractive index is calculated from SE measurements, i.e. from the Ψ and Δ spectra. Except in a very limited number of cases [99], Ψ and Δ cannot be directly converted into refractive index and/or film thickness. Indeed, the ellipticity is a complex quantity, which depends on the angle of incidence, the optical properties of the materials and the thickness of the layers. Taking into account the dispersion of the dielectric function, the equation of the ellipticity ρ (Eq. 5.1) has to be inverted in most cases using numerical methods, assuming specular reflection of light at ideal planar interfaces.

We begin this study by presenting the models used to describe the silver nanocomposites. After, once the optical properties of the nanocomposites are determined, we use a multivariate analysis in order to inspect the influence of the thickness of the film and the doping level on the resonance parameters.

5.5.1 Modeling of the optical properties

The models used to analyze the SE data are described hereinafter and illustrated in the figure 5.10. The description of the model used for the dielectric matrix has already be shown in the figure 5.2

PVA layer: A one-layer Cauchy model is chosen to represent the optical properties of the PVA films in the transparent range [95].

$$n_{\text{PVA}}(\lambda) = A_{\text{PVA}} + \frac{B_{\text{PVA}}}{\lambda^2} \quad \text{and} \quad k_{\text{PVA}}(\lambda) = 0 \quad (5.6)$$

Ag-PVA layer: A Lorentzian oscillator is added to that model to account for the localized absorption of the plasmon resonance in visible range [102].

The specific contribution of the plasmon resonance to the wavelength-dependent complex dielectric function $\varepsilon(\lambda)$ is given by

$$\varepsilon(\lambda) = \varepsilon_r(\lambda) + i\varepsilon_i(\lambda) \quad (5.7)$$

$$\varepsilon_r(\lambda) = \varepsilon_\infty + \frac{A\lambda^2(\lambda^2 - \Lambda_0^2)}{(\lambda^2 - \Lambda_0^2)^2 + \Gamma_0^2\lambda^2} \quad (5.8)$$

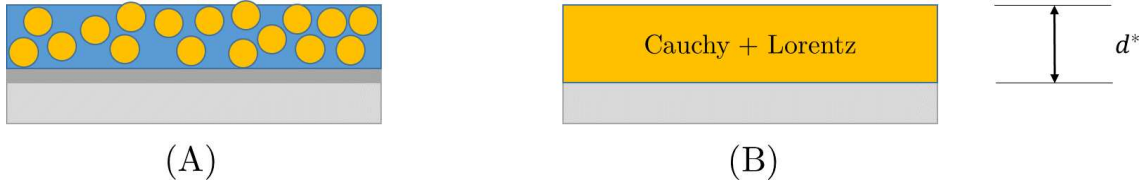


Figure 5.10: Schematic representation of the optical model used to interpret SE data: (A) AgNPs in PVA layer on Si and (B) a Cauchy model and Lorentzian oscillator used to describe the optical properties of AgNPs in PVA matrix. (Not to scale)

$$\varepsilon_i(\lambda) = \frac{A\lambda^3\Gamma_0}{(\lambda^2 - \Lambda_0^2)^2 + \Gamma_0^2\lambda^2} \quad (5.9)$$

where λ denotes the wavelength. Λ_0 is the resonance wavelength of the oscillator, A its oscillator strength (i.e. amplitude of the resonance) and Γ_0 its full-width at half maximum (FWHM) and is hereinafter referenced to as the ‘width’ of the resonance. ϵ_∞ represents the contributions of the resonances to ϵ_r at wavelengths much greater than the measurable wavelength range.

Figure 5.11 represents the SE data corresponding to a 25.4 nm-thick film (Fig. 5.11A) and to a 293.9 nm-thick film (Fig. 5.11B). Instead of representing the Ψ and Δ ellipsometric angles, we have chosen to represent the $\alpha = \cos(2\Psi)$ and $\beta = \sin(2\Psi) \cos(\Delta)$ Fourier coefficients, which are closer to the experimental quantities measured by the ellipsometer (Eq. 4.26). With respect to reference films of equivalent thicknesses, the ellipsometric data present a spectra distortion in the 3.0-3.5 eV range. This is unambiguously attributed to the LSPR associated to the AgNPs. This effect is more noticeable for the thick films (Fig. 5.11B): one can see three peaks in the α -spectrum (filled symbols) but the second is considerably damped due to the energy absorption at the resonance. The data generated by the optimized optical model are also presented in the figure 5.11 (dashed lines). They are in close agreement with the experimental data: the residual χ^2 values are respectively equal to $2.7 \cdot 10^{-4}$ and $2.9 \cdot 10^{-3}$ for the thin and thick films.

As previously described in the figure 5.10, the model of the optical behavior of our samples is a one-layer Cauchy model, chosen to represent the optical properties of the polymer matrix, complimented with a Lorentzian oscillator to account for the localized absorption of the plasmon resonance in the visible range. This model has already been used to model the optical behavior of these silver nanocomposites [73]. As already mentioned, the use of the Cauchy model for the polymer matrix is justified by the monotonous increase of the refractive index of the polymer, from the infrared to the UV, as expected for dielectric materials far from the fundamental absorption edge. Details of this model and of its application to pure PVA films are given in section 5.2. Concerning the AgNPs, the application of the Lorentzian oscillator in the model is equivalent to using the Maxwell-Garnett effective medium approximation (MG-EMA) in a view of obtaining the dielectric function of the nanocomposite films [118–120]. Here, we use the Lorentzian model since it depends less on the dielectric function of the bulk silver (see tables [86]), which can be slightly different from the dielectric function of the AgNPs. Moreover, the shape of the AgNPs is not considered in our Lorentzian model unlike with the generalization

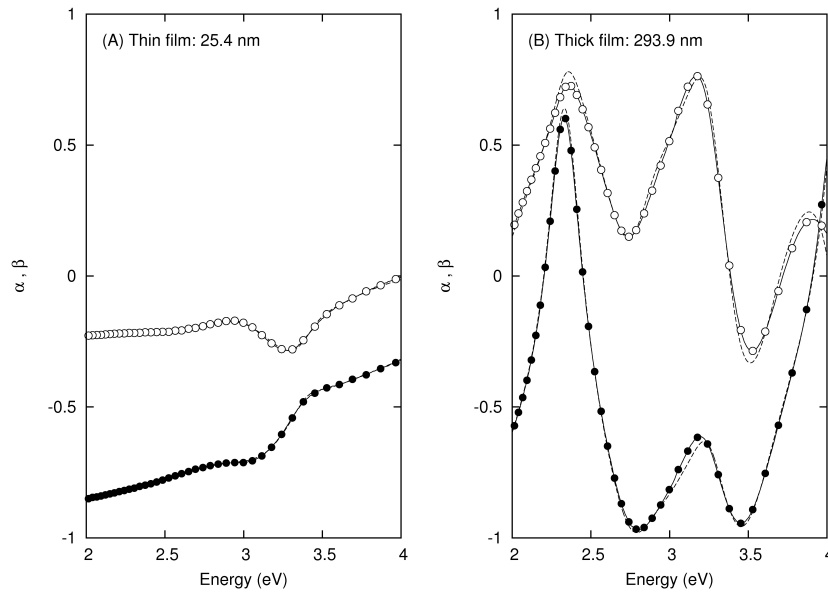


Figure 5.11: Ellipsometric spectra of Ag nanoparticles-doped PVA films ([Ag]/[PVA] ratio: 25% w:w): A, 'tH' thin films (thickness: 25.4 nm); B, 'TH' thick film (thickness: 293.9 nm). Experimental data: $\alpha = \cos(2\Psi)$ (filled circles) and $\beta = \sin(2\Psi) \cos(\Delta)$ (open circles). Dashed lines: optimized results from the optical model.

of the MG-EMA to take into account the statistical distribution of size and shape of the NPs. Our model is well-suited for spherical NPs [11, 72, 121] but more complex approaches are required for non spherical particles (see e.g. [12, 122, 123]). As we will see in a later section, the AgNPs in our nanocomposites seem to be spherical thanks to an analysis at the nanoscale by atomic force microscopy (AFM).

Problems related to the doping level of the films are also avoided: indeed, at high doping levels, it is expected that the nanocomposite films cannot be considered anymore as diluted solutions of NPs in a polymer matrix. We suppose low doping level since, in the present case, the volume fraction of silver in the nanocomposite is less than 3%, which means that the films can be considered as a diluted solutions of NPs in a polymer matrix. In the case of high doping level, the analysis of the optical response of nanocomposite is more relevant of the metal island model [124, 125] which has been recently generalized by Wormeester and co-workers [126, 127]. Adding roughness or void inclusions to the model does not significantly improve the quality of the fits, even for the thin samples.

The optical properties of the AgNPs-doped films (doping: 25%) are represented in the figure 5.12. For each type of film, the refractive index n and the extinction coefficient k of two different samples are represented, showing the reproducibility of the analysis and indirectly, of the sample preparation. The presence of the silver NPs considerably modifies the optical properties in the doped polymer films: the absorption peak in the 2.5 - 3.5 eV range of the extinction coefficient spectrum (Fig. 5.12B) induces a large oscillation in the refractive index value (Fig. 5.12A) because of the Kramers-Krönig consistency of the optical properties (Eq. 3.83) and the Lorentzian model of the peak. The perturbation of the refractive index takes place over the 1.5 - 4.5 eV range although the absorption peak is narrow. Moreover,

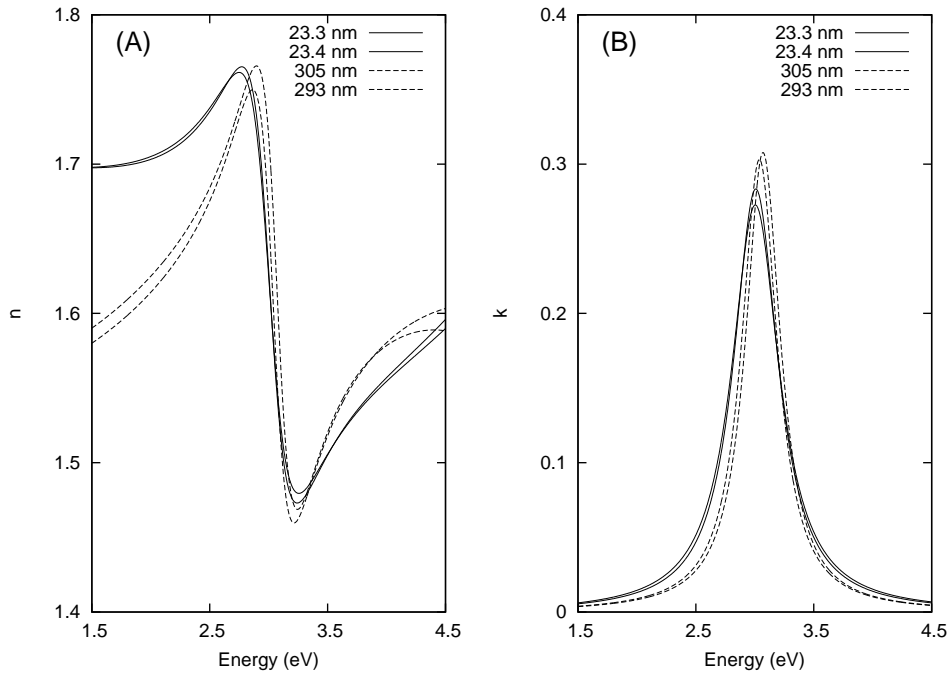


Figure 5.12: Optical properties of thin (plain lines) and thick (dashed lines) silver NPs-doped PVA films ([Ag]/[PVA] ratio: 25% w:w): A, refractive index n ; B, extinction coefficient k .

the refractive index values are higher than the ones of a pure polymer film. This variation over a large spectral range of the refractive index is shown in a published article of Voué and co-workers (Fig. 2.5).

The optical properties of thin and thick films are clearly different as experimentally demonstrated in the figure 5.12. The optimized parameters of the plasmon resonance peak are given in the table 5.3. As we can see, in thin films, the amplitude of the resonance is higher and the peaks wider than in thick films. Furthermore, the position of the resonance, Λ_0 , is 10 nm red-shifted between thick films and thin films.

Table 5.3: Typical parameters of the plasmon absorption peak (A : amplitude of the absorption peak; Λ_0 : position of the resonance; Γ_0 : width of the resonance) as a function of the film thickness for highly doped PVA films ([Ag]/[PVA] ratio: 25% w:w). Data correspond to the optical properties presented in Fig. 5.12.

Sample	d (nm)	A	Λ_0 (nm)	Γ_0 (nm)
Thin	23.4 ± 0.2	0.145 ± 0.006	414.2 ± 0.7	67.6 ± 2.9
	25.4 ± 0.3	0.133 ± 0.005	415.6 ± 0.6	69.0 ± 2.6
Thick	305.9 ± 1.7	0.117 ± 0.002	405.4 ± 0.7	47.3 ± 1.6
	293.4 ± 1.7	0.118 ± 0.002	409.5 ± 0.6	49.2 ± 1.5

		Doping	
		2.5%	25%
Thickness	thin	thin low (tl)	thin High (tH)
	Thick	Thick low (Tl)	Thick High (TH)

Figure 5.13: Graphical illustration of the four classes defined on the basis of the thickness and doping of the samples.

5.5.2 Multivariate analysis on the resonance parameters

As already explained, the 90 samples are distributed in four classes of relatively equivalent sizes. With this amount of experimental data, it is interesting to use a multivariate analysis in order to highlight the effect of an experimental parameter on the resonance parameters.

Keeping in mind that they are normally decorrelated from the thickness of the film, once the optical properties of the nanocomposites are determined, we considered the dispersion of the data cloud. The optical response of each nanocomposite is characterized by 3 parameters A , Λ_0 and Γ_0 :

- A represents the oscillator strength or the amplitude of the resonance,
- Λ_0 corresponds to the central resonance wavelength and depends on the size of the NPs,
- Γ_0 describes the width of the resonance and can be used to characterize the polydispersity of the NPs in the film.

Data clouds of the resonance parameters

The samples considered for this study are distributed among four classes of relatively equivalent sizes. These classes are defined on the basis of the thickness and doping of the samples (Table 5.2). Each of the four classes are represented by a different color as represented in the figure 5.13. As a reminder, there are four classes composed by:

- TH: thick samples with a high doping level, i.e. 25% w:w in green;
- tH: thin samples with a high doping level in red;
- Tl: thick samples with a low doping level, i.e. 2.5% w:w in yellow;
- tl: thin samples with a low doping level in blue.

The mean values and standard deviations of the resonance parameters as a function of the nanocomposites class are given in the table 5.4.

Let us first consider the link between the thickness of the film and the strength of the plasmon band A (Fig. 5.14). One can easily see that the data cloud is subdivided

Table 5.4: Classes size (N), means and standard deviations of the resonance parameters as a function of the nanocomposite type. Units for thickness (“*thick*”), peak position (“ $L0$ ” or Λ_0) and peak width (“*Gamma*” or Γ_0) are micrometers.

class	N	thick	Means			Standard deviations			
			A	L0	Gamma	thick	A	L0	Gamma
tH	17	0.028	0.125	0.421	0.095	0.014	0.050	0.006	0.046
TH	27	0.311	0.102	0.410	0.064	0.082	0.018	0.005	0.018
tl	16	0.030	0.013	0.437	0.064	0.019	0.014	0.014	0.036
TI	30	0.254	0.028	0.419	0.127	0.076	0.024	0.013	0.056

into four areas, each of those being assigned to one type of nanocomposite. Samples with high doping level are on the right side of the plot with a higher value of the amplitude of the oscillator A in both case (thin and thick films, green and red symbols, respectively). As expected, the samples with low doping level (i.e. yellow and blue symbols) are on the left part of the plot.

After this first analysis between the amplitude of the resonance and the thickness, it is interesting to plot the dispersion cloud for each pair of parameter. In other words, three plots can be obtained: A vs Λ_0 , A vs Γ_0 and Γ_0 vs Λ_0 . This scatter plot matrix of the resonance parameters is shown in the figure 5.15. As one can see in the first row of the matrix (left part of the scatter plot), different behavior can be identified between the nanocomposites prepared from solutions with a high AgNO_3 concentration (red and green circles) and those prepared from diluted AgNO_3 solutions (blue and yellow circles). In each plot, A vs Λ_0 and A vs Γ_0 , it is easy to draw a virtual vertical line to separate the data in two subclouds thanks to the value of absorbance A . However, it seems more complicated to separate samples from different category in the same subcloud: for example, red and green symbols are overlapping in the right subcloud for both graphs.

Moreover, the same trend is found in the case of the $\Gamma_0 - \Lambda_0$ plot where all subclouds are overlapping in a strong way, which complicates the interpretation of this plot. This graph can be related to the previously presented Berger diagram (Fig. 2 in [116]). As already mentioned, this diagram presents the width δ as a function of the peak position λ_{\max} for extinction bands, i.e. resonance peak, for silver particles. The variation of δ vs λ_{\max} is not a monotonous one. Starting for small particles (around 2 nm), an increase of the size of particles leads to a decrease of the FWHM and a blue shift of the position of the resonance peak until the radius of the particle has reached 10 nm. For larger particles, both FWHM and position of the resonance peak increase. As shown here, the analysis of the Γ_0 vs Λ_0 graph is complicated and rather difficult to interpret in our case.

This global picture of the data cloud is reinforced by the statistical dispersion of the resonance parameters in terms of box-and-whiskers plots (Fig. 5.16). The box-and-whiskers plot is a method to graphically depict groups of experimental data through their quartiles. This description of the data set is based on five parameters: the minimum and the maximum of the data but also the three quartiles Q_1 representing 25% of the data set, Q_2 (median) and Q_3 corresponding to 75% of the data

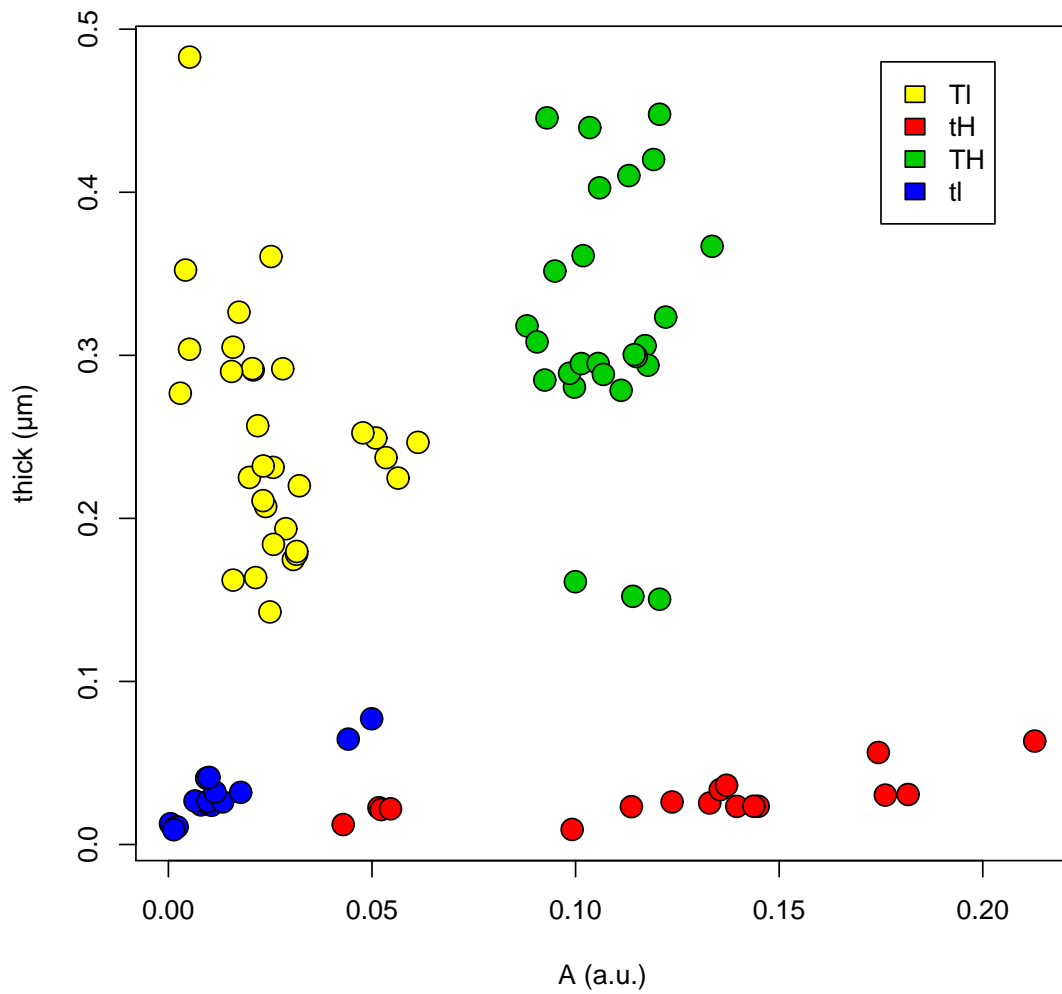


Figure 5.14: Scatterplot of the thickness of the film (in μm) versus the strength of the oscillator. Color coding of the categorical variables is given in the legend and refers to table 5.2.

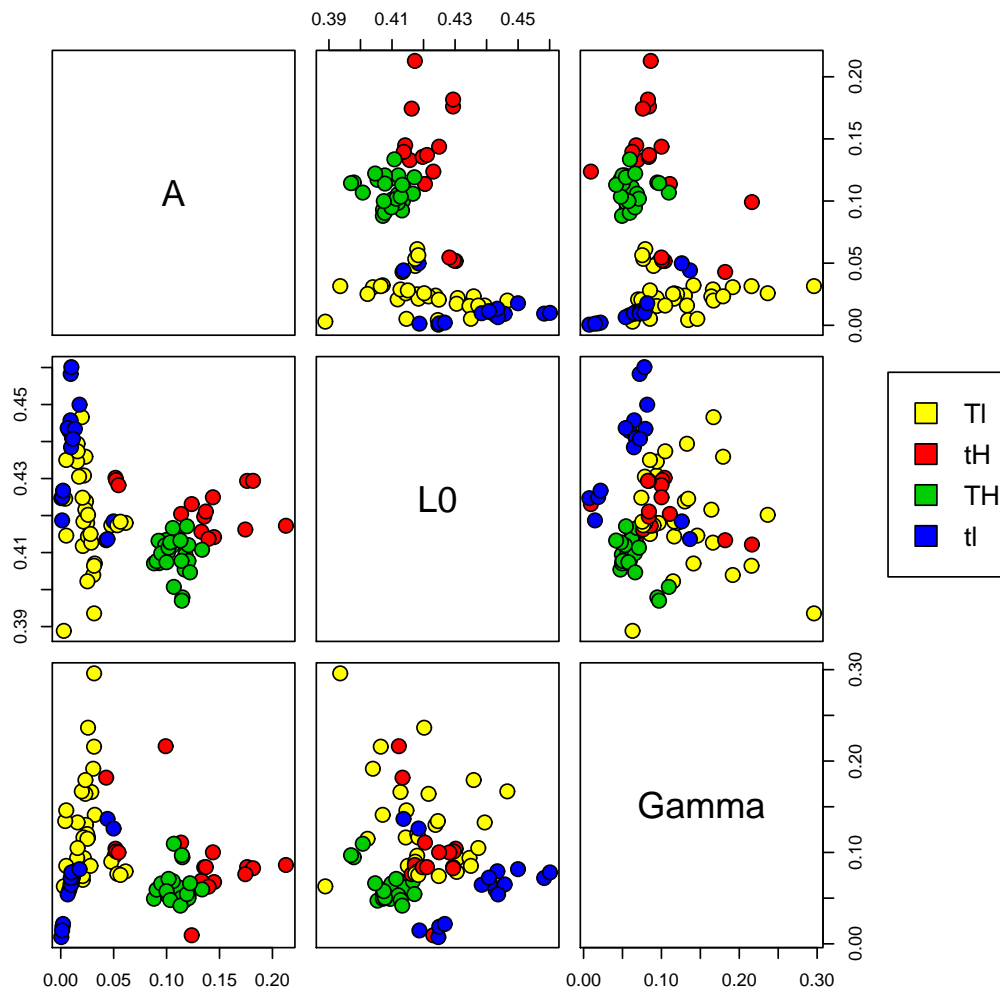


Figure 5.15: Scatterplot matrix of the resonance parameters. Colour coding of the categorical variables are given in the legend. Units for peak position (“ $L0$ ” or Λ_0) and peak width (“ Γ ” or Γ_0) are micrometers.

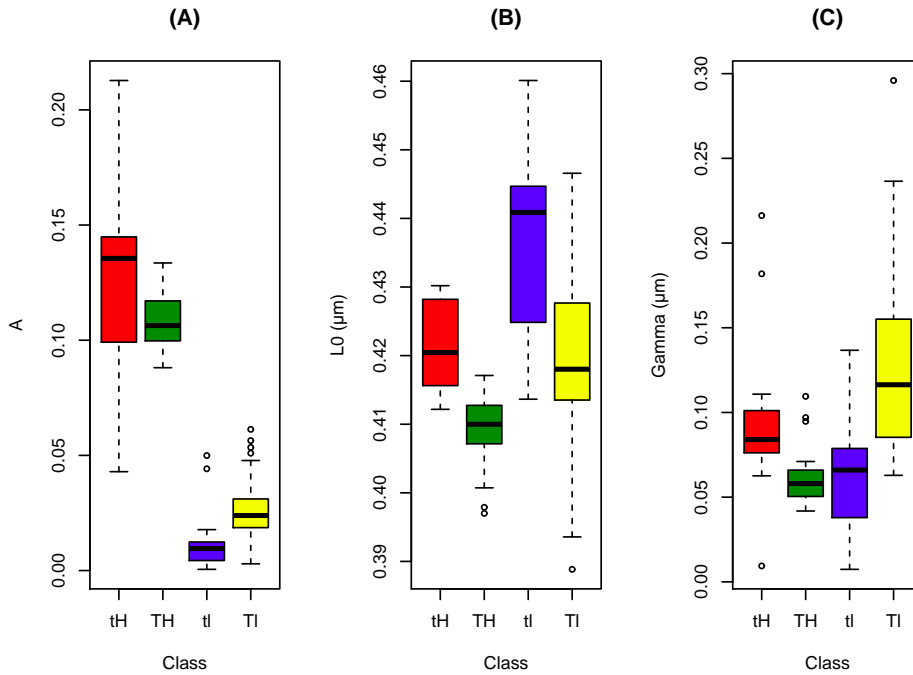


Figure 5.16: Box-and-whiskers plots of the resonance peaks parameters: (A) peak height (A), (B) peak position (L_0) and (C) peak width (Γ). Categorical class definitions are given in the text.

set. A last important element to construct the boxplot is the interquartile range (IQR) that is represented by the distance between Q_1 and Q_3 ($\text{IQR} = Q_3 - Q_1$). The box is drawn between Q_1 and Q_3 and the horizontal line represent the median of the data set (Q_2). Moreover, the size of the whiskers can be tuned by the interquartile range. In our case, the size of the upper and lower whiskers are given by $\min\{\max(x), Q_3 + 1.5 \text{ IQR}\}$ and $\max\{\min(x), Q_3 - 1.5 \text{ IQR}\}$, respectively. The boxplots are very useful to describe asymmetric statistical distributions for which the description in terms of $\text{mean} \pm \text{standard deviation}$ is sometimes meaningless.

Equality of variances or heteroscedasticity of the data was checked using a robust version of Levene's test. The results show that the null hypothesis H_0 (equality of all the variances) has to be rejected at a confidence level better than 1% (data not shown) for all the resonance parameters. Although classical analysis of variance (ANOVA) methods are relatively robust with respect to the non-normal distribution of the variables, differences in variances are more complicated to handle. As a rule of the thumb, classical ANOVA can be used if the ratio of the largest to the smallest variance is < 4 . This case is not met by our data. Non parametric tests are therefore required. Results issued from the Kruskal-Wallis test are presented in the table 5.5. In a given row of the table, classes represented by the same letter do not statistically differ from each other.

Boxplot representation of our data are given in the figure 5.16. As expected, the strength of the oscillator A is strongly dependent on the silver content of the film (Fig. 5.16A). Two trends emerge from the peak position dispersion: an increase of the amount of Ag^+ present in the films ($l \rightarrow H$) decreases the position of the

Table 5.5: Summary of the Kruskal-Wallis statistical test for the resonance parameters. In a given row, classes represented by the same letter do not statistically differ from each other. To be compared with the boxplots in the figure 5.16

Parameter	Class			
	tH	TH	tl	Tl
A	a	a	b	c
Λ_0	b	c	a	b
Γ_0	b	c	c	a

resonance peak, i.e. blue-shifts the resonance peak. Points corresponding to outliers are outside the box and whiskers. A decrease of the thickness of the films ($T \rightarrow t$) slightly red shifts the resonance wavelength (Fig. 5.16B). The modification of the film thickness induces a displacement of the position of the resonance peak. This displacement has been already show by spectrophotometry measurements. This supports the fact that thickness plays an important role on the resonance parameters and therefore on the *in situ* synthesis of the AgNPs.

The evolution of the resonance width is more complicated (Fig. 5.16C). For example, increasing the film thickness ($t \rightarrow T$) leads to an increase of the FWHM for high doped samples and a decrease of FWHM for low doped samples. Looking at the decrease of the amount of Ag^+ ($l \rightarrow H$) leads to an increase of the FWHM for thick samples and a decrease of the FWHM for thin samples. By considering only the FWHM, it is complicated to draw a trend. For that reason, the behaviors of the films with low and high silver contents have to be separately described in the remaining parts of this analysis.

Classification in the $\Gamma_0 - \Lambda_0$ plane

As we have seen from the scatter plot matrix and the box-and-whiskers plots, thick and thin films behave differently when we consider the resonance width (Γ_0) and the position of the plasmonic band (Λ_0). Therefore, we attempted to classify the films as a function of the silver content of the coated solution (2.5% or 25%). The classification task is performed for the thin and the thick films separately using support vector machines (SVM), as shown in the figure 5.17. SVMs are statistical classification algorithms used to find the best classifier (i.e. separator) between two sets of (eventually overlapping) data points [128]. The principle of this technique is to find the best classifier in order to separate two or more data sets. This is possible by finding a linear separator with the largest margins, which comes back to maximize the distance from the separator to the nearest data point on each side. For that reason, SVMs are also named “Large Margin Classifiers”. To this purpose, the algorithm defines support vectors that are selected data points, which allow calculating the optimum classifier. In the figure 5.17, these support vectors are represented by open symbols, the best classifiers are plain lines and the largest margins are dashed lines.

When the data are presented in the $\Gamma_0 - \Lambda_0$ plane, one can see that the set of data points corresponding to the highly doped films (circles) has only a slight overlap with the cloud of the films prepared from the 2.5% solution (triangles). To

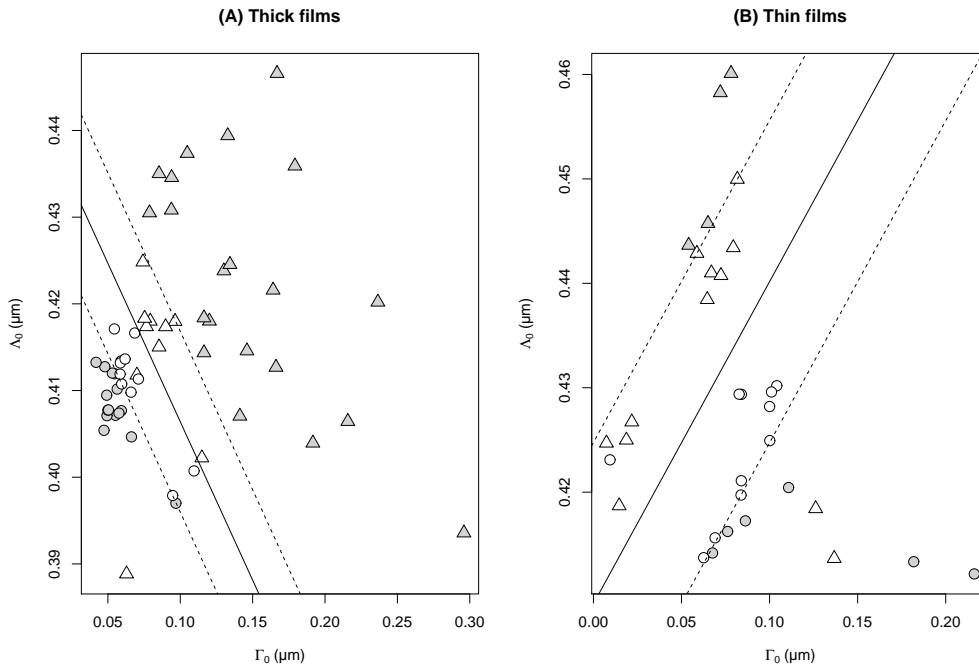


Figure 5.17: Classification of the weakly and highly Ag-doped film in the $\Gamma_0 - \Lambda_0$ plane. (A) Thick films (B) Thin films ([Ag]/[PVA] ratio: 25% (circles) and 2.5% (triangles); Open symbols: support vectors; Lines: optimum classifier (plain) and margin (dashed).

perform the classification task in a quantitative way, we used a SVM algorithm [129] derived from the original classification algorithm proposed by Vapnik [128]. In the case of overlapping data clouds, the classifier has to be tuned with respect to the penalty applied when an event is misclassified.

Optimum results for the classifiers are represented in the figure 5.17. The figure shows that, when applied to our data, SVMs discriminate between the high- and low-doping level films in a very efficient way: only 3 films over 33 are misclassified in the thin film case and 3 over 54 in the thick film one. The most striking feature of the classification is the behavior of the classifiers: when comparing panels (A) and (B) in Fig. 5.17, one can easily see that their slope have opposite signs. The classifiers slopes are respectively -0.36 (thick films) and $+0.30$ (thin films). The opposite sign in the slope of the separator confirm the difference in the optical behavior between thin and thick films in terms of position and width of the plasmonic band. According to this last analysis, we conclude that an experimental parameter, namely the thickness of the film, also controls on the resonance parameters.

5.6 Topographic surface characterization

After these previous multivariate analysis, we measure, at the nanoscale, the surface topography of the annealed film using an AFM in intermittent contact mode in order to get more information on the AgNPs embedded in the polymer matrix. The figure 5.18A and B represent the topography and phase images ($1 \mu\text{m} \times 1 \mu\text{m}$) of a

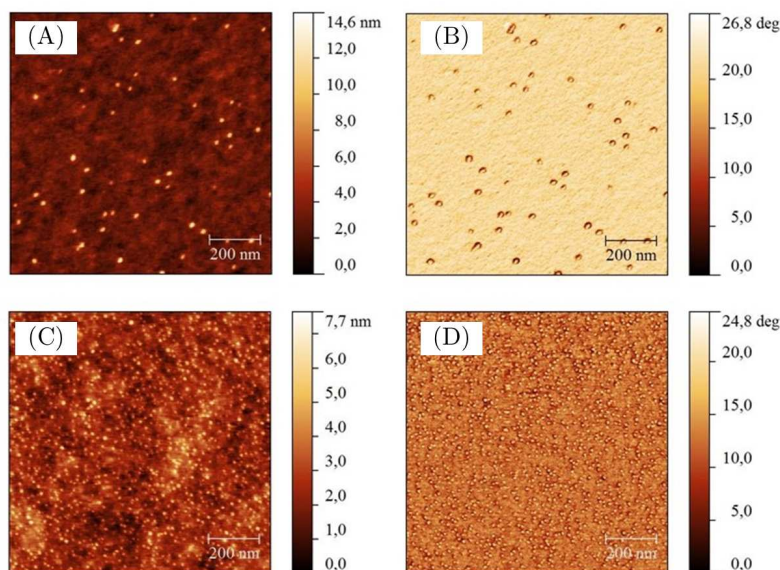


Figure 5.18: Topography (left) and phase (right) AFM images of Ag-PVA film doped with 25% AgNO_3 (w:w). (A, B) : $\simeq 30$ nm-thick film ; (C, D) : $\simeq 300$ nm-thick film. Image size: $1 \mu\text{m} \times 1 \mu\text{m}$ (256×256 pixels).

typical 30 nm-thick film. The mass ratio of $[\text{Ag}]/[\text{PVA}]$ is 25% (w:w). The nanoparticles of silver are clearly observed by a variation of the phase value (Fig. 5.18B), which provides a local information of the nature of the nanocomposite, and a local variation of the height. In the figure 5.18C and D, we represent the topography and the phase images corresponding to a 300 nm-thick film at the same $[\text{Ag}]/[\text{PVA}]$ mass ratio. Figure 5.19 presents the AFM images (topography and phase) of the control films, i.e the undoped PVA film. They do not show a structuration at the nanoscale. The height and the phase values are normally distributed. The surfaces are flat.

A first observation of these images of the figure 5.18 shows that the surface fraction occupied by the AgNPs embedded in thick films is higher than thin films. Due to the difference in polymer concentration between thick (8%) and thin (2%) films, it is easy to understand that there are less AgNPs embedded in thin films even if the $[\text{Ag}]/[\text{PVA}]$ mass ratio is kept constant. A second observation of these AFM images shows that the size of the particles is influenced by the thickness of the film even if the silver-to-polymer mass ratio is kept constant: the size of AgNPs embedded in thin films seems to be larger than in the thick films. By using a threshold technique, it is possible to have access to the average radius of the AgNPs in both case.

Figure 5.20 represents a boxplot of the radii r of the particles as determined from the AFM images. The radii are corrected for the embedding of the particles in the matrix following $r = (r_{eq}^2 + h^2) / (2h)$ where r_{eq} is the apparent radius of the particles and h the height emerging from the polymer matrix. The mean values are 8.2 ± 2.4 nm and 4.0 ± 2.5 nm for the 25 nm (tH) and 300 nm-thick (TH) films, respectively. The particles embedded at the surface of the thick sample are smaller than the particles in the thin one. Remember that previously we indirectly

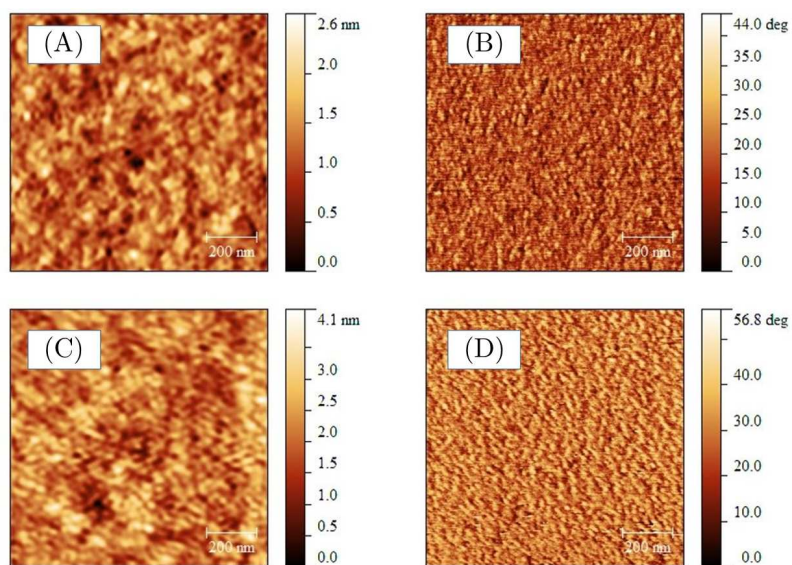


Figure 5.19: AFM topographic (left) and phase (right) images of the PVA control films. (A,B) 30 nm-thick films (C,D) 300 nm-thick films. Image size: $1 \mu\text{m} \times 1 \mu\text{m}$ (256×256 pixels).

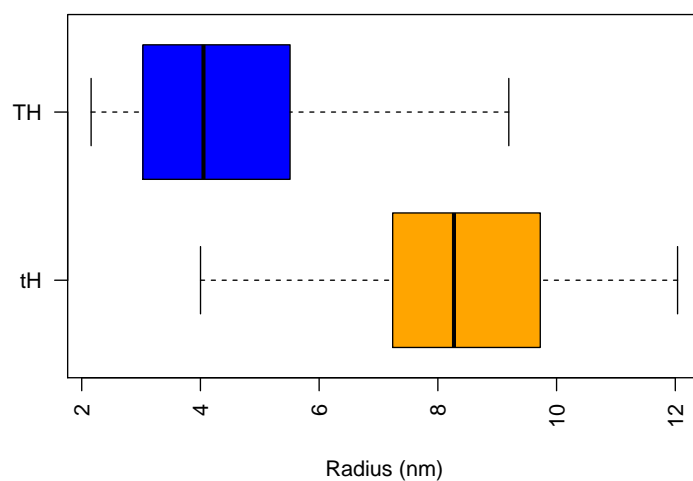


Figure 5.20: Box-and-whiskers plots of the radius of the particles ($[\text{Ag}]/[\text{PVA}]$ ratio: 25%; film thickness: 30 nm ('tH') and 300 nm ('TH')).

Table 5.6: Roughness parameters of the doped ($[\text{Ag}]/[\text{PVA}] = 25\%$) and undoped (pure PVA) films

	Thick film		Thin film	
	Doped	Undoped	Doped	Undoped
S_a (nm)	0.66	0.40	0.59	0.32
S_q (nm)	0.85	0.52	0.77	0.42

showed the particles size reduces with the film thickness, by relating the size with the position of the plasmon resonance. Here, we have experimental demonstrations that thickness induces variation on the resonance parameters. The size of the *in situ* synthesized AgNPs varies as a function of the thickness of the nanocomposite film confirming hypothesis formulated with the spectrophotometry analysis.

The roughness of doped and non-doped representative samples is characterized by the average surface roughness parameter (S_a) and by the root-mean-square surface roughness parameter (S_q) [130]. The measurements presented in the table 5.6, show a significant difference between doped and non-doped film in both cases (thick and thin films). As seen from both the S_a and the S_q surface roughness values, the growth of the nanoparticles induced by the annealing of the film controls the roughness of the surface, although this remains quite low (< 1 nm).

5.7 Conclusion

In summary, we have studied, in this part of the thesis, the surface topography and the optical properties of nanocomposite containing *in situ* grown silver nanoparticles, by means of AFM, spectrophotometry and SE techniques. In particular, we have focused on the influence of the thickness of the film and the silver concentration in the polymer matrix on the optical properties of the nanocomposite. We have experimentally observed a different behavior of the thick and thin films as a function of the silver concentration. Topography and phase images of thin and thick nanocomposites demonstrated that the size of the AgNPs seemed to be larger in thin films than in thick films. Moreover the statistical distribution of the plasmon resonance parameters (A , Λ_0 and Γ_0), obtained by spectroscopic ellipsometry, are analyzed using large margin classifiers. This multivariate analysis method leads to the conclusion that at a given Ag^+ doping level, thin and thick films behave differently.

These different optical behaviors are probably strongly related to the growth process of the NPs in films of different thicknesses. Since the pioneer work of Lamer and Dinegar [49], the kinetics of growth of nanoparticles in solution has been the subject of an increasing number of publications and reported mechanism has been partially transposed to explain the growth of NPs in films. For both types of system (films and solutions), one may expect the precursor solute to reach a critical level for nucleation. This prenucleation step is fed by the spatial distribution of the precursors (in our case, the Ag^+ ions), which we can consider to be isotropic within the film volume. As pointed out by Sugimoto [50], in films or sol-gel system,

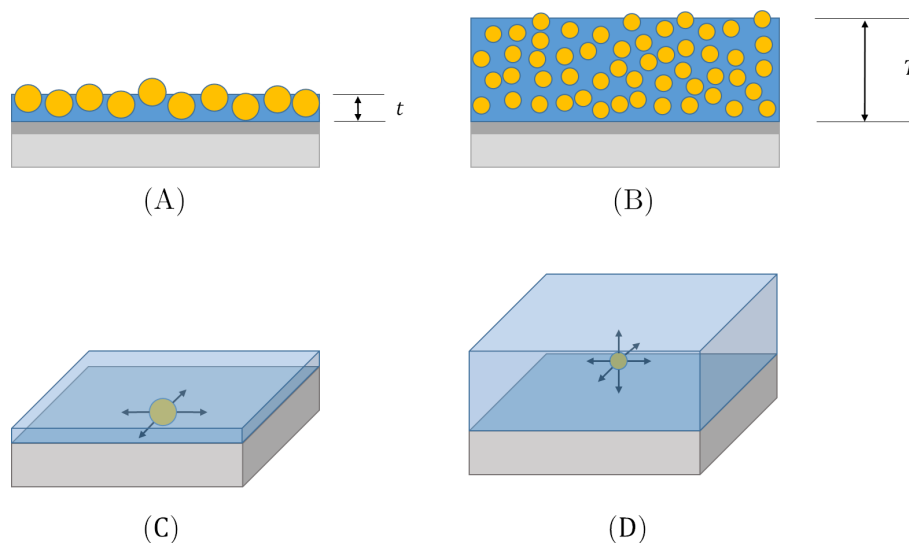


Figure 5.21: Scheme of the NPs growth in (A) thin and (B) Thick films. (C) and (D) represent the accessible dimensions for the diffusion process in thin (2D) and thick film (3D), respectively.

nucleation and growth of the generated nuclei are separated due to the reduction of the supersaturation with the stabilization of the matrix, in contrast to the Lamer mechanism. In our case, it seems that, after the nucleation, the growth process is limited by the diffusion of Ag^+ ions or of the Ag^0 atoms in the film. The shape of AgNPs are spherical in both case (i.e. thin and thick films) but their sizes are different as clearly demonstrated in Fig. 5.20. A possible explanation of the difference in the growth process can be associated to the diffusion process, as represented in the figure 5.21. In fact, in films whose thickness corresponds to a couple of NPs equilibrium diameter, NPs grown in a 2D-like matrix and the diffusion of silver ions or atoms is constrained in 2 dimensions by the substrate and the film/air interface (Fig. 5.21A and C). On the contrary, in thick films, the interfacial effect is expected to be less marked and the NPs rapidly form a 3D structure (Fig. 5.21B and D). This dimensional analysis constitutes a possible explanation for the discrepancy between thin and thick films, but the diffusion process of ions in thin solid films still an open question.

Gold nanoparticles embedded in PVA matrix

6.1 Introduction

Gold nanoparticles (AuNPs) are interesting nano-objects since their Localized Surface Plasmon Resonance (LSPR) is situated in the visible spectral range (near 530 nm). Moreover, AuNPs are usually used in numerous optical applications that require a dispersion of the nanoparticles in a dielectric matrix, as mentioned in the chapter 2. As previously explained, the most used synthesis method consists in a two step procedure: first, synthesis and the growth of the AuNPs in a colloidal solution and second their dispersion in a polymer or an inorganic film [38, 77]. As evidenced by Porel and co-workers [67], it is possible to prepare nanocomposites with *in situ* synthesized gold nanoparticles, as it is the case for the AgNPs. For AuNPs, the noble metal salt HAuCl_4 is directly mixed with the polymer solution (e.g. PVA), followed by a thermal annealing of the solid phase after spin coating of the solution on a solid substrate (glass or silicon). The gold cations Au^{3+} or the neutral atoms Au^0 can diffuse in the polymer due to a temperature of annealing higher than the glass transition temperature of the PVA ($T_g = 85^\circ\text{C}$ for bulk PVA) [55]. Despite the

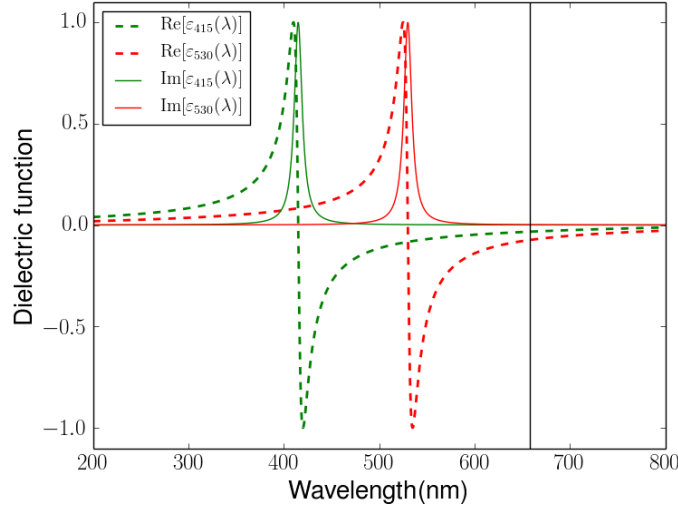


Figure 6.1: Representation of the real (dashed lines) and imaginary (plain lines) parts of theoretical complex dielectric functions. Green for AgNPs and red for AuNPs. Black line corresponds to the operating wavelength of the IE.

advantages of being simpler, faster and leading to a higher concentration of AuNPs than in colloidal solution [1], this approach is not often used.

Another reason to analyze this kind of nanocomposites is the opportunity of carrying out the single wavelength ellipsometer (IE) measurements slightly “off-resonance” ($\lambda_i = 658$ nm) with respect to the LSPR wavelength. The figure 6.1 represents theoretical calculations of the real and imaginary parts of the complex dielectric function in two different cases. In both case, the imaginary parts (plain lines in Fig. 6.1), which corresponds to $\varepsilon_2 = 2n\kappa$ (Eq. 3.9), show a sharp peak centered at 415 and 530 nm representing the effect of the LSPR of AgNPs (green) and AuNPs (red), respectively. As it is shown in the figure 6.1, the presence of the absorption peak in the imaginary part of the complex dielectric function induces a large oscillation in the real part of the dielectric function (dashed lines), i.e. $\varepsilon_1 = n^2 - \kappa^2$ (Eq. 3.8), because of the Kramers-Krönig consistency of the optical properties (Eq. 3.83). The operating wavelength of the IE is drawn in the figure 6.1 (black vertical line). As we can see, at 658 nm, the effect of the LSPR of AgNPs, located at 415 nm, on the refractive index is weak. Therefore, its detection by IE is not adapted. However, the operating wavelength of the IE is slightly closer for the LSPR of the AuNPs that can allow a detection of the variation of the real part of the dielectric function. The large variation in the refractive index induced by an absorption peak in the extinction coefficient has already been explained in the case of AgNPs in the section 5.5.

As we have just shown, IE is adapted to detect variations induced by the LSPR of AuNPs embedded in polymer matrix. In order to extract physical data of the IE measurements, we use the Maxwell-Garnett effective medium approximation (MG-EMA) to take into account of the optical properties of the polymer matrix and of the AuNPs. In this purpose, theoretical calculations are performed within the MG-EMA for spherical nanoparticles and are presented in the figure 6.2. On this

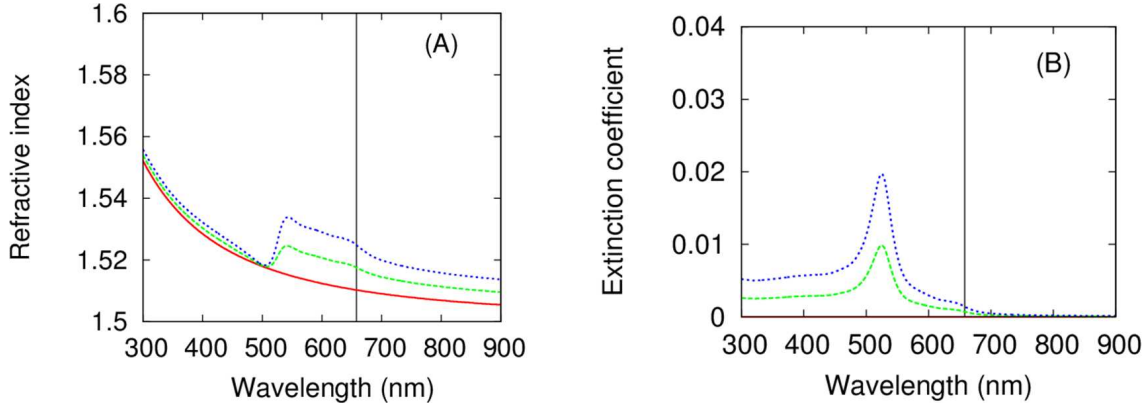


Figure 6.2: Theoretical calculations of the optical properties of Au-PVA nanocomposites using MG-EMA. (A) Refractive index, (B) extinction coefficient (Red plain line stands for pure PVA; dashed green line is the Au-PVA with a 0.15% Au volume fraction; dashed blue line is the same with volume fraction of 0.30%; vertical black line is the operating wavelength of the imaging ellipsometer).

graph, calculations are made for pure PVA (Cauchy model, section 5.2) in red, for volume fraction of gold equal to 0.15% in green and 0.30% in blue. As a reminder, the MG-EMA was developed for spherical particles completely encapsulated in an insulating matrix, supposing that their size is small compared to the wavelength of the incident light. It shows that at the operating wavelength of the ellipsometer (black vertical line) with a small doping level (in our case a volume fraction less than 0.3%), the variation of the refractive index can be detected by the IE due its large fluctuation in the visible range. The calculation of the dielectric function of the MG-EMA depends on the dielectric function of the insulating matrix, the dielectric function of the metallic nanoparticles and the volume fraction of metal in the polymer (Eq. 3.80). According to this theoretical analysis, the use of the single wavelength IE to study our AuNPs embedded in the PVA seems to be a valid option.

The experimental procedure to synthesize the AuNPs embedded in PVA matrix is explained in the section 4.2. As a reminder, a mass ratio of 2% of gold in polymer corresponding to a volume fraction $f_{Au} = 0.13\%$ in the dry film is chosen in this thesis. As we will discuss in this chapter, with this very small volume fraction some global experimental techniques such as spectroscopic ellipsometry (SE) and spectroscopic reflectometry (SR), lead to a non-detection of the LSPR of the AuNPs. In order to bypass this drawback, we adjust in the first series of experiments the mass ratio of gold in polymer (to 50%) to ensure the detection of the LSPR. The spin-coating conditions lead to a film thickness of approximatively 380 nm as determined by ellipsometry.

In the purpose of following the kinetics of growth of the AuNPs during the annealing, numerous samples are annealed with the THMS600 Linkam heating/cooling stage. This heating stage can be included in different experimental setups as the IE or the SR. In a typical annealing experiment, a temperature ramp of $10^\circ\text{C}/\text{min}$ starting at room temperature is applied. When the temperature reached 135°C , it is stabilized during 60, 90 or 120 minutes. Thermal fluctuations are less than 0.1°C .

As we can see, the temperature of annealing for AuNPs (135°C) is higher than the temperature applied of AgNPs (110°C). This difference can be explained by the different kinetics of growth between these two noble metals. The cations Ag^+ is easily promoted to his neutral state by one electron of the PVA. For the Au^{3+} , it seems that kinetics of growth is more complicated and needs more thermal energy to reduce the gold cations to neutral state. Typically, at 110°C, the growth of AuNPs can also be achieved but only after 20 hours. Comparing annealing conditions was not in the scope of this thesis.

In this chapter, we will first focus our study on the optical properties of the AuNPs embedded in PVA using spectrophotometry (Section 6.2). In a second time, we will study the surface topography of a thick annealed nanocomposite film to gather information of the AuNPs at nanoscale (Section 6.3). Finally, we will present the results obtained by IE on the kinetics of growth of the AuNPs embedded in the polymer matrix (Section 6.4). Indeed, the IE acquires images of the optical properties of the samples at the microscale. Following the evolution of the ellipsometric Ψ and Δ images, we will show the possibility to follow the variations of the optical properties of the nanocomposite at microscale. As it will be shown, this “off-resonance” analysis allows the detection of some heterogeneities on the sample during the annealing. These variations will be described by a simple model that we will discuss.

6.2 Spectrophotometry measurements of gold nanocomposites

In this section, we present the measurements obtained by UV-visible spectrophotometry. As already explained in the section 5.3, the absorption spectrum is appropriate for the study of the extinction of a light beam going through the AuNPs nanocomposite. In fact, the absorption spectrum allows to confirm the experimental process by measuring the LSPR of AuNPs and, moreover, it provides information on the *in situ* synthesized AuNPs. Finally, the real time variation of the absorbance will be shown in order to analyze the kinetics of growth of the AuNPs.

6.2.1 Absorption spectrum of highly doped films

In order to detect the LSPR of AuNPs, defined in the section 3.2.4, we perform a spectrophotometric measurement through a thick sample with a high doping level, i.e. 50% of gold in a 8% w:w PVA matrix. This absorption spectrum is shown in the figure 6.3 and reveals an absorption peak near $\lambda_{\text{LSPR}} = 530$ nm. The Fröhlich resonance condition for gold nanoparticles in PVA ($\epsilon_{\text{PVA}} = 2.18$) leads to $\epsilon_{\text{Au}} = -4.36$. The plot of the dielectric function of gold given by Johnson and Christy [86] confirms that this value of ϵ_{Au} corresponds to 530 nm. The inset shows the picture of the analyzed sample that was used for the spectrophotometry measurement, which is a high-doped sample (i.e. 50% [Au]/[PVA] mass ratio) in order to maximize the LSPR detection. The reddish color of the coated glass is the result of the absorption of the green part of the visible light causing a dip in the transmitted spectrum. It

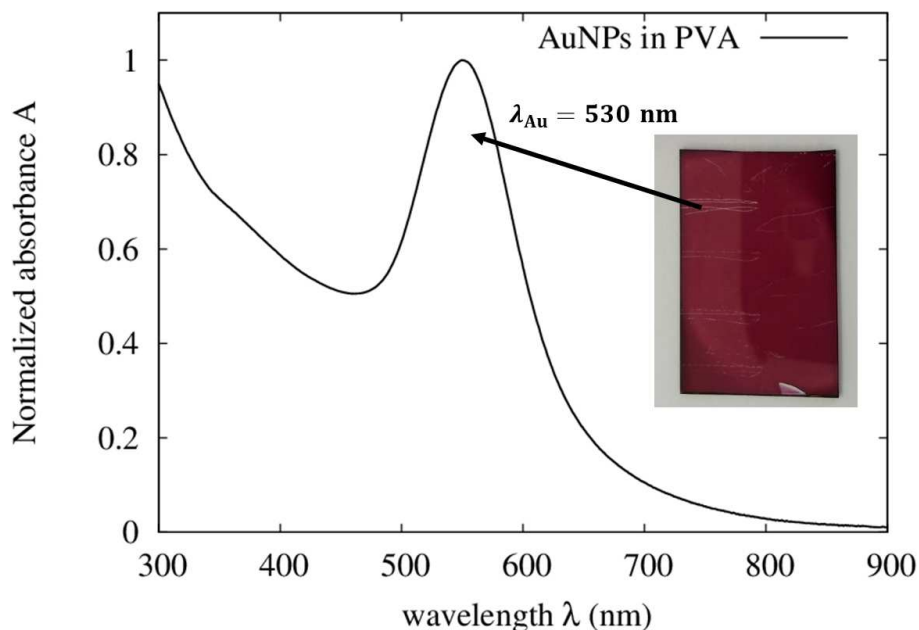


Figure 6.3: Absorption spectrum of a glass coated with AuNPs embedded in a PVA matrix. The inset represents a picture of the analyzed sample.

is the same explanation that we used for the yellow coloration of the Ag–PVA nanocomposite (Section 5.3.1).

With this absorption spectrum, we can make the same analyzes as in the silver nanocomposites case. Three parameters (the position, the width and the height of the resonance peak) are important and are good indicators of the optical response of AuNPs embedded in the polymer matrix:

- Via the Fröhlich equation, the position of the resonance peak is calculated from the dielectric function of the surrounding medium. Moreover, the position of the resonance is related to the size of the *in situ* synthesized AuNPs.
- The width of the peak resonance can be connected to the polydispersity of the AuNPs in the PVA matrix.
- Finally, the number of particles can be associated to the height of the absorbance peak.

The exact value of these parameters can be calculated by using Mie theory [11]. In the figure 6.3, the absorbance is normalized to equal 1 at the LSPR wavelength, improving the view of the LSPR.

After this first analysis that confirms the formation of AuNPs embedded in polymer matrix using the “one-pot” synthesis, we use the heating stage in order to study the absorption spectra of the AuNPs during the annealing of the sample.

6.2.2 Real-time absorption spectra of AuNPs in PVA matrix

With the same experimental setup as in the silver case and introduced in the section 5.3.2, we now study in real time the absorption spectra of the AuNPs during the annealing. The sample is installed on the heating stage that presents a small aperture in the heating block, so the light can reach the sample. The incident light comes from a fiber connected to the light source (Tungsten-halogen light source) and, behind the sample, the light is collected and guided towards the spectrometer (CCD spectrometer) with a second fiber.

The same procedure as the one for AgNPs is used in order to measure in real time the transmitted intensity. Python homemade routines record every 15 seconds the transmitted spectrum during 120 min, which corresponds to the total annealing time. Each spectrum is the result of an averaging process of 20 spectra taken every 10 ms. Thanks to the OSA software (Thorlabs), the recorded intensities are automatically transformed in 480 absorption spectra. Then, these spectra are analyzed by the SpectraGryph software.

As shown in the figure 6.4A, few minutes after the beginning of the annealing, an absorption peak near 530 nm appears: it can be associated to the growth of the AuNPs in the PVA film. In the figure 6.4B, the position of the resonance peak (λ_{LSPR}) as a function of the annealing time is plotted. The interpretation of the first part of the dynamics is tedious, since there is no absorption peak in the early stage of the experiment, and hence, no maximum of absorbance. However, after 20 minutes, the λ_{LSPR} slightly shifts as a function of the annealing time (t). The linear fit on the data for t between 20 and 120 min has the following equation: $\lambda(t) = (-0.0137 \pm 0.0023) t + (537.90 \pm 0.18)$. This negative slope means that the position of the resonance peak decreases during the annealing, a trend that is related to a small reduction of the size of the AuNPs in the polymer matrix [91].

In the figure 6.4C, the variation of the absorbance at λ_{LSPR} as a function of the annealing time is plotted. The first part, where the absorbance is null, corresponds to the beginning of the heating of the sample. Near ten minutes ($T \simeq 120^\circ\text{C}$), a large increase of the absorbance confirms the growth of the AuNPs in the polymer matrix. At this time, we can clearly see that the temperature of the nanocomposite has reached the glass transition temperature of the polymer ($T_g = 85^\circ\text{C}$) [55] (blue lines in the graph). The black dashed line corresponds to the temperature setup at the level of the heating stage. The last part of the graph shows a weak increase of the absorbance. The growth rate of the absorbance, which can be related to the increasing number of AuNPs in the polymer matrix, is given by the following equation: $A(t) = (2.577 \pm 0.033)10^{-4} t + (0.32424 \pm 0.00026)$ (with t corresponding to the time in minute). This rise of the absorbance is highlighted in the figure 6.4D, where the y -scale is rescaled to improve the analysis. In this graph, we can see two different increasing rates, a slow one before 90 min and a larger one after 90 min. These increasing rates are quantitatively expressed by:

- before 90 min: $(0.000132 \pm 0.000005) t + (0.33005 \pm 0.00027)$
- after 90 min: $(0.000323 \pm 0.000012) t + (0.318 \pm 0.0013)$

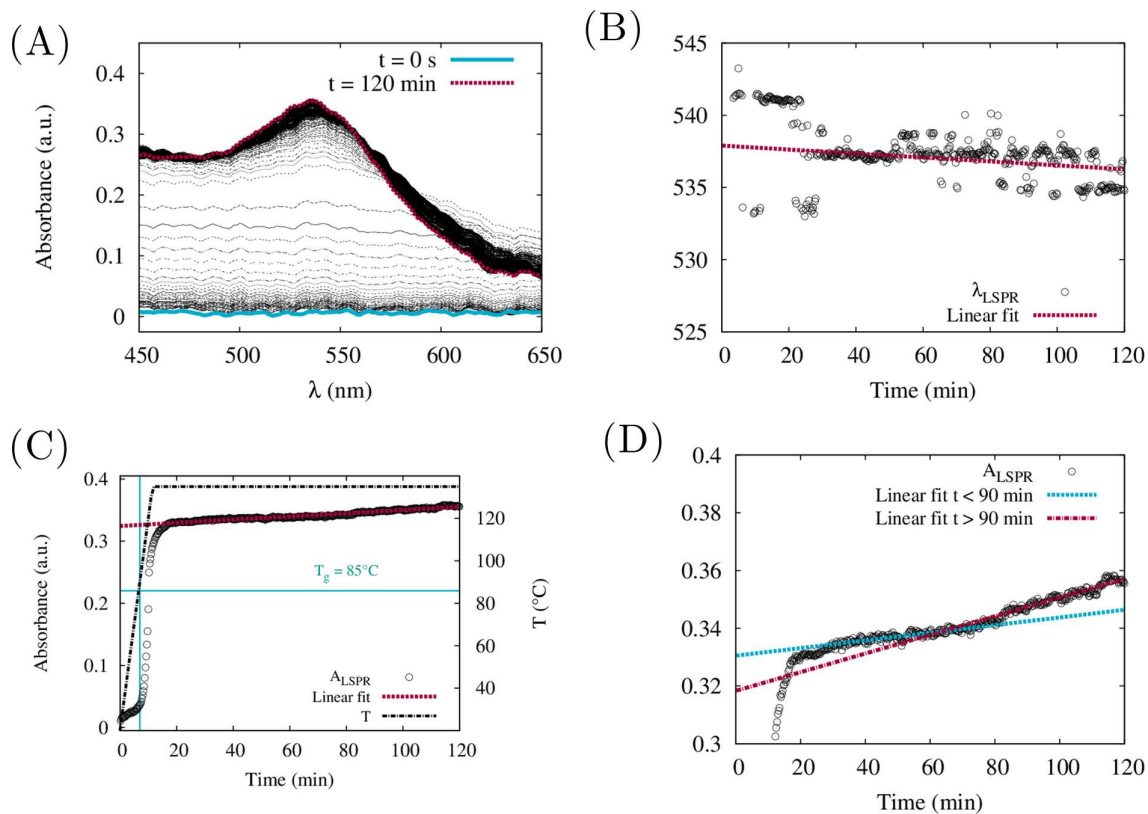


Figure 6.4: (A) Absorption spectra recorded during the annealing of a Au-PVA nanocomposite ([Au]/[PVA] = 20% w:w). (B) Variation of the λ_{LSPR} during the annealing time; open circles are the experimental data; dashed line is the linear fit on data after 20 min: $\lambda_{\text{LSPR}}(t) = (-0.0137 \pm 0.0023) t + (537.90 \pm 0.18)$. (C) Variation of the absorbance at the λ_{LSPR} as a function of time; open circles are experimental points; dashed line is the linear fit on data after 20 min: $A_{\text{LSPR}}(t) = (2.577 \pm 0.033)10^{-4} t + (0.32424 \pm 0.00026)$. The horizontal blue line is the glass transition temperature T_g and the vertical blue line shows the time when the temperature of the sample reaches T_g . (D) Variation of the absorbance at the λ_{LSPR} as a function of time in a limited range in order to detect two different increase rates; open circles are experimental points; dashed lines are the linear fit [blue fit on data before 90 min: $A_{\text{LSPR}}(t) = (0.000132 \pm 0.000005) t + (0.33005 \pm 0.00027)$; red fit on data after 90 min: $A_{\text{LSPR}}(t) = (0.000323 \pm 0.000012) t + (0.318 \pm 0.0013)$].

As we can see, the increasing rate after 90 min is 2.5 times higher than the one before 90 min. The rise of absorbance can be interpreted by an increasing number of AuNPs inside the polymer matrix. It seems that, after 90 min of annealing, the growing process changes and the number of *in situ* synthesized AuNPs raises faster.

These first analyzes of a highly doped gold nanocomposite confirm the growth of the AuNPs in the polymer matrix by the simplest “one-pot” synthesis method as already demonstrated by Porel and coworkers [67]. By using spectrophotometric measurements during the annealing, we provide some additional information on the kinetics of growth of the AuNPs:

- After a first period of heat, the resonance peak appears, i.e. the value of absorbance increases. That is attributed to the growth of the AuNPs inside the polymer.
- Remembering that the position of the λ_{LSPR} is related to the size of the nanoparticles using the Mie theory [91], another conclusion is the weak variation of the position of the resonance peak during the annealing that can be attributed to a slight decrease of the size of the AuNPs. In comparison with the growth of AgNPs (Fig. 5.7D in section 5.3.2), the size of the synthesized AuNPs seems to decrease during the annealing, while the size of the AgNPs increases during the annealing.
- Finally, the variation of the absorbance at λ_{LSPR} as a function of the annealing time shows two different behaviors. After 90 min, the variation rate is 2.5 times higher than the variation rate before 90 min. It seems that the number of AuNPs inside the polymer matrix rises faster after 90 min.

After this spectrophotometry analysis, we will use AFM to gather information on the topography of the surface of the Au-PVA nanocomposite at the nanoscale. Then, by using the IE, we will record the changes on the optical properties induced by the annealing of low-doped nanocomposites. As it will be shown, despite the weak volume fraction of gold in the PVA matrix, we are able to detect variations of the optical properties.

6.3 Topographic surface characterization

In order to get more information on the AuNPs embedded in the polymer matrix, we measure, at the nanoscale, the surface topography of a thick annealed film using an AFM in intermittent contact mode. A typical image at $5 \mu\text{m} \times 5 \mu\text{m}$ resolution is presented in the figure 6.5A. A detailed image ($1 \mu\text{m} \times 1 \mu\text{m}$) of the topography is given in the figure 6.5B. It unambiguously shows the presence of the AuNPs. The topography of the samples is characterized by the average surface roughness parameter (S_a) and by the root-mean-square surface roughness parameter (S_q) [130]. For the annealed sample, S_a and S_q were $S_a = 6.28 \text{ nm}$ and $S_q = 8.22 \text{ nm}$, respectively. These structural features do not appear on undoped films (Fig. 6.5C). As typical roughness parameters for pure PVA films of corresponding thickness are $S_a = 0.42 \text{ nm}$ and $S_q = 0.53 \text{ nm}$, respectively (i.e. 10 to 12 times less), it is clear that the

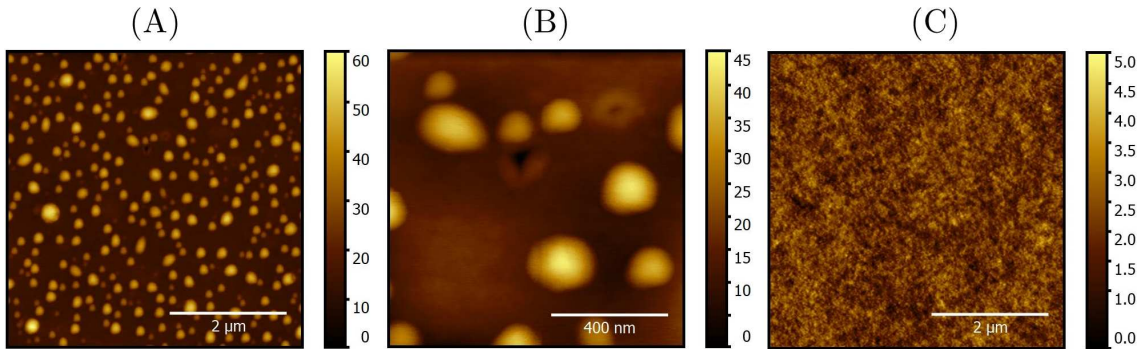


Figure 6.5: AFM topography images (Color scale-bars in nm). (A) PVA matrix with embedded *in situ* synthesized AuNPs (image size: $5 \mu\text{m} \times 5 \mu\text{m}$). (B) Details of the previous image (image size: $1 \mu\text{m} \times 1 \mu\text{m}$). (C) Undoped PVA matrix (image size: $5 \mu\text{m} \times 5 \mu\text{m}$).

annealing process induces roughness at the air/polymer interface, which can be attributed to the *in situ* synthesis of the AuNPs. At the end of annealing, we detect the laser spot on the sample, which was not visible at the beginning of the experiment. In order to have measurement of this scattering process, we measure the bidirectional reflectance distribution function of our samples before annealing and after annealing. It is clear that the annealing process induces back-reflection over a large area with also strong forward scattering out of the incidence plane [1].

As we can see, the size of the AuNPs seems larger than in the AgNPs case (Fig. 5.18). Although numerous particles have a diameter smaller than 50 nm, the diameter of some particles seems to be in the order of 200 nm. In the present case, we cannot assume anymore that the extinction of the light is solely due to the absorption by the particles, i.e. $\sigma_{\text{ext}} \approx \sigma_{\text{abs}}$ is not valid anymore. We should therefore take into account the scattering due to the larger particles embedded in the PVA matrix and, thus, $\sigma_{\text{ext}} = \sigma_{\text{abs}} + \sigma_{\text{scatt}}$. However, by looking at the shape of the absorbance spectrum presented in the figure 6.3, we do not see the scattering contribution for those particles. This scattering contribution generally appears in the absorption spectrum as a second weak peak located in larger wavelengths than the wavelength of the extinction peak of the absorption spectrum [41]. We can consequently assume that the number of large particle seems to be small and has few impact on the absorption spectra, which is dominated by the small particles.

In the detailed figure 6.5B, we observe, besides spherical NPs, AuNPs with nearly triangular or hexagonal shapes. Similar morphological characteristics were also usually observed at a larger scale by optical microscopy and scanning electron microscopy (SEM) [67, 131]. Recently, the shape of the AuNPs was shown to be also dependent on chemical nature of the counterions in the gold salt [79]. Using a threshold method, nanoparticles can be isolated from the polymer matrix image and their shape/size characteristics can be determined. In the present samples, shape starts deviating for the circular shape for which the perimeter/area relationship is given by $P = 2\pi^{1/2}A^{1/2} \simeq 3.55A^{1/2}$ where P is the perimeter of the nanoparticle and A its projected area (Fig. 6.6). Deviation from the later relation reveals the presence of more complex nanoscale structures, i.e. triangular and hexagonal shapes.

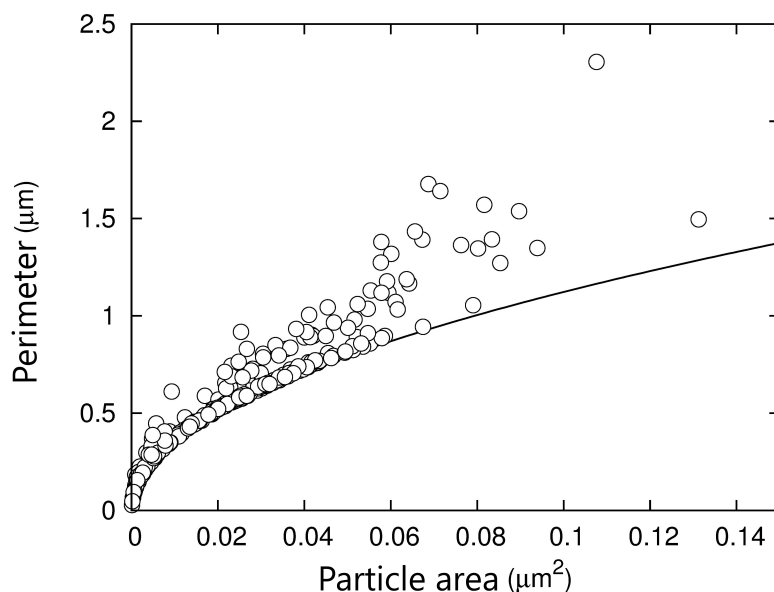


Figure 6.6: Perimeter-Area relationship of the AuNPs. Symbols: experimental data determined by height threshold method. Line: theoretical relationship ($P = 2\pi^{1/2}A^{1/2}$) between perimeter P and area A for circular AuNPs.

To conclude this section, we see that, despite the same experimental procedure to synthesize the NPs inside the polymer matrix, AuNPs are larger than AgNPs. This difference can be explained by the higher temperature used to form Au-PVA nanocomposites than the temperature of Ag-PVA nanocomposite [69]. Another difference is the shape of the AuNPs that seems on average spherical but could exhibit some deviation, as some triangular and hexagonal particles are observed (Fig. 6.5). As a reminder, the shape of the AgNPs seems to be spherical in the AFM images (Fig. 5.18). Concerning the ellipsometric measurements of weakly doped Au-PVA nanocomposites performed in next sections, we will assume that the shape of the AuNPs are spherical in order to use the MG-EMA, which supposes spherical particles.

The experimental procedure followed for the synthesis of Au-PVA nanocomposite is confirmed by the spectrophotometry measurements and the analysis at the nanoscale. In order to get more information on the optical properties of the sample during the annealing process, we use IE in the next section. It probes the sample at the microscale. By taking ellipsometric images of the samples during the annealing, we present the local modification of the optical properties induced by the growing process.

6.4 Annealing and local optical properties

Imaging ellipsometry measurements of the ellipsometric angles Ψ and Δ are performed with an EP3 nulling ellipsometer (Accurion GmbH) at $\lambda = 658$ nm. As explained in the section 4.1.4, the optical configuration for a nulling ellipsometer cor-

responds to a polarizer-compensator-sample-analyzer (PCSA) usually called “PCSA ellipsometer”. The combination of a polarizer and a compensator in the incident arm allows polarising elliptically the incident beam, such that the reflected beam is perfectly linearly polarized. By using, in the detector arm, an analyzer set to 90° position with respect to the axis of the reflected linear polarization, it is possible to extinguish the beam, which corresponding to the “nulling” conditions (Fig. 4.4). Let us note that the spectroscopic imaging ellipsometer (SIE), employed in the chapter 7, corresponds to the same experimental setup except for the light source, which is different. In the case of the IE, the light source is a laser diode with an operating wavelength $\lambda_i = 658$ nm. The light source for the SIE is a Xenon flash lamp and the requested wavelength is selected by a filter wheel (44 filters) that allows spectroscopic measurements in the visible range (360 – 1000 nm).

One of the advantages of using IE or SIE with respect to conventional SE is the possibility to acquire images of the optical response of the sample. In order to obtain a map of the optical properties of the sample, a microscope objective is placed before the analyzer. Furthermore, the detector located after the analyzer is a spatially resolved detector (a CCD camera, in our case). Thus, different zones with different optical properties cause a different signal at the CCD sensor level. It means that different areas can fulfil different nulling conditions, i.e. different areas can have different settings of polarizer, compensator and analyzer to extinguish the beam. The main advantage of using an IE or a SIE is that the received signal is not averaged over the entire laser spot section as it is for the conventional ellipsometry. The optical response is spatially resolved, which allows revealing the details of the sample at microscale. Two ellipsometric maps, Ψ and Δ maps, are usually recorded per wavelength. In the purpose of following the kinetics of growth of the AuNPs at the microscale, these Ψ and Δ maps can be recorded during the annealing of the sample. As these maps contain the optical properties of the probed sample, we are able to follow the changes of the optical response during the annealing and to extract from that response local information on the NPs growth.

Let us remember that IE provides local information about the optical properties of a (multilayered) material (Section 4.1.4). The information is given by the Ψ and Δ ellipsometric angles, which are related to the ellipticity ρ defined as the ratio of the p - to s -polarisation reflection coefficients:

$$\rho = \frac{r_p}{r_s} = \tan(\Psi) e^{i\Delta} \quad (6.1)$$

In PCSA imaging ellipsometer, the polarizer angle (P) and the analyzer angle (A) are varied in order to achieve extinction of the signal. P and A are the angle of the polarizer and analyzer, respectively, and are taken with respect to the incident plane. With a compensator angle (C) set to 45 degrees with respect to the incident plane, the angles P_{\min} and A_{\min} , at which the extinction is observed, are directly related to the Ψ and Δ ellipsometric angles by [99]:

$$\Delta = 90^\circ - 2P_{\min} \quad \text{and} \quad \Psi = -A_{\min} \quad (6.2)$$

Following this reminder of the IE principles and its advantages, we will present the time evolution of the Ψ and Δ maps recorded during the annealing of low doped

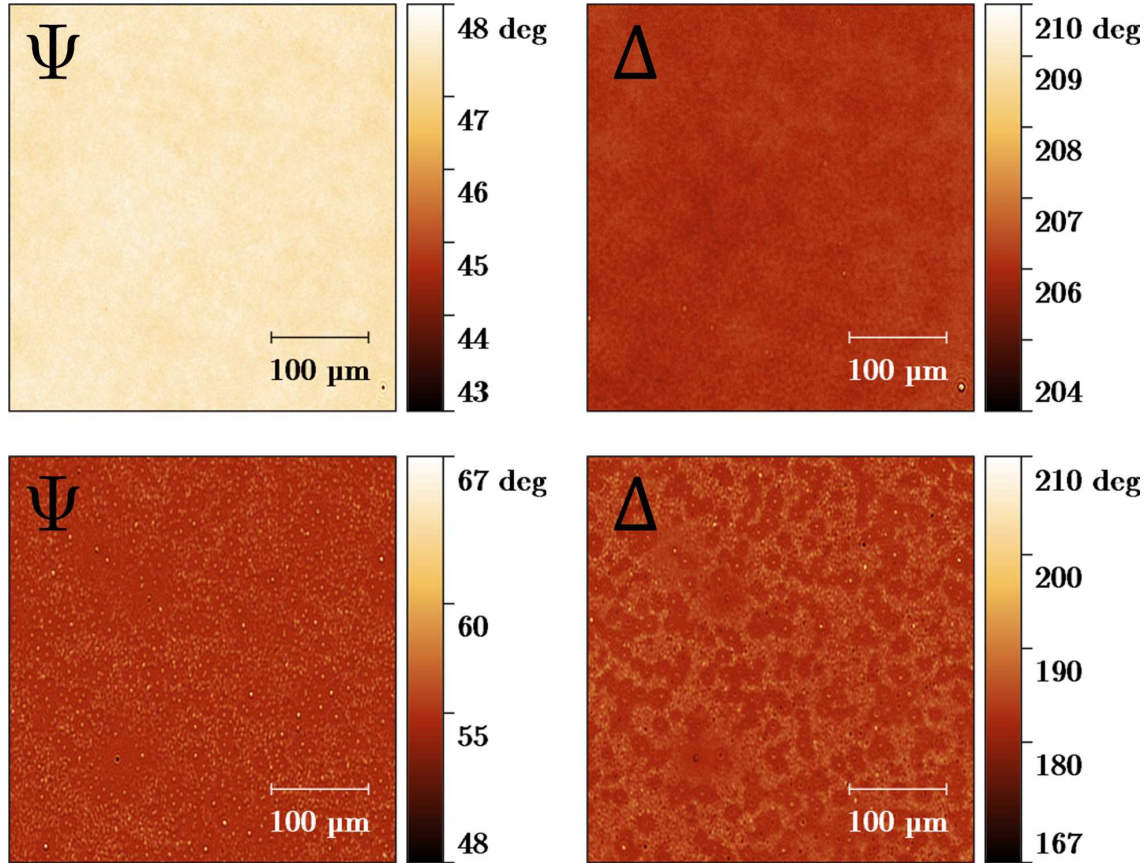


Figure 6.7: Ellipsometric Ψ and Δ angles maps of Au-doped PVA films. (Top) Before annealing. (Bottom) After annealing (135°C, 120 min). (Left) Ψ angle. (Right) Δ angle. (Image size: 450 μm \times 380 μm).

gold nanocomposite. We will show that despite the weakly doping level, the IE allows the detection of inhomogeneities on the sample. Afterwards, by using the statistical distribution of each Ψ and Δ recorded maps, we will study, in the section 6.4.2, the variation of the mean value of the statistical distribution and its standard deviations as a function of the annealing time. Then, we will present an unusual graph that gathers the mean values of the statistical distribution of Ψ and Δ maps, which are superimposed on theoretical curves of constant angle of incidence (CAI) in order to extract physical data (Section 6.4.3). As a result of this, the kinetics of growth can be decomposed in two regimes: a decrease of the film thickness followed by an increase of the refractive index.

6.4.1 Time evolution of Ψ and Δ mappings

The IE optical response of Au-doped PVA films ($[\text{Au}]/[\text{PVA}] = 2\%$ w:w) is recorded during the annealing. At the beginning of the experiment, the temperature is around 20°C (room temperature). The temperature is raised up to 135°C at a rate of 10°C/min. Figure 6.7 shows maps of the ellipsometric angles Ψ and Δ recorded at the beginning and at the end of the growth kinetics on a 365 nm-thick film. In order to maximize the contrast of the images, the angle ranges are different from one image

to the others. More Ψ and Δ maps corresponding to intermediate times are given in the figures 6.8 and 6.9. Before the annealing, the sample is clearly homogeneous (Fig. 6.7, top images). After 120 min at 135°C (Fig. 6.7, bottom images), spots can be observed in the Ψ and Δ images. They are suspected to be the manifestation of light intensity diffraction patterns from the AuNPs despite the low volume fraction of gold in our samples ($f_{\text{Au}} < 0.2\%$).

The bottom images of the figure 6.7 clearly show that different zones surrounding the NPs are present in the Δ image. They also appear, but in a less obvious manner, in the Ψ image. This supports the hypothesis of metallic NPs growth, whose primary effect is the local modification of the relative phase between the p and the s components of the impinging light, i.e. of the Δ ellipsometric angle. Under our experimental conditions, it appears that Δ is more sensitive to the local optical response when it remains low to moderate. Indeed, Ψ is closely related to the intensity changes of the reflected light, as measured in a conventional transmission or reflection UV-visible spectrophotometry with polarized light.

The growth of the AuNPs requires the diffusion of cations or metal atoms in the interlaced network of the polymer chains. This diffusion is facilitated by the annealing of the samples above T_g and it seems that the larger NPs (i.e. only those whose effect can be detected in the optical response) are built by some kind of drainage of the metal atoms in their neighborhood, leaving a depletion zone around the NPs.

As the IE is based on a nulling procedure, it does not provide a direct information about the depolarization of the sample. Nevertheless, as the signal can almost be extinguished on the whole images during the “nulling” procedure, the depolarization effect has to be negligible. Moreover, as mentioned before, the surface roughness is quite small ($S_a = 6.28$ nm and $S_q = 8.22$ nm) and we may therefore expect the effect of depolarization to be negligible. As shown by Fujiwara *et al* [82], AFM and ellipsometry measurements show the same trends when measuring the thickness of the roughness layer and the AFM roughness of thin films, although quantitative modeling is far more complex and requires e.g. the correlation length of the surface to be taken into account [132]. So, the changes in Ψ and Δ are most likely due to the growth of the AuNPs, which locally change the optical response of the film.

Other causes of the local changes of the optical response like temperature-induced thickness changes and refractive index of the substrate changes, can also be discarded. Indeed, the thermal expansion coefficient of the silicon oxide ($0.24 \times 10^{-6} K^{-1}$) and its thermo-optic coefficient dn/dT ($1.29 \times 10^{-5} K^{-1}$) [133, 134] lead to statistically insignificant effects on the optical response, while increasing the sample temperature from room temperature to 135°C. A similar behavior is expected for the polymer matrix: around $10^{-4} K^{-1}$ for the linear thermal expansion coefficient and a negative value around $-10^{-4} K^{-1}$ for dn/dT [135].

As previously expressed, the figures 6.8 and 6.9 show Ψ and Δ extra maps recorded during the annealing of the Au-PVA nanocomposite. Annealing time increases from left to right and from top to bottom: $t = 0, 15, 30, 45, 60, 75, 90, 105, 120$ min. As we can see, the Ψ and Δ maps are homogeneous at the beginning of the experiment. After 60 min, some spots can be observed and the number of these spots increases as a function of the annealing time. The last three images of each sequence

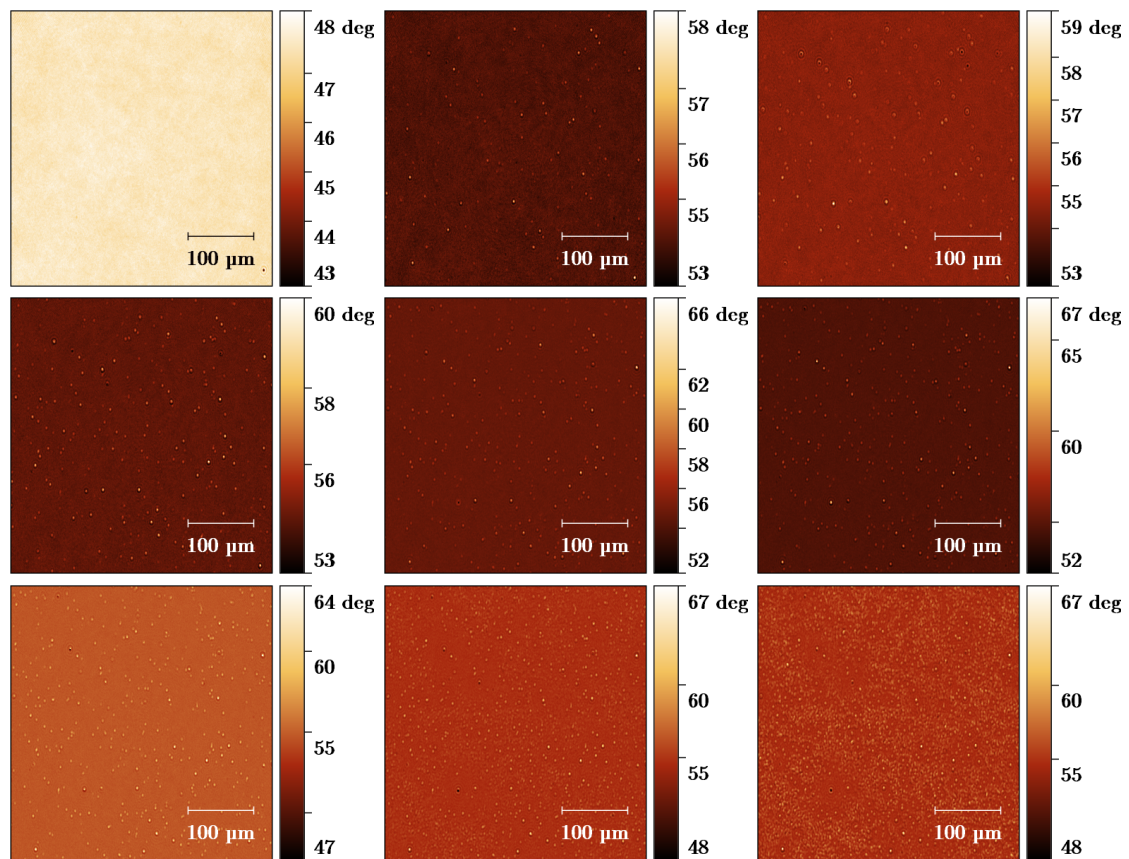


Figure 6.8: Ψ maps of Au-doped PVA films (image size: $450 \mu\text{m} \times 380 \mu\text{m}$). Annealing time increases from left to right and from top to bottom: $t = 0, 15, 30, 45, 60, 75, 90, 105, 120$ min. Temperature is maintained at 135°C , except for the first image for which $T = 31^\circ\text{C}$.

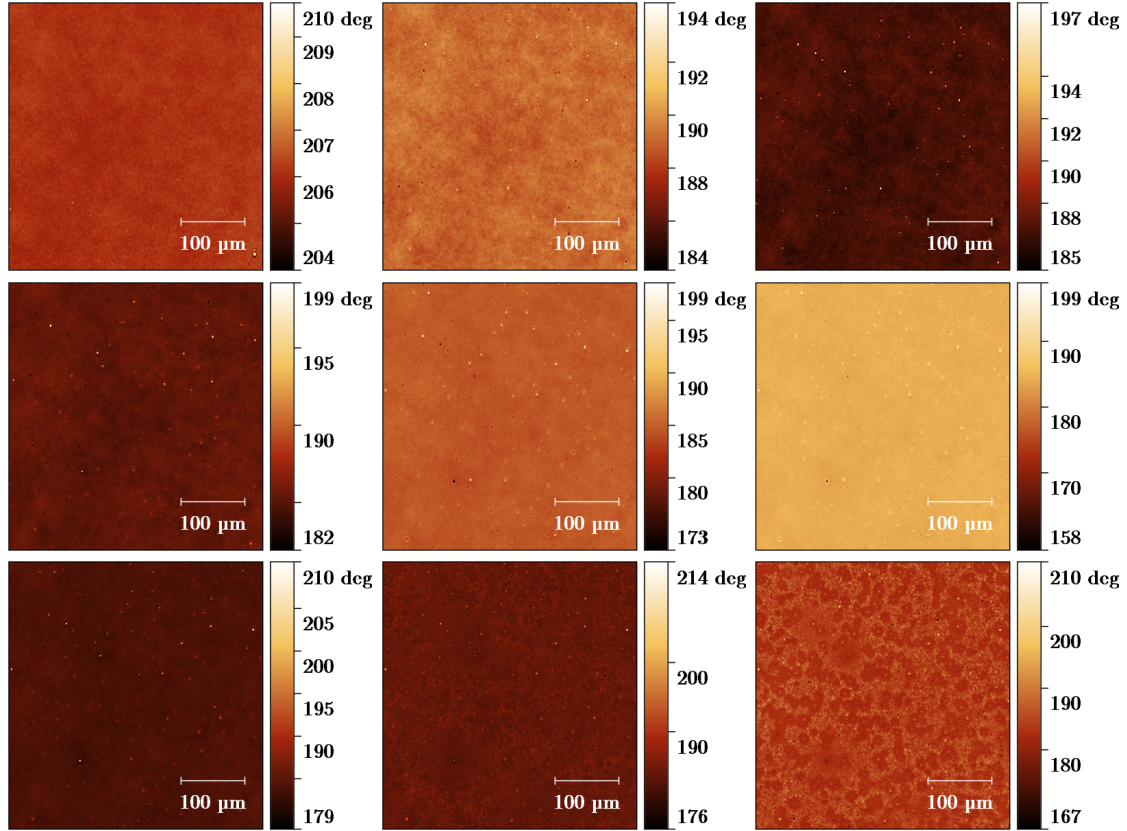


Figure 6.9: Δ maps of Au-doped PVA films (image size: $450 \mu\text{m} \times 380 \mu\text{m}$). Annealing time increases from left to right and from top to bottom: $t = 0, 15, 30, 45, 60, 75, 90, 105, 120$ min. Temperature is maintained at 135°C , except for the first image for which $T = 31^\circ\text{C}$.

shows large variations of the recorded ellipsometric angles at the microscale. These sequences suggest that the growing process has two parts: a first part with a weak variation of the optical properties followed by a second part that presents a larger modification on the optical properties after 90 min of annealing.

We also have recorded the Ψ and Δ maps of undoped PVA films presented in the figure 6.10. These ellipsometric maps do not show a structuration at the microscale at the end of the annealing as the gold nanocomposite films. These maps stay homogeneous during the annealing and the variations on the ellipsometric angles is due to the variation of the thickness of the film. This variation of thickness during the annealing will be shown in the section 6.4.3. This last analysis reveals, once again, that the variations detected on the ellipsometric maps during the annealing of gold nanocomposite films are due to the growth of the AuNPs inside the polymer matrix.

Summing up, the ellipsometric maps recorded during the annealing reveal the presence of spots that are suspected to be the manifestation of light intensity diffraction patterns from the AuNPs despite the low volume fraction of gold in our samples ($f_{Au} < 0.2\%$). As it will be shown in the next section, from these maps we calculate the statistical distribution of ellipsometric maps during the annealing in order to record quantitatively the modification of the optical properties of the sample.

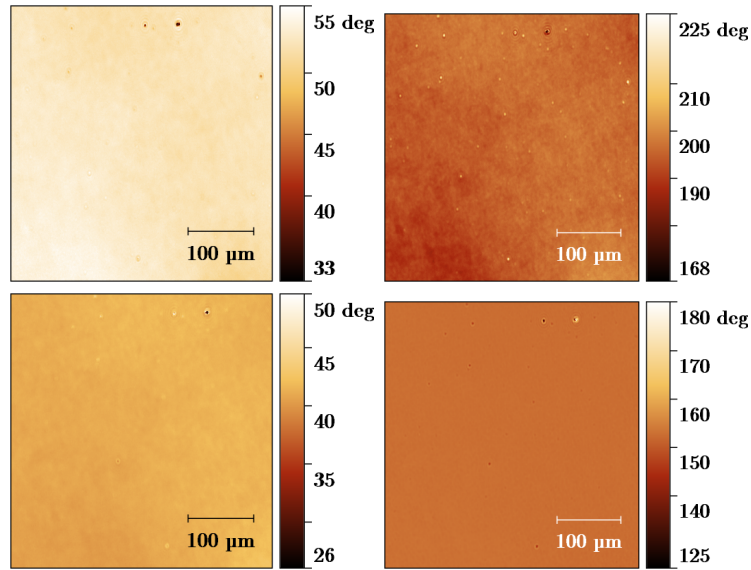


Figure 6.10: Ellipsometric Ψ and Δ angles maps of undoped PVA films. (Top) Before annealing. (Bottom) After annealing (135°C, 60 min). (Left) Ψ angle. (Right) Δ angle.

6.4.2 Statistical analysis of Ψ and Δ maps

When operated in the mapping mode, the IE allows us to perform statistics on the Ψ and Δ values of the sample over a large number of data (typically ca. 120×10^3) and therefore, it gives access to statistical distributions of the ellipsometric angle values. The analysis of these statistical distributions obtained from the ellipsometric maps recorded during the annealing is presented in this section.

We show in the figure 6.11 that, during the annealing, the statistical distribution shifts and the shape of the distribution starts to be asymmetric during the annealing and presents a tail. This asymmetry can be interpreted as the contribution of the growth of the AuNPs and is related to the increase of the standard deviations of the statistical distribution. By calculating the statistical distribution of each ellipsometric maps during the annealing, we are able to follow the variation of the mean value and the standard deviation of the statistical distribution, as it will be shown shortly.

In the figure 6.11, statistical distribution of the Ψ ellipsometric angles as a function of the annealing time are studied for the sample corresponding to the ellipsometric maps previously presented. Initially, the values follow a symmetric distribution around $\bar{m}_\Psi = 47.52$ degrees with standard deviation $\sigma_\Psi \simeq 0.16$ degrees (Fig. 6.11, left panel). During the annealing, the distribution shifts towards higher values while its shape starts showing an increasing tail on the right, which is attributed to the growth of the AuNPs (Fig. 6.11, right panel). At the end of the annealing, the mean values of the statistical distribution is $\bar{m}_\Psi = 54.96$ degrees and its standard deviation $\sigma_\Psi \simeq 0.74$ degrees (black curves in Fig. 6.11, right panel). As a consequence of the broadening, the height of the peak strongly decreases. Same results are obtained for the Δ angle (data not shown).

We can see that on spatially uniform and homogeneous samples (i.e. in the absence of thickness gradients or of materials change): it appears that these statistical

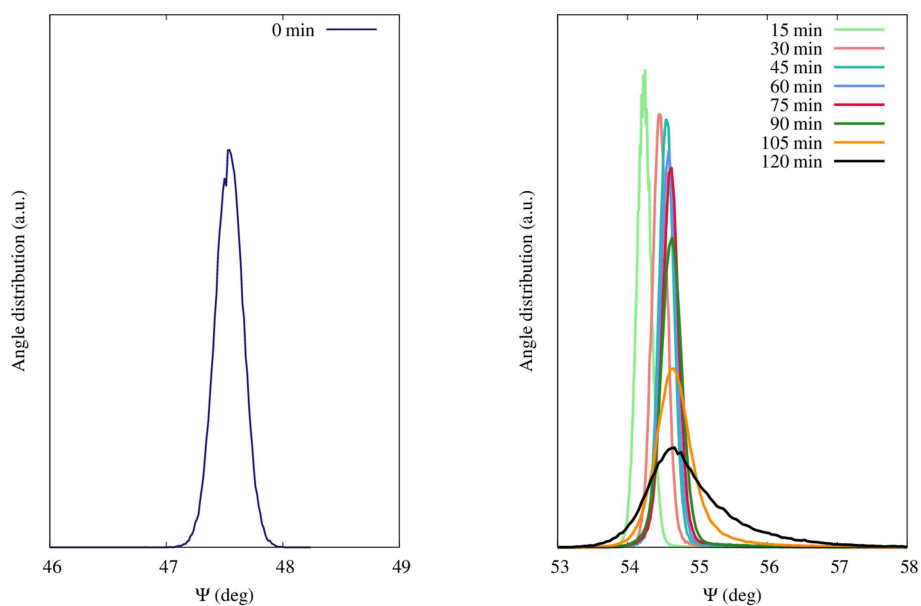


Figure 6.11: Statistical distributions of the Ψ angles. (Left) Before annealing. (Right) As function of annealing time. $[\text{Au}]/[\text{PVA}] = 2\%$ mass ratio, temperature of annealing 135°C during 120 min.

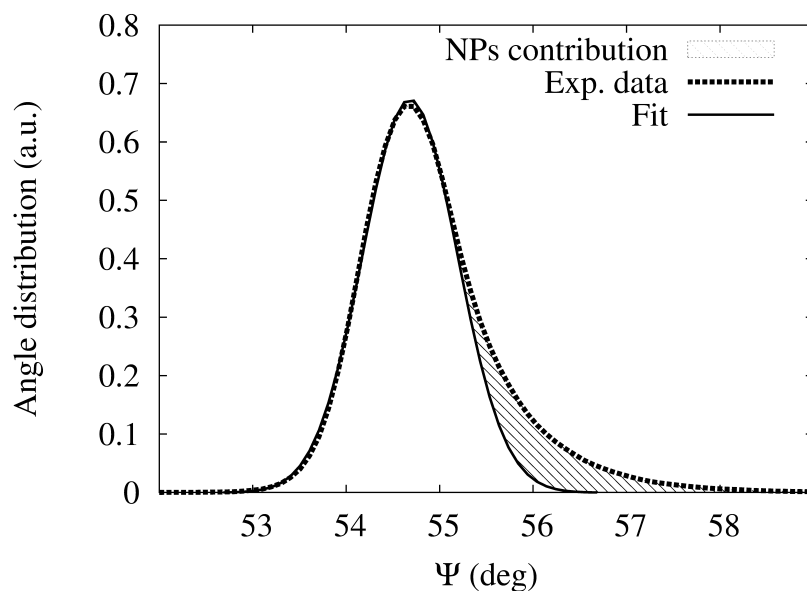


Figure 6.12: Statistical distribution of the Ψ angles after annealing ($t = 120$ min). Dashed line: experimental data; solid line: Gaussian fit using the left-most part of the data; Shaded area: contribution of the AuNPs.

distributions are Gaussian due to the measurement process. That is shown in the figure 6.11 (left panel) for the nanocomposite before annealing. On non-ideal samples, the width of the Gaussian depends on its surface state (including its roughness) and on the size of the region-of-interest over which the measurement is carried out. The smaller the region, the smaller the width of the statistical distribution. In conventional ellipsometric experiments, these local statistical fluctuations are averaged over the spot size. From a practical point of view, any deviation from this Gaussian statistical distribution of Ψ and Δ values is therefore a clue of some inhomogeneity (either structural or optical) of the sample.

As we have just discussed, the statistical distribution of Ψ , which is symmetric at the beginning of the annealing ($t = 0, 5, 10$ min), clearly becomes asymmetric as the annealing proceeds with a marked contribution of the AuNPs to the response at higher Ψ values. This is illustrated in the figure 6.12 at the end of the annealing ($t = 120$ min), where the Ψ experimental distribution is compared to a Gaussian fit performed on the lower experimental Ψ values. The deviation from the Gaussian fit corresponds to the contributions of the AuNPs growth and is represented by the shaded area.

By this last figure, we can see that the contribution of the AuNPs modifies the shape of the statistical distribution. This modification leads to an increase of the standard deviation. By plotting the variation of the mean value and the standard deviation of each maps as a function of the annealing time, we can detect the moment corresponding to the variation of these parameters.

Time evolution of the mean value of the ellipsometric maps

The mean values of Ψ and Δ maps as a function of time are reported in the figure 6.13. The behavior of the sample is complex during the first 10 minutes of the annealing. During that period, temperature rises from room temperature to 135°C at a rate of $10^\circ\text{C}/\text{min}$. We expect that the mechanical constraints induced by the spin coating relax as soon as the sample temperature reaches T_g , the glass transition temperature of the polymer. For bulk PVA, T_g equals 85°C [55]. As already reported for other polymers, T_g is also a function of the film thickness and differs from the bulk T_g (see e.g. Clémenson *et al* [69]). It can also be modified by doping. Since the pioneered work of Keddie and coworkers [136], it is well known that the ellipsometric response of films is modified when going through the glass transition. After this initial period (zone (a) in Fig. 6.13), the values stabilize and only undergo slow variations (zone (b) in Fig. 6.13). Then, the sample becomes heterogeneous due to the growth of nanoparticles, as shown by the increase of the standard deviation of the measurements (zone (c) in Fig. 6.13).

The evolution of the standard deviations of Ψ and Δ angles during the annealing is presented in the figure 6.14. There are clearly two regimes in the dynamics: the first part, before 90 min, corresponding to a slow variation of the standard deviations and, the second part, after 90 min, with large increase of the standard deviations of both angles corresponding to the growth of the AuNPs. In the dynamics, consecutive data point are separated by $\Delta t = 5$ min.

After the interpretation of the mean values and the standard deviations as a function of the annealing time, quantifying the evolution of pixels from different

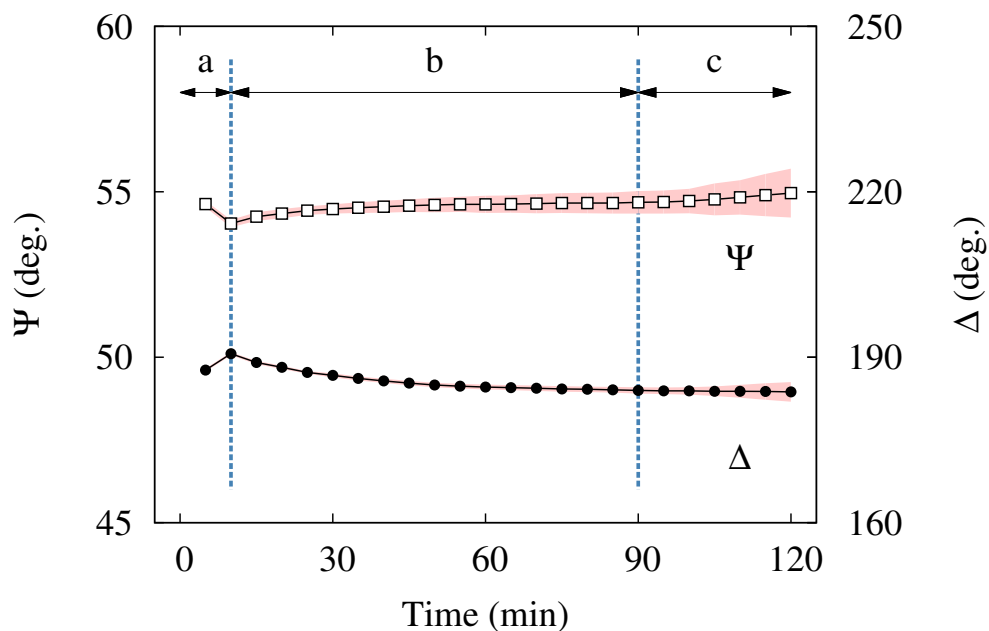


Figure 6.13: Time evolution of the mean values of ellipsometric angles during annealing. Open squares: Ψ . Closed circles: Δ . Shaded area: standard deviations. (a), (b) and (c) zones refer to the residual solvent evaporation, to the thickness relaxation and to the refractive index changes, respectively.

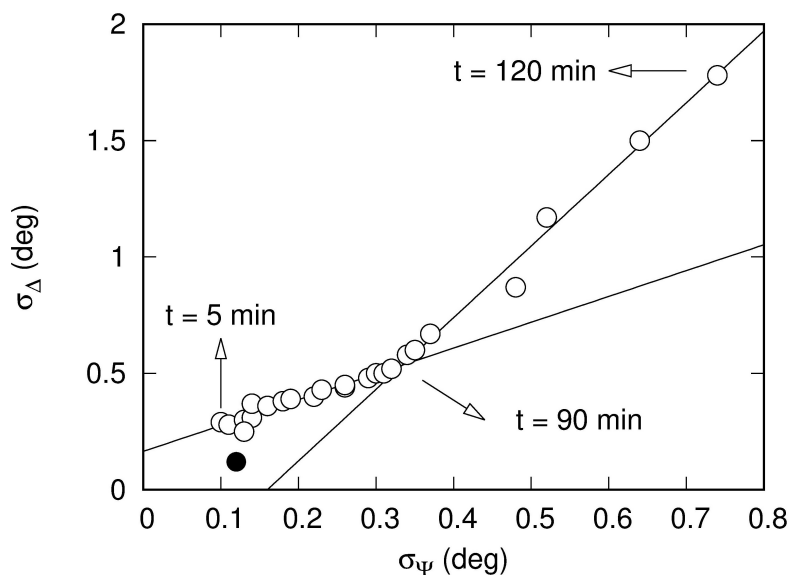


Figure 6.14: Correlation plot between the standard deviation of the Ψ and Δ ellipsometric angles during the film annealing (open circles: experimental data, lines: linear fits). Filled circle corresponds to $t = 0$ min.

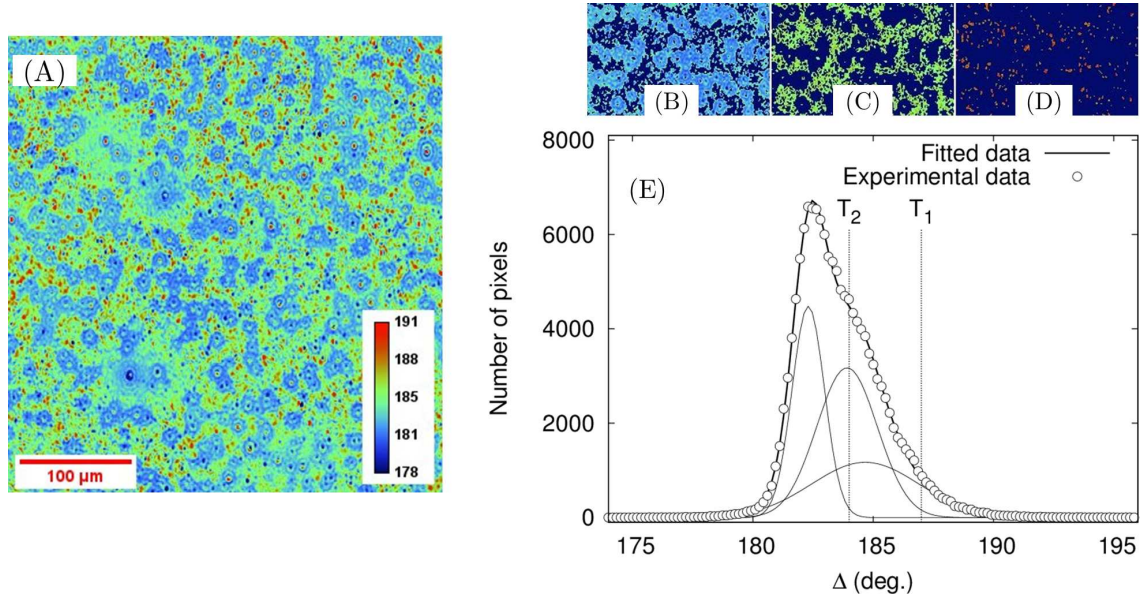


Figure 6.15: (A) Δ map of a Au–PVA film at the end of the annealing (135°C, AOI = 42°, $\lambda = 658$ nm). Film thickness: $\simeq 380$ nm. Color scale: Δ (°). (B–C–D) Details of the thresholded images (unselected pixels set to zero: dark blue color): (B) $\Delta < T_2$, (C) $T_2 \leq \Delta \leq T_1$, (D) $T_1 < \Delta$. Same color bar and same scalebar as in (A). (E) Deconvolution of the Δ histogram at the end of the annealing. Open circles: experimental data, plain lines: best-fit and Gaussian components. (RMSE: 1.35)

zones in the Δ map as a function of the time appears interesting to assess our analysis. As shown in the figure 6.7, at the end of the annealing, the Ψ and Δ maps present some heterogeneities due to the growth of the AuNPs. Practically, the formation of these heterogeneities can be followed by studying the evolution of selected zones on maps and reversing the time in the experiment.

Time evolution of selected zones of the Δ map

As already shown, the optical response is spatially homogeneous at the beginning of the annealing procedure and the growth of the nanoparticles induces heterogeneity as clearly seen in the figure 6.15A. As already demonstrated in the figure 6.12, the histogram of the ellipsometric angles cannot be described by a single Gaussian. It has to be deconvoluted and as it is shown in the figure 6.15E, it is well fitted by the sum of 3 Gaussian peaks. The sum of two Gaussian peaks was also tested but the root-mean-squared error (RMSE) was more than two times higher than in the retained option (two peaks: RMSE = 3.13; three peaks: RMSE = 1.35). A shoulder appears at the right of the maximum near 184°. This value was chosen to threshold the image 6.15A (T_2) and the rightmost tail of the distribution was chosen for $\Delta > 187^\circ$ (T_1).

Based on these two threshold values T_1 and T_2 , we were able to define three sets of pixels at the end of the annealing (Fig. 6.15E) and to follow their mean values as a function of the time (Fig. 6.16). The curves are similar to each other during the first 60 minutes of the experiment, confirming the homogeneity of the sample until the end of this period. Afterwards, the average value in the region $\Delta < T_1$ starts to

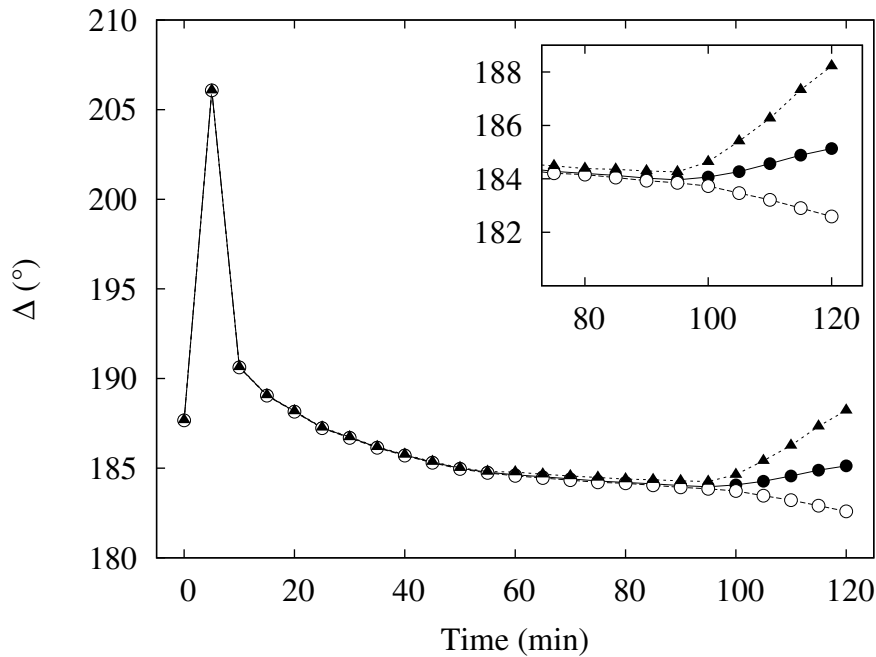


Figure 6.16: Evolution of the mean value of the Δ angle of each zones obtained from the threshold shown in Fig. 6.15E. Open circles: $\Delta < T_2$, closed circles: $T_2 < \Delta < T_1$ and triangles: $T_1 < \Delta$.

decrease. The most striking feature is the strong divergence of the curves for $t > 90$ minutes. This can be related to the figures 6.13 and 6.14, where it is shown that the standard deviation of the Δ and Ψ statistical distributions strongly increased at that time. As a reminder, the behavior of the Δ values is complex during the first ten minutes due to the residual solvent evaporation, the relaxation of the mechanical constraints induced by the spin coating and the glass transition temperature of the polymer.

As a conclusion of this section, we have shown that the statistical analysis of the Ψ and Δ maps combined with the analysis of batches of pixels allow to decompose the annealing of the sample in three different parts. Firstly, large modifications of the Ψ and Δ values due to the relaxation of the constraints induced by the spin coating. Secondly, a weak variation of the values between 20 and 90 minutes. The third part appears, after 90 minutes of annealing, by an increase of the standard deviation of the Ψ and Δ maps. This variation can be related to the increase of AuNPs in the polymer film. Moreover, the analysis of batch of pixels of the Δ map reveals that the growth of the AuNPs inhomogeneously occurred within the film. In the next section, we will try to extract variation of physical data, i.e. variation of the refractive index and the thickness, during the annealing.

6.4.3 Theoretical constant angle of incidence curves

Ellipsometric data have to be processed according to an optical model to extract physical data. This model assumes flat interfaces between adjacent layers, each of them being characterized by its thickness and its (frequency-dependent) complex re-

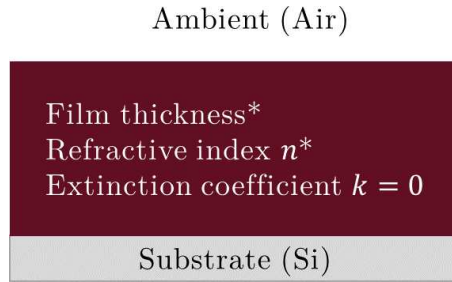


Figure 6.17: One-layer optical model with variable thickness and adjustable real refractive index (adjustable parameters are indicated by * in the figure), while the extinction coefficient being set to zero: operating wavelength of the IE ($\lambda = 658$ nm) is far from the LSPR of the AuNPs ($\lambda_{\text{LSPR}} = 530$ nm).

fractive index or dielectric function. In the case of layers containing mixed materials, which is the case for our nanocomposite layers, the optical properties of the components are combined according some mixing rules, the *Effective Medium Approximations* (EMAs) (Section 3.2.5). For non-interacting nanoparticles embedded in a host matrix, Maxwell-Garnett EMA (MG-EMA) is usually used to interpret standard spectroscopic ellipsometric data. However, for metal volume fractions in the composite less than 1%, the effect of doping is usually not experimentally detected using MG-EMA when the optical measurements are carried out out-of-resonance. Such an effect has been previously modelled in the figure 6.2. For those reasons, as the metal volume fraction used in our experiments is $\simeq 0.13\%$, our experimental data will be processed on the basis of a one-layer optical model with variable thickness and adjustable real refractive index, the extinction coefficient k being considered to be null. This model is schematically represented in the figure 6.17.

In our case, this model is suitable to interpret data obtained by the IE. As we have shown in the previous section, by using statistical distribution, we are able to follow the evolution of the ellipsometric Ψ and Δ maps as a function of the annealing time. In order to extract physical data, i.e. refractive index and thickness, it is convenient to study these data in the (Ψ, Δ) space [99, 137]. In other word, it may be convenient to plot Δ directly versus Ψ . On this graph, we can plot theoretical curves called “constant angle of incidence” (CAI) curves, which depend on the angle of incidence and the wavelength of the incident light. These curves are parametrized as a function of the film thickness and of the refractive index. Drawing this family of curves as well as our experimental data allows us to directly relate the kinetics to the changes of thickness and/or of refractive index. It should be kept in mind that this superimposition is only allowed for a valid optical model, as explained by the figure 6.2.

These CAI curves will be used hereinafter in order to have a physical interpretation of the measured ellipsometric data of three types of samples: (a) SiO_2 sample, (b) undoped film, i.e. PVA polymer without AuNPs and (c) Au–PVA nanocomposite films .

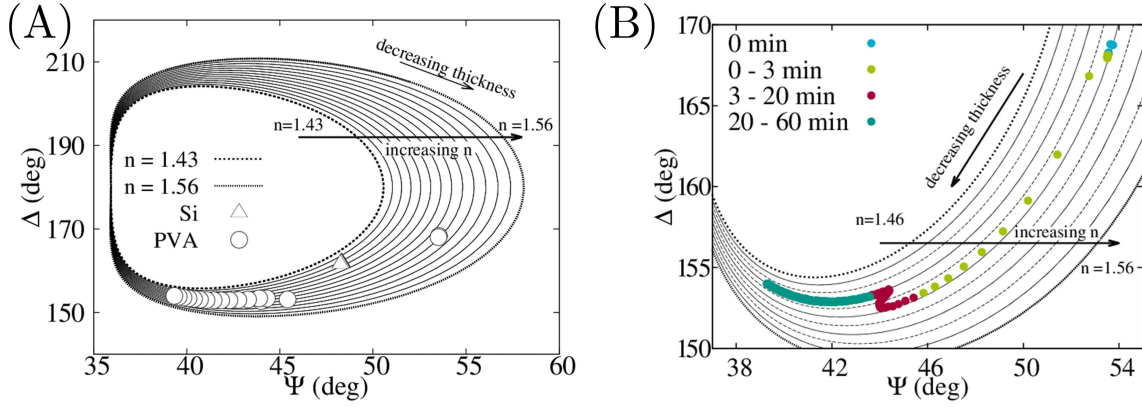


Figure 6.18: (A) Constant angle of incidence Ψ - Δ curves at wavelength $\lambda = 658$ nm and angle of incidence $\theta_i = 42^\circ$ for refractive index varying from $n = 1.43$ (left most curve) to $n = 1.56$ (right most curve) and varying film thickness. Open circles: ellipsometric response of the 350 nm-thick undoped PVA film during annealing. Open triangles: ellipsometric response of a 350 nm-thick SiO_2 sample during annealing. (B) CAI curves at wavelength $\lambda = 658$ nm and angle of incidence $\theta_i = 42^\circ$ for refractive index varying from $n = 1.46$ (left most curve) to $n = 1.56$ (right most curve) and varying film thickness. Color dots: ellipsometric response of the undoped PVA film during annealing (different color for different time labels).

Silicon substrate and polymer matrix

This paragraph summarizes the CAI curves analysis results for the (a) and (b) samples. The CAI curves are presented in the figure 6.18A, where each theoretical curve corresponds to a specific refractive index values, is calculated at $\theta_i = 42^\circ$ and at a fixed wavelength ($\lambda = 658$ nm). The direction of the variation of the film thickness among these curves is indicated by an arrow. The refractive index of the CAI curves increases from $n = 1.43$ to $n = 1.56$ (left to right), as shown by an arrow. As we can see, by varying the refractive index, the CAI curves form a group of curved lines with a common origin on the left part of the plot. This is consistent with the existence of a limit thickness above which the Ψ and Δ values are periodic, for a fixed wavelength. This limit thickness is given by [95]:

$$d = \frac{\lambda}{2\sqrt{n_1^2 - n_0^2 \sin^2 \theta_0}} \quad (6.3)$$

which corresponds to $\beta = \pi$ in the equation 3.97. We decide, in this first graph, to show the entire plot of the CAI curves in order to present the shape of this sort of curves.

In the figure 6.18A, the experimental data superimposed to the CAI curves correspond to the measured Ψ and Δ angles during the annealing of the SiO_2 sample (Δ) and an undoped PVA film (\circ). The thicknesses of these films are 345.1 ± 0.1 nm and 344.8 ± 0.4 nm for the SiO_2 sample and the PVA film, respectively. As we can see, the (Ψ, Δ) values of the SiO_2 , depicted by triangular symbols, do not present a variation during the annealing as shown by the superposition of the experimental points. As previously presented, the modifications of the SiO_2 during annealing are very weak and can be neglected due to the very low values of the

thermal expansion coefficient ($0.24 \times 10^{-6} K^{-1}$) and of the thermo-optic coefficient dn/dT ($1.29 \times 10^{-5} K^{-1}$) [133, 134].

In comparison, data for the PVA film, represented by open circle symbols, present large variations of the (Ψ, Δ) values. In order to highlight this shift, we plot all the data points taken during the annealing on a limited (Ψ, Δ) space as it is shown in the figure 6.18B. In this dynamics, consecutive data point are separated by $\Delta t = 15$ sec. At the beginning of the annealing, as already observed in the figure 6.13, we see a considerable variation of the Ψ and Δ values, which correspond to the relaxation of the mechanical constraints induced by the spin coating (green points on the plot). Afterwards, we observe a “zig-zag” feature in the data points that can be attributed to the large modification of the polymer induced by the glass transition temperature (red points). Finally, for the end of the annealing, the data points follow the theoretical curve for $n = 1.49$, which corresponds to a weak decrease of the thickness of the film at constant refractive index.

In the figure 6.19, we decide to represent Ψ and Δ as a function of the annealing time. We also plot the variation of the temperature stage (dashed lines). Starting at room temperature, a temperature ramp of $10^\circ\text{C}/\text{min}$ is applied. When the temperature reaches 135°C , it is stabilized during 60 minutes. Temperature stability is expected to be 0.1°C . The variation of Ψ and Δ values as a function of time are shown in the figure 6.19A and B, respectively. These evolutions can be compared to the plot obtained with the variation of the mean values of the statistical distribution of the Au-PVA nanocomposite (Fig. 6.13). Despite a different number of data points, we see that the evolution follows more or less the same trend with different parts corresponding to large modification in the initial period followed by a weak evolution of the ellipsometric angles.

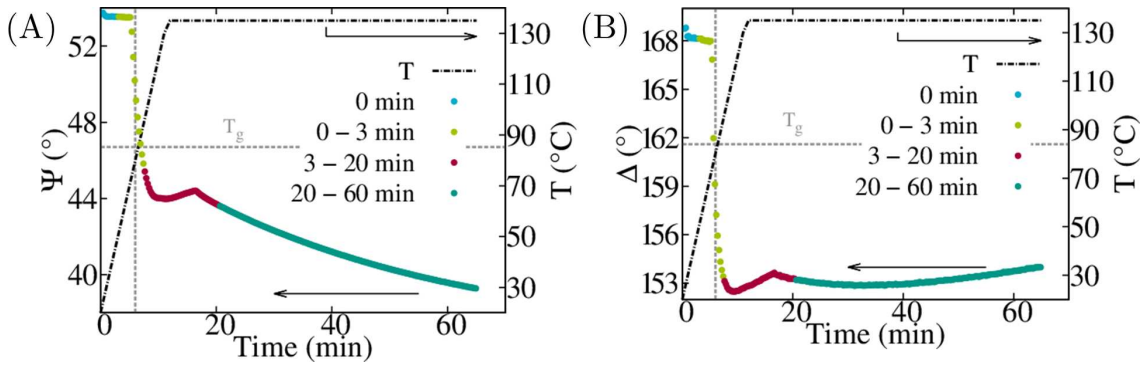


Figure 6.19: Time evolution of the ellipsometric angles during annealing. (A) Ψ angle and (B) Δ angle. Color circles: different time labels during the annealing: blue before the annealing, green from 0 to 3 min of annealing, red from 3 to 20 min of annealing and the blue-green from 20 to 60 min of annealing. Temperature profiles are given by the dashed line. The glass transition temperature is represented by an orange horizontal dashed lines ($T_g = 85^\circ\text{C}$ [55]).

The purpose of these graphs is to make the link between the expected temperature of the sample and the modification of the ellipsometric angles during the annealing. The first part of the dynamics, which correspond to the relaxation of the

constraints induced by the spin coating brings large modifications on the Ψ and Δ values, as represented by the green points. Then, just after the end of the annealing ramp, we can see an unusual behavior of the Ψ and Δ ellipsometric angles. In fact, these fast variations of the optical properties, in red in these graphs, are due to the modifications of the polymer when its temperature has reached the glass temperature of the polymer ($T_g = 85^\circ\text{C}$ for bulk PVA [55]). After this initial period, the values stabilize and only undergo slow variations due to the slow and weak decrease of the film thickness. Thanks to the plot of the temperature ramp, we can clearly see the effect of the annealing temperature on the polymer matrix.

After this analysis with the SiO_2 and the PVA matrix, we are able to analyze the result for the gold nanocomposite.

Gold nanocomposites

Let us now consider sample (c). As previously shown in the figure 6.2, in our case, the extinction coefficient of the film can be assumed to be neglected due to the operating wavelength of the IE and the low volume fraction of gold in the sample. Only the real part of the refractive index is expected to slightly vary according to the gold concentrations. For those reasons, our experimental data will be processed on the basis of a one-layer optical model with variable thickness and adjustable real refractive index.

On the figure 6.20, the refractive index of the CAI curves increases from $n = 1.46$ to $n = 1.56$ (left to right). The direction of the variation of the film thickness among these curves is also indicated by an arrow. The experimental data correspond to the mean value of the statistical distribution obtained from the Ψ and Δ ellipsometric maps, which are superimposed on CAI curves. The axes are adjusted in order to have an improved reading of the graph. Unfortunately, we never succeeded to measure the variation of Ψ and Δ directly during the annealing with a separation between consecutive point equals to $\Delta t = 15$ sec. In fact, changes of the experimental Ψ and Δ parameters are too fast with respect to the dynamics of the EP3 acquisition.

As we can see in the figure 6.20, a slow variation of the ellipsometric angles clearly appears as belonging to two different regimes: the first part of the dynamics ($t = 0$ min to $t = 90$ min) corresponds to a decrease of the film thickness (approximately from 370 nm after 10 min annealing to 365 nm after 90 min), while the second part ($t = 90$ min to $t = 120$ min), associated to the increase of the standard deviation of the data, corresponds to a local increase of the refractive index (Fig 6.14). As previously mentioned, the thermo-optic coefficient dn/dT of pure PVA is negative, inducing a decrease of refractive index when temperature increases. Thus, this local increase of the refractive index during the second part of the dynamics is unequivocally due to the growth of the AuNPs, and not the thermal response of the PVA film.

In fact, this two parts in the dynamics can be related to the results obtained by spectrophotometry (Fig. 6.4D) on different samples prepared under the same experimental conditions. As a reminder, in this graph, we showed two different increasing rates: one before 90 min and another one after 90 min. It seems that after 90 min, the number of AuNPs increase faster demonstrated by its increasing rate that is 2.5 times higher than the first one, i.e before 90 min. We show the

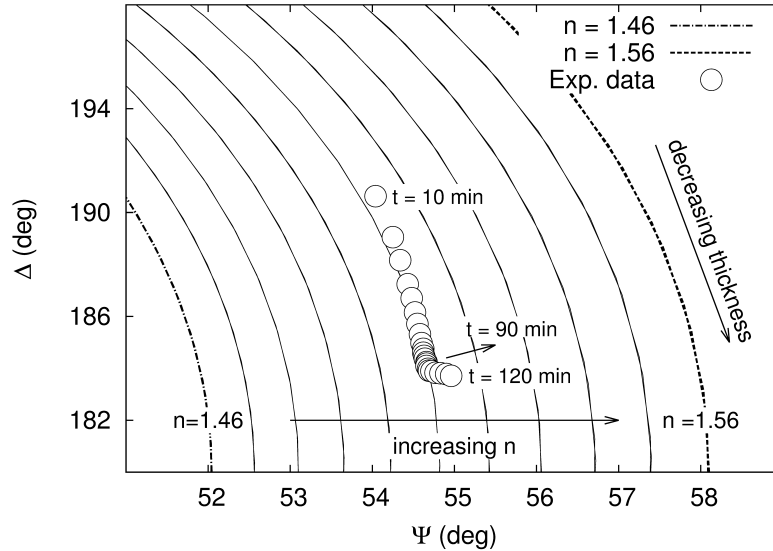


Figure 6.20: Constant angle of incidence Ψ - Δ curves at wavelength $\lambda = 658$ nm and angle of incidence $\theta_i = 42^\circ$ for refractive index varying from $n = 1.46$ (left most curve) to $n = 1.56$ (right most curve) and varying film thickness. Open circles: ellipsometric response of the Au-PVA nanocomposite during annealing (time labels added identify the time course).

same experimental trend here with another experimental technique. It seems that before 90 min of annealing at 135°C , the growth of AuNPs is different than after 90 min of the annealing leading to a higher growing rate. As shown in this section, the second part of the dynamics is attributed to an increase of the refractive index. This modification of the refractive index can be associated to an increase of the number of *in situ* synthesized AuNPs in the polymer film. The spectrophotometry measurements and analysis made from IE measurements show the same behavior, confirming the physical significance of our results.

As a conclusion of this section, we have presented an unusual way to extract physical data from experimental ellipsometric data obtained with an IE. By using theoretical $\Psi - \Delta$ CAI curves, we have studied the annealing of a SiO_2 sample, an undoped PVA-film and a gold nanocomposite. For the SiO_2 , as previously explained with the small thermal expansion coefficient and the weak thermo-optic coefficient, there are no evolution of the ellipsometric angles during the annealing as expected. The annealing of the PVA film brings more information: a fast modification of the $\Psi - \Delta$ values at the beginning of the experiment of the annealing and a large variation of the refractive index at the glass temperature transition. After this initial period, the evolution of the Ψ and Δ angles follows a CAI curve, which corresponds to a slow variation of the film thickness at a constant refractive index. For the gold nanocomposite, the same trend is found thanks to the CAI curves in the first part of the dynamics. However, after 90 min of annealing, due to the growth of the AuNPs in the film, there is a large variation of the refractive index. The dynamics can be

decomposed in two parts: the first one, at the early stage of annealing, corresponding to a decrease of film thickness, while the second one is attributed to an increase of the refractive index.

In the next section, we will present results obtained by SR. These measurements provide spectroscopic analysis of the reflectivity of the gold nanocomposite. As it will be shown, at this low doping level, the SR does not detect the presence of the AuNPs in the polymer film. This imposes us to increase the doping level of our films.

6.5 Spectroscopic reflectometry measurements

The reflectivity of the Au-PVA nanocomposite is recorded by using SR. As previously explained in the section 4.1.2, this technique is often used to measure the thickness of transparent or semi-transparent thin films usually on reflective substrates (silicon, metals, ...). As it has been illustrated in the figure 4.2A, we work with a home-built spectroscopic reflectometer. The light source is a SLS201L stabilized Tungsten-halogen lamp with a working range from 360 nm to 2600 nm and the spectrometer is a CSS200 CCD spectrometer (Thorlabs). With this instrument, we are able to analyze the intensity of the reflected light from a sample as a function of the wavelength. The measurements were made at normal incidence and therefore independently of the polarization state. As a reminder, the intensity recorded by the SR is given by:

$$I(\lambda) = R(\lambda) I_0(\lambda) \quad (6.4)$$

where $R(\lambda)$ is the reflectivity of the sample and $I_0(\lambda)$ corresponds to the intensity of the light source. As previously demonstrated in the section 4.1.2, it is possible to calculate the reflectivity of the sample, R_{sample} , by using the equations 4.5 and 4.6 and knowing the reflectivity of the substrate:

$$R_{\text{sample}}(\lambda) = \frac{R_{\text{ref}}(\lambda) I_{\text{sample}}(\lambda)}{I_{\text{ref}}(\lambda)} \quad (6.5)$$

where R_{ref} is the reflectivity of the reference, I_{sample} and I_{ref} are the recorded intensities of the sample and the reference, respectively. By using homemade routines, we are able to measure the reflectivity of the sample as a function of time, during the growing process of the nanoparticles. This sort of measurements give access to a map of the sample reflectivity with the wavelength as the ordinate (in nm), the annealing time as the abscissa (time in seconds) and the colorbar corresponding to the value of the reflectivity of the sample. Due to the interference fringes pattern of such kind of films, reflectivity spectra are usually more complex to interpret because this pattern is sensitive to both the layer thickness and to the refractive index changes. Caution should also be taken in the design of the experiments to avoid missing reflection order effects, i.e. energy absorption at a wavelength corresponding to a destructive interference valley in the spectra.

In the figure 6.21A, the reflectivity of the undoped PVA (i.e. without AuNPs) film is presented as a function of the time. As we can see, the reflectivity do not present large modification. We can see a weak shift of the darkest part, which solely

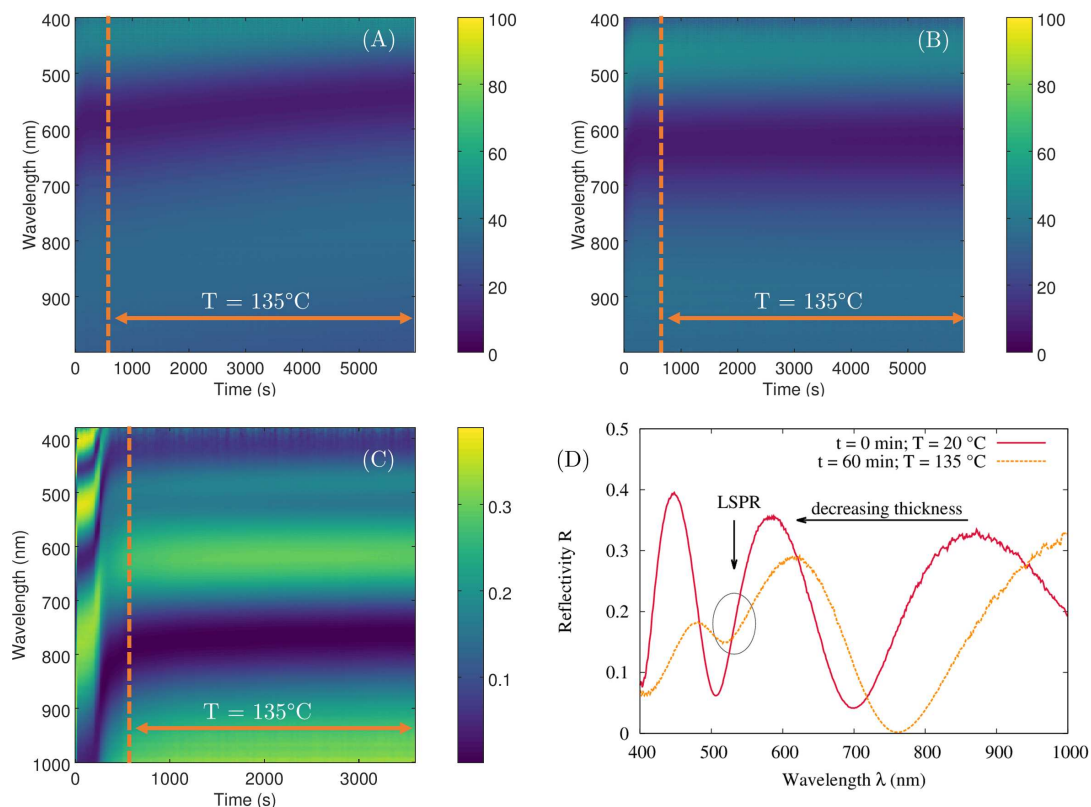


Figure 6.21: (A) Reflectivity map of the undoped PVA film as a function of the annealing time. (B) Reflectivity map of the weakly doped Au-PVA (2% w:w) film as a function of the annealing time. (C) Reflectivity map of the highly doped Au-PVA (50% w:w) film as a function of the annealing time. In (A)-(B)-(C), the orange dashed line represent the time when the temperature of the sample has reached 135°C . (D) Reflectivity spectra of the highly doped Au-PVA (50% w:w) film before (red curve) and after annealing (orange curve).

corresponds to the variation of the film thickness during the annealing (displacement of the interferometric peaks).

The figure 6.21B presents the reflectivity map of a gold nanocomposite with a low doping level corresponding to a mass ratio of $[\text{Au}]/[\text{PVA}]$ of 2%. The reflectivity map present the same trend that the one of the undoped PVA. The growth of AuNPs, which is generally noticed by a decrease of the reflectivity near 530 nm due to the LSPR, is not detected by the SR. It seems that the volume fraction of gold is too low to detect the presence of the AuNPs on the reflectivity map. In comparison to the IE, which is a local analysis of the optical properties. On the other hand, SR leads to a global measurement of the reflectivity, since it measures the mean value of the reflected intensity received by the sensor.

In order to bypass this non-detection of the AuNPs by the SR, we increase the mass ratio of gold in the polymer matrix. To ensure the detection of the LSPR, we choose a mass ratio of 50% w:w. The reflectivity map of this sample is shown in the figure 6.21C. As we can see, the reflectivity presents large variations at the beginning of the annealing because of the relaxation of the constraints due to the spin coating. After this initial period, as expected, we can see a dip in the reflectivity near 530 nm due to the presence of the AuNPs in the polymer matrix. This increase of the mass ratio, i.e increase of the volume fraction of gold in the polymer matrix (Eq. 4.40), leads to a detection of the LSPR.

The figure 6.21D presents the reflectivity spectra of the gold nanocomposite before and after the annealing. The process of annealing leads to a decrease of the film thickness, represented by an arrow in this graph, corresponding to a shift of the interferometric peaks. The LSPR due to the growth of the AuNPs in the polymer matrix produces a dip in the reflectivity spectrum of the sample after annealing.

Remembering that SR technique measures the mean value of the reflected intensity received by the sensor, one of the optical quantity is missing with this experimental method with respect to the IE experiments: the optical phase-shift. Actually, by recording the reflected intensity, the SR measurement leads to a detection of the $|r_p|/|r_s|$. As shown in the ellipsometric maps presented in the figure 6.7, the Ψ and Δ maps show that different zones surrounding the NPs are present at the microscale. Moreover, remembering that the Δ angle is related to the relative phase change undergone by the p - and s -polarized components of the incident light, the Δ maps clearly bring evidence for a local change of the relative phase upon reflection. Moreover, the reflectivity spectra obtained by the SR is measured at millimeterscale.

We will present in the next chapter results obtained by the spectroscopic imaging ellipsometer, which allows spectroscopic detection at the microscale. We will also compare our experimental data to a theoretical model in order to have physical information on the local optical properties.

6.6 Conclusion

In this chapter, we have studied the optical properties of nanocomposites containing *in situ* grown AuNPs. In particular, we have focused our study on the optical response of Au-doped PVA film during the annealing. By using spectrophotometry

during the annealing, we are able to extract information of the kinetics of growth of the AuNPs in the polymer matrix. Besides the weak variation on the position of the resonance peak, we have demonstrated two different behaviors in the growing process by analyzing the increasing rate of the absorbance of the film during the annealing. After 90 min of annealing, the variation rate of absorbance is 2.5 times higher than the increasing rate before 90 min, which can be explained by a larger increase of the AuNPs number inside the polymer matrix after 90 min.

We observe an increase of the surface roughness due to the growth of AuNPs thanks to the AFM measurements. The AFM images have revealed that, despite the same experimental procedure to synthesize the NPs inside the polymer matrix, AuNPs are larger than AgNPs. This difference can be explained by the higher temperature required to form Au-PVA nanocomposites than the temperature used for Ag-PVA nanocomposite [69].

Thanks to imaging ellipsometry, we clearly observed diffraction patterns due to the formation of AuNPs in spite of the low volume fraction of gold in the nanocomposite. The ellipsometric Ψ and Δ maps reveal that the growth of the AuNPs inhomogeneously occurred within the film. By using the mean value of the statistical distribution of each map, we have shown that the behavior of the sample is complex during the first 10 minutes of the annealing due to the relaxation of the constraints induced by the spin coating. After 90 min, the sample becomes heterogeneous due to the growth of nanoparticles, as shown by the increase of the standard deviation of the measurements.

In order to extract physical data, the ellipsometric data have been processed according to a simple model based on a one-layer optical model with variable thickness and adjustable real refractive index. Theoretical CAI curves are parametrized as a function of the film thickness and of the refractive index. Drawn in the (Ψ, Δ) space, these CAI curves are used to extract a physical interpretation of the measured ellipsometric data acquired by the IE. Superimposition of ellipsometric measurements of the PVA recorded during the annealing and theoretical $\Psi - \Delta$ curves allowed us to see the impact of the complex behavior of the sample at the beginning of the annealing. We have shown the variation of the refractive index induced by the modifications of the polymer at the glass transition temperature. After this period, only a variation of the film thickness at constant refractive index is recorded. In the case of gold nanocomposite, after this initial period, we have shown that the dynamics of the annealing is composed of two distinct parts: the first one corresponds to a decrease of film thickness, while the second one is attributed to an increase of the refractive index. This increase of the refractive index appears after 90 min of annealing and can be attributed to an increase of the number of *in situ* synthesized AuNPs in the polymer film. This experimental procedure gives the same results that the real time spectrophotometry measurements.

In the last section of this chapter, we have shown that the global measurement of a lowly doped gold nanocomposite obtained by the SR has led to a non-detection of the presence of the AuNPs in the polymer film. Indeed, SR measures the mean value of the reflected intensity received by the sensor and can not measure the phase-shift. This measure at low doping level reveals one of the advantages of the use of IE, bringing information on the local optical properties at the microscale. In order

to bypass this non-detection, we increased the mass ratio of gold in the polymer.

Beyond these results, we show that the two noble metals used in this thesis, silver and gold, have different behaviors during their growth as NPs in a polymer matrix. Indeed, the temperature of annealing has to be higher in the case of gold nanocomposite. The necessity of a higher temperature of annealing can lead to larger NPs as it has shown by the AFM analysis. This higher temperature can be explained by a different growing process. In the case of silver, the cations only need one electron to promote to their neutral state. It seems that it is more complicated in the case of gold.

Finally, as we have shown, the increase of the refractive index appearing after 90 min of annealing is related to the formation of inhomogeneities detected by the IE. The spectrophotometry measurements present a variation at this moment of the annealing and show an increase of the absorbance, corresponding to an increase of the AuNPs embedded in PVA. This result could be related to the work of Nadal [78], already explained in the chapter 2. As a reminder, they demonstrated the possibility to induce to formation of AuNPs in PVA matrix on glass substrates in interference patterns thanks to laser irradiation followed by a short thermal annealing. They explained that the photoreduction was not complete and the thermal annealing of the sample allowed the reduction of the gold cations located in the dark fringes. Then, those can diffuse towards growing AuNPs. They assumed that AuNPs acted as seeds and tended to effectively drag the surrounding gold atoms and contribute to the growth of AuNPs. In our case, the first part of the dynamics, i.e. before 90 min of annealing, allow the reduction of gold cations Au^{3+} to gold atoms Au^0 and the growth of AuNPs. The difference recorded during the second part of the dynamics, i.e. after 90 min of annealing, could be related to the grown AuNPs acting as seeds and dragging the surrounding gold atoms, leading to the growth of larger AuNPs. This effect has been shown in the bottom images of the figure 6.7, where the larger NPs (i.e. only those whose effect can be detected in the optical response) are built by some kind of drainage of the metal atoms in their neighborhood, leaving a depletion zone around the NPs.

Spectroscopic imaging ellipsometry of gold and silver nanocomposites

7.1 Introduction

In the previous chapter, we have shown that AuNPs at very low doping level (volume fraction f_{Au} around 0.13%) in a PVA matrix grow according to a two-step process. The steps are evidenced by a change of the optical properties of the nanocomposite film during the annealing. More precisely, the largest particles are surrounded by polymer film regions, whose optical response is clearly different from that of the background. This analysis was based on results obtained from the single wavelength ellipsometer operated slightly off-resonance (658 nm). Additional measurements could recently be carried out in spectroscopic mode using an upgraded version of the EP3 to EP3-SE. It allows us to determine the optical properties by using a theoretical model that takes into account the spectral dispersion.

In this chapter, we provide additional information about the AuNPs growth in polymer films by reporting on the local spectroscopic characterisation of these films. Moreover, by measuring ellipsometric angles on small selected regions of interest, we are able to extract physical data at the microscale, such as the volume fraction of gold. In the section 7.2.2, we also compare the analysis carried out by conventional

spectroscopic ellipsometry (SE) and by spectroscopic imaging ellipsometry (SIE). In order to justify the added value of a local analysis of the optical properties in this specific case. To the best of our knowledge, such results on the local optical response of low-doped Au–PVA films have never been reported. Finally, from Ψ and Δ ellipsometric maps near the Localized Surface Plasmon Resonance (LSPR) wavelength and with the Maxwell-Garnett effective medium approximation model, we are able to calculate two maps: one of the local thickness of the film and a second one of the local volume fraction of AuNPs (Section 7.2.3).

At the end of this chapter, we present the local spectroscopic characterisation of highly doped silver nanocomposites (Section 7.3.2). By selecting regions of interest on the sample, we can determine the optical properties based on a Cauchy model and Lorentzian oscillator, which we have already used to describe the optical properties of AgNPs in PVA matrix at the microscale.

7.2 Gold nanocomposites at low doping level

With ellipsometry as a non-destructive optical technique to analyze nanocomposites, the doping level of the polymer by the metal is a cornerstone parameter that plays a central role in probing the changes in the optical properties of the films. As already explained in the chapter 2, the volume fraction detected by a conventional spectroscopic ellipsometry (SE) is usually of the order of 1% in thin films [44, 77]. Under this level, the extinction spectrum is not significantly modified by the presence of the NPs.

In this section, we present the spectroscopic characterization of low-doped gold nanocomposite ($f_{\text{Au}} < 0.2\%$). The experimental procedure to prepare this gold nanocomposite has already been presented in the section 4.2. As a reminder, the gold-to-polymer mass ratio is equal to 2%. This leads to an average volume fraction of gold in the polymer matrix of $f_{\text{Au}} = 0.13\%$ in the dry film. The spinning conditions are 2000 rpm during 90 s. To induce the growth of the AuNPs, the samples are annealed using a THMS600 Linkam heating/cooling stage. In a typical experiment, temperature is raised from room temperature (around 23°C) to 135°C at the heating rate of 10°C per minute. After that, a plateau value is maintained to reach an experiment duration of 120 minutes.

In order to determine the optical properties at the microscale, spectroscopic imaging ellipsometry (SIE) measurements of the ellipsometric angles Ψ and Δ are performed on Au–PVA thin films with an EP3-SE spectroscopic (nulling) ellipsometer (Accurion GmbH, Gottingen). The SIE has already been presented in the section 4.1.4. The wavelength range is 360 – 1000 nm and the measurements are carried out at three different angles of incidence (AOI) (45°, 55° and 65°), as a function of the analysis type. Imaging ellipsometry techniques is extensively used to explore the local optical properties of the thin films, namely, the complex dielectric function and absorption coefficient along with the film thickness and roughness. Multiple regions of the sample are investigated at once, allowing us to record the local optical behavior. Data are processed using the EP4 software (Accurion GmbH). The spatial resolution is $1.07 \mu\text{m} \times 1.07 \mu\text{m}$ per pixel at 45° of incidence.

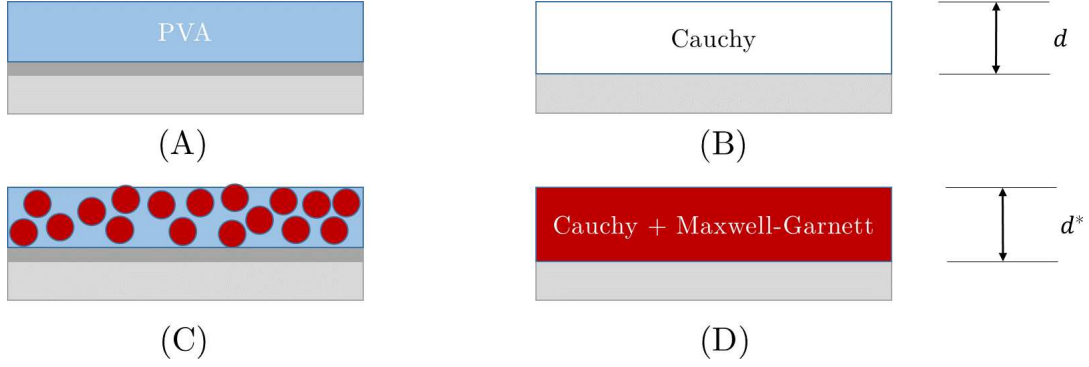


Figure 7.1: Schematic representation of the optical models used to interpret ellipsometric data: (A) PVA layer on silicon, (B) Cauchy model used to describe the optical properties of the PVA layer, (C) AuNPs in PVA layer on Si and (D) a Cauchy model and Maxwell-Garnett EMA used to describe the optical properties of AuNPs in PVA matrix. Shaded area between the polymer layer and the substrate: SiO_2 layer (Not to scale).

Conventional SE measurements are also performed with a SOPRA GESp5 spectroscopic ellipsometer in parallel beam configuration and at an angle of incidence of 70° (Section 4.1.3). The small diameter of the spot on the sample is about 4 mm.

As the size of the pixels in the Ψ and Δ maps obtained with the SIE is $1.07\mu\text{m}$, the lateral resolution is improved by a factor 4000 compared to the conventional SE. This improvement of the lateral resolution highlights the strength of the SIE as a local optical analysis technique compared to the SE.

7.2.1 Modeling of the optical properties

Two optical models are used to analyse our ellipsometric data. These models are schematically represented in Fig. 7.1. The optical constants of crystalline silicon and silicon dioxide are well known and are obtained from classical optical databases.

Model 1: As already presented in the section 5.2, and due to the high transparency of the polymer film in the visible range, the optical properties of PVA are adequately described by a Cauchy law for the index of refraction $n(\lambda)$, the extinction coefficient $k(\lambda)$ being set to 0 [73, 74, 95]. The undoped PVA samples are therefore described by a two-layers model including the polymer film, the native oxide layer and the $< 100 >$ silicon substrate. The thickness of the native silicon oxide layer is 2 nm and is not optimized throughout the rest of our study.

Model 2: In order to analyze the optical response of the plasmonic nanocomposites after annealing, a second optical model is proposed, as follows. The Cauchy dispersion law parameters determined on undoped film are kept constant (negligible effect of the particles on the polymer matrix itself) and a gold volume fraction f_{Au} is accounted within the Maxwell-Garnett effective medium approximation (MG-EMA) according to [95]:

$$\frac{\varepsilon_{\text{eff}} - \varepsilon_{\text{PVA}}}{\varepsilon_{\text{eff}} + 2\varepsilon_{\text{PVA}}} = f_{\text{Au}} \frac{\varepsilon_{\text{Au}} - \varepsilon_{\text{PVA}}}{\varepsilon_{\text{Au}} + 2\varepsilon_{\text{PVA}}} \quad (7.1)$$

where f_{Au} is the volume fraction of gold in the polymer matrix, ε_{Au} , ε_{PVA} and ε_{eff} are the complex dielectric functions of gold, of the polymer matrix and of the nanocomposite film, respectively.

This approach of data analysis is a standard approach in ellipsometry to account for the contribution of spherical inclusions at low volume fractions. Furthermore, in the limit of very small f_{Au} , the MG-EMA converges to the quasi-static Mie case [97]. This applies in particular to the AuNPs and the volume fractions considered in our study.

Effects of the metal nanoparticles embedded in a polymer film on the composite film optical properties can be described from different theories. They have been reviewed by Oates and coworkers [138] and their key points will be briefly reminded hereinafter. A spherical solution to Maxwell's equations was presented by Mie which accurately predicts the resonance frequency of spherical metal particles. This approach is commonly used within the quasi-static approximation for which only dipolar resonance are observed. In the dipolar-dominated small size limit, the particle may be considered as a classical oscillating dipole and the absorbed photons are thus efficiently reradiated. Mie theory results are quite often compared to the results of EMA theories. As quoted by Oates *et al* [138], MG-EMA uses *the Rayleigh formulas and takes the first order approximation of this relation, i.e., all particles give a similar change to the dielectric function and the change in the dielectric function of the host is negligible with the inclusion of more particles*. Although, the Mie theory is a 'single particle' theory, it is commonly used to describe the optical properties of colloidal solutions and the limit that would determine the use of either Mie theory or MG-EMA is not clearly defined. In this study, the number of particles per unit of volume is sufficiently large to consider the use of the MG-EMA in the analysis of our data.

As the models are defined, we are able to analyze the ellipsometric measurements obtained by the SE and the SIE on the low-doped gold nanocomposite. We decompose this analysis in two part:

- First, we report the measurements obtained by the conventional SE. This global optical analysis leads to a non-detection of the presence of the AuNPs in the nanocomposite.
- Secondly, SIE measurements are performed on the same kind of nanocomposite. Those reveal the presence of heterogeneities in the optical response. By selecting different regions of interest, the ellipsometric spectra of these zones appear to be slightly shifted in the spectral domain, where the LSPR is found, hence confirming the detection of the local optical properties of the gold nanocomposite by the IE.

7.2.2 Global optical properties of the Au–PVA thin films

Let us start this analysis by the measurements obtained with the SE. The ellipsometric angles Ψ and Δ are measured in the 1.5 – 4.0 eV energy range with a Sopra GESp5 ellipsometer. Control experiments have been carried out on undoped films under similar experimental conditions.

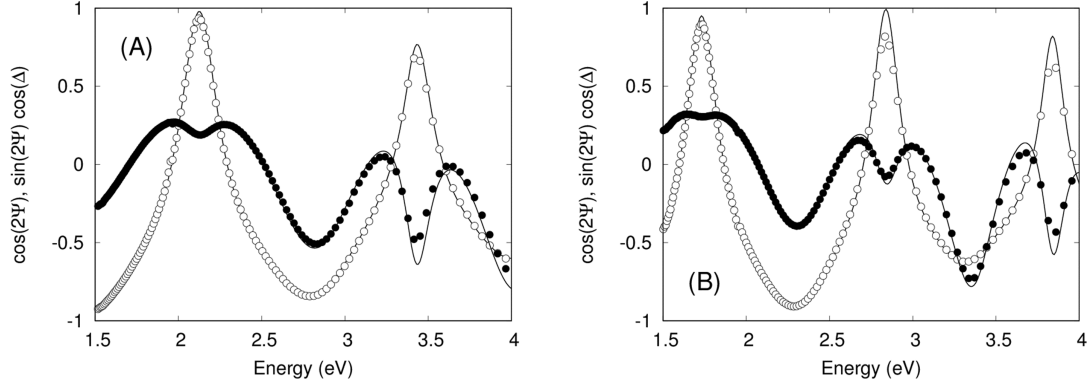


Figure 7.2: Global ellipsometric response of: (A) a 358 nm-thick undoped-PVA film and (B) a 441 nm-thick Au–PVA film with average $f_{Au} = 0.13\%$. Open symbols: $\cos(2\Psi)$, closed symbols: $\sin(2\Psi)\cos(\Delta)$. Plain lines: best-fit of the experimental data by (A) a Cauchy dispersion law (undoped polymer) or (B) a Cauchy dispersion law and a Maxwell-Garnett approximation that accounts for the contribution of the AuNPs.

As already shown in the section 5.5, the ellipsometric data are presented as $\alpha = \cos(2\Psi)$ (open symbols) and $\beta = \sin(2\Psi)\cos(\Delta)$ (closed symbols) in the figure 7.2. For clarity, only one experimental point over 10 is drawn in the figure. For the undoped samples (Fig. 7.2A), the optimized thickness is 358.1 ± 0.1 nm and the optimized spectra are in excellent agreement with the experimental data ($\text{RMSE} = 1.49 \times 10^{-3}$). As the annealing of the samples at 135°C (i.e. above the glass transition of the polymer, $T_g = 85^\circ\text{C}$ [55]) promotes the growth of the AuNPs in the film, the α and β spectra are analyzed on the basis of the second model (**Model 2**), i.e. including the contribution of the nanoparticles to the dielectric function via the MG-EMA. In this model, the thickness of the film and the gold volume fraction f_{Au} are the adjustable parameters.

After optimization of the ellipsometric data (Fig. 7.2B) using **Model 2**, the thickness of the film is found to be 441.8 ± 0.1 nm and f_{Au} is $2.6 \cdot 10^{-3} \pm 2.9 \cdot 10^{-3}\%$, a value much lower than the one expected on the basis of the experimental protocols ($f_{Au} = 0.13\%$). Moreover the relative error on the gold fraction is higher than 110% which means that this result is not significantly different from zero. No specific feature is seen in the ellipsometric spectra at about 2.33 eV. This energy corresponds to the energy of the localized plasmon as determined from the Fröhlich equation [90] and the complex refractive index of both gold and PVA. Furthermore, the optimization can be carried out using **Model 1**, i.e. without taking into account the gold contribution, yielding comparable thickness (441.9 ± 0.1 nm) and root-mean-squared error (RMSE) ($2.019 \cdot 10^{-3}$). It is therefore obvious that conventional SE does not allow us to distinguish between the undoped and the doped samples at low gold-to-polymer mass ratio. The main reasons for this lack of success in modeling lie probably in the spatial averaging of the optical response over the measurement spot area and of the local heterogeneity of the samples in thickness and chemical composition, as highlighted in the chapter 6.

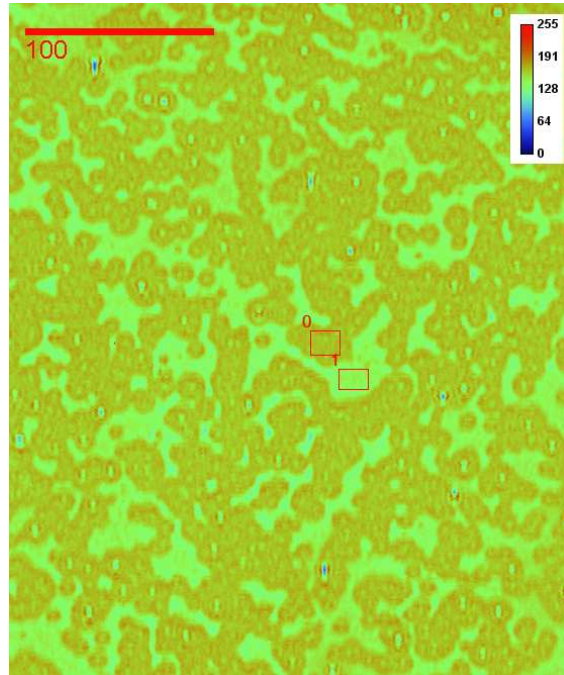


Figure 7.3: Ellipsometric enhanced contrast (grey levels, in false color) image of the Au–PVA film at the end of the annealing (Scalebar: 100 μm , wavelength: 533 nm, AOI: 55°). Red rectangles indicates the regions of interest “0” and “1” used for spectroscopic characterization.

7.2.3 Local optical properties of the Au–PVA thin films

As already explained, SIE provides access to the local optical response due to the improvement of the lateral resolution by a factor 4000 compared to the conventional SE. Based on the nulling concept, the polarizer and analyzer of the ellipsometer can be rotated respectively to each other in order to enhance the contrast of the images, hence determining the optical response in terms of ellipsometric angles Ψ and Δ . This technique is usually referred to “ellipsometric enhanced contrast microscopy”. A typical ellipsometric enhanced contrast image taken at 533 nm is presented in the figure 7.3 and clearly reveals the heterogeneity of the optical response.

To strengthen our analysis, ellipsometric Ψ and Δ maps have been measured in the 360 – 1000 nm spectral range. Some of them are presented in the figure 7.4 for $\lambda = 533, 660$ and 920 nm. The wavelengths have been chosen close to the resonance (533 nm) and far from it (920 nm). The middle one is chosen in the purpose of comparison with our previous study (Chapter 6) with the single wavelength ellipsometer (658 nm). The contrast of the images is strongly influenced by the wavelength but also depends on the choice of the ellipsometric angle (Ψ and Δ). Images obtained in the NIR region only bring little information on the optical response heterogeneity.

In order to take into account the heterogeneity of the optical response, ellipsometric spectra in Ψ and Δ are measured in two different regions-of-interest labelled ROI_0 and ROI_1 as indicated by the rectangles in the figure 7.3. The ellipsometric spectra are presented in the figure 7.5 (average size of ROIs: $700.32 \mu\text{m}^2$). The insets in the left (Fig. 7.5A) and right (Fig. 7.5B) panels show the details of the

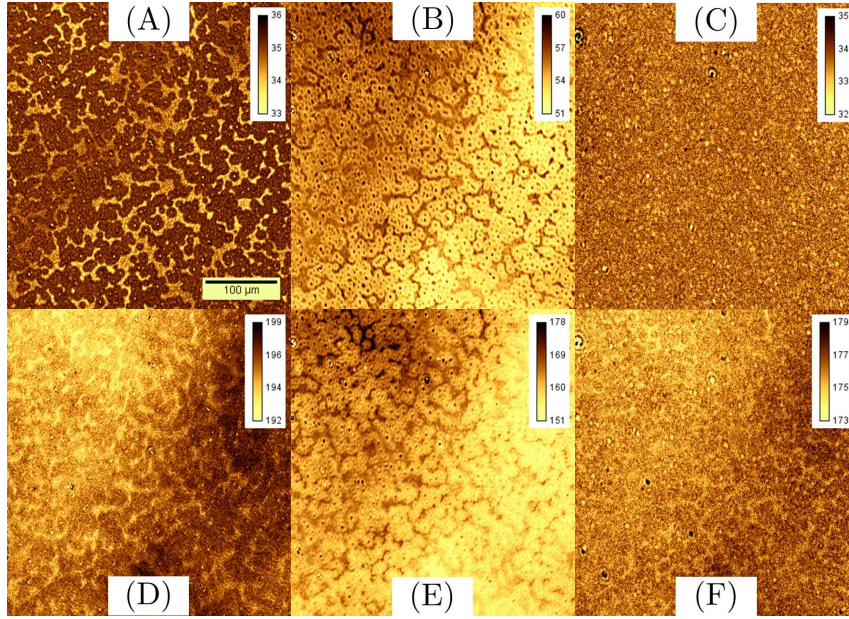


Figure 7.4: Ψ (A-B-C) and Δ (D-E-F) images of the Au–PVA film ($\text{AOI} = 45^\circ$). Each image corresponding to a different incident light wavelength: (A) and (D) $\lambda = 533$ nm, (B) and (E) $\lambda = 660$ nm, (C) and (F) $\lambda = 920$ nm. (Image size: $430 \mu\text{m} \times 400 \mu\text{m}$ and color scale in ($^\circ$)).

ellipsometric response in the plasmonic band region (500-600 nm). Although the data coincide with each other for wavelengths smaller than 400 nm and larger than 700 nm, they appear to be slightly shifted in the spectral domain where the LSPR has to be found. The insets of the figure 7.5A and B enhance the details of this effect.

As already done in the case of conventional SE data, the SIE data are analyzed based on our second model, i.e. including a MG-EMA contribution to the dielectric function of the nanocomposite layer and fitting on both the thickness of the layer and its gold volume fraction. For the PVA matrix, the optical properties of the polymer matrix is well described by a Cauchy dispersion law (Section 5.2). Optimized parameters for the PVA matrix are $A_n = 1.509 \pm 0.002$ and $B_n = 3170 \pm 300 \text{ nm}^2$ (RMSE = 0.966). Then, the value of the A_n and B_n are fixed for the MG-EMA used in the second optical model. For both ROIs, **Model 2** adequately describes the experimental data as shown in the figure 7.5. The best-fit parameters as well as the RMSE are given in the table 7.1. The correlation coefficients between the thickness of the film and the gold volume fraction f_{Au} in the film are -0.769 and -0.742 for ROI_0 and ROI_1 , respectively. The thickness in the different ROIs are slightly different but this difference cannot completely explain the shift between the Ψ and Δ curves. The gold volume fraction f_{Au} is significantly higher in ROI_1 ($f_{\text{Au}} = 0.103 \pm 0.013$) than in ROI_0 ($f_{\text{Au}} = 0.006 \pm 0.013$). The f_{Au} of ROI_0 is not statistically relevant and its relative error is around 216%. This result could be equivalently associated to a null volume fraction of gold in the polymer in this area.

The heterogeneity of the optical response can therefore be attributed to a local change of the metal fraction. Our results also show that the growth of the AuNPs

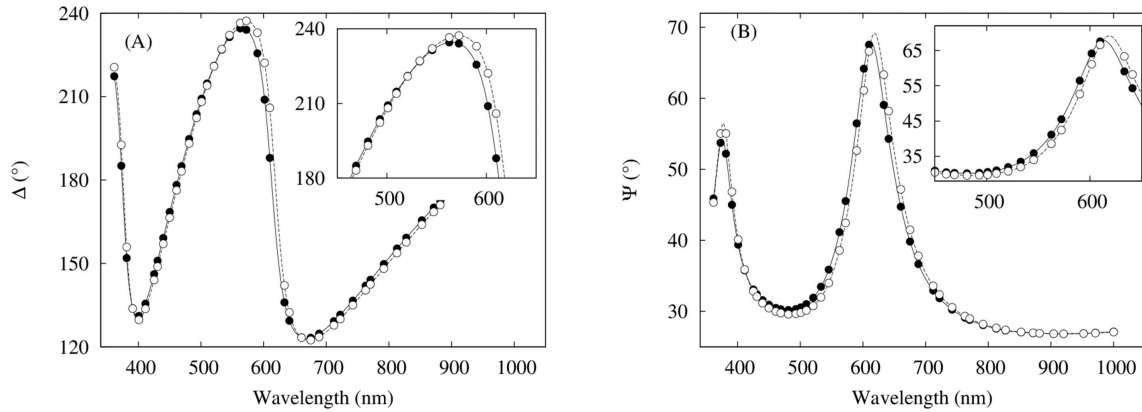


Figure 7.5: Local spectroscopic optical response of the Au–PVA film. (A) Δ ($^{\circ}$) (B) Ψ ($^{\circ}$). Open and close symbols respectively corresponds to ROI₀ and ROI₁ in Fig. 7.3. Plain and dashed lines: best-fit data. Insets: details of the ellipsometric spectra in the plasmonic response wavelength range.

Table 7.1: Best-fit results of the ellipsometric data presented in figure 7.5 within the Maxwell-Garnett approximation. Optical properties of gold are from Johnson and Christy’s paper. [86]

ROI	Thickness (nm)	Gold fraction f_{Au} (%)	RMSE	Correlation
0	359.8 ± 0.2	0.006 ± 0.013	0.682	-0.736
1	360.8 ± 0.1	0.103 ± 0.013	0.688	-0.730

inhomogeneously occurs in the polymer matrix. Furthermore, our results demonstrate the possibility of detecting gold-doping with SIE at low concentration. Due to the (sub)microscale analysis of our Au–PVA nanocomposites, we are able to detect a volume fraction of gold around 0.1%, while the volume fraction detected by a conventional SE is usually admitted to be higher than 1% in thin films. At a lower doping level, corresponding to a volume fraction of 0.06%, the optical properties of Au–PVA nanocomposites do not significantly differ from those of a pure PVA film (data not shown). It seems that a gold doping level of 0.10% is rather close to the lower limit of detection of the technique.

The optical properties of the selected zones of the film, i.e. ROI₀ and ROI₁, are represented in the figure 7.6. For each region of interest, the refractive index n and the extinction coefficient k as a function of the wavelength are drawn, based on the optimized parameters of table 7.1. The difference in the volume fraction between the two ROIs considerably modifies the optical properties of the doped polymer film. For ROI₁, the presence of the absorption peak near 530 nm in the extinction coefficient spectrum (Fig. 7.6B) induces a large oscillation in the refractive index value (Fig. 7.6A) due to the Kramers-Krönig consistency of the optical properties (Eq. 3.83). We can see here, the variation over a large spectral range of the refractive index, which allowed the detection of the growth of the AuNPs with the single wavelength ellipsometer (Section 6.4). For ROI₀, we can see that the extinction coefficient is near zero over the spectral range. This leads to a variation of the refractive index over the spectral range induced by the PVA matrix. Let us note

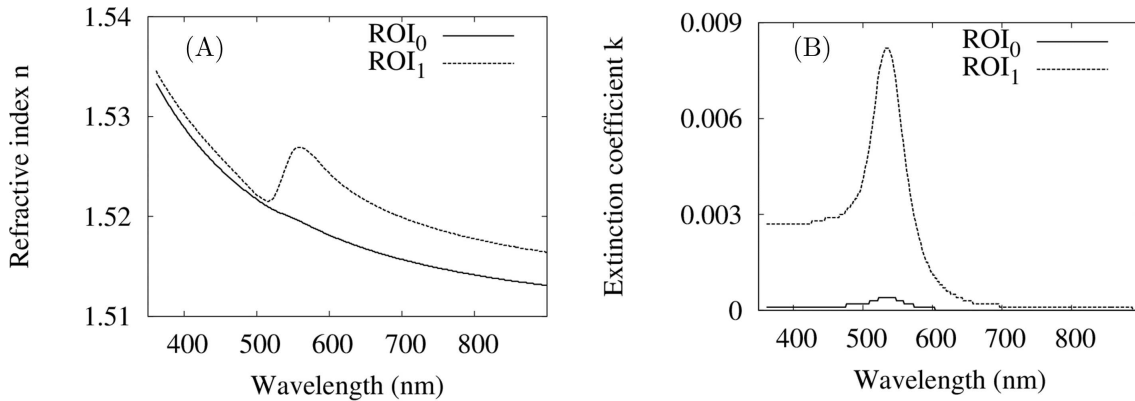


Figure 7.6: Optical properties of 365 nm-thick gold nanocomposite film ([Au]:[PVA] ratio: 2% w:w): A, refractive index n ; B, extinction coefficient k .

that the values of the extinction coefficient are very small, which demonstrates the power of detection of the IE.

Finally, from the Ψ and Δ ellipsometric maps measured near the LSPR wavelength ($\lambda = 533$ nm), it is possible to calculate using **Model 2** both the local thickness of the layer $d(x, y)$ and the local gold fraction $f_{\text{Au}}(x, y)$ for each pixel of the image. The starting parameters of the optimization are the parameters obtained by our SIE analysis over ROIs 0 and 1 (Table 7.1). These results as well as the relative error on f_{Au} are given in the figure 7.7A to C. During the numerical inversion of the ellipsometric equations, the parameters are constraint as follows: $300 \text{ nm} \leq d \leq 400 \text{ nm}$ and $0\% \leq f_{\text{Au}} \leq 1\%$. From the comparison between the figure 7.3 and the figure 7.7A, it appears that the regions with the same color than the ROI₁ in the figure 7.3 are regions for which f_{Au} is significantly different from zero and that the relative error on f_{Au} is small contrary to the remaining part of the image ($f_{\text{Au}} \simeq 0$) for which the associated relative error is several orders of magnitude larger (red regions in Fig. 7.7B). This can be explained by local values of f_{Au} close to the lower bound imposed to the optimization algorithm and to the lack of significance of this parameter in these regions (almost undoped polymer). The thickness map (Fig. 7.7C) does not reveal specific features, which allows us to confirm that the optical heterogeneities come from the growth of the AuNPs. Additional analysis of the data presented in the figure 7.5 to include surface roughness or void inclusions in the models are not conclusive. The thickness and the metal volume fraction presented in the figure 7.7 have also been plotted as a function of each other, without providing us additional significant information on their correlation. This lead us to conclude that the main effect of the annealing of the film is a modification of the local refractive index due to the increase of the gold volume fraction in some regions of the film.

As a conclusion of this section, we have shown an experimental study of the optical properties of gold-doped nanocomposites using SIE. At a low doping level ($f_{\text{Au}} < 0.2\%$), the optical constant determined by the conventional SE spectra is only relevant for the polymer matrix. We have also shown the advantage of using spatially-resolved spectroscopic ellipsometry by choosing areas on the image with a different intensity contrast. The ellipsometric spectra of each region of interest

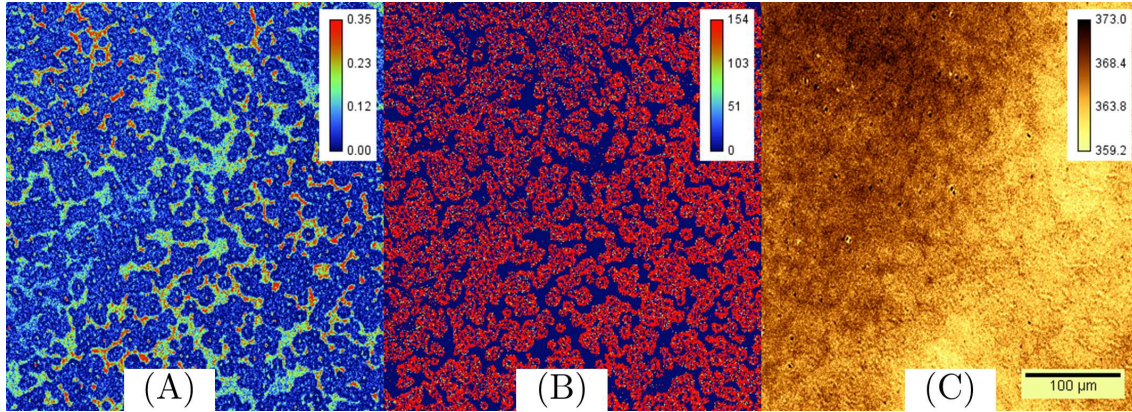


Figure 7.7: Results maps for the (A) Gold fraction f_{Au} (%), (B) Relative error $\delta f_{Au}/f_{Au}$ (%) and (C) Film thickness (nm). Images at $\lambda = 533$ nm. Scalebar: 100 μm .

are different, especially between 400 nm and 600 nm, i.e. the spectral region corresponding to the localized surface plasmon resonance of gold nanoparticles. Using the MG-EMA model, we have shown that each zone presents a point-to-point variation of the volume fraction of gold in the polymer. From Ψ and Δ ellipsometric maps near the LSPR wavelength and with the MG-EMA model, we are able to calculate two maps: one of the local thickness of the film and a second one of the local volume fraction of AuNPs. This last result highlights the strength of the spectroscopic imaging ellipsometry as a local optical analysis technique.

7.3 Silver nanocomposites at high doping level

In this section, we study the local optical properties of silver nanocomposites by SIE. By using the same analysis procedure than in the AuNPs case, we are able to extract physical data: the refractive index n and the extinction coefficient k as a function of the wavelength.

The experimental procedure to synthesize the AgNPs embedded in PVA matrix is explained in the section 4.2. The analyzed nanocomposite is a thick and highly doped sample, i.e. the silver-to-polymer mass ratio is 25% and the polymer solution is 8% w:w (volume fraction $f_{Ag} = 2.9\%$). The spinning conditions are 60 sec at 1600 rpm. After drying in open-air atmosphere, the coatings are annealed 60 min at 110°C.

As previously explained for the AuNPs case, we use the EP3-SE in order to measure the ellipsometric angles Ψ and Δ at the microscale. The wavelength range is 360 – 1000 nm and the measurements are carried out at an angle of incidence of 42°. The spatial resolution is 1.07 $\mu\text{m} \times 1.07 \mu\text{m}$ per pixel at 42° of incidence.

We start this study by the description of the models used to extract the optical properties of the silver nanocomposite. Then, we measure the ellipsometric angles in two selected regions of interest presenting different optical contrast. By using the model, we can compare the values of the refractive index and the extinction coefficient of these zones.

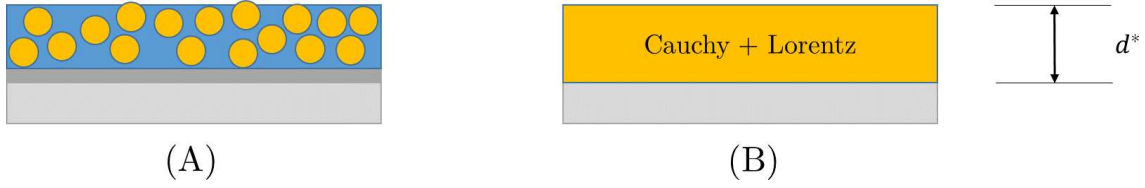


Figure 7.8: Schematic representation of the optical model used to interpret SIE data: (A) AgNPs in PVA layer on Si and (B) a Cauchy model and Lorentzian term used to describe the optical properties of AgNPs in PVA matrix. Shaded area between the polymer layer and the substrate: SiO_2 layer. (Not to scale).

7.3.1 Modeling of the optical properties

The model used for AgNPs embedded in PVA matrix is illustrated in the figure 7.8 (already discussed in section 5.5). The description of the model used for the dielectric matrix has already been shown in the figure 5.2 (Section 5.2).

PVA layer: A one-layer Cauchy model is chosen to represent the optical properties of the PVA films in the transparent range [95].

$$n_{\text{PVA}}(\lambda) = A_{\text{PVA}} + \frac{B_{\text{PVA}}}{\lambda^2} \quad \text{and} \quad k_{\text{PVA}}(\lambda) = 0 \quad (7.2)$$

Ag-PVA layer: A Lorentzian oscillator is added to that model to account for the localized absorption of the plasmon resonance in visible range [102].

In the EP4 software the Lorentzian term is given by:

$$\varepsilon(E) = 1 + \frac{AE_0}{E_0^2 - E^2 - i\Gamma E} \quad (7.3)$$

where E and E_0 are given in eV and correspond to $h\nu$ and $h\nu_0$, respectively. ν_0 is the resonance frequency of the oscillator, AE_0 (eV^2) its oscillator strength and Γ_0 (eV) its full-width at half maximum (FWHM), the damping of the oscillator.

Once these models defined, we are now able to analyze the ellipsometric measurements obtained by the SIE.

7.3.2 Local optical properties of the Ag–PVA thin films

We start this analysis by taking an ellipsometric enhanced contrast image as we have shown for the Au-PVA nanocomposite. This image is presented in the figure 7.9 and reveals few heterogeneities of the optical response of the silver nanocomposite. As we can see, this enhanced image is quite different than the one obtained for the AuNPs case (Fig. 7.3). This difference can be explained by the use of Ag^+ instead of Au^{3+} as the precursors for the metal nanoparticles or by different annealing settings. For AgNPs, these settings are 110°C during 60 min while, for the AuNPs these are 135°C during 120 min. Another difference is the doping level between Au-PVA and Ag-PVA nanocomposite (2.9% for AgNPs and 0.13% for AuNPs). Nevertheless, we can see different zones on the enhanced image, which correspond to areas with different nulling parameters. These regions of interest are represented by red rectangles in the figure 7.9 and named ROI_0 and ROI_1 . These rectangles surround two areas that seem to present different optical contrast.

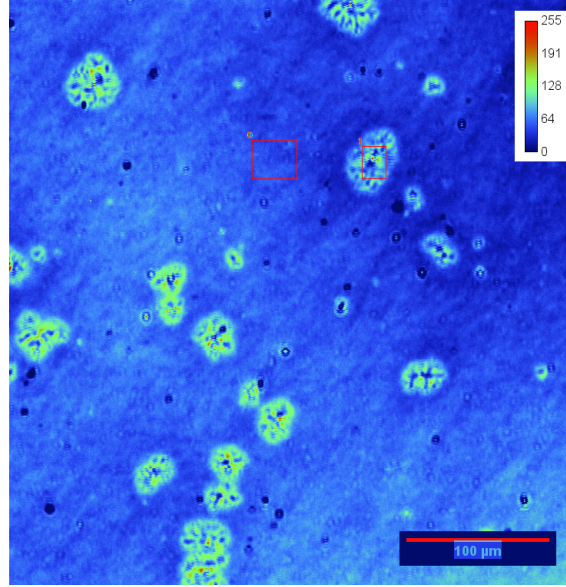


Figure 7.9: Ellipsometric enhanced contrast (grey levels, in false color) image of the Ag-PVA film at the end of the annealing (Scalebar: 100 μm , wavelength: 545 nm, AOI: 42°). Red rectangles indicates the regions of interest “0” and “1” used for spectroscopic characterization.

Table 7.2: Best-fit results of the ellipsometric data obtained with the SIE on AgNPs embedded in PVA matrix within the Lorentzian term in order to take into account the absorption peak.

ROI	Thickness (nm)	Amplitude (eV^2)	Frequency (eV)	Damping (eV)	RMSE
0	445.7 ± 3.0	0.786 ± 0.021	3.000 ± 0.014	0.480 ± 0.021	3.179
1	445.2 ± 3.3	0.608 ± 0.021	2.979 ± 0.012	0.378 ± 0.027	3.405

We measure the ellipsometric spectra in Ψ and Δ in these two regions of interest labelled ROI₀ and ROI₁. The SIE data are analyzed thanks to the model previously described, i.e. a Cauchy law for the matrix and a Lorentzian term for the resonance. The optical properties of the polymer matrix is described by a Cauchy dispersion law (Section 5.2) with the following optimized parameters for the PVA matrix: $A_n = 1.538 \pm 0.009$ and $B_n = 4600 \pm 760 \text{ nm}^2$. The value of the A_n and B_n are fixed in order to determine the oscillator parameters. The best-fit parameters, as well as the RMSE, are given in the table 7.2. The thickness and the oscillator parameters in the different ROIs are slightly different. The amplitude of the oscillator is smaller for the ROI₁ than for ROI₀, while its damping is higher. These differences lead to a variation of the optical properties of the two selected zones as presented in the figure 7.10.

For each region of interest, the refractive index n and the extinction coefficient k as a function of the wavelength are drawn based on the optimized values of the table 7.2. The difference in the two ROIs modifies the optical properties of the doped polymer film. For both ROI₁ and ROI₀, the presence of the absorption peak near 415 nm in the extinction coefficient spectrum k (Fig. 7.10B) induces a large oscillation

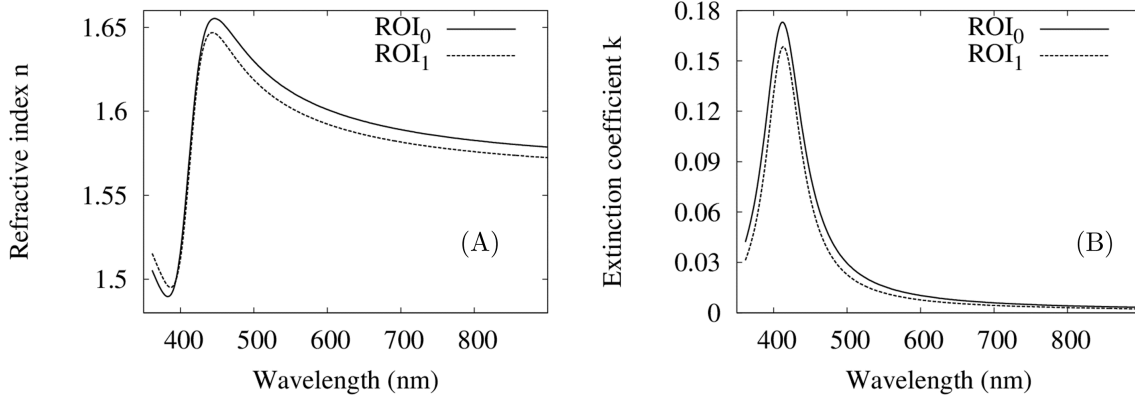


Figure 7.10: Optical properties of 445.7 nm-thick silver nanocomposite film ([Ag]:[PVA] ratio: 25% w:w): A, refractive index n ; B, extinction coefficient k .

in the refractive index value (Fig. 7.10A) due to the Kramers-Krönig consistency of the optical properties (Eq. 3.83). Due to the high doping of the sample, the extinction coefficient at the LSPR is large, which leads to an important oscillation in the refractive index compared to the AuNPs case.

To sum up, we used the EP3-SE in order to determine the local optical properties of silver nanocomposite at microscale. By using the same method as in the AuNPs case, we are able to compare the optical properties of different areas, which seem different on the enhanced grey scale image. This promising method, that we validated in these two previous section, can be used in other experiments in order to analyze the local optical properties of this kind of nanocomposites.

7.4 Conclusion

In this chapter, we have presented an experimental study of the optical properties of lowly doped gold and highly doped silver nanocomposites using spectroscopic imaging ellipsometry.

Concerning AuNPs, despite a very limited volume fraction of gold ($f_{Au} < 0.2\%$) in the polymer matrix, we have shown that the growth of the AuNPs inhomogeneously occurred within the film. At this low doping level, the optical constant determined by the conventional spectroscopic ellipsometry spectra is only relevant for the polymer matrix. We have also shown the advantage of using spatially-resolved spectroscopic ellipsometry by choosing areas on the image with a different intensity contrast. The ellipsometric spectra of each region of interest are different, especially between 400 nm and 600 nm, the spectral region corresponding to the localized surface plasmon resonance of gold nanoparticles. Using the MG-EMA model, we have shown that each zone presents a point-to-point variation of the volume fraction of gold in the polymer. From Ψ and Δ ellipsometric maps near the LSPR wavelength and with the MG-EMA model, we are able to calculate two maps: a first one of the local thickness of the film and a second one of the local volume fraction of AuNPs. This last result highlights the strength of the spectroscopic imaging ellipsometry as a local optical analysis technique. Compared to the conventional spectroscopic

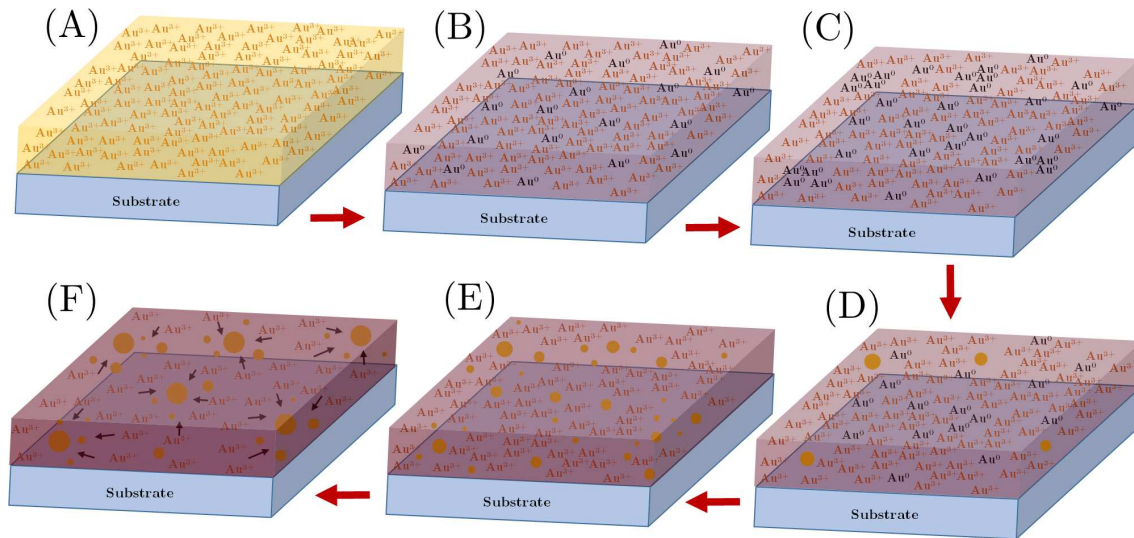


Figure 7.11: Mechanism of growth of AuNPs in PVA matrix at very low doping level during the thermal annealing at 135°C. (A) Homogeneous distribution of the metallic precursor within the film. (B) Isotropic reduction of Au³⁺ to Au⁰ in the film. (C) Gold atoms start to gather to form small clusters. (D) Growth of the small gold clusters on AuNPs. (E) Increase of the number of small AuNPs in the film. (F) Large AuNPs acting like seeds to drag isolated gold atoms and/or gold cations remaining in the film.

ellipsometry, the SIE allows to detect the optical response of a local volume fraction of gold nanoparticles of ca. 0.1% in the polymer film at a (sub)microscale. It seems that the detection limit of the average gold volume fraction by the SIE is near 0.06%, while the conventional SE presents difficulties for less than 1%.

We have also presented an ellipsometric enhanced contrast image (Fig. 7.3) and Ψ and Δ images of the gold nanocomposites taken at different wavelengths (Fig. 7.4). As we showed in the chapter 6, we clearly see from the ellipsometric images that the AuNPs grow inhomogeneously within the film. As explained in the chapter 6, this result could be related to the work of Nadal [78], already introduced in the chapter 2. They assumed that gold atoms (Au⁰) and gold cations (Au³⁺) can diffuse in the polymer towards growing AuNPs, this latter which act as seeds and tend to drag the surrounding gold atoms to contribute to the growth of AuNPs. The analysis of the local volume fraction map calculated from the MG-EMA model confirms that larger AuNPs are built by some kind of drainage of the metal atoms in their neighborhood, leaving a depletion zone around the AuNPs.

In this context, we try to propose a mechanism leading to this nanostructuration at this very low doping level. At the beginning of the annealing, the reduction of Au³⁺ in Au⁰ is isotropic within the film. These Au⁰, which can diffuse in the polymer, start to gather, leading to the formation Au clusters. This local agglomeration induces an optical response detected by the SIE. With their growth, these clusters become AuNPs but cannot diffuse in the polymer anymore due to their too large size. These large AuNPs start to act as seeds and drag the surrounding gold atoms or cations to contribute to their growth. This drainage of the metal atoms leads to a depletion zone surrounding the AuNPs as we can see in the figures 7.3 and 7.4. Indeed, the optical response of Au³⁺ and isolated Au⁰ cannot be detected

by the SIE due to their small size. This probable mechanism is presented in the figure 7.11 and can be explained as follows. After the spin coating, the metallic precursor is homogeneously distributed in the film (Fig. 7.11A). After the start of the thermal annealing, the reduction of the gold cations Au^{3+} to gold atoms Au^0 occurs (Fig. 7.11B). These gold atoms diffuse in the polymer in order to form small gold clusters (Fig. 7.11C). The figure 7.11D presents the transformation of gold clusters to small AuNPs. The constant thermal annealing leads to a higher concentration of the AuNPs within the film (Fig. 7.11E). These first images (A to E) correspond to the first part of annealing. After 90 min, in our case, some AuNPs are too large and cannot diffuse in the film. These large AuNPs start to act like seeds and try to drag the smaller AuNPs and/or the gold cations remaining in the film, as represented by an arrow in the figure 7.11F. This should be the explanation of the growth mechanism of AuNPs in the PVA matrix. However, at this time, this growth mechanism is still to be experimentally or numerically confirmed.

Concerning AgNPs, we have first shown that the ellipsometric enhanced contrast image is clearly different than the ellipsometric image of AuNPs. That difference can be explained by the difference between optical properties of the metals used, but also by the different heating conditions for gold (135°C, 120 min) or silver (110°C, 60 min) nanocomposites or by the difference in the doping level. By selecting two areas, which seem to present different optical properties, we have calculated the optical properties of each zones. The optical properties between the two zones slightly differ as it is demonstrated on the extinction coefficient spectra.

Finally, the spatially resolved optical response obtained by the SIE reveals the details of the sample at the microscale. Therefore, the ellipsometric measurements can be reduced to a particular region of interest. These zones can present different optical properties leading to different optical responses in the camera images. These different signals are interpreted by different setting of the angles of polarizer and analyzer to extinguish the beam, leading to a different recorded value of Ψ and Δ angle of each areas. Thus, it is possible to measure, over the visible range, the optical properties of these regions of interest that lead to a detection of the optical properties at the microscale.

This experimental process is probably also valid for another type of nanocomposites or samples. Here, we demonstrated the strength of the spectroscopic imaging ellipsometry as a local optical analysis technique.

Conclusion and outlook

Throughout this thesis, we studied the optical properties of nanocomposites embedding silver or gold nanoparticles. This class of new attractive materials, composed of a dielectric matrix and embedded metal nanoparticles (NPs), is often studied due to one aspect of their optical properties: the Localized Surface Plasmon Resonance (LSPR). At the beginning of the analysis of both silver nanocomposites and gold nanocomposites, we demonstrated that the preparation method called “one-pot synthesis” is convenient to synthesize this type of nanocomposites. This synthesis approach has numerous advantages: it is simpler, faster and lead to higher concentration of NPs in the nanocomposite than other synthesis schemes. We especially focused our study on the optical properties of a model system: silver nanoparticles (AgNPs) and gold nanoparticles (AuNPs) embedded in a polymer dielectric matrix, the poly-(vinyl) alcohol (PVA).

We started in chapter 5 by studying the LSPR parameters of AgNPs in a PVA matrix. More precisely, our goal was to study the impact of the thickness of the film and of the silver concentration in the polymer matrix on the LSPR parameters. We experimentally observed a different behavior between the thick and thin films as a function of the silver concentration. The measurements made at the nanoscale by atomic force microscopy (AFM), i.e. topography and phases images, have shown that the size of the AgNPs seems to be larger in thin films than in thick films. This

trend has also been evidenced by spectrophotometry. By keeping the same silver-to-polymer mass ratio, we measured a red-shift of the position of the resonance peak while changing the thickness of the film from thick to thin samples. Since the position of the resonance peak can be related to the size of the AgNPs embedded in the polymer matrix, we concluded that thin nanocomposite films induce a larger size of the grown nanoparticles than in the thicker ones.

At the end of the chapter 5, we measured samples with different thicknesses and different silver concentration in the polymer by using spectroscopic ellipsometry. We acquired ellipsometric spectra and determined the plasmon resonance parameters (A , Λ_0 and Γ_0). By using multivariate analysis on these samples, we have shown that at a given Ag^+ doping level, thin and thick films behave differently. These differences can be related to the growing process of the AgNPs in the polymer matrix: the AgNPs differently growth in thick and thin films. A possible explanation of this different growth process can be associated to the diffusion process. More precisely, in thin films, the NPs grow in a 2D-like matrix due the thickness of the film constrained by the substrate and the film/air interface. The diffusion process of silver ions or atoms is therefore limited leading to larger NPs. On the contrary, in thick films, the interfacial effect is expected to be less marked and the NPs rapidly form a 3D structure.

In chapter 6, we studied the optical properties of nanocomposites containing *in situ* grown AuNPs. In particular, we focused the study on the optical response of Au-doped PVA films during the annealing, i.e. during the growth of AuNPs. The samples were annealed during 120 min at 135°C and we measured their optical properties by spectrophotometry and imaging ellipsometry. By measuring the absorption spectra during the annealing, we experimentally showed that the variation rate of absorbance, at the LSPR wavelength, changes near 90 min. More precisely, it was 2.5 times larger after 90 min than the increase rate before 90 min. This can be explained by a larger increase of the AuNPs number inside the polymer matrix after 90 min.

Afterwards, we focused our analysis on a weakly doped gold nanocomposite, which correspond to a theoretical volume fraction $f_{\text{Au}} = 0.13\%$. Thanks to imaging ellipsometry, we have clearly observed diffraction patterns due to the formation of AuNPs in spite of the low volume fraction of gold in the nanocomposite. The ellipsometric Ψ and Δ maps reveal that the growth of the AuNPs inhomogeneously occurred within the film. We have presented ellipsometric maps taken during the annealing of the sample. By calculating the statistical distribution of each maps, we plotted the variation of the mean value and the standard deviation of these Ψ and Δ maps, which highlight the increase of the standard deviation after 90 min of annealing corresponding to an increase of the AuNPs in the polymer matrix.

Also in chapter 6, we presented an unusual analysis of these mean value of the statistical distribution of each map during the annealing. Due to the operating wavelength of the imaging ellipsometer ($\lambda_i = 658 \text{ nm}$), we showed that we can process our ellipsometric data by using a simple model based on an one-layer optical model with variable thickness and adjustable real refractive index. In order to extract physical parameters, we plotted the constant angle of incidence (CAI) curves and superimposed our experimental data, hence providing the variation of the thick-

ness and the refractive index during the annealing. We showed that after an initial period, the dynamics of the annealing is composed by two distinct parts: the first one corresponds to a decrease of film thickness, and the second one is attributed to an increase of the refractive index. This increase of the refractive index, appearing after 90 min, can be related to the increase rate of the absorbance in the spectrophotometric measurements. Based on the result obtained by Nadal and coworkers [78], this variation could be related to the grown AuNPs acting as seeds and dragging the surrounding gold atoms, leading to the growth of larger AuNPs and leaving a depletion zone around the AuNPs.

Finally, we measured the reflectivity spectra of weakly doped gold nanocomposite. This weak doping level induce a non-detection of the presence of the AuNPs in the polymer film. The reason of this non-detection is found in the measurement of the reflectivity. In fact, the spectroscopic reflectometer measures the mean value of the reflected intensity received by the sensor and moreover, cannot measure the phase-shift. With a higher gold-to-polymer mass ratio, we showed that it is possible to detect the LSPR by spectroscopic reflectometry (SR).

At the beginning of chapter 7, we used spectroscopic ellipsometry (SE) on low-doped gold nanocomposite in order to measure the phase-shift missing in the SR measurements. The ellipsometric spectra did not reveal the presence of the AuNPs at this low doping level. In fact, the SE measurement is an averaged measure of the reflected light on the spot size. More precisely, at this low doping level, the optical constant determined by the SE spectra is only relevant for the polymer matrix.

These drawbacks are bypassed with the spectroscopic imaging ellipsometry (SIE). Despite a very limited volume fraction of gold ($f_{\text{Au}} < 0.2\%$) in the polymer matrix, we have shown that the growth of the AuNPs inhomogeneously occurred within the film. We have also shown the advantage of using spatially-resolved spectroscopic ellipsometry by choosing areas on the image with a different intensity contrast. The ellipsometric spectra of each region of interest are different, especially between 400 nm and 600 nm, the spectral region corresponding to the LSPR of gold nanoparticles. By using the Maxwell-Garnett effective medium approximation (MG-EMA), we have presented the optical properties of these two regions of interest at microscale. From Ψ and Δ ellipsometric maps near the LSPR wavelength and with the MG-EMA model, we have presented two physical data maps: one of the local thickness of the film and a second one of the local volume fraction of AuNPs. This last result highlights the strength of the SIE as a local optical analysis technique. Compared to the conventional SE, the SIE allows to detect the optical response of a local volume fraction of gold nanoparticles of ca. 0.1% in the polymer film at a (sub)micron scale.

In the last chapter of the thesis, we also proposed a mechanism of growth of AuNPs in the PVA matrix at very low doping level. The reduction of Au^{3+} in Au^0 is isotropic within the film at the beginning of the thermal annealing. These reduced gold atoms diffuse in the film and start to gather to form small gold clusters. This local agglomeration allows the formation of small AuNPs, which can be detected by the SIE. The growth of these small AuNPs leads to larger AuNPs that cannot diffuse in the film due to their large size. The growing process is determined by the seeds effects of the AuNPs, which try to drag the isolated gold atoms and/or

the gold cations remaining within the film. This drainage of the metal atoms leads to a depletion zone surrounding the AuNPs. Let us note that this explanation to depict the growing process is only valid in the weak doping level. At a larger doping level, the growing process could be different due to the higher concentration of AuNPs within the film. Nevertheless, this growth mechanism has to be confirmed by experimental or numerical results.

At the end of chapter 7, we showed that the detection of the optical properties at microscale can be used for other types of nanocomposites. We have measured the local optical properties of AgNPs embedded in the polymer matrix. This experimental process can be used for another type of nanocomposites or samples. We have evidenced here the strength of the spectroscopic imaging ellipsometry as a local optical analysis technique.

Let us now consider some outlooks or further possible developments. This thesis is an experimental work, which means that there are numerous experimental parameters playing a role in the preparation of these nanocomposites. This work has partially lifted the veil on the reduction mechanisms of noble metals in nanoplasmonic compounds but, despite these results, several questions remain open. More precisely, our work has unravelled the effect of some experimental parameters in the onset of the plasmon resonance for nanocomposites.

Concerning AuNPs, a first idea for a future work is to change the ramp temperature from 10°C/min to 1°C/min in order to follow the kinetics of growth of NPs with different annealing conditions. We can also bypass this annealing ramp by directly setting the temperature at 135°C. We can expect a variation in the growing process leading finally to different sizes of AuNPs for example. Secondly, another prospect is to achieve to follow the cations or the atoms during the annealing of the nanocomposite. A possibility is to attach fluorescent markers on cations or atoms. This experiment can be interesting to understand the relative change in the optical properties after 90 min of annealing. By adjusting the temperature of annealing and the mass concentration of gold in the polymer, it could be possible to experimentally confirm this impact.

For AgNPs, it could be interesting to change the temperature of annealing to 135°C, the same temperature as AuNPs. As shown by Clémenson [69, 113], higher temperature of annealing induces larger AgNPs in the polymer. These larger AgNPs can produce diffraction patterns on the sample detected by SIE as in the AuNPs case. By using the same experimental procedure than for the growth of AuNPs (i.e. 135°C, 10°C/min and 120 min of annealing), we could detect different variation rate of absorbance, at the LSPR wavelength, during the annealing with real time spectrophotometric measurements. We could make more experiments in order to interpret the size difference of AgNPs in thinner films than in thicker films. One possibility is to measure the spatial distribution of the AgNPs in the polymer film thickness by using transmission electron microscopy (TEM). These measurements are highly challenging due to two factors: the rigidity contrast between the polymer matrix and their substrate and the very low thickness of the films (< 50 nm).

For both AuNPs and AgNPs, an interesting outlook could be the measurement of the surface parameters of the nanocomposite films at the nanoscale during the annealing. By placing the sample on a heating stage attached to the atomic force

microscope, it could be possible to measure the topography and the phase during the annealing of the sample. This experiment can provide numerous information about the growth of NPs and more precisely, in the case of AuNPs, on the variation rate of growth observed after 90 min of annealing.

Another future work could be the measure of the optical properties as a function of the temperature of a prepared sample, i.e. after the formation of the NPs in the PVA matrix. With this, we could measure the thermo-optic coefficient dn/dT of the prepared nanocomposite, for example.

Finally, the experimental procedure to analyze the sample at the microscale thanks to the SIE can be used for other materials. More precisely, materials composed of different areas presenting different optical contrasts can be measured at the same time. As presented in chapter 6, we are able to calculate physical data map of the sample by using theoretical model. Nevertheless, this pixel-by-pixel calculation is time-consuming. We have already tested a new approach to improve and speed up this calculation by using hierarchical clustering. More precisely, each pixel of the ellipsometric maps can be gathered in clusters. By using agglomerative hierarchical clustering, we can finally have two clusters containing the other clusters. Then, we can process models on these two clusters. Finally, the optimized parameters are repropagated on all pixels of the Ψ and Δ map. This improvement has to be tested on different samples.

As shown by this thesis, the preparation of these kind of nanocomposites is simple, but understanding the growth process is challenging. Besides the experimental results presented in this thesis, more experimental and numerical works are needed to clearly understand all mechanisms playing a role during the growth of NPs. Without a doubt that one day, we will be able to successfully unravel the mysteries of the growth of NPs in a polymer matrix.

Bibliography

- [1] C. Guyot, P. Vandestrück, I. Marenne, O. Deparis, and M. Voué, “Growth dynamics and light scattering of gold nanoparticles in situ synthesized at high concentration in thin polymer films,” *Beilstein Journal of Nanotechnology*, vol. 10, pp. 1768–1777, 2019.
- [2] C. Guyot, P. Leclère, and M. Voué, “Gold nanoparticles growing in a polymer matrix: What can we learn from spectroscopic imaging ellipsometry?,” *Journal of Vacuum Science & Technology B*, vol. 38, p. 013602, Jan. 2020.
- [3] M. Faraday, “The bakerian lecture: —experimental relations of gold (and other metals) to light,” *Philosophical Transactions of the Royal Society of London*, vol. 147, pp. 145–181, Dec. 1857.
- [4] J. Kunckel, “Ars vitraria experimentalis,” p. 192, 1679.
- [5] F. Kirchner and R. Zsigmondy, “The causes of the color changes of gold-gelatine compounds,” *Annalen der Physik*, vol. 15, pp. 573–595, 1904.
- [6] J. C. M. Garnett, “Colours in metal glasses and in metallic films,” *Philosophical Transactions of the Royal Society A: Mathematical, Physical and Engineering Sciences*, vol. 203, pp. 385–420, Jan. 1904.
- [7] G. Mie, “Beiträge zur optik trüber medien, speziell kolloidaler metallösungen,” *Annalen der Physik*, vol. 330, no. 3, pp. 377–445, 1908.
- [8] D. Pines and D. Bohm, “A collective description of electron interactions: II. collective vs individual particle aspects of the interactions,” *Physical Review*, vol. 85, pp. 338–353, Jan 1952.

- [9] E. Kretschmann and H. Raether, "Notizen: Radiative decay of non radiative surface plasmons excited by light," *Zeitschrift für Naturforschung A*, vol. 23, pp. 2135–2136, Dec. 1968.
- [10] A. Otto, "Excitation of nonradiative surface plasma waves in silver by the method of frustrated total reflection," *Zeitschrift für Physik A Hadrons and nuclei*, vol. 216, pp. 398–410, Aug. 1968.
- [11] U. Kreibig and M. Vollmer, *Optical Properties of Metal Clusters*. Springer series in materials science, Springer, 1995.
- [12] D. D. Evanoff and G. Chumanov, "Synthesis and optical properties of silver nanoparticles and arrays," *ChemPhysChem*, vol. 6, no. 7, pp. 1221–1231, 2005.
- [13] J. Turkevich, P. C. Stevenson, and J. Hillier, "A study of the nucleation and growth processes in the synthesis of colloidal gold," *Discussion Faraday Society*, vol. 11, pp. 55–75, 1951.
- [14] G. Frens, "Particle size and sol stability in metal colloids," *Kolloid-Zeitschrift und Zeitschrift für Polymere*, vol. 250, pp. 736–741, Jul 1972.
- [15] T. J. Davis, D. E. Gómez, and A. Roberts, "Plasmonic circuits for manipulating optical information," *Nanophotonics*, vol. 6, Jan. 2016.
- [16] J. R. Morones, J. L. Elechiguerra, A. Camacho, K. Holt, J. B. Kouri, J. T. Ramírez, and M. J. Yacaman, "The bactericidal effect of silver nanoparticles," *Nanotechnology*, vol. 16, pp. 2346–2353, aug 2005.
- [17] N. Bhat, N. Karmakar, and D. Kothari, "Synthesis of nanocomposites of polyvinyl alcohol with silver nanoparticles and their use," *International Journal of Nanoscience*, vol. 12, p. 1350029, 2013.
- [18] M.-C. Daniel and D. Astruc, "Gold nanoparticles : Assembly, supramolecular chemistry, quantum-size-related properties, and applications toward biology, catalysis, and nanotechnology," *Chemical Reviews*, vol. 104, pp. 293–346, 2004.
- [19] X. Huang and M. A. El-Sayed, "Gold nanoparticles: Optical properties and implementations in cancer diagnosis and photothermal therapy," *Journal of Advanced Research*, vol. 1, pp. 13–28, Jan. 2010.
- [20] C. Louis and O. Pluchery, *Gold nanoparticles for physics, chemistry and biology*. 2012.
- [21] P. Mandal and S. Sharma, "Progress in plasmonic solar cell efficiency improvement: A status review," *Renewable and Sustainable Energy Reviews*, vol. 65, pp. 537–552, Nov. 2016.
- [22] H. Peeters, M. Keulemans, G. Nuyts, F. Vanmeert, C. Li, M. Minjauw, C. Detavernier, S. Bals, S. Lenaerts, and S. W. Verbruggen, "Plasmonic gold-embedded TiO₂ thin films as photocatalytic self-cleaning coatings," *Applied Catalysis B: Environmental*, vol. 267, p. 118654, June 2020.

- [23] K. Awazu, M. Fujimaki, C. Rockstuhl, J. Tominaga, H. Murakami, Y. Ohki, N. Yoshida, and T. Watanabe, "A plasmonic photocatalyst consisting of silver nanoparticles embedded in titanium dioxide," *Journal of the American Chemical Society*, vol. 130, pp. 1676–1680, Feb. 2008.
- [24] P. Kumar, M. C. Mathpal, A. K. Tripathi, J. Prakash, A. Agarwal, M. M. Ahmad, and H. C. Swart, "Plasmonic resonance of Ag nanoclusters diffused in soda-lime glasses," *Physical Chemistry Chemical Physics*, vol. 17, no. 14, pp. 8596–8603, 2015.
- [25] L. Nicolais and G. Carotenuto, eds., *Nanocomposites*. John Wiley & Sons, Inc, Dec. 2013.
- [26] H. Ambrohn and R. Zsigmondy, "Ueber pleochroismus doppelbrechender gelatine nach färbung mit gold-und silberlösungen," *Ber. Verhandlungen Königl. Sächs. Ges. Wiss. Leipzig Math. Phys. Klasse*, vol. 51, pp. 13–15, 1899.
- [27] E. Kolbe. PhD thesis, Jena, 1913.
- [28] R. Kuladeep, L. Jyothi, S. Chakradhar, and D. Rao, "Fabrication of metal nanostructures in a polymer matrix using femtosecond laser writing technique," *Optical Engineering*, vol. 53, p. 071823, 2014.
- [29] E. Cattaruzza, G. Battaglin, F. Gonella, R. Polloni, B. Scremin, G. Mattei, P. Mazzoldi, and C. Sada, "Au / Cu nanoparticles in silica glass as composite material for photonic applications," *Applied Surface Science*, vol. 254, pp. 1017 – 1021, 2007.
- [30] S. Anthony, S. Porel, D. Rao, and T. Radhakrishnan, "Thin films of metal-organic compounds and metal nanoparticle-embedded polymers for nonlinear optical applications," *Pramana - Journal of Physics*, vol. 65, pp. 871–879, 2005.
- [31] X. Chen, J. Tao, G. Zou, Q. Zhang, and P. Wang, "Nonlinear optical properties of nanometer-size silver composite azobenzene containing polydiacetylene film," *Applied Physics A: Materials Science and Processing*, vol. 100, pp. 223–230, 2010.
- [32] H. Chowdhury, X. Xu, P. Huynh, and M. B. Cortie, "Radiative heat transfer across glass coated with gold nano-particles," *Journal of Solar Energy Engineering*, vol. 127, pp. 70–75, 2005.
- [33] X. Xu, M. Stevens, and M. B. Cortie, "In situ precipitation of gold nanoparticles onto glass for potential architectural applications," *Chemistry of Materials*, vol. 16, pp. 2259–2266, 2004.
- [34] J. Yin, G. Feng, S. Zhou, H. Zhang, S. Wang, and H. Zhang, "The shape effect of Au particles on random laser action in disordered media of Rh6G dye doped with PMMA polymer," *Journal of Modern Optics*, vol. 63, pp. 1998–2002, 2016.

- [35] X. Meng, K. Fujita, Y. Moriguchi, Y. Zong, and K. Tanaka, "Metal–dielectric core–shell nanoparticles: Advanced plasmonic architectures towards multiple control of random lasers," *Advanced Optical Materials*, vol. 1, pp. 573–580, 2013.
- [36] L. De Boni, E. Wood, C. Toro, and F. E Hernandez, "Optical saturable absorption in gold nanoparticles," *Plasmonics*, vol. 3, p. 171, 2008.
- [37] T. Jiang, Y. Xu, Q. Tian, L. Liu, Z. Kang, R. Yang, G. Qin, and W. Qin, "Passively Q-switching induced by gold nanocrystals," *Applied Physics Letters*, vol. 101, p. 151122, Oct. 2012.
- [38] D. Wu, J. Peng, Z. Cai, J. Weng, Z. Luo, N. Chen, and H. Xu, "Gold nanoparticles as a saturable absorber for visible 635 nm q-switched pulse generation," *Optics Express*, vol. 23, pp. 24071–24076, Sep 2015.
- [39] E. Stratakis and E. Kymakis, "Nanoparticle-based plasmonic organic photovoltaic devices," *Materials Today*, vol. 16, pp. 133–146, Apr. 2013.
- [40] H. A. Atwater and A. Polman, "Plasmonics for improved photovoltaic devices," *Nature Materials*, vol. 9, pp. 205–213, Feb. 2010.
- [41] P. K. Jain, X. Huang, I. H. El-Sayed, and M. A. El-Sayed, "Review of some interesting surface plasmon resonance-enhanced properties of noble metal nanoparticles and their applications to biosystems," *Plasmonics*, vol. 2, pp. 107–118, July 2007.
- [42] C. F. Bohren and D. R. Huffman, *Absorption and Scattering of Light by Small Particles*. Wiley, Apr. 1998.
- [43] K. L. Kelly, E. Coronado, L. L. Zhao, and G. C. Schatz, "The optical properties of metal nanoparticles: The influence of size, shape, and dielectric environment," *Journal of Physical Chemistry B*, vol. 107, pp. 668–677, 2003.
- [44] Y. Battie, I. Izquierdo-Lorenzo, A. Resano-Garcia, A. E. Naciri, S. Akil, P. M. Adam, and S. Jradi, "How to determine the morphology of plasmonic nanocrystals without transmission electron microscopy?," *Journal of Nanoparticle Research*, vol. 18, p. 217, Aug 2016.
- [45] D. A. G. Bruggeman, "Berechnung verschiedener physikalischer konstanten von heterogenen substanzen. i. dielektrizitätskonstanten und leitfähigkeiten der mischkörper aus isotropen substanzen," *Annalen der Physik*, vol. 416, no. 7, pp. 636–664, 1935.
- [46] S. Kéki, J. Török, G. Deák, L. Daróczi, and M. Zsuga, "Silver nanoparticles by PAMAM-assisted photochemical reduction of Ag^+ ," *Journal of Colloid and Interface Science*, vol. 229, pp. 550–553, Sept. 2000.
- [47] X. Huang, S. Neretina, and M. A. El-Sayed, "Gold nanorods: From synthesis and properties to biological and biomedical applications," *Advanced Materials*, vol. 21, pp. 4880–4910, 2009.

- [48] C. J. Murphy, L. B. Thompson, D. J. Chernak, J. A. Yang, S. T. Sivapalan, S. P. Boulos, J. Huang, A. M. Alkilany, and P. N. Sisco, "Gold nanorod crystal growth: From seed-mediated synthesis to nanoscale sculpting," *Current Opinion in Colloid & Interface Science*, vol. 16, pp. 128–134, 2011.
- [49] V. K. LaMer and R. H. Dinegar, "Theory, Production and Mechanism of Formation of Monodispersed Hydrosols," *Journal of the American Chemical Society*, vol. 72, pp. 4847–4854, Nov. 1950.
- [50] T. Sugimoto, "Underlying mechanisms in size control of uniform nanoparticles," *Journal of Colloid and Interface Science*, vol. 309, pp. 106–118, May 2007.
- [51] N. T. K. Thanh, N. Maclean, and S. Mahiddine, "Mechanisms of nucleation and growth of nanoparticles in solution," *Chemical Reviews*, vol. 114, pp. 7610–7630, July 2014.
- [52] Z. H. Mbhele, M. G. Salemane, C. G. C. E. van Sittert, J. M. Nedeljković, V. Djoković, and A. S. Luyt, "Fabrication and characterization of silver-polyvinyl alcohol nanocomposites," *Chemistry of Materials*, vol. 15, pp. 5019–5014, 2003.
- [53] M. I. Baker, S. P. Walsh, Z. Schwartz, and B. D. Boyan, "A review of polyvinyl alcohol and its uses in cartilage and orthopedic applications," *Journal of Biomedical Materials Research Part B: Applied Biomaterials*, vol. 100B, pp. 1451–1457, Apr. 2012.
- [54] M. L. Hallensleben, R. Fuss, and F. Mummy, *Polyvinyl Compounds, Others*, pp. 1–23. American Cancer Society, 2015.
- [55] C. Wilkes, J. Summers, C. Daniels, and M. Berard, *PVC Handbook*. Hanser, 2005.
- [56] C. Luo, Y. Zhang, X. Zeng, Y. Zeng, and Y. Wang, "The role of poly(ethylene glycol) in the formation of silver nanoparticles," *Journal of Colloid and Interface Science*, vol. 288, pp. 444–448, Aug. 2005.
- [57] I. Washio, Y. Xiong, Y. Yin, and Y. Xia, "Reduction by the end groups of poly(vinyl pyrrolidone): A new and versatile route to the kinetically controlled synthesis of Ag triangular nanoplates," *Advanced Materials*, vol. 18, pp. 1745–1749, July 2006.
- [58] R. Abargues, K. Abderrafi, E. Pedrueza, R. Gradess, J. Marqués-Hueso, J. L. Valdés, and J. Martínez-Pastor, "Optical properties of different polymer thin films containing in situ synthesized ag and au nanoparticles," *New Journal of Chemistry*, vol. 33, pp. 1720–1725, 2009.
- [59] P. Khanna, N. Singh, S. Charan, V. Subbarao, R. Gokhale, and U. Mulik, "Synthesis and characterization of Ag/PVA nanocomposite by chemical reduction method," *Materials Chemistry and Physics*, vol. 93, pp. 117–121, Sept. 2005.

- [60] A. N. Ananth, S. Umapathy, J. Sophia, T. Mathavan, and D. Mangalraj, "On the optical and thermal properties of in situ/ex situ reduced Ag NP's/PVA composites and its role as a simple SPR-based protein sensor," *Applied Nanoscience*, vol. 1, pp. 87–96, July 2011.
- [61] B. Karthikeyan, "Spectroscopic studies on Ag–polyvinyl alcohol nanocomposite films," *Physica B: Condensed Matter*, vol. 364, pp. 328–332, July 2005.
- [62] S. Porel, S. Singh, and T. P. Radhakrishnan, "Polygonal gold nanoplates in a polymer matrix," *Chemical Communications*, pp. 2387–2389, 2005.
- [63] S. Porel, S. Singh, S. S. Harsha, D. N. Rao, and T. P. Radhakrishnan, "Nanoparticle-Embedded Polymer: In Situ Synthesis, Free-Standing Films with Highly Monodisperse Silver Nanoparticles and Optical Limiting," *Chemistry of Materials*, vol. 17, pp. 9–12, Jan. 2005.
- [64] S. Porel, N. Venkatram, D. Narayana Rao, and T. P. Radhakrishnan, "In Situ Synthesis of Metal Nanoparticles in Polymer Matrix and Their Optical Limiting Applications," *Journal of Nanoscience and Nanotechnology*, vol. 7, pp. 1887–1892, June 2007.
- [65] S. Porel, N. Venkatram, D. N. Rao, and T. P. Radhakrishnan, "Optical power limiting in the femtosecond regime by silver nanoparticle–embedded polymer film," *Journal of Applied Physics*, vol. 102, p. 033107, Aug. 2007.
- [66] G. Ramesh, B. Sreedhar, and T. Radhakrishnan, "Real time monitoring of the in situ growth of silver nanoparticles in a polymer film under ambient conditions," *Physical Chemistry Chemical Physics*, vol. 11, pp. 10059–10063, 2009.
- [67] G. V. Ramesh, S. Porel, and T. P. Radhakrishnan, "Polymer thin films embedded with in situ grown metal nanoparticles," *Chemical Society Reviews*, vol. 38, pp. 2646–2656, 2009.
- [68] S. Clémenson, P. Alcouffe, L. David, and E. Espuche, "Structure and morphology of membranes prepared from polyvinyl alcohol and silver nitrate: influence of the annealing treatment and of the film thickness," *Desalination*, vol. 200, pp. 437–439, 2006.
- [69] S. Clémenson, L. David, and E. Espuche, "Structure and morphology of nanocomposite films prepared from polyvinyl alcohol and silver nitrate: Influence of thermal treatment," *Journal of Polymer Science Part A: Polymer Chemistry*, vol. 45, pp. 2657–2672, 2007.
- [70] T. Oates, H. Wormeester, and H. Arwin, "Characterization of plasmonic effects in thin films and metamaterials using spectroscopic ellipsometry," *Progress in Surface Science*, vol. 86, no. 11-12, pp. 328 – 376, 2011.
- [71] T. Oates, "Real time spectroscopic ellipsometry of nanoparticle growth," *Applied Physics Letters*, vol. 88, p. 213115, 2006.

- [72] T. Oates and E. Christalle, “Real-time spectroscopic ellipsometry of silver nanoparticle formation in poly(vinyl alcohol) thin films,” *Journal of Physical Chemistry C*, vol. 111, pp. 182–187, 2007.
- [73] N. Dahmouchène, S. Coppée, M. Voué, and J. De Coninck, “Silver nanoparticles embedded in polymer matrices - a ftir-se study,” *physica status solidi (c)*, vol. 5, pp. 1210–1214, 2008.
- [74] M. Voué, N. Dahmouchène, and J. De Coninck, “Annealing of polymer films with embedded silver nanoparticles: Effect on optical properties,” *Thin Solid Films*, vol. 519, pp. 2963–2967, 2011.
- [75] M. Sakamoto, T. Tachikawa, M. Fujitsuka, and T. Majima, “Two-color two-laser fabrication of gold nanoparticles in a PVA film,” *Chemical Physics Letters*, vol. 420, no. 1, pp. 90 – 94, 2006.
- [76] C. Sun, R. Qu, C. Ji, Y. Meng, C. Wang, Y. Sun, and L. Qi, “Preparation and property of polyvinyl alcohol-based film embedded with gold nanoparticles,” *Journal of Nanoparticles Research*, vol. 11, pp. 1005–1010, 2009.
- [77] J. Vieaud, *Effective optical properties of polymer - gold nanoparticle composite film*. PhD thesis, Université de Bordeaux 1, Bordeaux, France, 2011.
- [78] E. Nadal, N. Barros, H. Glénat, J. Laverdant, D. S. Schmool, and H. Kachkachi, “Plasmon-enhanced diffraction in nanoparticle gratings fabricated by in situ photo-reduction of gold chloride doped polymer thin films by laser interference patterning,” *Journal of Materials Chemistry C*, vol. 5, no. 14, pp. 3553–3560, 2017.
- [79] R. Omar, *New way of synthesis of uniform gold nanoparticles for the detection of few molecules*. PhD thesis, Université de Lorraine et Université Libanaise, 2017.
- [80] E. Nadal, N. Barros, L. Peres, V. Goetz, M. Respaud, K. Soulantica, and H. Kachachi, “In situ synthesis of gold nanoparticles in polymer films under concentrated sunlight: control of nanoparticle size and shape with solar flux,” *Reaction Chemistry & Engineering*, vol. 5, no. 2, pp. 330–341, 2020.
- [81] M. Fox, *Optical Properties of Solids (Oxford Master Series in Physics)*. Oxford University Press, 2002.
- [82] H. Fujiwara, J. Koh, P. I. Rovira, and R. W. Collins, “Assessment of effective-medium theories in the analysis of nucleation and microscopic surface roughness evolution for semiconductor thin films,” *Physical Review B*, vol. 61, pp. 10832–10844, Apr 2000.
- [83] H. Fujiwara, *Spectroscopic Ellipsometry*. John Wiley & Sons, Ltd, Jan. 2007.
- [84] R. C. Jones, “A new calculus for the treatment of optical systems. description and discussion of the calculus,” *J. Opt. Soc. Am.*, vol. 31, pp. 488–493, Jul 1941.

- [85] K. Johansen, H. Arwin, I. Lundström, and B. Liedberg, “Imaging surface plasmon resonance sensor based on multiple wavelengths: Sensitivity considerations,” *Review of Scientific Instruments*, vol. 71, pp. 3530–3538, Sept. 2000.
- [86] P. B. Johnson and R. W. Christy, “Optical constants of the noble metals,” *Physical Review B*, vol. 6, pp. 4370–4379, Dec. 1972.
- [87] H.-M. Kim, M. Uh, D. H. Jeong, H.-Y. Lee, J.-H. Park, and S.-K. Lee, “Localized surface plasmon resonance biosensor using nanopatterned gold particles on the surface of an optical fiber,” *Sensors and Actuators B: Chemical*, vol. 280, pp. 183 – 191, 2019.
- [88] E. Hutter and J. Fendler, “Exploitation of localized surface plasmon resonance,” *Advanced Materials*, vol. 16, no. 19, pp. 1685–1706, 2004.
- [89] N. Bhalla, H.-J. Chiang, and A. Q. Shen, “Chapter 10 - cell biology at the interface of nanobiosensors and microfluidics,” in *Microfluidics in Cell Biology Part C: Microfluidics for Cellular and Subcellular Analysis* (D. A. Fletcher, J. Doh, and M. Piel, eds.), vol. 148 of *Methods in Cell Biology*, pp. 203 – 227, Academic Press, 2018.
- [90] H. H. Fröhlich, *Theory of dielectrics : dielectrics constant and dielectric loss*. Oxford : Clarendon Press, 2nd ed ed., 1986.
- [91] M. Quinten, *Optical Properties of Nanoparticle Systems*. Wiley-VCH Verlag GmbH & Co. KGaA, Jan. 2011.
- [92] “Mem. di mathem. e fisica in modena,” *La Revue des revues.*, vol. 24, p. 49, 1850.
- [93] R. Clausius, “Die mechanische U’grmetheorie 2,” *book, pg*, vol. 62, 1879.
- [94] R. Ruppin, “Validity range of the Maxwell-Garnett Theory,” *Physica Status Solidi (b)*, vol. 87, pp. 619–624, June 1978.
- [95] H. Tompkins, *A User’s Guide to Ellipsometry*. Academic Press, 1993.
- [96] A. Heilmann, *Polymer Films with Embedded Metal Nanoparticles*. Springer, 2003.
- [97] A. H. Sihvola, *Electromagnetic mixing formulas and applications*. No. 47 in IEE electromagnetic waves series, London: Institution of Engineering and Technology, 1st ed. ed., 1999.
- [98] S. Adachi, *Optical Properties of Crystalline and Amorphous Semiconductors*. Springer US, 1999.
- [99] R. Azzam and N. Bashara, *Ellipsometry and Polarized Light*. Amsterdam: Elsevier Science B.V., 2nd ed., 1987.
- [100] J. D. Ingle and S. R. Crouch, *Spectrochemical analysis*. Englewood Cliffs, N.J. : Prentice Hall, 1988.

- [101] M. A. Green, “Self-consistent optical parameters of intrinsic silicon at 300 k including temperature coefficients,” *Solar Energy Materials and Solar Cells*, vol. 92, p. 1305–1310, 2008.
- [102] H. Tompkins and E. Irene, *Handbook of Ellipsometry*. Springer Berlin Heidelberg, 2005.
- [103] R. M. A. Azzam and N. M. Bashara, *Ellipsometry and Polarized Light*. North-Holland, 1977.
- [104] F. Bernoux, J.-P. Piel, B. Castellon, C. Defranoux, J.-H. Lecat, P. Boher, and J.-L. Stehlé, “Ellipsométrie théorie,” *Techniques de l’ingénieur Métrologie optique et photonique*, no. ref. article : r6490, 2003.
- [105] R. J. Archer, *Manual on ellipsometry*. Gaertner Scientific Corp., Chicago, 1968.
- [106] G. Binnig, C. F. Quate, and C. Gerber, “Atomic force microscope,” *Physical Review Letters*, vol. 56, pp. 930–933, Mar. 1986.
- [107] D. Necas and P. Klapetek, “Gwyddion: an open-source software for SPM data analysis,” *Central European Journal of Physics*, vol. 10, pp. 181–188, 2012.
- [108] W. O. Herrmann and W. Haehnel, 1924.
- [109] X. Tang and S. Alavi, “Recent advances in starch, polyvinyl alcohol based polymer blends, nanocomposites and their biodegradability,” *Carbohydrate Polymers*, vol. 85, no. 1, pp. 7 – 16, 2011.
- [110] C. J. Murphy, T. K. Sau, A. M. Gole, C. J. Orendorff, J. Gao, L. Gou, S. E. Hunyadi, and T. Li, “Anisotropic metal nanoparticles: Synthesis, assembly, and optical applications.,” *The Journal of Physical Chemistry. B*, vol. 109, pp. 13857–13870, 2005.
- [111] A. G. Emslie, F. T. Bonner, and L. G. Peck, “Flow of a viscous liquid on a rotating disk,” *Journal of Applied Physics*, vol. 29, pp. 858–862, May 1958.
- [112] J. Danglad-Flores, S. Eickelmann, and H. Riegler, “Deposition of polymer films by spin casting: A quantitative analysis,” *Chemical Engineering Science*, vol. 179, pp. 257–264, Apr. 2018.
- [113] S. Clémenson, D. Léonard, D. Sage, L. David, and E. Espuche, “Metal nanocomposite films prepared in situ from PVA and silver nitrate. study of the nanostructuration process and morphology as a function of the in situ routes,” *Journal of Polymer Science, Part A: Polymer Chemistry*, vol. 46, pp. 2062–2071, 2008.
- [114] L. Nicolais and G. Carotenuto, *Nanocomposites : In Situ Synthesis of Polymer-Embedded Nanostructures*. Wiley, 2014.

- [115] M. J. Schnepf, M. Mayer, C. Kuttner, M. Tebbe, D. Wolf, M. Dulle, T. Al-tantzis, P. Formanek, S. Förster, S. Bals, T. A. F. König, and A. Fery, “Nanorattles with tailored electric field enhancement,” *Nanoscale*, vol. 9, no. 27, pp. 9376–9385, 2017.
- [116] K. J. Berg, A. Berger, and H. Hofmeister, “Small silver particles in glass surface layers produced by sodium-silver ion exchange – their concentration and size depth profile,” *Zeitschrift für Physik D Atoms, Molecules and Clusters*, vol. 20, pp. 309–311, Mar. 1991.
- [117] U. Kreibig and C. V. Fragstein, “The limitation of electron mean free path in small silver particles,” *Zeitschrift für Physik*, vol. 224, pp. 307–323, Aug. 1969.
- [118] D. E. Aspnes, J. B. Theeten, and F. Hottier, “Investigation of effective-medium models of microscopic surface roughness by spectroscopic ellipsometry,” *Physical Review B*, vol. 20, pp. 3292–3302, Oct 1979.
- [119] D. E. Aspnes, “Plasmonics and the effective-medium theory,” in *Ellipsometry at the Nanoscale* (M. Losurdo and K. Hingerl, eds.), ch. 5, pp. 225–256, Springer-Verlag, 2013.
- [120] H. Wormeester and T. Oates, “Thin films of nanostructured noble metals,” in *Ellipsometry at the Nanoscale* (M. Losurdo and K. Hingerl, eds.), ch. 6, pp. 225–256, Springer-Verlag, 2013.
- [121] A.-S. Keita and A. En Naciri, “Size distribution dependence of the dielectric function of si quantum dots described by a modified maxwell-garnett formulation,” *Physical Review B*, vol. 84, p. 125436, 2011.
- [122] J. Toudert, L. Simonot, S. Camelio, and D. Babonneau, “Advanced optical effective medium modeling for a single layer of polydisperse ellipsoidal nanoparticles embedded in a homogeneous dielectric medium: Surface plasmon resonances,” *Physical Review B - Condensed Matter and Materials Physics*, vol. 86, p. 045415, 2012.
- [123] Y. Battie, A. En Naciri, W. Chamorro, and D. Horwat, “Generalized effective medium theory to extract the optical properties of two-dimensional nonspherical metallic nanoparticle layers,” *Journal of Physical Chemistry C*, vol. 118, pp. 4899–4905, 2014.
- [124] J. Lekner, *Theory of Reflection of Electromagnetic and Particle Waves*. Martinus Nijhoff Publishers, 1987.
- [125] D. Bedeaux and J. Vlieger, *Optical Properties of Surfaces*. Imperial College Press, 2002.
- [126] E. S. Kooij, H. Wormeester, E. A. M. Brouwer, E. van Vroonhoven, A. van Silfhout, and B. Poelsema, “Optical characterization of thin colloidal gold films by spectroscopic ellipsometry,” *Langmuir*, vol. 18, no. 11, pp. 4401–4413, 2002.

- [127] H. Wormeester, E. S. Kooij, and B. Poelsema, “Unambiguous optical characterization of nanocolloidal gold films,” *Physical Review B*, vol. 68, p. 085406, 2003.
- [128] C. Cortes and V. Vapnik, “Support-vector networks,” *Machine Learning*, vol. 20, no. 3, pp. 273–297, 1995.
- [129] D. Meyer, E. Dimitriadou, K. Hornik, A. Weingessel, and F. Leisch, *e1071: Misc Functions of the Department of Statistics (e1071)*, TU Wien, 2014. R package version 1.6-2.
- [130] P. Klapetek, *Quantitative Data Processing in Scanning Probe Microscopy – SPM Applications for Nanometrology*. Elsevier, 2012.
- [131] K. Banu and T. Shimura, “A novel electroless method for the deposition of single-crystalline gold nanocrystals on and inside an organic solid-matrix,” *New Journal of Chemistry*, vol. 35, pp. 1031–1041, 2011.
- [132] A. Yanguas-Gil and H. Wormeester, *Relationship Between Surface Morphology and Effective Medium Roughness*, pp. 179–202. Berlin, Heidelberg: Springer Berlin Heidelberg, 2013.
- [133] C. Tsou, Y. S Huang, and H. C Chang, “On the determination of thermal expansion coefficient of thermal oxide,” *Sensors and Materials*, vol. 17, pp. 339–342, 01 2005.
- [134] T. Toyoda and M. Yabe, “The temperature dependence of the refractive indices of fused silica and crystal quartz,” *Journal of Physics D: Applied Physics*, vol. 16, no. 5, p. L97, 1983.
- [135] A. Noorjahan and P. Choi, “Thermodynamic properties of poly(vinyl alcohol) with different tacticities estimated from molecular dynamics simulation,” *Polymer*, vol. 54, pp. 4212–4219, 07 2013.
- [136] J. L. Keddie, R. A. L. Jones, and R. A. Cory, “Size-dependent depression of the glass transition temperature in polymer films,” *Europhysics Letters*, vol. 27, p. 59, 1994.
- [137] R. J. Archer, “Determination of the properties of films on silicon by the method of ellipsometry,” *Journal of the Optical Society of America*, vol. 52, p. 970, Sept. 1962.
- [138] T. Oates, H. Wormeester, and H. Arwin, “Characterization of plasmonic effects in thin films and metamaterials using spectroscopic ellipsometry,” *Prog. Surf. Sci.*, vol. 86, no. 11-12, pp. 328–376, 2011.

Plasmonic nanocomposites embedding gold and silver nanoparticles: *in situ* synthesis and local optical properties by spectroscopic imaging ellipsometry

During the last 40 years, research on metallic nanoparticles found an increasing interest due to the development of new techniques to probe the nanoworld. Numerous scientists developed new materials called nanocomposite and composed of nano-objects integrated in a dielectric matrix. Among them, plasmonic nanocomposites based on noble metals have numerous applications such as optical sensors, spectrally selective coatings and sensors for bio-medical diagnostics. This class of new attractive materials is a great topic of research due to a peculiar aspect of their optical properties: the Localized Surface Plasmon Resonance.

In this experimental thesis, we try to have a better understanding on the growth process of gold and silver nanoparticles *in situ* synthesized in a polymer matrix. The *in situ* synthesis is a simpler and a faster preparation method than conventional methods for plasmonic nanocomposites but less control on the size and shape of the nanoparticles is possible. As the *in situ* growth of metallic nanoparticles is not completely understood, we used advanced optical techniques to unravel the detailed mechanism linking the optical properties of the nanocomposite to their structural parameters.

In this context, we have prepared nanocomposites embedding silver or gold nanoparticles. We first studied the impact of the thickness of the film on the localized surface plasmon resonance parameters. We have shown that this experimental parameter has a large impact on the size of the nanoparticles *in situ* synthesized in the polymer matrix. Furthermore, we presented an experimental study of the optical properties of gold-doped nanocomposites using single wavelength imaging ellipsometry. We have found that, for a thin polymer film and at gold-doping level less than 0.2%, the growth of the gold nanoparticles inhomogeneously occurred within the film. Finally, at this low doping level, the optical constant determined by the conventional spectroscopic ellipsometry spectra is only relevant for the polymer matrix. We have shown the advantage of using imaging spectroscopic ellipsometry by choosing areas on the image with a different intensity contrast and have access to the local optical properties at microscale.

Université de Mons
20, Place du Parc, B7000 Mons - Belgique
Tél: +32(0)65 373111
Courriel: info.mons@umons.ac.be
www.umons.ac.be



